

# INAUGURAL DISSERTATION

for  
obtaining the doctoral degree  
of the

Combined Faculty of Mathematics, Engineering and  
Natural Sciences

of the  
Ruprecht - Karls - University  
Heidelberg

presented by  
Mariam Amghar  
Master of Science in Pharmaceutical Biotechnology  
born in: Prato, Italy

Date of oral examination: 18.07.2025



$[^{225}\text{Ac}]\text{Ac-}/[^{177}\text{Lu}]\text{Lu-PSMA-617}$  mutational  
landscape in circulating tumor DNA (ctDNA):  
early clinical outcome prediction in metastatic  
castration-resistant prostate cancer

Referees:

Prof. Dr. rer. nat. Gert Fricker  
Prof. Dr. rer. nat. Nina Papavasiliou





*This thesis was financially supported by a PhD grant (Ca 201) from the German Cancer Research Center (DKFZ) & Ministry of Science, Technology and Space (MOST) joint funding.*

## **Thesis Declaration**

Hereby, I declare that I wrote this Doctoral Thesis independently under the supervision of Dr. Martina Benešová-Schäfer and Dr. Mareike Roscher and have not used any other than permitted reference sources or materials nor engaged in any plagiarism. All references and other sources used by me have been appropriately acknowledged in the work. I further declare that the work has not been submitted for the purpose of academic examination, either in its original or similar form, anywhere else.

Heidelberg, 05.05.2025

Mariam Amghar



**Author:** MSc. Mariam Amghar

**Supervisor:** Dr. Martina Benešová-Schäfer & Dr. Mareike Roscher

**Institution:** Heidelberg University / German Cancer Research Center (DKFZ)

**[<sup>225</sup>Ac]Ac-/ [<sup>177</sup>Lu]Lu-PSMA-617 mutational landscape in circulating tumor DNA (ctDNA): early clinical outcome prediction in metastatic castration-resistant prostate cancer**

## ABSTRACT

Metastatic castration-resistant prostate cancer (mCRPC) represents one of the most intractable challenges in contemporary clinical oncology. In this context, prostate-specific membrane antigen (PSMA)-targeted radioligand therapy (TRNT) with [<sup>177</sup>Lu]Lu-PSMA-617 has emerged as a transformative therapeutic approach, offering new hope for patients with otherwise limited treatment options. Despite its promise, resistance to [<sup>177</sup>Lu]Lu-PSMA ligands is observed in approximately 30% of patients, underscoring the urgent need for improved strategies to overcome primary treatment failure. In response to these limitations, the field has shifted toward innovative radiotherapeutic combinations. Among them, tandem therapy—uniting the potent alpha-emitting [<sup>225</sup>Ac]Ac-PSMA-617 with the clinically approved [<sup>177</sup>Lu]Lu-PSMA-617—has demonstrated remarkable potential to enhance antitumor efficacy while minimizing dose-limiting toxicities. The aim of this work is to deliver a comprehensive evaluation of clinical real-world data from patients with mCRPC treated with [<sup>225</sup>Ac]Ac-/ [<sup>177</sup>Lu]Lu-PSMA-617 under compassionate care regulations. This thesis explores the use of tumor fraction (TFx) estimation, derived *via* the ichorCNA algorithm from ultra-low-pass whole genome sequencing (ULP-WGS) of circulating free DNA (cfDNA), as a biomarker to monitor treatment response and resistance in mCRPC patients receiving tandem actinium-lutetium therapy. Serial cfDNA samples from 78 mCRPC patients revealed that TFx strongly correlated with PSA levels and offered superior sensitivity in capturing metastatic burden. High pre-treatment TFx was linked to a markedly increased risk of relapse, while genomic profiling uncovered two distinct subgroups—one with low TFx and minimal copy number variations (CNVs), and another with elevated TFx and high genomic instability. Strikingly, patients with lower CNV burden experienced longer survival, underscoring its potential as a powerful prognostic biomarker. Pre-treatment status emerged as a critical determinant of survival, offering key insights into the role of prior exposure to TRNT and chemotherapy in influencing long-term outcomes. Gene signature linked to high CNV burden was identified, highlighting key chromosomes and relapse-associated genes as potential drivers of poor prognosis and therapeutic targets.

## Key Words

Metastatic Castration-Resistant Prostate Cancer (mCRPC), Prostate-Specific Membrane Antigen (PSMA), Targeted Radioligand Therapy (TRNT), [ $^{225}\text{Ac}$ ]Ac-PSMA-617, Tandem Alpha-Beta Therapy, Tumor Fraction (TFx), Ultra-Low-Pass Whole Genome Sequencing (ULP-WGS), ichorCNA Algorithm, Circulating Tumor DNA (ctDNA), Circulating Free DNA (cfDNA), Copy Number Variations (CNV).

**Autor:** MSc. Mariam Amghar

**Betreuer:** Dr. Martina Benešová-Schäfer & Dr. Mareike Roscher

**Institution:** Universität Heidelberg / Deutsches Krebsforschungszentrum (DKFZ)

**Die Mutationslandschaft zirkulierender Tumor-DNA nach [<sup>225</sup>Ac]Ac-/[<sup>177</sup>Lu]Lu-PSMA-617  
Behandlungszyklen: frühe klinische Vorhersage von Therapieansprechen bei metastasiertem  
kastrationsresistentem Prostatakarzinom**

## ZUSAMMENFASSUNG

Das metastasierte kastrationsresistente Prostatakarzinom (mCRPC) stellt eine der größten Herausforderungen der modernen klinischen Onkologie dar. Die zielgerichtete Radioligandentherapie (TRNT) mit dem klinisch zugelassenen Therapeutikum [<sup>177</sup>Lu]Lu-PSMA-617 gegen das prostataspezifische Membranantigen (PSMA) konnte sich hier in den vergangenen Jahren als transformative therapeutische Strategie etablieren und bietet neue Hoffnung für Patienten mit ansonsten begrenzten Behandlungsmöglichkeiten. Trotz ihres Potenzials wird dennoch bei etwa 30 % der Patienten eine Resistenz gegenüber [<sup>177</sup>Lu]Lu-PSMA-Liganden beobachtet, was den dringenden Bedarf verbesserter Strategien zur Überwindung des primären Therapieversagens hervorhebt. Als Antwort auf diese Limitationen hat sich das Feld der Nuklearmedizin in Richtung innovativer, radiotherapeutischer Kombinationen weiterentwickelt. Besonders vielversprechend ist hierbei eine Tandemtherapie – die Kombination des potenten alpha-emittierenden [<sup>225</sup>Ac]Ac-PSMA-617 mit dem etablierten beta-emittierenden [<sup>177</sup>Lu]Lu-PSMA-617. Diese Therapie soll die antitumorale Wirksamkeit steigern und gleichzeitig dosislimitierende Toxizitäten minimieren.

Ziel dieser Arbeit ist die umfassende Analyse klinischer „Real-World“-Daten von mCRPC-Patienten, die im Rahmen von Härtefallregelungen mit [<sup>225</sup>Ac]Ac-/[<sup>177</sup>Lu]Lu-PSMA-617 behandelt wurden. Untersucht wurde insbesondere der mögliche Einsatz der Tumorfraktion (TFx), die mithilfe des ichorCNA-Algorithmus aus *ultra-low-pass* Ganzgenomsequenzierung (ULP-WGS) von zellfreier DNA (cfDNA) berechnet wurde. Die TFx dient als Biomarker zur Überwachung von Therapieansprechen und Resistenzentwicklung bei Patienten, die eine Tandemtherapie mit Actinium und Lutetium erhielten. Serielle cfDNA-Proben von 78 mCRPC-Patienten zeigten, dass die TFx stark mit dem PSA-Spiegel korrelierte und eine überlegene Sensitivität zur Erfassung der Metastasierung aufwies. Eine hohe TFx vor Therapiebeginn war mit einem signifikant erhöhten Rückfallrisiko assoziiert. Zudem identifizierte das genomische Profiling zwei unterschiedliche Subgruppen – eine mit niedriger TFx und minimalen Kopienzahlveränderungen (CNVs) und eine weitere mit hoher TFx und ausgeprägter genomischer Instabilität. Bemerkenswerterweise wiesen Patienten mit geringer CNV-Belastung ein längeres Überleben auf, was die prognostische Relevanz dieses Biomarkers unterstreicht. Der prätherapeutische Status erwies sich als entscheidender Faktor für das Überleben und liefert wichtige Erkenntnisse zur Rolle früherer Therapien mit TRNT und Chemotherapie in Bezug auf langfristige

Behandlungsergebnisse. Darüber hinaus wurde eine Gen-Signatur identifiziert, die mit hoher CNV-Belastung assoziiert ist und somit sogenannte Schlüsselchromosomen sowie Rückfall-assoziierte Gene als potenzielle Indikatoren einer schlechten Prognose aber auch als eine mögliche Zielstruktur zur Therapie darstellen können.

## SCHLÜSSELWÖRTER

metastasiertes kastrationsresistentes Prostatakarzinom (mCRPC), prostata-spezifisches Membrantigen (PSMA), zielgerichtete Radioligandentherapie (TRNT), [<sup>225</sup>Ac]Ac-PSMA-617, Tandem-Alpha-Beta-Therapie, Tumorfraction (TFx), Ultra-Low-Pass Ganzgenomsequenzierung (ULP-WGS), ichorCNA-Algorithmus, zirkulierende Tumor-DNA (ctDNA), zirkulierende freie DNA (cfDNA), Kopienzahlveränderungen (CNV).

# Table of Contents

<b>ABSTRACT</b>	<i>i</i>
<b>ZUSAMMENFASSUNG</b>	<i>iii</i>
<b>LIST OF FIGURES</b>	<i>ix</i>
<b>LIST OF TABLES</b>	<i>xiii</i>
<b>I INTRODUCTION</b>	<b>1</b>
<b>1.CANCER</b>	<b>1</b>
1.1 Prostate Cancer	2
1.2 Clinical management of PCa	4
1.3 Metastatic castration resistant PCa	7
1.4 Tumor Markers for PCa and mCRPC	8
<b>2. Prostate-specific membrane antigen (PSMA)</b>	<b>10</b>
2.1 PSMA as a treatment target	11
<b>3.NUCLEAR MEDICINE</b>	<b>11</b>
3.1 Imaging strategies	12
<b>3.2 PSMA-targeted radioligand therapy</b>	<b>12</b>
<b>4. LIQUID BIOPSY</b>	<b>15</b>
4.1 Circulating free DNA (cfDNA)	17
4.2 Circulating tumor DNA (ctDNA)	17
4.3 Applications of ctDNA in the clinic	18
<b>II AIM OF THE STUDY</b>	<b>21</b>
<b>III MATERIAL &amp; METHODS</b>	<b>23</b>
<b>1. ETHICAL APPROVAL</b>	<b>23</b>
<b>2. PATIENTS</b>	<b>23</b>
<b>3. SAMPLES</b>	<b>24</b>
3.1 Sample collection & processing	25
3.2 cfDNA extraction quantification and quality control	27
3.3 cfDNA library preparation	29

<b>4. NEXT GENERATION SEQUENCING</b>	32
4.1 ULP-WGS data analysis	32
<b>5. BIOSTATISTICAL ANALYSIS</b>	33
5.1 Biomarker dynamics across treatment cycles	33
5.2 Analysis of TM distribution across metastasis stages	34
5.3 Correlation analyses	34
5.4 Longitudinal biomarker dynamics and correlation	34
<b>6. RISK ANALYSIS</b>	36
6.1 Predictive performance using ROC analysis	36
6.2 Cox hazard ratio analysis	37
6.3 Survival analysis	37
<b>7. GENOMIC ANALYSIS</b>	38
7.1 Tfx clustering and CNV burden correlation analysis	38
7.2 Tfx correlation with CNV burden	39
7.3 GISTIC analysis	39
7.4 Identification of oncogenes and tumor suppressors	40
7.5 EnrichR analysis	41
<b>IV RESULTS</b>	43
<b>1. PATIENTS</b>	43
1.2 Patient cohort characterization	43
<b>2. TM DYNAMICS</b>	47
2.1 Tfx across treatment cycles	47
2.2 PSA across treatment cycles	49
2.3 ALP across treatment cycles	51
2.4 LDH across treatment cycles	53
<b>3. CORRELATION ANALYSIS</b>	55
3.1 Correlation analysis: Tfx & PSA	55
3.2 Correlation analysis: Tfx & LDH	56
3.3 Correlation analysis: Tfx & ALP	57



3.4 Correlation with clinical outcomes	58
<b>4. Distribution of TFx and PSA across metastasis group</b>	61
4.1 PSA distribution across metastasis groups	61
4.2 TFx distribution across metastasis groups	63
<b>5. RISK ANALYSIS: TFx AS A PREDICTIVE BIOMARKER</b>	65
5.1 ROC analysis: sensitivity and specificity Test	65
5.2 Cox hazard ratio analysis: TFx increases and risk of relapse	66
5.3 OS based on CNV burden	68
5.4 OS based on pre-treatment	69
5.5 OS based on TFx stratification	70
<b>6. CNV ANALYSIS</b>	71
6.1 CNVs clustering	71
6.2 TFx and CNV burden correlation	73
<b>7. GENOMIC ANALYSIS</b>	74
7.1 GISTIC analysis on baseline ctDNA samples	75
7.2 Validation of baseline ctDNA alterations using tumor tissue data	76
7.3 GISTIC analysis on Cluster 1	77
7.4 GISTIC analysis on Cluster 2	78
7.5 GISTIC analysis on baseline and PD samples	79
<b>8. GENE SIGNATURE IDENTIFICATION</b>	81
8.1 Baseline vs. Cluster 2 gene signatures	81
<b>9. EnrichR</b>	83
9.1 EnrichR pathway analysis of oncogenes in Cluster 2	83
9.2 EnrichR pathway analysis of tumor suppressor genes in Cluster 2	85
<b>10. CASE STUDIES: CHEMO-RESISTANT PATIENTS</b>	86
10.1 Patient 5	88
10.2 Patient 10	92
10.3 Patient 38	99
10.4 Patient 37	103
10.5 Patient 11	106

10.6 Patient 34	112
10.7 Patient 40	115
10.8 Patient 91	119
<b>11. CASE STUDIES: CHEMO-NAIVE PATIENTS</b>	<b>124</b>
11.1 Patient 25	126
11.2 Patient 60	128
11.3 Patient 95	130
11.4 Patient 96	132
11.5 Patient 23	134
<b>V DISCUSSION</b>	<b>137</b>
<b>VI CONCLUSION</b>	<b>147</b>
<b>VII OUTLOOK</b>	<b>149</b>
<b>VIII REFERENCES</b>	<b>151</b>
<b><i>ACKNOWLEDGEMENTS</i></b>	<b><i>165</i></b>
<b><i>LIST OF PUBLICATIONS</i></b>	<b><i>167</i></b>
<b><i>ABSTRACTS FROM CONFERENCES</i></b>	<b><i>169</i></b>
<b><i>LIST OF ABBREVIATIONS &amp; ACRONYMS</i></b>	<b><i>171</i></b>
<b><i>APPENDIX</i></b>	<b><i>175</i></b>

# LIST OF FIGURES

**Figure 1:** This figure illustrates the progression, classification, and survival outcomes associated with prostate cancer, integrating visual staging, tumor classification, and treatment resistance categories.

**Figure 2:** Schematic representation of clinical management of prostate cancer and the different therapies options.

**Figure 3:** Schematic representation of PSMA, illustrating its cellular receptor and structural features.

**Figure 4:** Schematic representation of the rationale behind PSMA-targeting radiopharmaceuticals.

**Figure 5:** Schematic representation of liquid biopsy concept and different applications in the clinical field.

**Figure 6:** Schematic representation of ctDNA clinical application that range from early cancer detection, surveillance for micrometastatic disease and treatment selection and response monitoring.

**Figure 7:** Overview of the study's objective to stratify mCRPC patients undergoing PSMA-targeted radioligand therapy.

**Figure 8:** Schematic depiction of the molecular workflow from cfDNA extraction to sequencing.

**Figure 9:** Overview of the bimonthly blood collection schedule prior to therapy administration, including the associated sample processing.

**Figure 10:** Optimal cfDNA profile obtained using the TapeStation.

**Figure 11:** Suboptimal cfDNA profile obtained using the TapeStation.

**Figure 12:** Colibri PS DNA Library Prep Kit steps from the manufacturer manual description.

**Figure 13:** cfDNA library quality showing a primary ~300 bp peak starting from an optimal cfDNA, assessed using the Bioanalyzer.

**Figure 14:** cfDNA library quality showing a primary ~300 bp peak starting from a suboptimal cfDNA, assessed using the Bioanalyzer.

**Figure 15:** cfDNA library profile after adapter dimer removal, showing a primary peak at ~300 bp.

**Figure 16:** Distribution and median age of the patients in the included cohort.

**Figure 17:** Upset plot representing the patient's pretreatments intersection.

**Figure 18:** Pie chart illustrating the distribution of radionuclide therapies administered as pre-treatment.

**Figure 19:** Tfx dynamics across  $[^{225}\text{Ac}]\text{Ac-}/[^{177}\text{Lu}]\text{Lu-PSMA-617}$  treatment cycles.

**Figure 20:** PSA dynamics across  $[^{225}\text{Ac}]\text{Ac-}/[^{177}\text{Lu}]\text{Lu-PSMA-617}$  treatment cycles.

**Figure 21:** ALP dynamics across  $[^{225}\text{Ac}]\text{Ac-}/[^{177}\text{Lu}]\text{Lu-PSMA-617}$  treatment cycles.

**Figure 22:** LDH dynamics across  $[^{225}\text{Ac}]\text{Ac-}/[^{177}\text{Lu}]\text{Lu-PSMA-617}$  treatment cycles.

**Figure 23:** Scatter plot showing the correlation between Tfx (x-axis) and PSA levels (y-axis).

**Figure 24:** Scatter plot showing the correlation between Tfx values (x-axis) and LDH levels (y-axis).

**Figure 25:** Scatter plot showing the correlation between Tfx values (y-axis) and ALP levels (x-axis).

**Figure 26:** Heatmap illustrating fold changes in LDH, Tfx, and PSA levels across individual patients.

**Figure 27:** Violin plots showing the distribution of baseline PSA levels across three metastasis groups: bone-only, bone and lymph node, and bone, lymph node, and additional organ involvement.

**Figure 28:** Violin plots illustrating the distribution of baseline Tfx levels across three metastasis groups: bone-only, bone and lymph node, and bone, lymph node, and additional organ metastases.

**Figure 29:** The ROC curves depict the predictive performance of pre-cycle PSA levels (black line), pre-cycle Tfx (red line), and a combined model of PSA, Tfx, and LDH (green line).

**Figure 30:** Swimmer plot visualizing treatment cycles for individual patients, with green and pink bars indicating non-progressive and progressive disease, respectively, and symbols marking Tfx increases and key clinical milestones.

**Figure 31:** Kaplan-Meier survival curves stratified by CNV burden.

**Figure 32:** Kaplan-Meier survival curves stratified by pre-treatment regimens.

**Figure 33:** Kaplan-Meier survival curves stratified by Tfx groups.

**Figure 34:** Heatmap displaying hierarchical clustering of CNVs across 1 Mb chromosomal bins.

**Figure 35:** Box plot showing the distribution of Tfx values across high and low CNV burden groups.

**Figure 36:** GISTIC analysis of cfDNA from 57 mCRPC patients, highlighting significant genomic alterations.

**Figure 37:** GISTIC analysis of tissue samples from the cBioPortal mCRPC dataset, identifying significant genomic deletions (left panel, blue) and amplifications (right panel, red).

**Figure 38:** GISTIC analysis of Cluster 1 (low CNV burden), showing limited genomic alterations.

**Figure 39:** GISTIC analysis of Cluster 2 (high CNV burden), highlighting significant genomic alterations.

**Figure 40:** GISTIC analysis of baseline ctDNA samples from 17 mCRPC patients with Tfx > 0.10, highlighting key genomic alterations.

**Figure 41:** GISTIC on 17 patients testing the respective progressive disease group of samples.

**Figure 42:** Gene signature baseline – progressive disease.

**Figure 43:** EnrichR pathway analysis of oncogenes with gain-of-function alterations in Cluster 2.

**Figure 44:** EnrichR pathway analysis of tumor suppressor genes with loss-of-function alterations in Cluster 2.

**Figure 45:** Imaging overview of Patient 5 throughout actinium-lutetium PSMA-TRNT.

**Figure 46:** Overview image sequence for Patient 5.

**Figure 47:** Comprehensive overview of the dynamic changes in A) PSA, B) Tfx, C) LDH and D) ALP in Patient 5, following  $[^{225}\text{Ac}]\text{Ac-}/[^{177}\text{Lu}]\text{Lu-PSMA-617}$  regimen.

**Figure 48:** CNA profiles for Patient 5 across multiple treatment timepoints.

**Figure 49:** Imaging overview of Patient 10 undergoing actinium-lutetium PSMA-TRNT.

**Figure 50:** Imaging conducted after a two-year treatment hiatus and subsequent transition to Olaparib and Abiraterone therapy for Patient 10.

**Figure 51:** Comprehensive overview of the dynamic changes in A) PSA, B) Tfx, C) LDH and D) ALP in Patient 10, following  $[^{225}\text{Ac}]\text{Ac-}/[^{177}\text{Lu}]\text{Lu-PSMA-617}$  regimen.

**Figure 52:** Comprehensive overview of the dynamic changes in A) PSA, B) Tfx, C) LDH and D) ALP in Patient 10, following a two-year treatment break and a therapy switch to Olaparib and Abiraterone.

**Figure 53:** CNA profiles for Patient 10 across four treatment timepoints. Each panel represents a distinct timepoint, starting with the baseline (pre-treatment) followed by sequential post-treatment cycles.

**Figure 54:** CNA profiles for Patient 10 one treatment cycle.

**Figure 55:** Imaging overview of Patient 38 throughout [ $^{225}\text{Ac}$ ]Ac-/ [ $^{177}\text{Lu}$ ]Lu-PSMA-617.

**Figure 56:** Comprehensive overview of the dynamic changes in A) PSA, B) Tfx, C) LDH and D) ALP in Patient 38, following with [ $^{225}\text{Ac}$ ]Ac-/ [ $^{177}\text{Lu}$ ]Lu-PSMA-617 regimen.

**Figure 57:** CNA profiles for Patient 38 across four treatment timepoints.

**Figure 61:** Imaging overview of Patient 37 treated with [ $^{225}\text{Ac}$ ]Ac-/ [ $^{177}\text{Lu}$ ]Lu-PSMA-617.

**Figure 62:** Comprehensive overview over the dynamic changes in A) PSA, B) Tfx, C) LDH and D) ALP in Patient 37, following [ $^{225}\text{Ac}$ ]Ac-/ [ $^{177}\text{Lu}$ ]Lu-PSMA-617 regimen.

**Figure 63:** CNA profiles for Patient 37 across four treatment timepoints.

**Figure 64:** Imaging overview of Patient 11 treated with [ $^{225}\text{Ac}$ ]Ac-/ [ $^{177}\text{Lu}$ ]Lu-PSMA-617 therapy.

**Figure 65:** Imaging five months staging post-PSMA-RLT in Patient 11 treated with PSMA-TRNT using PSMA-SPECT using [ $^{99\text{m}}\text{Tc}$ ]Tc-PSMA-GCK01, followed by treatment scan upon 4<sup>th</sup> treatment administration.

**Figure 66:** Comprehensive overview over the dynamic changes in A) PSA, B) Tfx, C) LDH and D) ALP in Patient 11, following [ $^{225}\text{Ac}$ ]Ac-/ [ $^{177}\text{Lu}$ ]Lu-PSMA-617 regimen. Data points are plotted over the treatment period, providing insights into disease progression.

**Figure 67:** CNA profiles for Patient 11 across four treatment timepoints. Each panel represents a distinct timepoint, starting with the baseline (pre-treatment) followed by sequential post-treatment cycles.

**Figure 58:** Imaging overview of Patient 34 treated with [ $^{225}\text{Ac}$ ]Ac-/ [ $^{177}\text{Lu}$ ]Lu-PSMA-617.

**Figure 59:** Comprehensive overview over the dynamic changes in A) PSA, B) Tfx, C) LDH and D) ALP in Patient 34, following [ $^{225}\text{Ac}$ ]Ac-/ [ $^{177}\text{Lu}$ ]Lu-PSMA-617 regimen.

**Figure 60:** CNA profiles for Patient 34 across four treatment timepoints. Each panel represents a distinct timepoint, starting with the baseline (pre-treatment) followed by sequential post-treatment cycles.

**Figure 68:** Imaging overview of Patient 40 treated with [ $^{225}\text{Ac}$ ]Ac-/ [ $^{177}\text{Lu}$ ]Lu-PSMA-617.

**Figure 69:** Comprehensive overview over the dynamic changes in A) PSA, B) Tfx, C) LDH and D) ALP in Patient 40, following [ $^{225}\text{Ac}$ ]Ac-/ [ $^{177}\text{Lu}$ ]Lu-PSMA-617 regimen.

**Figure 70:** CT imaging overviews of Patient 40.

**Figure 71:** CNA profiles for Patient 40 across four treatment timepoints.

**Figure 72:** Imaging of Patient 91 treated with [ $^{225}\text{Ac}$ ]Ac-/ [ $^{177}\text{Lu}$ ]Lu-PSMA-617.

**Figure 73:** Mid-therapy CT overviews of Patient 91, showing liver metastasis progression.

**Figure 74:** Comprehensive overview over the dynamic changes in A) PSA, B) Tfx, C) LDH and D) ALP in Patient 91, following [ $^{225}\text{Ac}$ ]Ac-/ [ $^{177}\text{Lu}$ ]Lu-PSMA-617 regimen.

**Figure 75:** CNA profiles for Patient 91 across four treatment timepoints.

**Figure 76:** Imaging overview of Patient 25. Baseline staging was performed using [ $^{18}\text{F}$ ]PSMA-1007 PET imaging.

**Figure 77:** CNA profiles for Patient 25 at the baseline (pre-treatment).

**Figure 78:** Imaging overview of Patient 60.

**Figure 79:** CNA profiles for Patient 60 at the baseline (pre-treatment).

**Figure 80:** Imaging overview of Patient 95.

**Figure 81:** CNA profiles for Patient 95 at the baseline (pre-treatment).

**Figure 82:** Imaging overview of Patient 96. Baseline staging was performed using [ $^{68}\text{Ga}$ ]Ga-PSMA-11.

**Figure 83:** CNA profiles for Patient 96 at the baseline (pre-treatment).

**Figure 84:** Imaging overviews of Patient 23.

**Figure 85:** CNA profiles for Patient 23 at the baseline (pre-treatment).

# LIST OF TABLES

**Table 1:** Patient grouping strategy for clinical and molecular evaluations.

**Table 2:** Number of patients and samples in total included in the study.

**Table 3:** Number of samples per cycle in total included in the study.

**Table 5:** Initial diagnosis status of the case studies patients.

**Table 6:** Pre-treatments status of the case studies patients.

**Table 7:** Longitudinal assessment of GFR-CKD-EPI, creatinine, hemoglobin and leukocyte count during [<sup>225</sup>Ac]Ac-/[<sup>177</sup>Lu]Lu-PSMA-617 application of Patient 5.

**Table 8:** Longitudinal assessment of GFR-CKD-EPI, creatinine, hemoglobin and leukocyte count during [<sup>225</sup>Ac]Ac-/[<sup>177</sup>Lu]Lu-PSMA-617 therapy of Patient 10.

**Table 9:** Longitudinal assessment of GFR-CKD-EPI, creatinine, hemoglobin and leukocyte count following a two-year treatment break and a therapy switch to Olaparib and Abiraterone.

**Table 10:** Longitudinal assessment of GFR-CKD-EPI, creatinine, hemoglobin and leukocyte count during [<sup>225</sup>Ac]Ac-/[<sup>177</sup>Lu]Lu-PSMA-617 of Patient 38.

**Table 11:** Longitudinal assessment of GFR-CKD-EPI, creatinine, hemoglobin and leukocyte count during [<sup>225</sup>Ac]Ac-/[<sup>177</sup>Lu]Lu-PSMA-617 of Patient 37.

**Table 12:** Longitudinal assessment of GFR -CKD-EPI, creatinine, hemoglobin and leukocyte count during [<sup>225</sup>Ac]Ac-/[<sup>177</sup>Lu]Lu-PSMA-617 of Patient 11.

**Table 13:** Longitudinal assessment of GFR-CKD-EPI, creatinine, hemoglobin and leukocyte count during [<sup>225</sup>Ac]Ac-/[<sup>177</sup>Lu]Lu-PSMA-617 of Patient 34.

**Table 14:** Longitudinal assessment of GFR-CKD-EPI, creatinine, hemoglobin and leukocyte count during [<sup>225</sup>Ac]Ac-/[<sup>177</sup>Lu]Lu-PSMA-617 of Patient 40.

**Table 15:** Longitudinal assessment of GFR-CKD-EPI, creatinine, hemoglobin and leukocyte count during [<sup>225</sup>Ac]Ac-/[<sup>177</sup>Lu]Lu-PSMA-617 of Patient 91.

**Table 16:** Initial diagnosis status of the chemo naïve patient.

**Table 17:** Pre-treatments status of the chemo naïve patients.

**Table 18:** Comprehensive overview of PSA, Tfx, LDH and ALP in Patient 25, following [<sup>225</sup>Ac]Ac-/[<sup>177</sup>Lu]Lu-PSMA-617 regimen.

**Table 19:** Baseline assessment of GFR-CKD-EPI, creatinine, hemoglobin and leukocyte count during [<sup>225</sup>Ac]Ac-/[<sup>177</sup>Lu]Lu-PSMA-617 of Patient 25.

**Table 20:** Comprehensive overview of PSA, Tfx, LDH and ALP in Patient 60, following [<sup>225</sup>Ac]Ac-/[<sup>177</sup>Lu]Lu-PSMA-617 regimen.

**Table 21:** Baseline assessment of GFR-CKD-EPI, creatinine, hemoglobin and leukocyte count during [<sup>225</sup>Ac]Ac-/[<sup>177</sup>Lu]Lu-PSMA-617 of Patient 60.

**Table 22:** Comprehensive overview of PSA, Tfx, LDH and ALP in Patient 95, following [<sup>225</sup>Ac]Ac-/[<sup>177</sup>Lu]Lu-PSMA-617 regimen.

**Table 23:** Baseline assessment of GFR-CKD-EPI, creatinine, hemoglobin and leukocyte count during [ $^{225}\text{Ac}$ ]Ac-/ $^{177}\text{Lu}$ ]Lu-PSMA-617 of Patient 95.

**Table 24:** Comprehensive overview over the dynamic changes in PSA, Tfx, LDH and ALP in Patient 96, following [ $^{225}\text{Ac}$ ]Ac-/ $^{177}\text{Lu}$ ]Lu-PSMA-617 regimen.

**Table 25:** Overview of GFR-CKD-EPI, creatinine, hemoglobin and leukocyte count during [ $^{225}\text{Ac}$ ]Ac-/ $^{177}\text{Lu}$ ]Lu-PSMA-617 of Patient 96.

**Table 26:** Comprehensive overview over the dynamic changes in PSA, Tfx, LDH and ALP in Patient 23, following [ $^{225}\text{Ac}$ ]Ac-/ $^{177}\text{Lu}$ ]Lu-PSMA-617 regimen.

**Table 27:** Overview of GFR-CKD-EPI, creatinine, hemoglobin and leukocyte count during [ $^{225}\text{Ac}$ ]Ac-/ $^{177}\text{Lu}$ ]Lu-PSMA-617 of Patient 23.



*“Nella ricerca scientifica né il grado di intelligenza né la capacità di eseguire e portare a termine il compito intrapreso sono fattori essenziali per la riuscita e per la soddisfazione personale. Nell'uno e nell'altro contano maggiormente la totale dedizione e il chiudere gli occhi davanti alle difficoltà.”*

RITA LEVI MONTALCINI

(22.04.1909 – 30.12.2012)



# I INTRODUCTION

## 1.CANCER

Cancer arises from a single cell that progressively accumulates genetic alterations over time, which can be inherited, induced through environmental exposures (such as radiation or chemical carcinogens), or occur spontaneously due to replication errors. These mutations often lead to genomic instability—a critical enabling feature that fosters the acquisition of additional cancer traits by creating a genetically heterogeneous cell population (1-3). Moreover, defects in the mechanisms underlying high-fidelity DNA replication significantly contribute to genome instability, thus promoting the evolution of cancer cells (4). Once the genetic changes occur, affected cells begin to proliferate uncontrollably, forming a tumor. Tumors are classified as benign or malignant. While benign tumors are non-cancerous, their growth can cause local complications such as compression of adjacent structures or hormonal imbalances, malignant tumors are capable of invading surrounding tissues and metastasizing to distant organs, which constitutes the primary cause of cancer-associated mortality (5). The metastatic process involves several steps including local invasion, intravasation into blood or lymphatic vessels, survival in circulation, extravasation, and colonization at secondary sites. This process is aided by changes in cellular adhesion properties and activation of proteolytic enzymes, as has been delineated in studies of epithelial-mesenchymal transition (6, 7). Cancers are also commonly classified by the tissue from which they originate. Approximately 85% of human cancers are carcinomas that arise from epithelial tissues. Carcinomas include adenocarcinomas, which form from glandular tissues (e.g., breast and prostate), and squamous cell carcinomas, which originate from the skin or other mucosal linings (8). Other cancer types include sarcomas (from connective tissues), leukemias (blood cancers), lymphomas (lymphatic system cancers), melanomas (from pigment-producing cells), and gliomas (originating in the nervous system). Other cancer types include sarcomas (from connective tissues), leukemias (blood cancers), lymphomas (lymphatic system cancers), melanomas (from pigment-producing cells), and gliomas (originating in the nervous system). Underlying the development and progression of cancer are a series of biological capabilities or “hallmarks” that provide cancer cells a competitive advantage over normal cells. Originally described by Hanahan and Weinberg, these hallmarks include sustained proliferative signaling, evasion of growth suppressors, resistance to programmed cell death, replicative immortality, induction of angiogenesis, and activation of invasion and metastasis (1). Subsequent research expanded these hallmarks to incorporate emerging features such as deregulated cellular metabolism, evasion of immune destruction, genomic instability, and tumor-promoting inflammation. Collectively, these traits facilitate the growth and survival of cancer cells and underlie the capacity of malignant tumors to

disseminate via the bloodstream or lymphatic system—a process that ensures that circulating tumor cells can seed metastases in distant organs and thus drive the high mortality rate associated with cancer (9, 10). Risk factors for cancer are multifaceted, involving both intrinsic factors such as the natural aging process—which impairs DNA repair and cellular homeostasis—and extrinsic factors including dietary habits, physical inactivity, smoking, alcohol consumption, infections, and various environmental exposures (11).

## 1.1 Prostate Cancer

Prostate cancer (PCa), or prostatic adenocarcinoma, is the second most frequently diagnosed cancer in men worldwide, following skin cancer, and is responsible for about 15% of all male cancer cases. It also ranks as the fifth leading cause of cancer-related mortality among men globally (12, 13). The prostate gland, situated in the pelvic region beneath the bladder, is a critical part of the male reproductive system. Interestingly, a female anatomical equivalent known as the Skene's gland has also been associated with certain pathological conditions, including adenocarcinoma, making it clinically relevant as well (14, 15). Although commonly associated with hormonal imbalances, the exact underlying cause of prostate cancer remains uncertain. Elevated levels of testosterone, which may be influenced by high-fat diets, are believed to increase susceptibility to the disease (16). Additional risk factors include advancing age (age >55), African ancestry, certain viral infections, cadmium exposure—found in sources like cigarettes—and a family history of PCa. Men with affected first- or second-degree relatives have a higher risk of developing the disease (14). Prostate tumors often grow slowly and are asymptomatic in early stages, making detection difficult. Autopsy studies show undiagnosed prostate cancer in about one-third of men in their 50s and up to 80% in their 70s, with many dying of unrelated age-related causes (17). When symptoms do emerge, they may resemble those of benign prostatic hyperplasia, a non-cancerous prostate enlargement. These symptoms include frequent urination, especially at night (nocturia), reduced urine flow, blood in the urine (hematuria), and pain during urination (dysuria) or ejaculation (18). Not all cases are slow-growing—aggressive forms of prostate cancer, particularly in younger individuals, can spread rapidly *via* the lymphatic system or bloodstream. Common metastatic sites include the seminal vesicles, lymph nodes, lungs, and bones, especially in the vertebral column, hips, and pelvis (19). Prostate cancer screening often involves measuring prostate-specific antigen (PSA) levels in the blood. Men with PSA concentrations above 4 ng/mL are typically advised to undergo a digital rectal examination (DRE) or transrectal ultrasound (TRUS) (Chapter 1.3.1) (20). In recent years, positron emission tomography (PET) imaging has gained traction as a valuable tool for prostate cancer diagnosis, even in the early stages, particularly with the use of specific radiotracers (Chapter 3.2) (21). Cancer staging

is conducted using clinical evaluation, histological analysis, or both. The most commonly applied system is the TNM classification, which considers tumor size (T), lymph node involvement (N), presence of distant metastases (M), PSA levels, and the Gleason score (GS), derived from microscopic tissue analysis (Figure 1) (22-25).

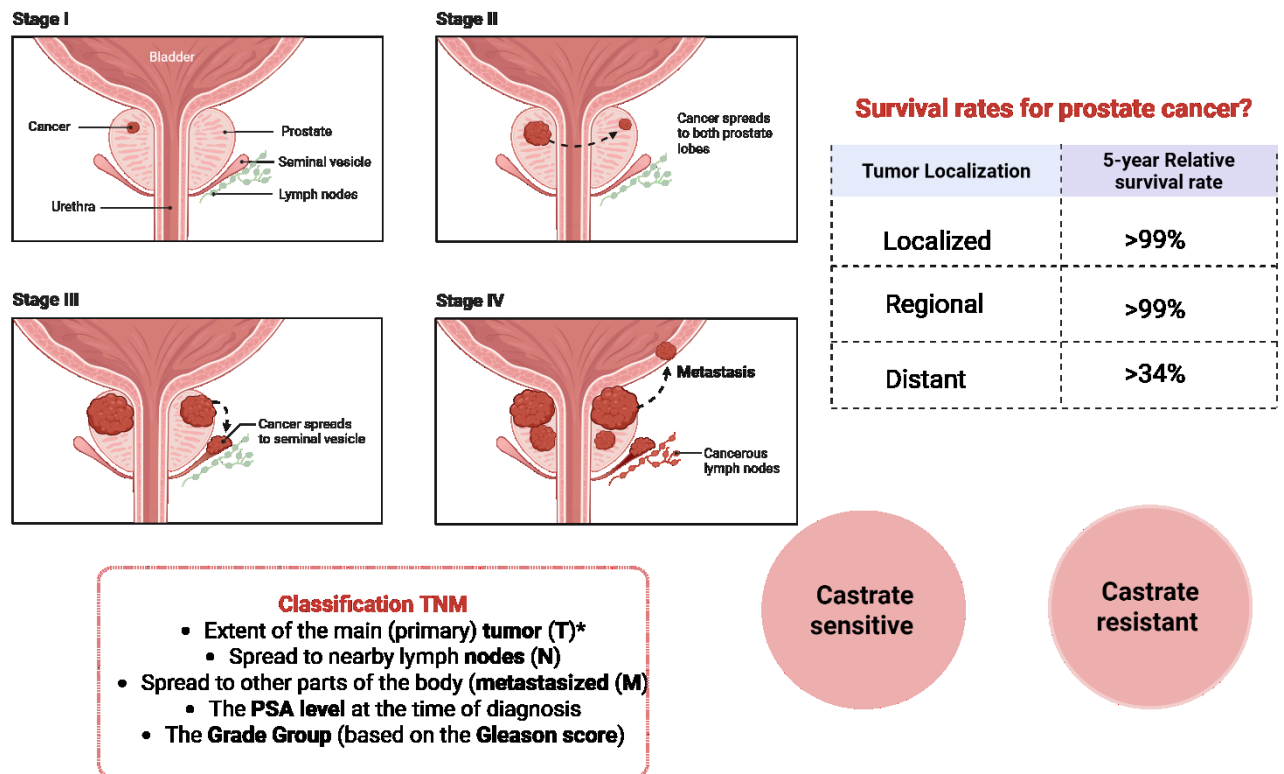


**Figure 1:** This figure illustrates the progression, classification, and survival outcomes associated with prostate cancer, integrating visual staging, tumor classification, and treatment resistance categories. Top Left: Prostate cancer stages with four schematic diagrams show prostate cancer progression from stage I to stage IV. Top Right: Survival rates vary by tumor localization. Bottom Left: TNM Classification T (Tumor size/local invasion) N (Lymph node involvement) M (Distant metastasis). Bottom Right: Hormone Sensitivity Subtypes Castrate Sensitive prostate cancer (responds to androgen deprivation) Castrate Resistant prostate cancer (progresses despite androgen deprivation therapy). Figure created in BioRender.

## 1.2 Clinical management of PCa

The clinical management of PCa involves a range of treatment options (Figure 2), including surgical intervention, hormone deprivation therapy, chemotherapy (e.g., Docetaxel), and various forms of radiation therapy (Chapter 3.2). Treatment selection depends largely on the patient's age, general health, and the extent and progression of the disease.

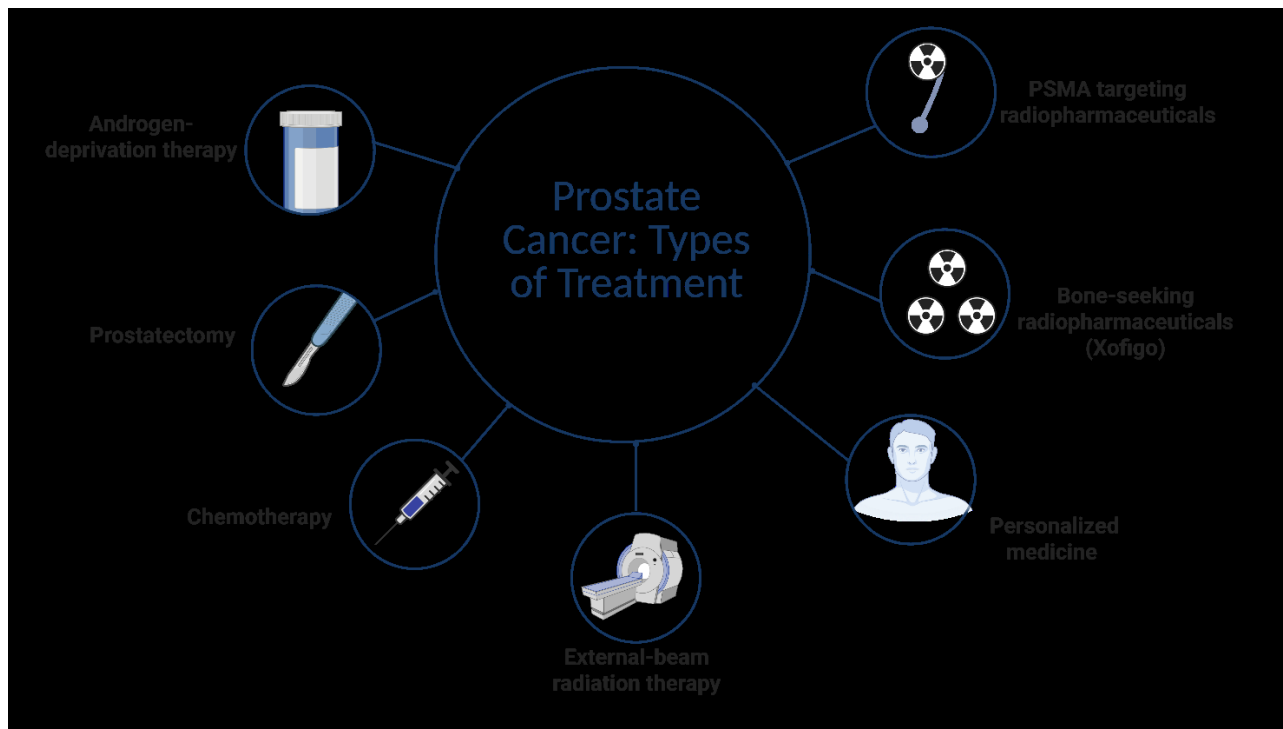


**Figure 2:** Schematic representation of clinical management of prostate cancer and the different therapies options. Figure created in BioRender.

### 1.2.1 Surgery

Radical prostatectomy, performed through open or laparoscopic approaches, involves complete removal of the prostate gland (26). This procedure requires incisions either in the abdominal region or the perineum. Ideal candidates for radical prostatectomy are patients under 70 years old with organ-confined disease, a life expectancy greater than 10 years, and minimal comorbidities. Common complications include urinary incontinence and erectile dysfunction due to potential damage to the urinary sphincter and neurovascular bundles (27). Cryotherapy is another surgical method involving the insertion of cryoprobes into the prostate under ultrasound guidance, reducing the gland's temperature to between  $-100^{\circ}\text{C}$  and  $-200^{\circ}\text{C}$  for approximately 10 minutes. Though effective, this

method has been linked to complications such as urinary retention, erectile dysfunction, rectal pain, and fistula formation (28).

### 1.2.2 Radiation therapy

Radiation therapy is a widely utilized and effective method to destroy prostate cancer cells using targeted high-energy radiation. It can be delivered through techniques such as brachytherapy, where radioactive seeds are implanted directly into the prostate, and external beam radiation therapy (EBRT), which projects energy from outside the body onto cancerous tissue. Additionally, targeted radionuclide therapy (TRNT, e.g., PSMA-617-based therapies) is discussed in later chapters. The primary goal of radiation therapy is to deliver high doses of energy to cancerous cells while minimizing damage to surrounding healthy tissue. It is particularly suitable for patients ineligible for surgery (29). Brachytherapy involves placement of radioactive materials *via* seeds, wires, or injections under TRUS guidance. EBRT is commonly used to deliver high-dose radiation directly to the prostate while sparing adjacent tissues. In intermediate- and high-risk prostate cancer cases, EBRT is often combined with androgen deprivation therapy (ADT) for better outcomes (30). Radium-223 dichloride ( $^{223}\text{RaCl}_2$ , Xofigo®, Bayer, Germany) is used for patients with metastatic disease resistant to hormone therapy. Mimicking calcium, radium-223 is selectively absorbed in bones, helping target bone metastases and alleviate symptoms like fractures and pain (31).

### 1.2.3 Hormonal Therapy

Hormonal therapy, or androgen deprivation therapy (ADT), is a standard treatment for advanced or metastatic prostate cancer. It aims to reduce or block testosterone and other androgens that fuel tumor growth. ADT can be achieved through bilateral orchiectomy or pharmacologically *via* luteinizing hormone-releasing hormone (LHRH) analogues or antagonists. LHRH agonists, such as leuprolide, goserelin, triptorelin, and histrelin, initially stimulate the pituitary to release LH and FSH before eventually downregulating receptors and suppressing testosterone production. In contrast, LHRH antagonists act by directly blocking pituitary receptors, leading to immediate testosterone suppression (32, 33). While effective, ADT is associated with a range of side effects including hot flashes, fatigue, hyperlipidaemia, osteoporosis, cardiovascular complications, insulin resistance, anaemia, and sexual dysfunction (34).

### 1.2.4 Abiraterone

Abiraterone (Zytiga®, Janssen Biotech, USA & Yonsa®, Sun Pharma, India) is a second-generation hormonal therapy that targets androgen production in adrenal glands, the tumor itself, and the testes.

It works by inhibiting the CYP17A enzyme and 3 $\beta$ -hydroxysteroid dehydrogenase, which are involved in androgen biosynthesis (35). Administered orally in combination with prednisone and ongoing ADT, abiraterone further suppresses testosterone levels beyond what is typically achieved with LHRH agonists alone. However, it may cause elevated levels of upstream mineralocorticoids, leading to side effects such as hypertension, edema, fatigue, hypokalemia, and liver toxicity, including rare cases of acute liver failure (36).

### 1.2.5 Chemotherapy

Chemotherapy involves the use of cytotoxic drugs to eliminate or inhibit the growth of cancer cells. Docetaxel (Taxotere®, Sanofi, France) remains the standard first-line chemotherapeutic agent for treating castration-resistant prostate cancer. As an antimicrotubule compound, it binds to  $\beta$ -tubulin, preventing microtubule depolymerization, thereby disrupting mitotic division and promoting apoptosis (33, 37, 38). Docetaxel mechanism of action depends largely on the cytochrome P450 enzyme CYP3A. Resistance to docetaxel, often linked to disease relapse, has been associated with the overexpression of the multidrug resistance (MDR1) gene, which encodes the efflux transporter P-glycoprotein (39). To address this resistance, cabazitaxel—a second-generation taxane—was developed (Jevtana®, Sanofi, France). It is a semi-synthetic compound derived from yew tree needles (*Taxus* species) and specifically designed to overcome P-glycoprotein-mediated resistance. Due to additional methyl groups, cabazitaxel has a lower affinity for P-glycoprotein. It undergoes hepatic metabolism primarily via CYP3A4/5 and, to a lesser extent, CYP2C8 (10–20%) (40–42). Common adverse effects include fatigue, neurotoxicity, alopecia, hypotension, bronchospasm, renal impairment, and skin reactions such as erythema or rash. In rare cases, severe diarrhea resulting in dehydration and electrolyte disturbances has been reported following cabazitaxel treatment.

### 1.2.6 Enzalutamide

Enzalutamide (Xtandi®, Astellas Pharma, Japan & Pfizer, USA), approved in 2012, is a second-generation androgen receptor (AR) inhibitor used in the treatment of prostate cancer. Its therapeutic mechanism is multifaceted, targeting critical steps in androgen signaling, which is crucial for the growth and survival of prostate cancer cells. Enzalutamide exerts its antineoplastic activity primarily through three mechanisms. First, it competitively inhibits the binding of androgens—specifically testosterone and dihydrotestosterone—to the AR. By occupying the ligand-binding domain, enzalutamide prevents endogenous androgens from activating the receptor, subsequently reducing downstream gene transcription that drives tumor proliferation (43). Second, the agent impedes the nuclear translocation of the activated AR. Under normal physiological conditions, upon ligand binding,



the AR translocates from the cytoplasm to the nucleus, where it recruits cofactors and binds to DNA. Enzalutamide disrupts this intracellular trafficking, inhibiting the recruitment of coactivators and the receptor's association with DNA, thus blocking the transcription of target genes essential for cancer cell survival. Finally, by inhibiting the binding of the activated AR complex to DNA, enzalutamide curtails the transcriptional activation of genes involved in cell proliferation and survival. Collectively, these sequential actions block AR signaling at multiple junctures, distinguishing enzalutamide from earlier antiandrogens that demonstrated a more limited scope of inhibition (44-46). Clinically, the efficacy of enzalutamide in patients with mCRPC is well-documented, where the interruption of the androgen signaling cascade translates to significant prolongation of survival and delay in disease progression.

### 1.3 Metastatic castration resistant PCa

For over seven decades, the primary approaches for treating prostate cancer have included surgery, radiation therapy, and pharmacologic strategies aimed at lowering testosterone and its derivatives through androgen deprivation. This approach, commonly achieved using LHRH agonists—with or without antiandrogens—has been effective in controlling tumor growth for a defined period in many cases (47). However, disease progression often occurs despite continued hormone suppression, leading to the development of castration-resistant prostate cancer (CRPC). CRPC is particularly debilitating due to its strong tendency to metastasize to the bone, significantly increasing the risk of pathological fractures and skeletal complications such as spinal cord compression and hypercalcemia. Although only around 3% of patients show bone metastases at initial diagnosis, this figure escalates to approximately 90% in those with metastatic CRPC (mCRPC) (48). Visceral metastases—including those affecting the lungs, liver, adrenal glands, and kidneys—occur in about 25% of cases and are typically associated with a more aggressive disease phenotype (49). A major advancement occurred in 2022 with the approval of [<sup>177</sup>Lu]Lu-PSMA-617 (Pluvicto®, Novartis, Switzerland) by the Food and Drug Administration (FDA) and European Medicines Agency (EMA) for treating mCRPC. This radioligand therapy demonstrated significant clinical benefits in patients who had previously undergone multiple lines of treatment (50). Despite these achievements, approximately 30% of mCRPC patients eventually fail to respond to beta radiation, owing to inherent or acquired resistance (51). Pioneering clinical trials have explored the combination of PSMA-617 with the alpha-emitting radionuclide <sup>225</sup>Ac ([<sup>225</sup>Ac]Ac-PSMA-617), demonstrating remarkable efficacy in heavily pre-treated mCRPC patients with diffuse bone marrow infiltration who no longer respond to conventional therapies (Chapter 3.4) (52-54). PSA is often used as a monitoring tool for the progression of the mCRPC disease. Nevertheless, the level of PSA and PSA kinetics are treatment-sensitive parameters.

For example, non-rising PSA with metastatic radiographic progression is often observed in mCRPC patients treated with enzalutamide (54, 55). Several other biomarkers can also be found as factors in multivariable analysis, improving the prognostic model performance. Besides the previously mentioned biomarkers, such as PSA, PSA kinetics, and inflammatory response cells, the other biomarkers can be divided into several categories. General cancer-related biomarkers are represented by alkaline phosphatase (ALP) – an indicator of bone metastatic tumor load (56), lactate dehydrogenase (LDH) – an increased biomarker of highly proliferating cancer cells connected with enhanced glycolysis (57). Furthermore, the amount of tumor-originated ctDNA (Chapter 4.1) in plasma has been suggested as an independent prognostic biomarker for mCRPC, in particular in combination with PSA evaluation (54, 58, 59).

## 1.4 Tumor Markers for PCa and mCRPC

Tumor markers (TM) are critical tools in the diagnosis and clinical management of PCa, including its advanced stage, mCRPC. While PSA remains the most widely used biomarker, its limitations—especially in the setting of emerging therapeutic approaches—have prompted extensive investigation into molecular and genetic biomarkers that may offer improved prediction of disease trajectory, treatment efficacy, and the onset of resistance.

### 1.4.1 Prostate-specific antigen (PSA)

PSA is a serine protease believed to play a physiological role in liquefying seminal fluid. In PCa, PSA is released into the bloodstream, often elevating serum levels by up to  $10^5$ -fold. However, elevated PSA can also result from benign conditions such as benign prostatic hyperplasia (BPH) or prostatitis, which limits its specificity. Despite these limitations, PSA has been widely adopted as a biomarker for both the detection and monitoring of PCa (60). In the United States, the FDA approved PSA as a monitoring tool for PCa patients in 1986 and later, in 1994, as a diagnostic marker. The widespread use of PSA screening led to an increased detection rate of prostate cancer, contributing to stage migration and a reduction in the number of cases diagnosed at advanced or metastatic stages (61, 62). PSA transcription is regulated by androgens, which limits its expression predominantly to prostate epithelial cells. It is produced in normal prostate tissue, in BPH, and across all stages and grades of PCa. PSA is primarily secreted into seminal fluid, where its concentration typically ranges from approximately 0.3 to 3 mg/mL (10–100  $\mu$ mol/L). Because PSA is specific to prostate tissue rather than prostate cancer, elevated levels can also be found in non-malignant conditions. Consequently, a prostate biopsy is often required to confirm a cancer diagnosis in men with elevated PSA levels (38, 63). Functionally, PSA acts as a chymotrypsin-like serine protease that cleaves gel-forming proteins in

seminal fluid, such as semenogelin I and II, contributing to the liquefaction of semen. PSA is part of the kallikrein family of serine proteases. The genes encoding the 15-known human kallikreins, including PSA, are located on chromosome 19q13.3–4, within a locus spanning approximately 280 kb. The gene for PSA, KLK3, is regulated by androgen response elements within its promoter region. KLK2, which encodes human kallikrein 2 (hK2), is the closest paralog of KLK3 and is also regulated by androgens through similar elements (64, 65).

#### 1.4.2. Lactate dehydrogenase (LDH)

LDH is a key metabolic enzyme present in various tissues and measurable in serum. It plays a central role in energy metabolism by catalysing the reversible conversion between pyruvate and lactate during glycolysis and gluconeogenesis. Elevated LDH levels have long been associated with multiple malignancies, often exceeding those found in normal tissues (66). In many solid tumors, LDH serves as a prognostic marker, correlating with tumor burden and believed to reflect the aggressiveness and proliferative capacity of the cancer (67). As tumors grow and infiltrate surrounding tissues, increased cell turnover and necrosis can lead to LDH release from both malignant cells and damaged neighbouring tissue, contributing to elevated serum concentrations (68). Clinical evidence from a range of cancers—including lung, colorectal, breast, and ovarian—has consistently highlighted the prognostic significance of LDH levels in assessing disease progression and patient outcomes (69-71).

#### 1.4.3. Alkaline phosphatase (ALP)

ALP refers to a group of enzymes that play a vital role in several biological processes (72). These enzymes function by catalysing the hydrolysis of phosphate esters under alkaline conditions, resulting in the release of inorganic phosphate (73). ALP is expressed in multiple tissues throughout the body, including the bones, liver, intestines, and placenta. Its enzymatic activity is especially important for bone development and growth, particularly during childhood and adolescence. Alterations in ALP levels have been noted in various malignancies, where elevated expression often correlates with pathological processes. In the context of cancer, increased ALP levels are commonly linked to bone and liver involvement, reflecting tumor activity or metastasis in these regions (74, 75). Overproduction of ALP in these settings can lead to its leakage into the bloodstream, making it a useful biomarker in certain cancers. At the molecular level, ALP expression in tumors is influenced by several signaling pathways. For instance, activation of the Wnt/ $\beta$ -catenin pathway has been shown to upregulate ALP expression in various cancers, including those of the colon, liver, and bone. In this pathway, nuclear translocation of  $\beta$ -catenin enhances the transcription of ALP-related genes (76). Additionally, the bone morphogenetic protein (BMP) signaling pathway has been implicated in the upregulation of ALP,

especially in bone metastases of solid tumors where cancer cells exhibit osteoblast-like characteristics (77).

## 2. Prostate-specific membrane antigen (PSMA)

Prostate-specific membrane antigen (PSMA) was initially discovered in 1987 using the LNCaP human prostate adenocarcinoma cell line (78). It is a type II transmembrane glycoprotein composed of 750 amino acids, with a molecular weight of approximately 84 kDa. Structurally (Figure 3), PSMA features a short cytoplasmic tail, a transmembrane region, and a large extracellular domain (amino acids 44–750), which includes apical, helical, and protease-like regions involved in substrate binding and enzymatic activity (79). The PSMA gene is located on the short arm of chromosome 11 in humans (80). Functionally, PSMA exists either as a monomer or a homodimer, though enzymatic activity is confined to its dimeric form (81).

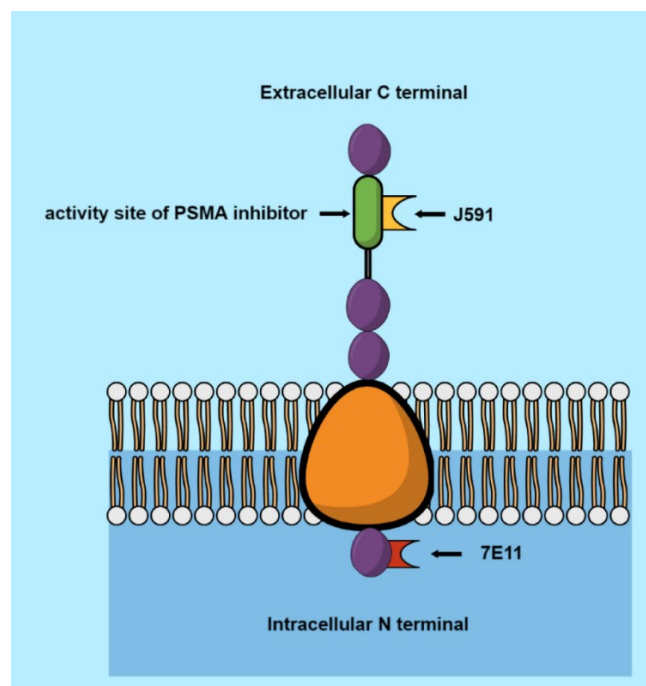


**Figure 3:** Schematic representation of PSMA, illustrating its cellular receptor and structural features. PSMA is expressed in over 90% of prostate cancer cases. Its expression increases with tumor progression and metastasis, showing particularly strong expression in advanced, androgen-independent prostate cancers. The 7E11 antibody targets an intracellular epitope of PSMA, whereas J591 binds to an extracellular domain (82).

## 2.1 PSMA as a treatment target

Although PSMA is primarily associated with prostate tissue, low levels of physiological expression have been identified in several non-prostatic organs, including the kidneys, salivary glands, spleen, small intestine, liver, testes, ovaries, and brain (83, 84). In prostate cancer, however, PSMA expression is markedly increased—typically 8- to 12-fold higher than in normal prostate tissue—and is further elevated in metastatic and treatment-resistant forms of the disease. Estimates suggest that up to  $10^6$  PSMA molecules may be present on a single PCa cell, underscoring its value as a molecular target. This overexpression has been correlated with higher Gleason scores, suggesting a potential role for PSMA in tumor progression and invasiveness. Notably, variations in PSMA glycosylation have been observed across different PCa cell lines, and these distinct glycan patterns may influence the invasive capacity of tumor cells (85-87). While PSMA is a well-established marker for prostate cancer, elevated expression has also been reported in other malignancies, such as kidney and bladder cancers, as well as in the neovasculature of various solid tumors (88). As a result, PSMA is no longer regarded as exclusively prostate-specific, but rather as a broader tumor-associated antigen with relevance across multiple cancer types.

## 3. NUCLEAR MEDICINE

Nuclear medicine is an evolving interdisciplinary field that integrates elements of physics, chemistry, and medicine to diagnose and treat diseases through the use of radioactive substances. In this approach, radionuclides are typically linked to biologically active molecules that guide their distribution within the body (89). These specialized compounds, known as radiopharmaceuticals or radiotracers, enable both diagnostic imaging and targeted therapy for a wide range of conditions—including various cancers, endocrine disorders, cardiovascular diseases, and neurological dysfunctions such as alterations in dopamine receptor density (90, 91). One of the distinguishing features of nuclear medicine is its ability to provide functional and metabolic information at the cellular and even molecular level, offering insights that go beyond anatomical imaging. Radiopharmaceuticals can be designed to target specific cellular receptors or biological pathways, allowing for highly specific imaging of individual organs or even full-body scans when systemic targeting is required—such as in the case of white blood cell tracking (91). This capacity enables the early detection of disease processes, often before structural changes or clinical symptoms appear, and supports the monitoring of real-time responses to therapeutic interventions.

### 3.1 Imaging strategies

Accurate diagnostic assessment is fundamental for developing an effective treatment strategy in PCa and mCRPC. Imaging plays a central role across various stages of disease management, including diagnosis, prognosis, treatment planning, and monitoring. The diagnostic workup typically begins with cross-sectional anatomical imaging, most commonly *via* computed tomography (CT) or magnetic resonance imaging (MRI). MRI, owing to its superior soft tissue contrast and ability to capture images in multiple sequences, provides enhanced detail for tumor localization, tissue differentiation, and evaluation of disease extent—making it particularly valuable for precise treatment planning (92). However, CT continues to serve as the first-line modality in certain clinical scenarios, such as the evaluation of new or worsening neurological symptoms, due to its widespread availability and rapid acquisition speed. CT is also preferred when MRI is contraindicated, for example, in patients with pacemakers or other non-compatible implants, and remains useful for detailed assessment of bone structures (93). Beyond anatomical imaging, nuclear medicine techniques—particularly single-photon emission computed tomography (SPECT) and positron emission tomography (PET)—offer functional insights that enhance the diagnostic landscape in PCa and mCRPC. These methods rely on the administration of radiotracers that reflect specific physiological processes. Both PET and SPECT produce three-dimensional images, but differ in their detection mechanisms. SPECT captures gamma emissions using rotating photomultiplier detectors, while PET detects photons produced by positron annihilation, with detectors arranged in circular arrays for high sensitivity and resolution. The tomographic capability of SPECT significantly enhances the differentiation of abnormal tracer uptake from normal physiological activity (94-97), while PET offers even greater spatial resolution. Common tracers, such as Tc-99m-labeled pertechnetate and Ga-68-labeled diethylenetriaminepentaacetic acid (DTPA), provide high-contrast resolution for various clinical applications. In recent years, radiotracers targeting PSMA—including Tc-99m-, <sup>68</sup>Ga-, and <sup>18</sup>F-labeled compounds—have demonstrated substantial clinical value for detecting and evaluating bone metastases in prostate cancer patients, further advancing imaging precision in both SPECT and PET modalities (89, 98).

### 3.2 PSMA-targeted radioligand therapy

The introduction of [<sup>177</sup>Lu]Lu-PSMA-617 (Pluvicto®) in 2022 represented a major advancement in the treatment landscape for prostate cancer, receiving regulatory approval from both the FDA and EMA due to its demonstrated efficacy in patients who had undergone multiple prior therapies (99-102). More recently, on March 28, 2025, the FDA approved an expanded indication for Pluvicto®, allowing its use in PSMA-positive mCRPC patients who have progressed following treatment with androgen receptor pathway inhibitors (ARPIs) and are candidates for delaying chemotherapy (103-105).

Considering that nearly 50% of mCRPC patients may not survive to receive second-line therapy, integrating effective and well-tolerated treatments earlier in the disease course is of critical importance. Once internalized by the target cell, the radiopharmaceutical releases the radionuclide lutetium-177 ( $^{177}\text{Lu}$ ), which has a half-life of approximately 6.6 days and emits beta-minus ( $\beta^-$ ) particles with a relatively low linear energy transfer (LET) of around 0.2 keV/ $\mu\text{m}$  (106). These particles travel short distances—on average 0.67 mm—within tissues, delivering cytotoxic radiation primarily to PSMA-positive tumor cells while inducing cellular damage by causing DNA lesions, including both single-strand breaks (SSBs) and more lethal double-strand breaks (DSBs) (Figure 4) (107). The radiation-induced damage is particularly effective in the presence of oxygen, which facilitates the formation of reactive oxygen species (ROS) and free radicals that enhance cellular injury (108). Approximately 30% of patients exhibit primary resistance to this treatment. In such cases, therapies based on alpha-emitting radionuclides may present a promising alternative. Alpha particles are characterized by a much higher LET, approximately 80 keV/ $\mu\text{m}$ , and a limited tissue penetration range of up to 100  $\mu\text{m}$ . These physical properties allow for highly localized and potent cytotoxic effects, primarily through the generation of more frequent and long-lasting DSBs (109, 110). However, this intense energy deposition can also impact healthy tissues that express PSMA physiologically—such as the salivary glands—potentially leading to off-target toxicity and imposing limitations on the maximum tolerable dose (50, 111-113). Despite the challenges, targeted alpha therapy represents an attractive option for patients that develop resistance to the beta-emitting [ $^{177}\text{Lu}$ ]Lu-PSMA-617 or are not responsive in the first place (51, 114). Pioneering clinical trials have explored the combination of PSMA-617 with the alpha-emitting radionuclide  $^{225}\text{Ac}$  ([ $^{225}\text{Ac}$ ]Ac-PSMA-617), demonstrating remarkable efficacy in heavily pre-treated mCRPC patients with diffuse bone marrow infiltration who no longer respond to conventional therapies, including Pluvicto® (52, 53). [ $^{225}\text{Ac}$ ]Ac-PSMA-617 seems to be highly effective against microscopic metastatic disease, leveraging its short range (50–100  $\mu\text{m}$ ) for precise, cell-specific ionization (115). Actinium-225 ( $^{225}\text{Ac}$ ), with a half-life of approximately 10 days, possesses potent radiobiologic properties ideal for localized tumor ablation. However, its use as a standalone therapy poses challenges in treating larger tumor masses and is often associated with significant toxicities, such as higher-grade xerostomia (116-118). Over time, various radiotherapeutic strategies have been evaluated, with tandem therapy emerging as a means to optimize efficacy and minimize adverse effects (52, 119, 120). Despite the clinical success of tandem [ $^{225}\text{Ac}$ ]Ac-/ [ $^{177}\text{Lu}$ ]Lu-PSMA-617 (actinium-lutetium) therapy, which leverages the complementary benefits of both radionuclides, identifying and addressing resistance mechanisms remains a significant challenge in treating mCRPC (52).

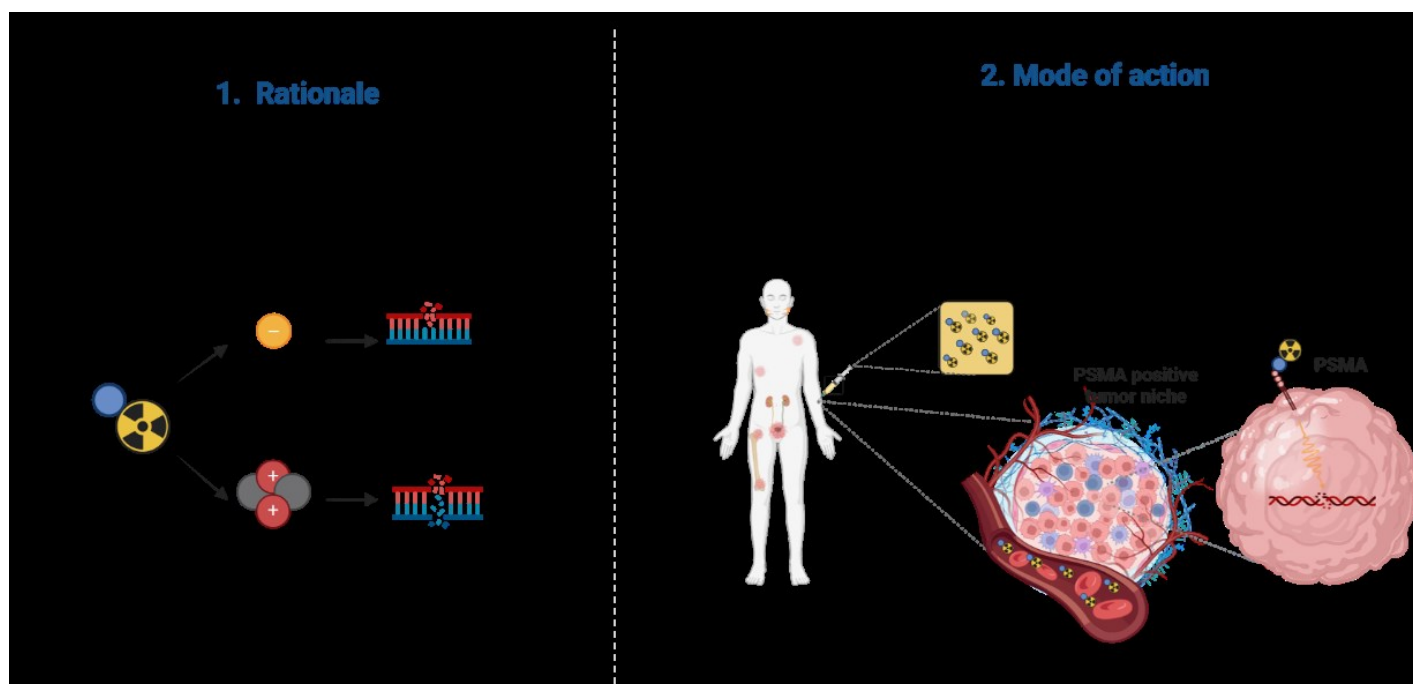


**Figure 4:** Schematic representation of the rationale behind PSMA-targeting radiopharmaceuticals. A targeting moiety is conjugated to a chelator, which coordinates a radioactive isotope emitting either beta or alpha particles. Upon intravenous administration, the radiopharmaceutical circulates through the body and selectively binds to its molecular target on tumor cells, in this case PSMA. Such interaction also often leads to internalization of the compound. The emitted radiation induces DNA damage—primarily SSBs or DSBs—ultimately leading to cancer cell death. Figure created in BioRender.



## 4. LIQUID BIOPSY

Liquid biopsy has rapidly emerged as a transformative tool in oncology, enabling detailed molecular analysis of body fluids—most commonly blood—to gather tumor-related information. Its minimally invasive nature allows for repeated sampling, making it ideal for monitoring disease progression, treatment response, and emerging resistance mechanisms. The foundation of this technology dates back to 1948, when circulating free DNA (cfDNA) and RNA were first identified in human blood, marking the earliest observation of what would later become a cornerstone of modern cancer diagnostics. Since then, liquid biopsy approaches have evolved significantly, becoming a routine part of clinical practice while also accelerating cancer research by revealing key insights into tumor biology. (121) These approaches have rapidly expanded beyond cfDNA to include additional tumor-derived components such as circulating cell-free RNA—including both messenger and noncoding RNA—extracellular vesicles, and tumor-educated platelets and circulating tumor cells (CTCs) (122-126). The clinical utility of liquid biopsy is multifaceted. By providing real-time insights into the tumor's genetic and epigenetic landscape, liquid biopsies facilitate early detection, monitor disease progression, evaluate treatment response, and help uncover mechanisms of drug resistance (Figure 5)(127). Unlike traditional tissue biopsies, liquid biopsies can be performed repeatedly with minimal risk and discomfort, allowing clinicians to monitor tumor heterogeneity and evolution over time. This dynamic approach not only enhances our understanding of malignant growth at the molecular level but also supports personalized therapeutic strategies that are critically needed in modern oncology. Moreover, the liquid biopsy platform has expanded research capabilities by enabling the interrogation of tumor-derived biomarkers from easily accessible blood samples. This has accelerated efforts to decipher the complex molecular events underlying tumor initiation and progression, ultimately contributing to a more robust integration of molecular diagnostics into routine clinical practice (128-131). In ongoing interventional studies, the clinical utility of CTCs and ctDNA for treatment decisions is being evaluated. In particular, the use of CTCs and ctDNA as real-time liquid biopsy has received attention over the past years (126, 132, 133). Both CTCs and ctDNA occur at very low concentrations in the peripheral blood, which poses a serious challenge for any analytic system (126). With the introduction of next-generation sequencing (NGS) technologies, the diverse and often complex genomic landscape of cancer has been deciphered in major cancer types. Based on these studies, genetic events which are strongly linked to tumor cell transformation and appear to 'drive' the disease evolution have been identified (134).

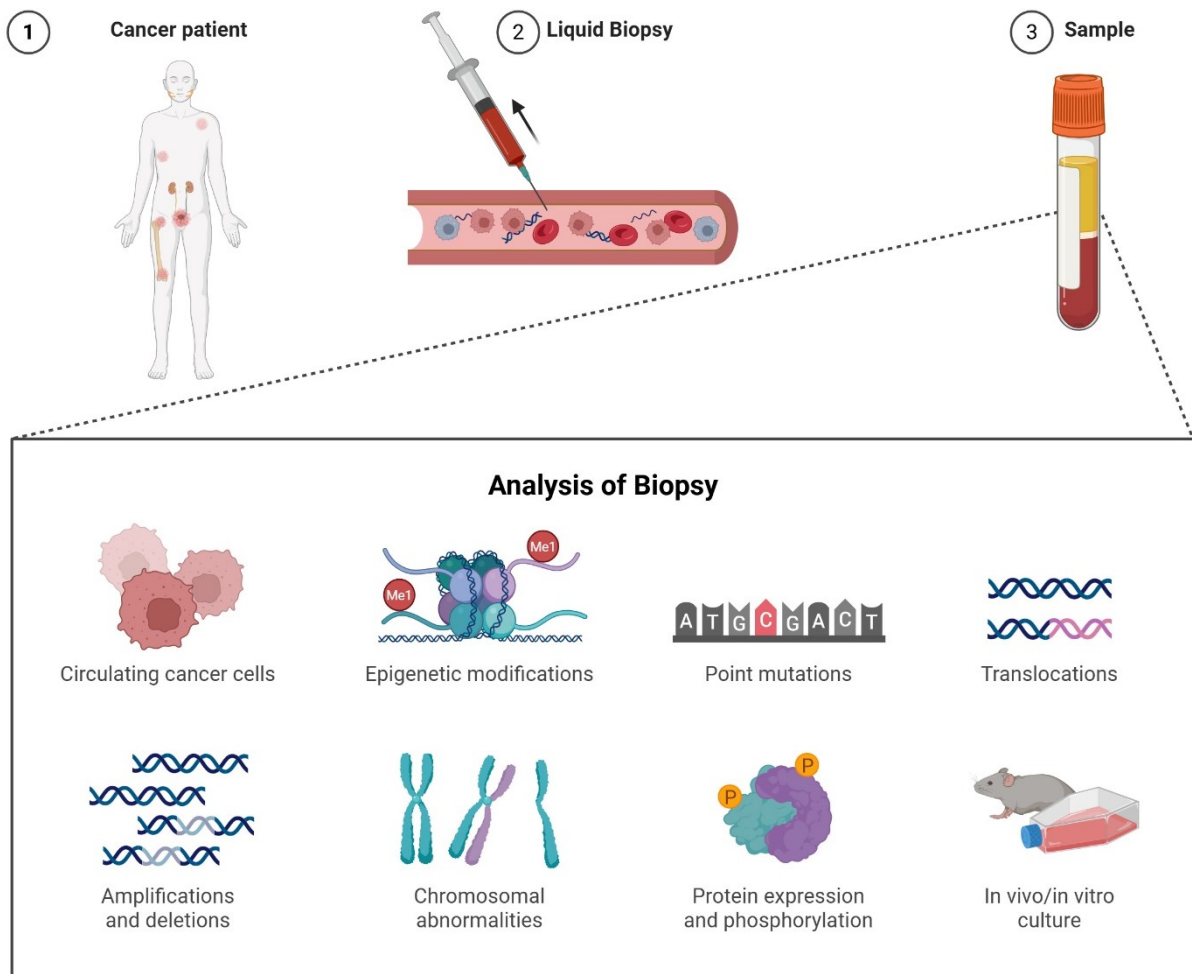


**Figure 5:** Schematic representation of liquid biopsy concept and different applications in the clinical field. The analysis of liquid biopsy can be used to identify CTCs, epigenetic modification, point mutations, translocations, amplifications & deletions, chromosomal abnormalities, protein expression phosphorylation and in vivo/in vitro culture of isolated cells. Figure created in BioRender.

## 4.1 Circulating free DNA (cfDNA)

cfDNA refers to short DNA fragments found circulating in plasma and other bodily fluids, including saliva, lymph, breast milk, bile, urine, cerebrospinal fluid, and amniotic fluid (135, 136). This DNA originates from both nuclear and mitochondrial sources and is released by various cell types throughout the body (134, 137). cfDNA enters the extracellular space primarily through cell death processes such as apoptosis and necrosis, although active secretion has also been described. The characteristics of cfDNA—its size and composition—can reflect the underlying mechanism of release. For instance, apoptosis typically produces DNA fragments around 160–180 base pairs in length, corresponding to DNA segments wrapped around nucleosomes. Other release mechanisms may generate different fragment patterns, and ongoing research continues to explore which of these signatures are most relevant for specific physiological or disease states (134, 138). In healthy individuals, most cfDNA found in plasma—about 60% to 90%—originates from hematopoietic cells. The liver contributes an additional 2% to 18%, while the rest comes from a variety of tissues (137, 139, 140). cfDNA is rapidly cleared from circulation, with a half-life ranging from approximately 16 minutes to 2.5 hours. This clearance occurs via degradation by nucleases, phagocytosis in the liver and spleen, and excretion through the kidneys (141, 142). Under normal physiological conditions, cfDNA concentrations in the bloodstream typically range from 1 to 10 ng/mL, with an average level of 6 ng/mL—equivalent to roughly 2,000 haploid genome copies per milliliter of plasma (134).

## 4.2 Circulating tumor DNA (ctDNA)

In cancer patients, circulating levels of total cfDNA are significantly elevated in comparison to healthy individuals, often exceeding 1000 ng/mL, with average concentrations around 180 ng/mL. This marked increase suggests that tumor cells contribute substantially to the total cfDNA pool. The term circulating tumor DNA (ctDNA) was introduced after researchers studying pancreatic cancer detected matching mutations in both tumor tissue and DNA fragments isolated from patient plasma (143-146). Interestingly, cfDNA fragments derived from malignant cells tend to be shorter than those released by non-malignant cells. This finding has driven the development of size-selection approaches aimed at enriching shorter DNA fragments, thereby improving the sensitivity of ctDNA detection as a cancer-specific biomarker (147, 148). The evolution of next-generation sequencing (NGS) technologies has further advanced the field by allowing comprehensive, high-resolution analysis of ctDNA. These techniques enable the identification of point mutations, gene fusions, epigenetic alterations, and large-scale chromosomal changes using very small quantities of input DNA, supporting applications such as tumor monitoring, minimal residual disease detection, and prediction of treatment response (149). As a result, many new molecular biomarkers are being uncovered, offering opportunities for

earlier and more accurate cancer diagnosis. Among these, copy number alterations (CNAs) are particularly prevalent. CNAs involve gains or losses of chromosomal segments, which can result in gene dosage imbalances that promote oncogenesis through oncogene amplification or tumor suppressor gene loss. These genomic alterations are key drivers of tumor heterogeneity and progression, making them valuable both diagnostically and therapeutically (150-158).

### 4.3 Applications of ctDNA in the clinic

The clinical applications of liquid biopsy are broad and span multiple tumor types. For instance, in thyroid cancer, the use of liquid biopsy to detect cell-free nucleic acids and other circulating biomarkers has shown promise in improving early diagnosis and guiding treatment decisions, although further integration into routine clinical practice is still needed (128, 159). ctDNA has emerged as a promising non-invasive biomarker with broad applications across the cancer care continuum. Derived from tumor cells undergoing apoptosis or necrosis, ctDNA reflects the genomic landscape of malignancies in real time and offers significant advantages over traditional tissue biopsies, particularly in capturing tumor heterogeneity and enabling longitudinal monitoring (160). Clinically, ctDNA is increasingly utilized for early cancer detection (Figure 6), where it enables the identification of molecular alterations in asymptomatic individuals, including somatic mutations and epigenetic changes. It is also a powerful tool for minimal residual disease (MRD) detection, capable of identifying microscopic disease post-surgery or treatment, thus predicting relapse well before radiological evidence emerges. Furthermore, ctDNA serves as a dynamic marker for treatment response, with changes in ctDNA levels correlating closely with therapeutic efficacy or resistance. Its application extends to the identification of resistance mechanisms, allowing the detection of emergent mutations and guiding subsequent therapy decisions without the need for repeat biopsies. ctDNA analysis also supports tumor genotyping, providing actionable insights for personalized treatment, and has demonstrated prognostic value, with elevated ctDNA levels often associated with higher tumor burden and poorer clinical outcomes (150, 161-163).

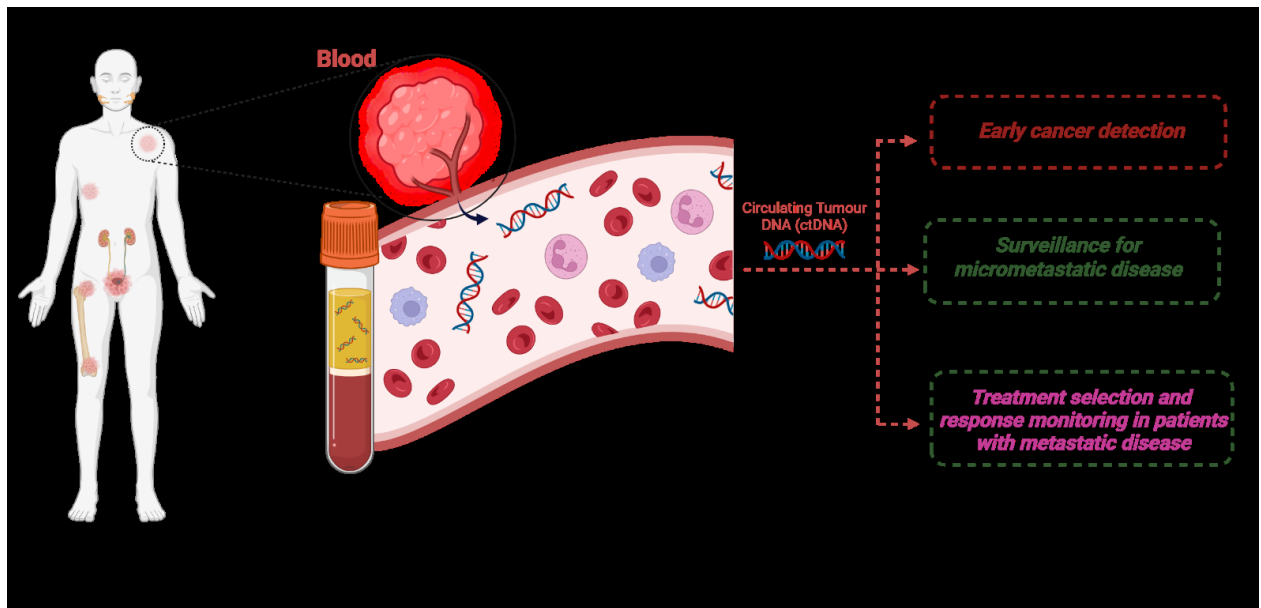


**Figure 6:** Schematic representation of ctDNA clinical application that range from early cancer detection, surveillance for micrometastatic disease and treatment selection and response monitoring in patients with metastatic disease. Figure created in BioRender.



## II AIM OF THE STUDY

PCa is the most frequently diagnosed malignancy among elderly men in Western societies and remains a leading cause of cancer-related mortality within this demographic. Despite notable advancements in diagnostic modalities and therapeutic interventions, the prognosis for patients diagnosed with advanced mCRPC remains poor. This is primarily due to the limited efficacy and durability of existing treatment options, particularly in later stages of the disease (51). The clinical challenges underscore an urgent need for improved strategies in patient stratification and the development of novel, more effective therapeutic approaches capable of addressing the aggressive nature of mCRPC.

A major advancement in recent years has been the clinical introduction of [ $^{177}\text{Lu}$ ]Lu-PSMA-617, a beta minus-emitting radiopharmaceutical for targeted radioligand therapy. Approved in 2022 by multiple regulatory bodies—including the FDA, MHRA, Health Canada, and EMA—this radiopharmaceutical is indicated as a third-line treatment for patients with advanced-stage mCRPC (100). Commercially available under the trade name Pluvicto® (Novartis, Switzerland), [ $^{177}\text{Lu}$ ]Lu-PSMA-617 has demonstrated a substantial clinical benefit by reducing both the risk of disease progression and mortality by up to 60%. However, up to 30% of patients either fail to respond adequately to this therapy or eventually develop resistance to beta minus radiation. To address this limitation, an alpha-emitting targeted radioligand therapy with [ $^{225}\text{Ac}$ ]Ac-PSMA-617 has emerged as a promising alternative, demonstrating encouraging efficacy, particularly in patients who are refractory to [ $^{177}\text{Lu}$ ]Lu-PSMA-617. Nevertheless, therapeutic resistance and suboptimal outcomes are still observed, with approximately 37% of patients showing either poor responses or early resistance to [ $^{225}\text{Ac}$ ]Ac-PSMA-617 (164). This highlights a critical unmet need for further research to elucidate the biological mechanisms driving resistance to alpha emitters and to identify robust predictive biomarkers for patient stratification. In response to these challenges, combination—or “tandem”—therapies that incorporate both [ $^{225}\text{Ac}$ ]Ac-PSMA-617 and [ $^{177}\text{Lu}$ ]Lu-PSMA-617 are currently being explored. These tandem approaches aim to exploit the complementary therapeutic advantages of beta and alpha emitters to improve clinical efficacy and reduce resistance rates.

This study aims to comprehensively investigate the therapeutic potential and associated limitations of [ $^{225}\text{Ac}$ ]Ac-/ [ $^{177}\text{Lu}$ ]Lu-PSMA-617. A key component of this investigation involves the integration of non-invasive liquid biopsy techniques, such as cfDNA and ctDNA analysis, with clinical, molecular, and imaging data to identify predictive biomarkers for treatment response and resistance ( Figure 7).

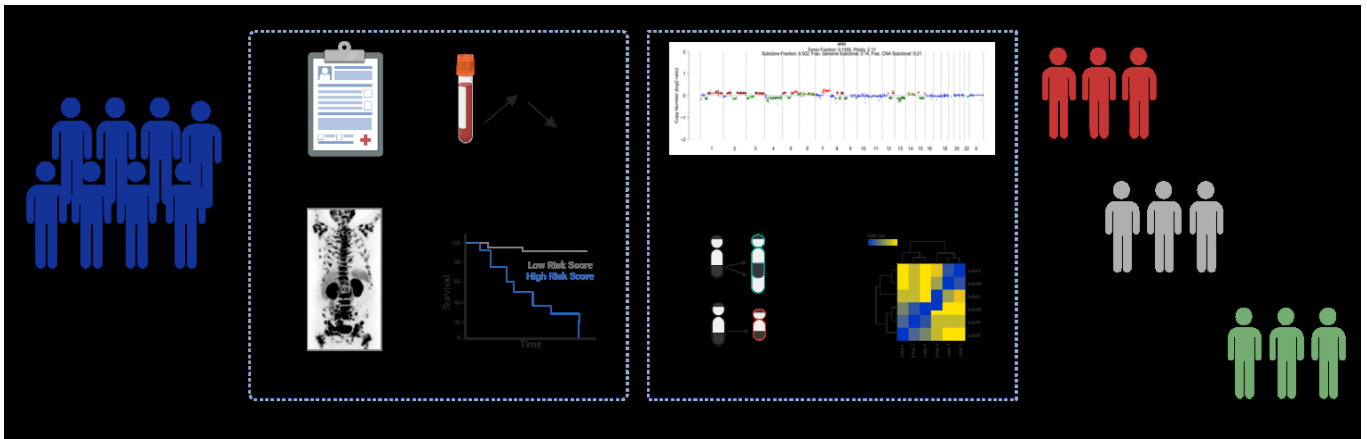


**Figure 7:** Overview of the study's objective to stratify mCRPC patients undergoing PSMA-targeted radioligand therapy. Clinical data, imaging, and plasma-derived cfDNA are analyzed to evaluate tumor burden and resistance. Patients are classified as responders, non-responders, or mixed responders, aiming to enhance treatment prediction and optimize therapeutic strategies. Figure created in BioRender.

Plasma samples were collected at bimonthly intervals prior to each treatment cycle and processed to isolate cfDNA. Subsequent analyses using the IchorCNA platform enable the assessment of tumor burden dynamics, clonal evolution, and emerging resistance patterns over time (Figure 8).

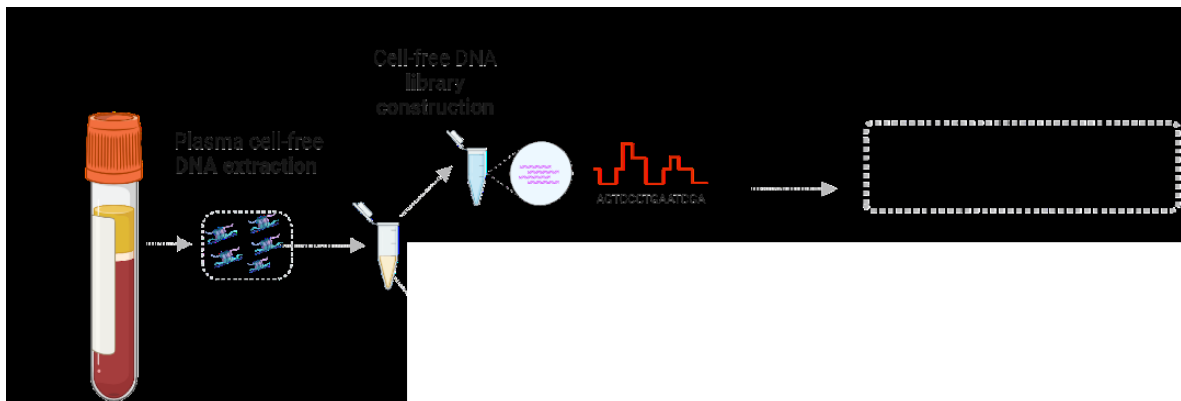


**Figure 8:** Schematic depiction of the molecular workflow from cfDNA extraction to sequencing. Figure created in BioRender.

By elucidating the mechanisms underlying resistance to both beta minus and alpha emitter-based radioligand therapies, and by evaluating the efficacy of tandem treatment regimens, this study seeks to refine current patient selection criteria and improve the predictive accuracy of a treatment response. Ultimately, the goal is to advance the development of more effective, individualized therapeutic strategies that will enhance clinical outcomes for patients with mCRPC.



# III MATERIAL & METHODS

## 1. ETHICAL APPROVAL

The study, titled *“Molekulare Charakterisierung der Tumorevolution im Rahmen von Endoradiotherapien des metastasierten Prostatakarzinoms”* (“*Molecular Characterization of Tumor Evolution in the Context of Endoradiotherapies for Metastatic Prostate Cancer*”), received ethical approval (S-882/2020) from the Ethics Committee of the Medical Faculty at Heidelberg University. This project is a non-interventional, exploratory investigation focusing on therapy resistance in patients treated with  $[^{225}\text{Ac}]\text{Ac}-/[^{177}\text{Lu}]\text{Lu-PSMA-617}$ . The study complies with national regulations, the *Declaration of Helsinki*, and *Good Clinical Practice (GCP)* guidelines. Furthermore, in accordance with *Paragraph 13(2b) of the German Pharmaceuticals Law*, the therapy was administered as a salvage treatment for patients with mCRPC who had progressive disease and were either resistant to or ineligible for approved therapeutic options. Written informed consent was obtained from all participants prior to inclusion, ensuring that patients could withdraw their consent at any time without repercussions. The study involves the collection of blood samples from mCRPC patients scheduled for bimonthly  $[^{225}\text{Ac}]\text{Ac}-/[^{177}\text{Lu}]\text{Lu-PSMA-617}$  cycles, with no additional risks or burdens to participants. Subsequent to the blood collection, samples were pseudonymized to protect patient confidentiality in accordance with the *EU General Data Protection Regulation (GDPR)*. The protocol was designed to ensure compliance with ethical and legal standards, and the study does not involve any commercial sponsorship or conflicts of interest.

## 2. PATIENTS

This doctoral thesis encompasses a cohort of 78 patients who received  $[^{225}\text{Ac}]\text{Ac}-/[^{177}\text{Lu}]\text{Lu-PSMA-617}$  under the conditions of the updated declaration of Helsinki, paragraph 37 (Unproven Interventions in Clinical Practice). The clinical work was performed at the Heidelberg University Hospital under the supervision of Dr. med. Clemens Kratochwil and the support of Dr. med. Erik Winter, Dr. Jorge Hoppner and Dr. Andreas Merkel. Clinical and imaging data, were generously provided by Dr. med. Clemens Kratochwil. Survival data were provided from both Dr. med. Clemens Kratochwil and PD Dr. med. Hendrik Rathke consulting the national death record registers. The cohort included individuals with mCRPC who had exhausted all approved standard therapies, including second-generation androgen receptor inhibitors, taxane-based chemotherapy, or other unproven clinical interventions. Following a comprehensive evaluation by the tumor board and in light of the absence of alternative treatment options, PSMA-directed RLT was proposed as a last-resort intervention for these patients. All included

patients demonstrated a PSMA-positive tumor phenotype as confirmed by imaging with either [<sup>68</sup>Ga]Ga-PSMA-11 and [<sup>18</sup>F]PSMA-1007 in PET(/CT), or [<sup>99m</sup>Tc]Tc-PSMA-GCK01 in SPECT. The selection of patients for [<sup>225</sup>Ac]Ac-/ [<sup>177</sup>Lu]Lu-PSMA-617 therapy was primarily based on the presence of extensive bone marrow infiltration and diffuse liver or other organs metastases, which precluded the use of [<sup>177</sup>Lu]Lu-PSMA-617 (Pluvicto®) as stand-alone therapy (165). From the total cohort, 41 patients had available paired samples at baseline and one follow-up, 57 patients had only baseline samples, and 17 patients had baseline and relapse samples (Table 1). These subsets were selected for subsequent molecular and clinical analyses.

**Table 1:** Patient grouping strategy for clinical and molecular evaluations.

Group	Number of patients
Total cohort	78
Baseline sample only	57
Baseline + 1 follow-up sample	48
Baseline + 1 relapse sample	17

### 3. SAMPLES

A total of 172 samples were collected from 78 patients enrolled in this study (Table 2). The number of samples per patient varied between 1 and 7, depending on the clinical context and the number of treatment cycles completed (Table A1, Appendix). Samples were obtained at various treatment stages, including baseline (cycle 0) and subsequent treatment cycles. Of the total, 57 samples were collected at baseline (treatment cycle 0), representing the highest number of samples at a single time point. The majority of the remaining samples were obtained during the early treatment phases, with treatment cycle 1 contributing a significant proportion. The number of samples decreased progressively in later treatment cycles, primarily due to patient dropout, therapy discontinuation, or unknown clinical constraints (Table 3).

**Table 2:** Number of patients and samples in total included in the study.

Group	Count
Total number of Patients	78
Total number of samples	172

**Table 3:** Number of samples per cycle in total included in the study.

Cycle treatment	Sample count
0	57
1	55
2	33
3	14
4	8
5	3
6	2

### 3.1 Sample collection & processing

Venous blood samples (7-14 mL) were prospectively collected in EDTA-coated tubes (BD Biosciences) and processed within 30 minutes of collection upon the patients' arrival at the clinic, prior to undergoing therapy. Once collected, the clinic notified the research team, and the samples were transported from the Nuclear Medicine Department (Nuklearmedizin) of the University Hospital (Universitätsklinikum Heidelberg) to the DKFZ for processing as shown in Figure 9. The samples underwent density gradient centrifugation at 2000 x g for 10 minutes at 4°C without braking to separate the plasma and buffy coat employing Heraeus Christ Minifuge GL 4400 centrifuge (Heraeus Christ, Osterode am Harz, Germany). The plasma was carefully isolated, transferred to 15 mL Falcon tubes, and separated from the buffy coat. Immediately after processing, the plasma samples were frozen at –80°C to ensure preservation until further analysis.

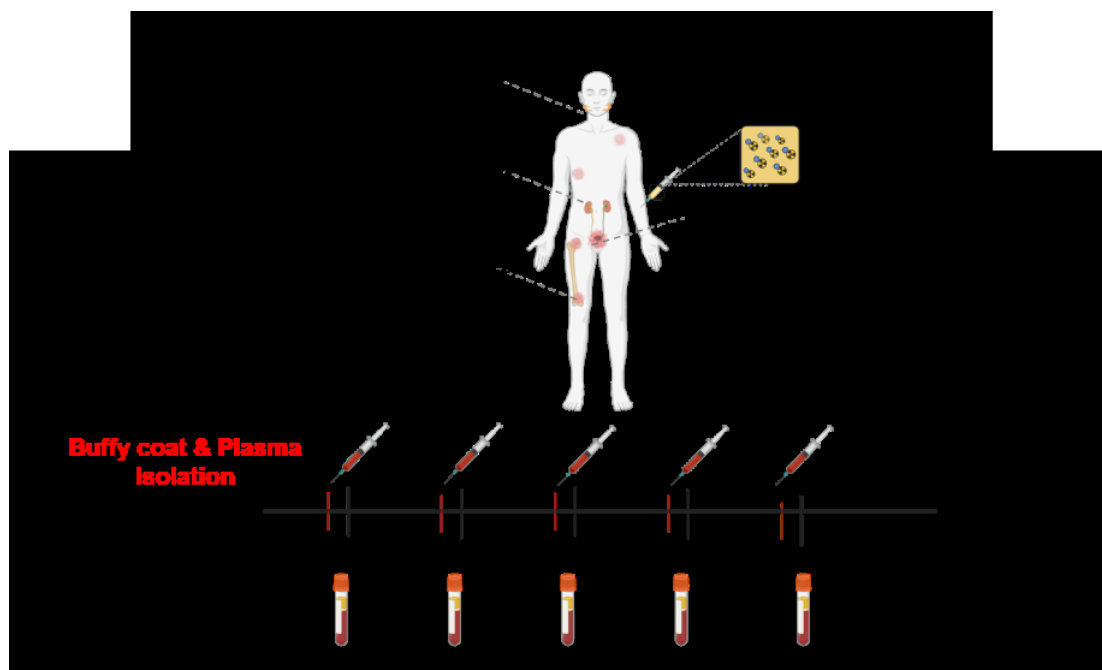
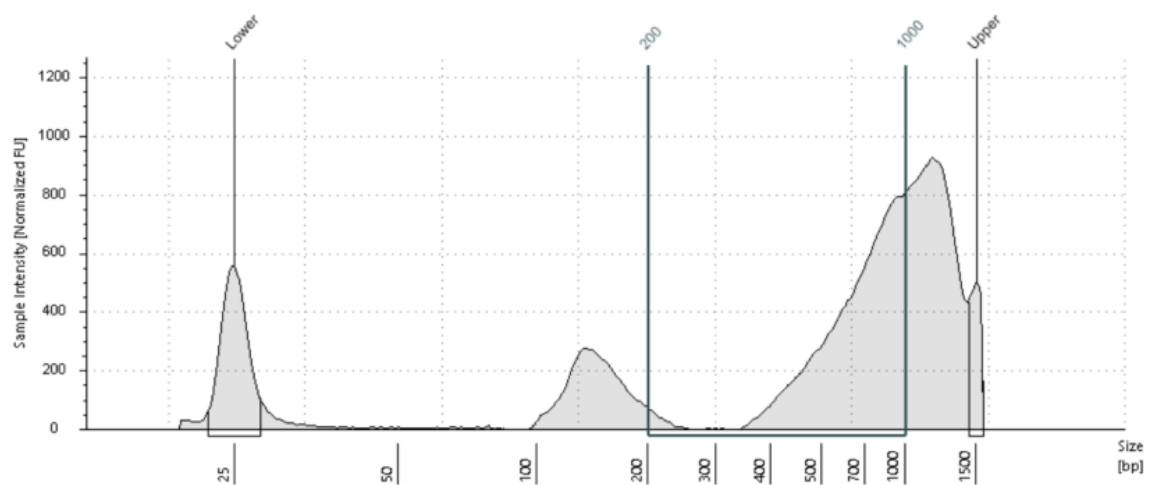


**Figure 9:** Overview of the bimonthly blood collection schedule prior to therapy administration, including the associated sample processing workflow. Figure created in BioRender.

### 3.2 cfDNA extraction quantification and quality control

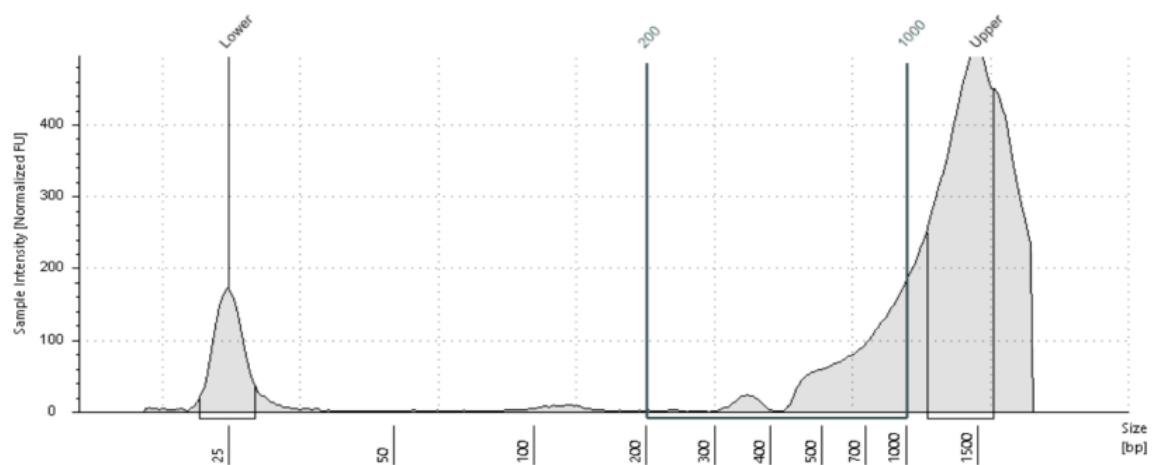
cfDNA was extracted from thawed plasma aliquots using the QIAamp MinElute ccfDNA Midi Kit (Qiagen, Hagen, Germany; Cat. No./ID: 55284) following the manufacturer's protocol. Prior to extraction, buffers ACB and ACW2 were prepared by adding isopropanol and ethanol, respectively, as instructed. Magnetic bead suspension was vortexed and maintained in suspension during pipetting. Plasma samples were first incubated with bead binding buffer and magnetic beads in 15 mL tubes at room temperature with gentle agitation. After magnetic separation and washing, the beads were resuspended in bead elution buffer and transferred to Eppendorf 5415D Digital microcentrifuge (Eppendorf, Hamburg, Germany). Following additional incubation and magnetic separation, the supernatant was mixed with Buffer ACB and applied to QIAamp UCP MinElute columns for DNA binding. Subsequent wash steps were performed using Buffer ACW2, followed by high-speed centrifugation to dry the membrane. DNA was eluted in 50  $\mu$ L of ultra-clean water, with an additional re-elution step to maximize yield. The extracted cfDNA, eluted in 50  $\mu$ L, was stored at  $-80^{\circ}\text{C}$  until further analysis. Quantification of the extracted cfDNA was performed using the Qubit 1X dsDNA High Sensitivity (HS) Assay Kit (Thermo Fisher, Karlsruhe, Germany) on a Qubit 4 Fluorometer (Thermo Fisher, Karlsruhe, Germany; Q33238). For DNA fragment analysis, including quantification, sizing, and purity determination, the High Sensitivity D1000 ScreenTape assay (Agilent, Waldbronn, Germany) was employed. This method allowed for precise sizing of DNA fragments within the range of 35 to 1000 bp and detection of low-abundance samples with concentrations as low as 5 pg/ $\mu$ L (Figure 10, Figure 11). In the graph displays the quality control assessment of optimal cfDNA samples. The x-axis represents fragment size in base pairs (bp), while the y-axis indicates sample intensity, reflecting the fluorescence signal generated by DNA fragments binding to an intercalating dye during capillary electrophoresis. This signal is directly proportional to the DNA concentration at each fragment size. Lower and upper markers provide size references for evaluating fragment distribution. As expected, the cfDNA profile shows a predominant peak between 100–200 bp, consistent with high-quality mononucleosomal ctDNA suitable for downstream analysis. Data analysis was conducted using TapeStation Analysis Software 5.1, with 150 bp defined as the target fragment size. In Figure 11 a suboptimal cfDNA profile is observed, characterized by low overall sample intensity, which reflects a low cfDNA concentration across the fragments size range.



Region Table

From [bp]	To [bp]	Average Size [bp]	Conc. [pg/μl]	Region Molarity [pmol/l]	% of Total	Region Comment	Color
200	1000	699	2000	4900	45.48	C&R	

**Figure 10:** Optimal cfDNA profile obtained using the TapeStation.



Region Table

From [bp]	To [bp]	Average Size [bp]	Conc. [pg/μl]	Region Molarity [pmol/l]	% of Total	Region Comment	Color
200	1000	704	99.0	241	36.64	C&R	

**Figure 11:** Suboptimal cfDNA profile obtained using the TapeStation.

### 3.3 cfDNA library preparation

The cfDNA samples were transported to the EMBL GeneCore Facility, where library preparation and next-generation sequencing were conducted under the supervision of Dr. Vladimír Beneš, Head of the GeneCore Facility, with technical support provided by Hilal Ozgur. cfDNA library preparation was conducted using the Colibri PS DNA Library Prep Kit (Thermo Fisher, Karlsruhe, Germany) for Illumina sequencing platforms (Illumina Inc., San Diego, CA, USA) as illustrated in Figure 12.

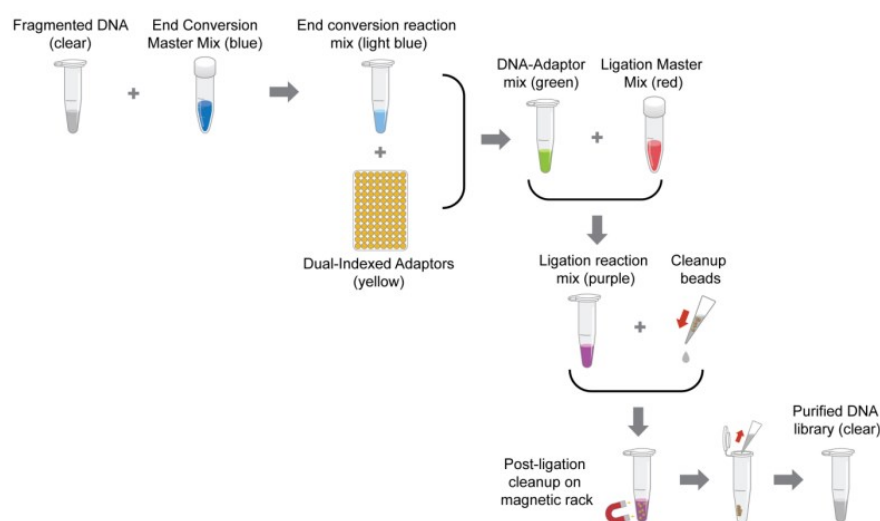


**Figure 12:** Colibri PS DNA Library Prep Kit steps from the manufacturer manual description.

Input cfDNA amounts ranged from 3–20 ng, with a size selection of 100–200 bp, optimized for ultra-low-pass whole genome sequencing (ULP-WGS). Briefly, cfDNA was first subjected to end-repair and dA-tailing in a single reaction tube to prepare DNA fragments for adaptor ligation. Dual-indexed Illumina-compatible adaptors were then ligated to the end-repaired DNA fragments. After dual-index adapter ligation, a 1X clean-up was conducted using magnetic beads, and libraries were eluted in 20  $\mu$ L of elution buffer. Subsequently, library amplification by PCR was conducted with the number of cycles optimized based on the input DNA concentration. PCR amplification was tailored to the quality of the cfDNA: optimal-quality samples underwent 8 cycles, while suboptimal-quality samples required 12 cycles. All subsequent steps, including the preparation and clean-up of amplified libraries, adhered to the manufacturer's standard protocol to ensure high-quality libraries while minimizing over-amplification. Following library preparation, quality control (QC) was performed using the Bioanalyzer High Sensitivity DNA Assay (Agilent, Waldbronn, Germany) to verify the fragment size distribution, targeting a peak at 300 bp (Figure 13). As previously described, the x-axis in Figure 13 and Figure 14 represents the fragment size in bp, while the y-axis displays the fluorescence intensity, which

reflects the concentration of the cfDNA library. cfDNA concentrations were measured using the Qubit 4 Fluorometer (Thermo Fisher, Karlsruhe, Germany) using the Qubit High Sensitivity Kit (Thermo Fisher, Karlsruhe, Germany). Occasionally, a minor peak corresponding to adapter dimers (~150 bp) was observed. This observation is consistent with the information provided in the Collibri™ PS DNA Library Prep protocol (see pages 16 and 41). To address the impact of primer dimers on sequencing coverage, a clean-up was performed on each individual sample was performed. This involved a 0.85X magnetic bead clean-up to effectively remove primer dimers, followed by a second QC using the Qubit and Bioanalyzer. Libraries were pooled based on cfDNA concentration and size distribution, ensuring a consistent fragment size selection of approximately 300 bp. Library molarity was calculated using the standard formula (Equation 1):

**Equation 1: DNA molarity calculation**

$$Molarity (M) = \frac{DNA\ concentration\ \left(\frac{ng}{\mu l}\right)}{(650 * fragment\ size(bp))} * 1,000,000$$

To normalize the libraries, the volume of each sample was calculated by dividing its measured molarity by a predefined target molarity, which was selected based on the range between the highest and lowest molarity values of the processed samples. This ensured equimolar representation of each sample in the final pool. The calculated volume was consistent across all samples, allowing for proportional molarity-based normalization (Equation 2). The normalized libraries were then pooled together and used for subsequent sequencing steps.

**Equation 2: Volume required for pooling**

$$Volume\ (\mu l) = \frac{Measured\ Molarity\ (M)}{Target\ Molarity\ (M)}$$



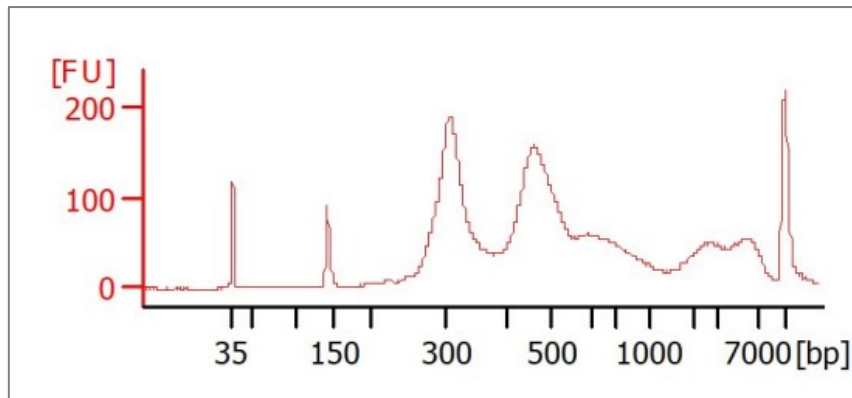


**Figure 13:** cfDNA library quality showing a primary ~300 bp peak starting from an optimal cfDNA, assessed using the Bioanalyzer.

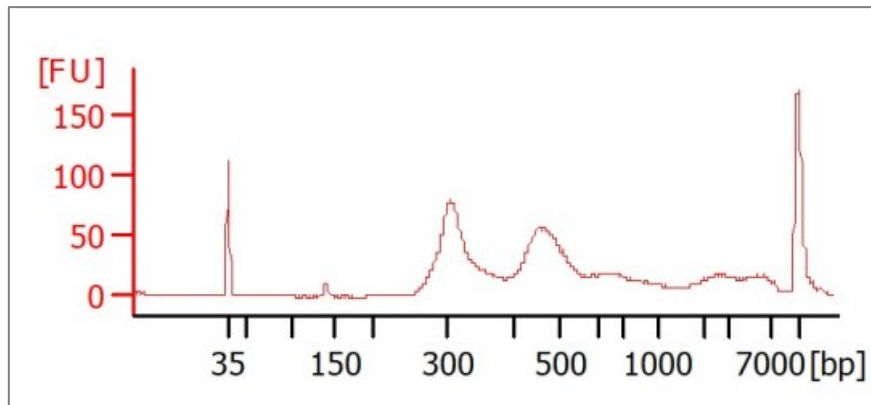


**Figure 14:** cfDNA library quality showing a primary ~300 bp peak starting from a suboptimal cfDNA, assessed using the Bioanalyzer.

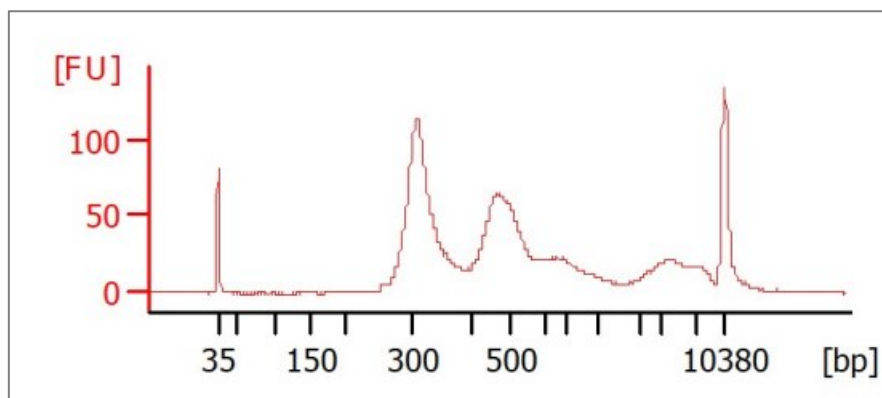


**Figure 15:** cfDNA library profile after adapter dimer removal, showing a primary peak at ~300 bp.

After verifying the pool concentration and Bioanalyzer profile, the molarity was recalculated using Equation 1. The sample was then diluted to 2 nM. A final loading concentration of 650 pM was used for insertion into the sequencing cartridge.

## 4. NEXT GENERATION SEQUENCING

Libraries were sequenced on the Illumina NextSeq 2000 platform (Illumina Inc., San Diego, CA, USA) with sequencing kits selected based on the number of samples processed per time point. For 16 samples, the P2 200 cycles kit (100 PE); and for larger sample pools of up to 32 samples, the P3 200 cycles kit (100 PE) was employed. "PE" refers to paired-end sequencing, where both ends of the DNA fragment are read, and "200 cycles" indicates the total number of sequencing cycles—100 cycles for each end, resulting in a total read length of 200 base pairs ( $2 \times 100$  bp). The number of reads generated per sequencing run varied depending on the flow cell kit used. Specifically, the P2 kit yielded around 400 million paired-end reads, while the P3 kit generated up to 1 billion paired-end reads. Given the human genome size of approximately 3 billion base pairs, resulting in mean theoretical coverage of  $\sim 1.67\times$  for 16 samples (P2), and  $\sim 0.83\times$  for 32 samples (P3). To ensure comparability between datasets generated from different kits and depths, coverage normalization was performed using Samtools to downsample all samples to a uniform depth suitable for ultra-low-pass whole genome sequencing (ULP-WGS) analysis using ichorCNA.

### 4.1 ULP-WGS data analysis

The upstream analysis was conducted with the support of Dr. Tobias Rausch at the EMBL Gene Core Facility in Heidelberg. ULP-WGS of cfDNA was performed, achieving an average genome-wide coverage of approximately 2x. From this data, segmental copy number alterations and TFX were estimated using the ichorCNA tool (166, 167). In brief, the genome was segmented into non-overlapping bins of 1 megabase (Mb), and aligned sequencing reads were quantified within each bin using the HMMcopy Suite. To avoid artifacts, centromeric regions were excluded based on chromosome gap coordinates from the UCSC Genome Browser for hg38 (GRCh38), along with 1 Mb upstream and downstream flanking regions. Normalization of read counts was carried out using the HMMcopy R package, correcting for GC content and mappability biases. Log2 copy number ratios were then calculated for each bin by comparing them to a reference panel of ULP-WGS data from 27 healthy donors. Since cfDNA represents a mixture of tumor- and non-tumor-derived fragments, copy number calling and TFX estimation were performed using a hidden Markov model (HMM) approach. This method assigns discrete copy number states, including hemizygous deletion (HETD, 1 copy), copy-neutral (NEUT, 2 copies), gain (GAIN, 3 copies), amplification (AMP, 4 copies), and high-level

amplification (HLAMP,  $\geq 5$  copies). Due to resolution limitations, homozygous deletions, which tend to occur at smaller scales than 1 Mb, were not included in the analysis (167). The software ichorCNA is available at <https://github.com/broadinstitute/ichorCNA>.

## 5. BIOSTATISTICAL ANALYSIS

All statistical analyses were conducted under the guidance and support of Thomas Hielscher from the Biostatistics Core Facility at DKFZ. Using R Studio (version 4.3.1), a range of biostatistical methods was applied to evaluate biomarker dynamics, survival outcomes, and their correlations with clinical and genomic parameters. The analyses included survival analyses (e.g., Kaplan-Meier and Cox proportional hazards models), correlation studies (e.g., Pearson and Spearman coefficients), group comparisons (e.g., t-tests, ANOVA, and non-parametric tests), and regression modelling to assess associations between variables. All the packages used can be found in Table A2 (Appendix). Graphs were created using the ggplot2 package in R and further refined using Adobe Illustrator for publication-quality figures. All codes are available in the group's GitHub repository <https://git.dkfz.de/m076r/mcrpc-cfdna>.

### 5.1 Biomarker dynamics across treatment cycles

The dynamics of tumor markers across treatment cycles were assessed to evaluate biomarker trends throughout the treatment cycles. Key variables, including PSA, ALP, and LDH, were integrated and processed using anonymized clinical reports kindly provided by Dr. med. Clemens Kratochwil. Tfx was derived from ichorCNA analysis. Data were reshaped into a wide format to enable paired observations across treatment cycles. Both patients with complete and incomplete biomarker measurements for any treatment cycle were included in the analysis. Pairwise comparisons of biomarkers across treatment cycles (0–5) were performed using the Wilcoxon signed-rank test, appropriate for non-parametric paired data. p-values for these comparisons were calculated and adjusted to identify significant differences ( $p < 0.05$ ). Visualizations of biomarker dynamics, including Tfx, PSA, LDH, and ALP, were generated as box plots with overlaid dot plots using the ggpubr and ggplot R packages. Pairwise comparisons were annotated on the box plots using the stat\_pvalue\_manual function from ggpubr, with p-values displayed directly on the plots. Statistical significance thresholds were set to  $p < 0.05$ , and significant changes between treatment cycles were highlighted in the visualizations.

## 5.2 Analysis of TM distribution across metastasis stages

Given the relevance of PSA and Tfx, the distribution of PSA and Tfx was analysed to evaluate their utility for stratifying patients based on metastasis burden. This analysis was performed at a single time point, baseline (prior to treatment cycle 1), and included only patients with documented metastatic stages and available baseline assessments for both tumor markers (TM). Clinical and TM data were merged using patient identifiers to incorporate metastasis stage information. Patients were categorized into three groups based on metastasis localization: (1) *bone-only*, (2) *bone and lymph nodes*, and (3) *bone, lymph nodes, and additional organs*. TM were stratified according to these metastasis categories for statistical analysis and visualization. The Kruskal-Wallis test, a non-parametric method, was used to compare the distributions of PSA and Tfx across the metastasis groups, assessing whether the median values differed significantly between categories. Violin plots were generated using the `ggpubr` package in R to visualize the distributions of PSA and Tfx across the metastasis groups, with Kruskal-Wallis p-values displayed on the plots to highlight the statistical significance of observed differences.

## 5.3 Correlation analyses

The relationships between Tfx and the biomarkers PSA, ALP, and LDH were assessed using Pearson's correlation coefficients and linear regression models. All patients were included and considering all the timepoints available in the dataset. For each patient, correlations were analyzed comparing Tfx values with corresponding PSA, ALP, and LDH measurements. Scatter plots with regression lines and 95% confidence intervals were created to visualize these associations. Pearson's correlation coefficients ( $r$  values) and p-values were reported to quantify the strength and significance of each correlation.

## 5.4 Longitudinal biomarker dynamics and correlation

Clinical and biomarker data were integrated using unique patient identifiers to align relevant clinical information with treatment cycles. The analysis included 41 patients who had recorded both a baseline and at least one follow-up treatment cycle. Variables of interest included Tfx, PSA, LDH, and treatment cycles. Only those patients were included in this analysis for whom a complete set of data (i.e. baseline to last treatment cycle) were included to ensure data quality and comparability. To evaluate the dynamic relationships between changes in Tfx and changes in PSA, ALP, or LDH over time, fold-change analyses were conducted. The fold-change was calculated using biomarker values at the baseline and the latest recorded time point for each patient. For each patient, fold-change calculations were performed to assess the dynamic relationships between biomarkers over time. The Tfx fold

change was calculated as the difference between Tfx at the latest recorded treatment cycle and the baseline (Equation 3).

**Equation 3: Tfx fold change calculation**

$$Tfx \text{ fold change} = Tfx \text{ latest cycle} - Tfx \text{ baseline}$$

For PSA and LDH, the differences were normalized using a logarithmic transformation to reduce variability and minimize the influence of extreme values. This approach was proposed by Dr. Thomas Hielscher. The PSA fold change was calculated as the log2 ratio of the baseline PSA level to the latest recorded PSA level (Equation 4).

**Equation 4: PSA fold change calculation**

$$\text{Log}_2(\text{PSA fold change}) = \text{Log}_2\left(\frac{\text{PSA baseline}}{\text{PSA latest cycle}}\right)$$

Similarly, the LDH fold change was determined as the log2 ratio of the baseline LDH level to the latest recorded LDH level (Equation 5).

**Equation 5: LDH fold change calculation**

$$\text{Log}_2(\text{LDH fold change}) = \text{Log}_2\left(\frac{\text{LDH baseline}}{\text{LDH latest cycle}}\right)$$

These calculations allowed for a standardized evaluation of biomarker dynamics across patients while accounting for variability in baseline and follow-up measurements. Biomarker values were scaled to a standard deviation of 1 (without centring) to retain the directionality of changes while ensuring comparability across variables. This integrated approach facilitated the evaluation of longitudinal biomarker associations across treatment cycles, providing insight into dynamic relationships between Tfx, PSA, ALP, and LDH changes over time.

## 6. RISK ANALYSIS

Based on treatment response and disease progression, the potential of ctDNA-based markers as predictive and prognostic indicators was evaluated in mCRPC patients. Receiver Operating Characteristic (ROC) curve analysis was used to assess the predictive value of pre-treatment biomarkers, including PSA, Tfx, and LDH, in determining therapy cycle response. Furthermore, a multi-marker model was developed to evaluate whether integrating multiple biomarkers enhanced predictive accuracy. To examine prognostic significance, Cox Proportional Hazards analysis was performed to assess Tfx dynamics over time, investigating whether increases in Tfx during treatment cycles correlated with a higher risk of disease progression. Additionally, survival analysis was conducted to evaluate the impact of clinical and genomic factors on overall survival (OS). Kaplan-Meier survival analysis and Cox Proportional Hazards modeling were employed to estimate survival distributions and identify key risk factors influencing patient outcomes.

### 6.1 Predictive performance using ROC analysis

ROC curve analysis was performed to evaluate the predictive performance of pre-treatment biomarkers in distinguishing clinical response and disease progression. Biomarkers analysed included PSA, Tfx, and LDH. Data were filtered to include only patients with complete pre-treatment biomarker measurements (PSA, Tfx, and LDH) and corresponding clinical outcome information for at least two consecutive treatment cycles. Logistic regression models were employed to calculate predictive probabilities for treatment response. Two types of models were used: (1) individual biomarker models for PSA or Tfx (2) a multi-marker model that combined Tfx, PSA, and LDH. For the multi-marker model, PSA and LDH values were log-transformed to account for right-skewed distributions and reduce variability. Fitted probabilities from these models were used as inputs for the ROC analysis. ROC curves were generated to assess the ability of each biomarker and the multi-marker model to distinguish between response outcomes. Sensitivity and specificity discrimination were assessed by ROC curve analysis and corresponding AUC with 95% confidence interval. To account for the clustered structure of the data, with repeated measures within patients, a nonparametric clustered ROC analysis was performed based on the methodology described by Obuchowski (1997) (168). This approach adjusted for intra-patient correlations, ensuring robust comparisons of AUCs between individual biomarkers and the multi-marker model. Data pre-processing involved aligning pre-treatment biomarker values (PSA, Tfx, and LDH) with clinical response outcomes for each cycle. Logistic regression models were fitted for each biomarker and for the combined multi-marker model to predict treatment response (e.g., partial response versus progressive disease). Sensitivity and specificity calculations for varying thresholds allowed the construction of ROC curves, while AUC values with 95% confidence intervals

were calculated to quantify predictive performance. Finally, ROC curves were plotted for individual biomarkers and the multi-marker model, enabling a visual comparison of their predictive capabilities.

## 6.2 Cox hazard ratio analysis

The prognostic significance of increases in Tfx as a time-dependent risk factor for progressive disease was assessed using a Cox Proportional Hazards model. Patient and clinical data were organized by treatment cycles, and only those patients with multiple Tfx measurements and corresponding clinical response data across different cycles were included in the analysis. Patients with fewer than two Tfx assessments or those who experienced progressive disease at the first available Tfx measurement were excluded to ensure accurate evaluation of Tfx dynamics over time. For each patient, the time to progressive disease was calculated as the treatment cycle when progressive disease was first observed during the follow-up period. The time to the first increase in Tfx was defined as the treatment cycle when Tfx first showed an increase prior to the occurrence of progressive disease. Changes in Tfx between consecutive treatment cycles were determined to identify increases, and an increase in Tfx was defined as any positive change observed before the clinical onset of progressive disease. Patients were followed until the occurrence of progressive disease or their last documented follow-up cycle, whichever occurred first. The Cox Proportional Hazards model was used to evaluate the relationship between increases in Tfx and the time to progressive disease annotation. The outcome variable was the time at which progressive disease was first documented, while the primary predictor variable was the time at which an increase in tumor fraction was first observed. The model estimated the hazard ratio and the corresponding confidence intervals to quantify the relative risk associated with increases in Tfx. To visualize the treatment course and Tfx dynamics for individual patients, swimmer plots were generated.

## 6.3 Survival analysis

The prognostic value of clinical and genomic factors on OS was assessed using Kaplan-Meier survival analysis and Cox Proportional Hazards (Cox PH) modelling. Kaplan-Meier curves were generated to estimate OS distributions, with patient stratifications performed based on different grouping modalities. Survival times, defined as months since therapy initiation, were compared using the log-rank test to determine statistical significance. Median survival times were calculated to summarize survival outcomes across groups. Specifically, comparisons were made between patients with low versus high copy number variation (CNV) burden, as well as among those receiving different treatment regimens, including chemotherapy naive, ADT combined with chemotherapy, and ADT in combination with chemotherapy and PSMA-TRNT. Additionally, survival outcomes were evaluated based on Tfx,

which was stratified into three categories: low Tfx (0.000–0.225), intermediate Tfx (0.225–0.434), and high Tfx (0.434–0.794). To evaluate the impact of individual clinical and genomic markers on OS, univariable Cox PH models were applied. Hazard ratios (HRs) and 95% confidence intervals (CIs) were calculated to quantify the risk associated with each factor. The analysis was conducted using the R survival package, and Kaplan-Meier curves were visualized using the prodlim package. All statistical tests were two-sided, with a significance threshold set at  $p < 0.05$ . This approach allowed for the assessment of both independent and combined effects of clinical and genomic factors on OS within the studied cohort.

## 7. GENOMIC ANALYSIS

To gain deeper insights into the genomic landscape of mCRPC and radiation resistance, a comprehensive genomic analysis was conducted, focusing on copy number alterations (CNAs), oncogene and tumor suppressor identification, and pathway enrichment analysis. By leveraging bioinformatics tools, this study aimed to improve patient stratification and treatment response predictions, providing valuable insights for precision oncology strategies. To achieve this, CNAs and Tfx distributions were analysed using hierarchical clustering, correlating these genomic features with clinical outcomes. The GISTIC algorithm was employed to identify significant regions of genomic amplification and deletion, distinguishing key driver events from background alterations and pinpointing genomic instabilities that may contribute to disease progression. Following the identification of key CNAs, the COSMIC database (<https://cancer.sanger.ac.uk/cosmic/census>) was utilized to classify altered genes as potential oncogenes or tumor suppressors, assessing their biological relevance radiation resistance. To further investigate the functional implications of these genomic alterations, pathway enrichment analysis was conducted using EnrichR, identifying key biological processes and signalling pathways associated with the affected genes.

### 7.1 Tfx clustering and CNV burden correlation analysis

CNAs were assessed using logR values extracted from 1Mb chromosomal bins. Hierarchical clustering of samples was performed using the pheatmap function in R, stratifying patients based on tumor fraction and baseline response. To evaluate the chromosomal distribution of logR values and their correlation with clinical features, heatmaps were constructed using processed logR data from common 1 Mb chromosomal bins. The logR values for each sample were extracted from segment files (\*.cna.seg) using the ichorCNA pipeline. To analyse logR values for a specific treatment cycle, samples from Cycle 0 were filtered based on patient data. Chromosome start and end positions were



standardized across samples. Chromosome identifiers were converted to numeric values. Data were organized into a matrix for visualization, with rows representing chromosomal regions and columns representing samples. Heatmaps were generated using the pheatmap package in R to visualize logR values across all samples. Columns (samples) were clustered using hierarchical clustering with Ward's minimum variance method (ward.D), which iteratively merges clusters to minimize the total within-cluster variance, resulting in compact and homogeneous groupings. Row clustering was omitted. A continuous color gradient from blue (low logR values) to red (high logR values) was applied to enhance visual interpretation. Clinical metadata—including treatment cycle, metastasis status, and overall response—was annotated on the columns. The resulting dendrogram was cut to define two main sample clusters, representing low and high CNV groups. These cluster assignments were added as metadata for downstream analyses.

## 7.2 Tfx correlation with CNV burden

The Tfx for each cluster was extracted, and normality of the distributions was assessed using the Shapiro-Wilk test. Since one cluster was not normally distributed, the Wilcoxon rank-sum test was used to compare Tfx values between clusters. Boxplots of Tfx by cluster were created using the ggplot2 package. Statistical significance between clusters was indicated with p-values annotated directly on the plots, formatted in scientific notation. Custom colour palettes were applied for visualization. This approach allowed for the integration of genomic data with clinical features, enabling detailed clustering and analysis of tumor fractions in relation to chromosomal regions and treatment response.

## 7.3 GISTIC analysis

To identify significant CNAs across samples, the Genomic Identification of Significant Targets in Cancer (GISTIC) algorithm (version 2.0.23) was employed (169). This analysis aimed to pinpoint regions of genomic amplification and deletion, distinguishing biologically relevant driver events from background alterations. CNA data were processed using seg.txt files generated from the ichorCNA pipeline. Key columns included the sample identifier (ID), chromosome number (chrom), segment start and end positions (start and end), the number of markers supporting the segment (num.mark), and the corrected copy number for the segment (Corrected\_Copy\_Number). Baseline samples were selected, and segment copy number values were transformed using the formula:

**Equation 6: Segment copy number alteration normalization**

$$seg.cn = \log_2 \left( \frac{\text{Corrected\_Copy\_Number}}{2} \right)$$

This transformation normalized the copy number values relative to the diploid state, producing *seg.cn* values, which were subsequently used as input for the GISTIC analysis. The GISTIC algorithm was executed with the following configuration: broad events analysis was enabled with a length cut-off of 0.7 (range 0-1), amplification and deletion thresholds were set to 0.1 (considering  $\log_2 = 0$  as a neutral copy number). To limit the influence of extreme values,  $\log_2$  copy number ratios were capped at 1.5. The analysis was performed with a confidence level of 0.75 and a q-value threshold of 0.25 to ensure statistical power. Additional settings included enabling gene-centric analysis, peeling off chromosomal arms for better delineation of focal alterations, and using the extreme G-score calculation mode. The analysis incorporated a reference gene file (hg38.UCSC.add\_miR.160920.refgene.mat), and outputs were generated in a specified directory. The GISTIC analysis provided several outputs, including significant regions of amplification and deletion annotated with associated genes, genome-wide CNA profiles highlighting regions of genomic instability, G-scores quantifying the magnitude of CNA significance, and q-values representing the statistical significance of each region. Gene-centric outputs detailed alterations at the individual gene level.

## 7.4 Identification of oncogenes and tumor suppressors

To identify potential oncogenes and tumor suppressors associated with significant genomic alterations, the Catalogue of Somatic Mutations in Cancer (COSMIC) database (<https://cancer.sanger.ac.uk/cosmic/census>) was used as a reference. Genes identified through GISTIC analysis, specifically those located within significant amplification and deletion peaks at a 75% confidence interval, were selected for further evaluation. Key genes were extracted from the GISTIC output files, including the Amplification Genes File (amp\_genes.conf\_XX.txt, where XX represents the confidence level) and the Deletion Genes File (del\_genes.conf\_XX.txt). Each amplification peak file contained the following information:

- Cytoband
- Q-value
- Residual Q-value
- Wide peak boundaries

These rows defined the lesion boundaries, while subsequent rows listed the genes within each wide peak region. In cases where no genes were directly mapped to a peak, the nearest gene was listed in brackets. The deletion gene file followed the same format, detailing deletion peaks and associated

genes. The gene list was refined by excluding entries with minimal functional relevance based on literature review and known annotations. The remaining genes were cross-referenced with the COSMIC database, which provides curated annotations for oncogenes and tumor suppressors. Only genes explicitly categorized as oncogenes or tumor suppressors were retained for further analysis. The final set of genes was examined within the context of prostate cancer biology, evaluating their potential roles in disease progression and their correlation with clinical parameters, such as tumor fraction and therapeutic outcomes. This approach allowed for the prioritization of biologically significant genomic alterations, providing insights into their potential implications for tumor behavior and treatment response.

## 7.5 EnrichR analysis

To explore pathways and biological processes enriched within the genomic regions identified by GISTIC analysis, functional enrichment analysis was conducted using EnrichR (<https://maayanlab.cloud/Enrichr/>), a publicly available web-based tool. Genes associated with significant amplification or deletion peaks from GISTIC analysis, with a confidence interval of 75%, were selected as the input for the enrichment analysis. The analysis focused on enrichment within three key databases available through the Enrichr platform: Gene Ontology (GO) Biological Processes, the Kyoto Encyclopedia of Genes and Genomes (KEGG), and the Reactome Pathway Database. The selected gene list was uploaded to EnrichR, where enrichment scores, adjusted p-values, and fold changes were calculated for each pathway or biological process based on the provided input. EnrichR ranked the results according to adjusted p-values (false discovery rate, FDR), enabling the identification of statistically significant pathways and biological processes. Pathways with an adjusted p-value below 0.05 were considered significant and prioritized for further analysis. The results were visualized through bar plots and tables, highlighting the top enriched terms and their corresponding gene counts, providing insights into the biological processes and pathways potentially influenced by the identified genomic alterations.



# IV RESULTS

## 1. PATIENTS

This doctoral thesis is based on a well-defined cohort of 78 patients, selected based on the predefined inclusion criteria outlined in the ethical approval S-882/2020. Patients presenting with a diffuse pattern of bone marrow infiltration were included and stratified for treatment with actinium-lutetium (165). Comprehensive demographic, clinical, and biomarker data were collected for all participants to enable an in-depth analysis of TM dynamics and their association with clinical outcomes. Clinical data included a detailed account of each patient's medical history up to the initiation of treatment. The biomarkers taken into consideration were PSA, LDH, and ALP. Patients were stratified into distinct groups to facilitate comparisons and assess the prognostic value of tumor markers across various clinical scenarios.

### 1.2 Patient cohort characterization

The study cohort comprised 78 patients, from whom 172 samples were collected across various treatment cycles. The median age of the cohort was 76 years, with a range spanning from 55 to 91 years. The age distribution is illustrated in Figure 16, which approximates a Gaussian distribution. The histogram reveals a slightly right-skewed pattern, with the majority of patients falling within the 70–80 age range. The most frequent age group is between 65 and 70 years, as indicated by the tallest bar. In contrast, fewer patients were observed at the extremes, with relatively low counts below 60 and above 90 years. The cohort displayed considerable heterogeneity in pre-treatment regimens, which included hormonal therapy, chemotherapy, external radiation therapy, PSMA-targeted radioligand therapy, prostatectomy, and adjuvant treatments. These regimens varied among patients, reflecting diverse clinical characteristics and therapeutic strategies. To enable a detailed analysis of pre-treatment patterns, I stratified the cohort based on the number and type of therapies received. Patients who underwent all six pre-treatment modalities—comprising hormonal therapy, chemotherapy, external radiation therapy, PSMA-targeted radioligand therapy, prostatectomy, and adjuvant treatments—constituted the largest subgroup, accounting for 30 patients (38.5%). The second largest subgroup, consisting of 28 patients (35.9%), received either four or five pre-treatment modalities. This subgroup primarily included combinations of hormonal therapy, chemotherapy, and external radiation therapy, with or without PSMA-targeted radioligand therapy or adjuvant treatments. A further 20 patients (25.6%) received two or three therapies, most commonly involving hormonal therapy combined with either chemotherapy or external radiation therapy. One patient

(1.3%) underwent a single pre-treatment modality, which was hormonal therapy. The distribution of treatment modalities and their combinations is visualized in an UpSet plot Figure 17. Analyzing single treatment modalities, hormonal therapy was the most frequently administered single modality, whereas adjuvant therapy was the least common. The largest intersection, comprising 30 patients, represents the combination of hormonal therapy and chemotherapy. Among the 78 patients, 48.7% (38 patients) received PSMA-targeted radioligand therapy as part of their treatment. To further characterize this subgroup, I stratified the patients based on the specific combinations of additional therapies administered alongside PSMA-targeted radioligand therapy. The distribution of radionuclides used in these treatments is presented in a pie chart in Figure 18. The largest segment, representing 48.7%, corresponds to patients who are radioligand therapy (RLT) naive. 33.3% of the patients were treated with [ $^{177}\text{Lu}$ ]Lu-PSMA-617, making it the most frequently used radionuclide. 6.4% received [ $^{223}\text{Ra}$ ]RaCl<sub>2</sub>. A total of 5.1% of patients received combination radionuclide therapies as part of their pre-treatment. These included either a dual-treatment regimen with [ $^{177}\text{Lu}$ ]Lu-PSMA-617 and [ $^{225}\text{Ac}$ ]Ac-PSMA-617, or a combination of [ $^{90}\text{Y}$ ]Y-PSMA-617 with [ $^{177}\text{Lu}$ ]Lu-PSMA-617. The smallest segment, 1.3%, corresponds to patients treated with [ $^{188}\text{Re}$ ]Re-HYNIC-PSMA + [ $^{177}\text{Lu}$ ]Lu-PSMA-617.

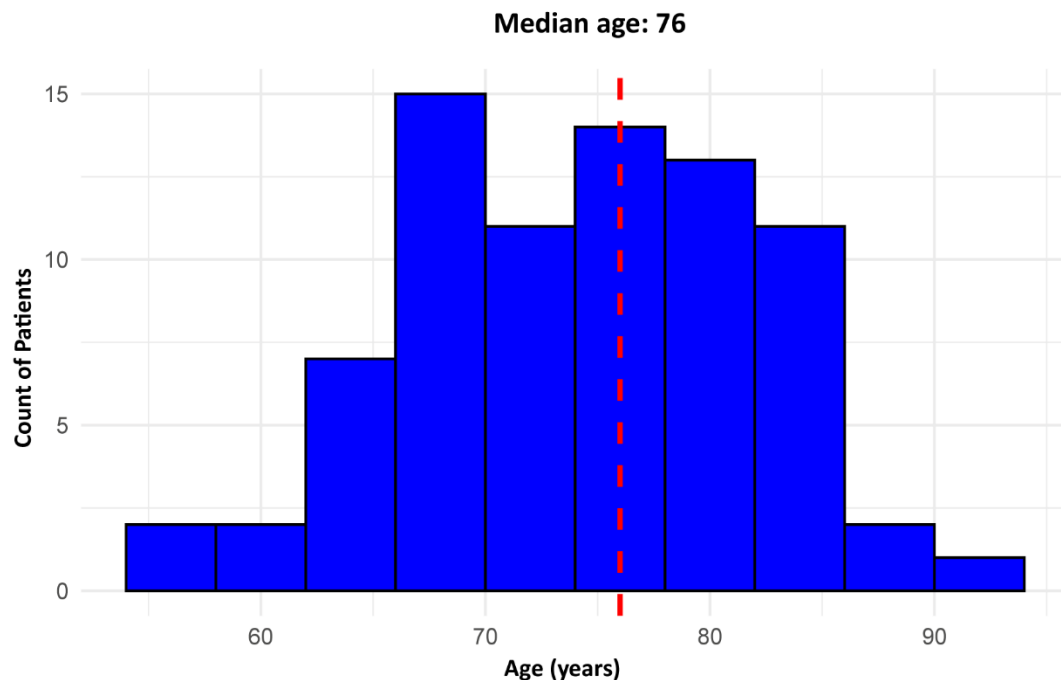


**Figure 16:** Distribution and median age of the patients in the included cohort. Age distribution of the patient cohort. The x-axis shows age (55–95 years), and the y-axis indicates patient count. Blue bars represent age intervals; the red dashed line marks the mean age (76 years).

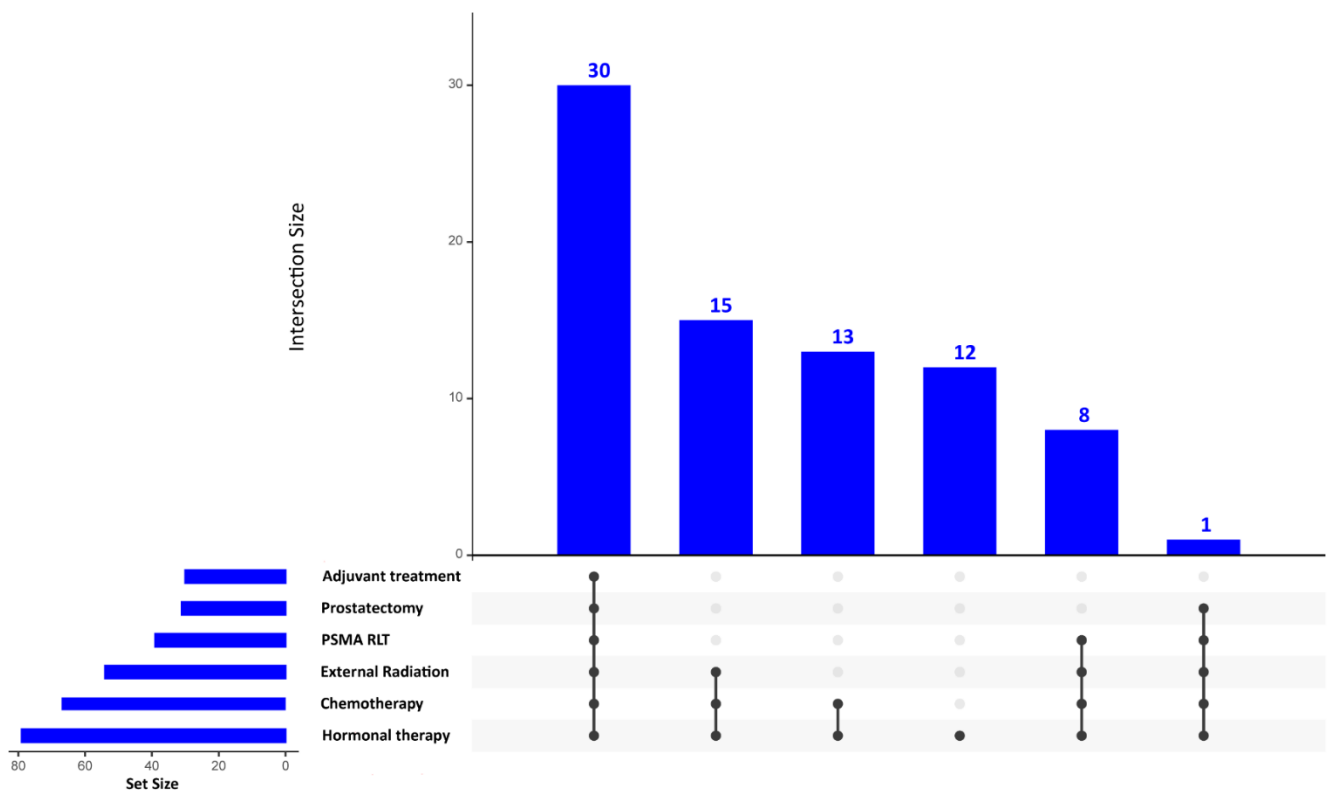


**Figure 17:** Upset plot representing the patient's pretreatments intersection. The vertical bar chart represents the number of patients receiving specific combinations of therapies, while the horizontal bar chart illustrates the overall number of patients treated with each individual modality. The matrix below highlights the combinations of treatments, with black dots indicating the inclusion of specific therapies and connected lines representing multi-treatment combinations.

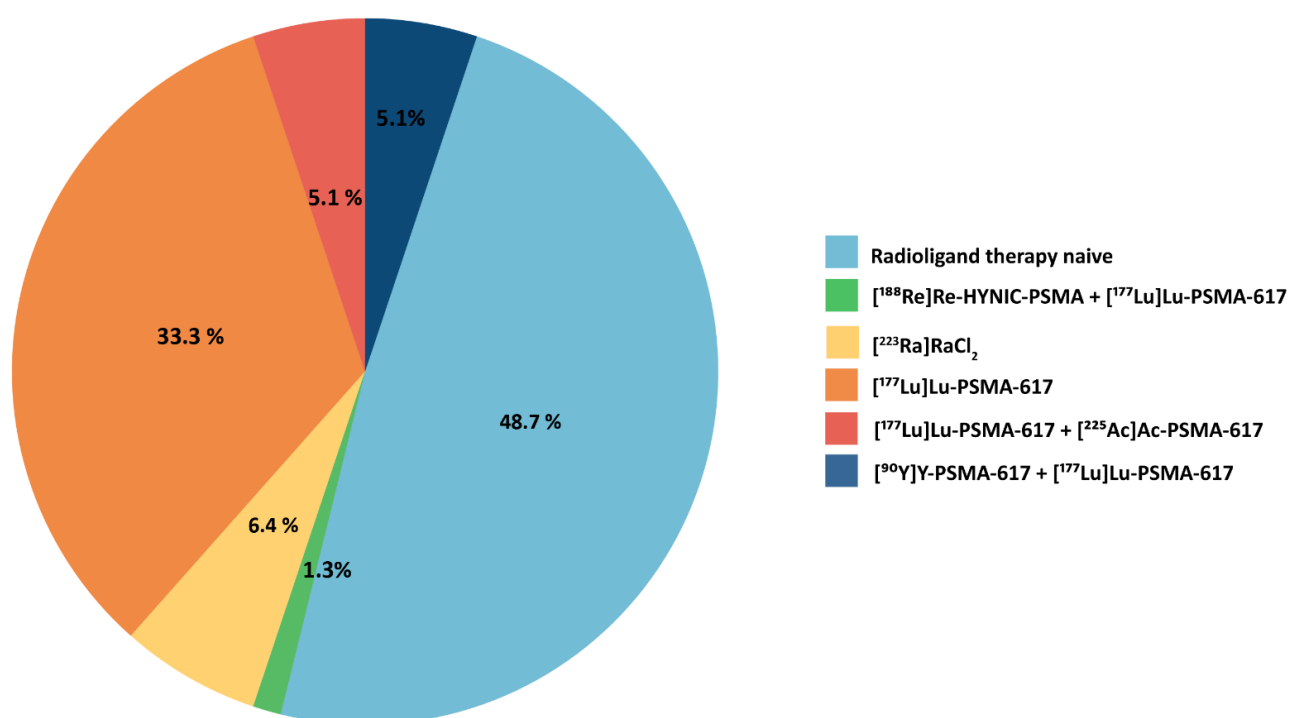


**Figure 18:** Pie chart illustrating the distribution of radionuclide therapies administered as pre-treatment. 48.7% of patients were RLT-naïve, 33.3% received [<sup>177</sup>Lu]Lu-PSMA-617, 6.4% received [<sup>223</sup>Ra]RaCl<sub>2</sub>, and 5.1% received combination therapies (either [<sup>177</sup>Lu]Lu-PSMA-617 + [<sup>225</sup>Ac]Ac-PSMA-617 or [<sup>90</sup>Y]Y-PSMA-617 + [<sup>177</sup>Lu]Lu-PSMA-617). The smallest group (1.3%) received [<sup>188</sup>Re]Re-HYNIC-PSMA + [<sup>177</sup>Lu]Lu-PSMA-617.



## 2. TM DYNAMICS

TM dynamics—including TFx, PSA, ALP, and LDH—were analysed across five cycles of RLT. These markers are routinely used in clinical practice to monitor disease progression and treatment response. The analysis aimed to evaluate TFx in comparison with the gold standard PSA, as well as LDH and ALP, to determine whether TFx could serve as a reliable surrogate for monitoring therapy kinetics and tumor burden over time.

### 2.1 TFx across treatment cycles

TFx levels were assessed at baseline (treatment cycle 0) and across five subsequent [<sup>225</sup>Ac]Ac-/[<sup>177</sup>Lu]Lu-PSMA-617 treatment cycles to monitor tumor burden dynamics during therapy. The distribution of TFx values over these cycles is visualized in Figure 19. The figure shows a progressive decrease in TFx levels during the initial treatment cycles, suggesting a reduction in tumor burden. The decrease pattern has been observed from the baseline to the 3<sup>rd</sup> cycle. I performed a statistical analysis using the Wilcoxon signed-rank test, which is appropriate for paired data comparisons. The analysis I performed confirmed significant reductions in TFx between baseline (cycle 0) and the following cycle 1 ( $p < 0.01$ ), cycle 2 ( $p = 0.021$ ), and cycle 3 ( $p = 0.014$ ). While I observed a statistically significant reduction in the early treatment cycles, this trend plateaued in the later cycles, with no significant differences detected in cycle 4 ( $p = 0.873$ ) and cycle 5 ( $p = 0.417$ ). The observed increase in TFx during treatment cycles 3 and 5 may indicate a general disease relapse or the emergence of therapy resistance. My results show that while the treatment initially reduced tumor burden, the effect plateaued in the later cycles, suggesting that the therapy may lose its effectiveness over time.

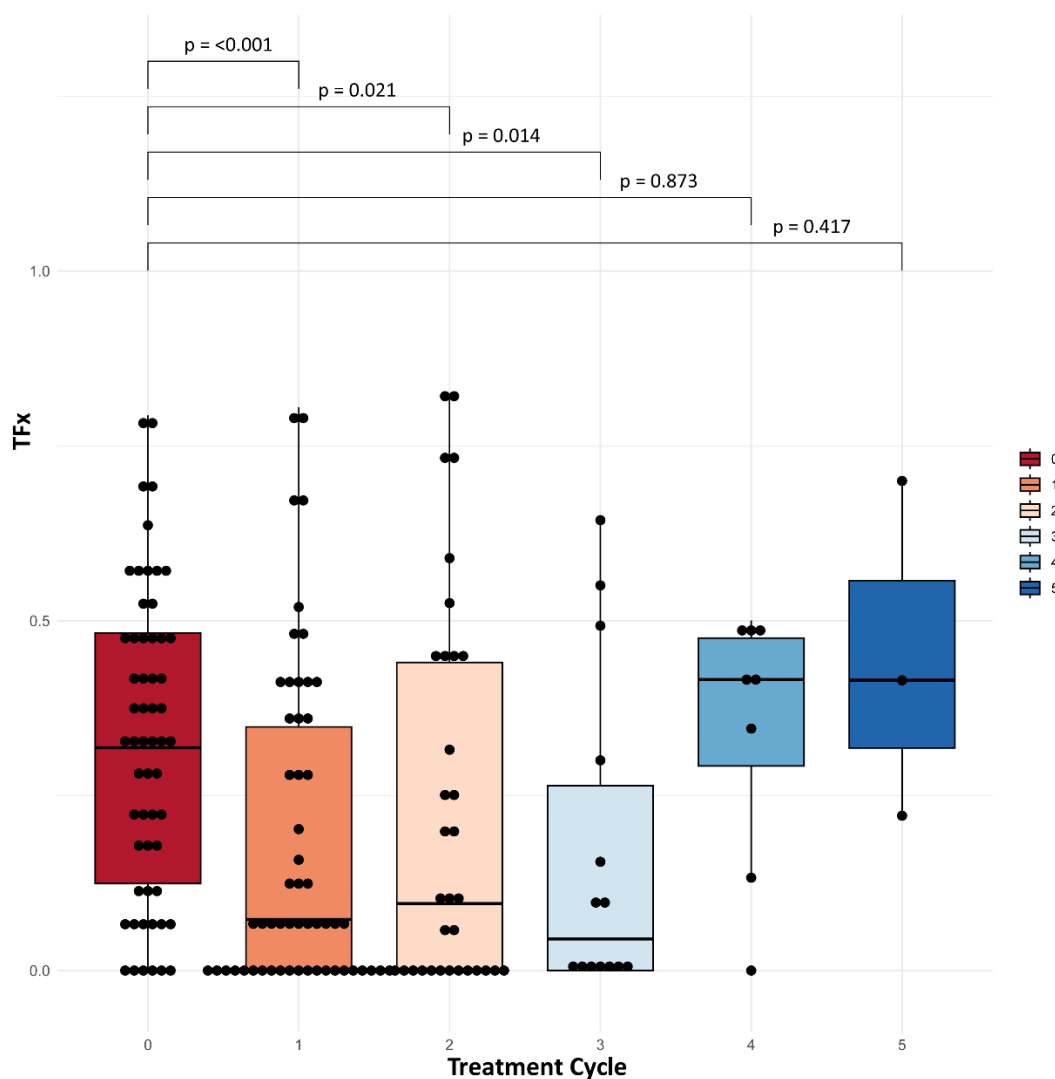


**Figure 19:** TFX dynamics across  $[^{225}\text{Ac}]\text{Ac-}/[^{177}\text{Lu}]\text{Lu-PSMA-617}$  treatment cycles. The x-axis represents treatment cycles from baseline (cycle 0) to cycle 5, while the y-axis shows the TFX values. Box plot illustrates the interquartile range (IQR), with the median TFX marked by a horizontal line within each box. Whiskers extend to capture the full range of observed values, while individual data points represent patient-specific TFX measurements.

## 2.2 PSA across treatment cycles

PSA levels, a key biomarker for tumor activity in mCRPC, were measured longitudinally across five treatment cycles to evaluate therapeutic response. The distribution of PSA values over these cycles is visualized in Figure 20. The box plot illustrates the interquartile range (IQR), with the median PSA level marked by a horizontal line within each box. Whiskers extend to the full range of observed values, while individual dots represent patient-specific PSA measurements. Figure 20 demonstrates a significant decrease in PSA levels from baseline (cycle 0) through the initial treatment cycles (cycles 1 to 3), indicating a robust early therapeutic effect. I performed a statistical analysis using the Wilcoxon signed-rank test, appropriate for paired observations since PSA levels were repeatedly measured in the same patient cohort. Pairwise comparisons between baseline and subsequent cycles confirmed significant PSA reductions during the early treatment phase: baseline and cycle 1 ( $p < 0.001$ ), baseline and cycle 2 ( $p < 0.001$ ), and baseline and cycle 3 ( $p = 0.005$ ). While I observed an initial sharp decline in PSA levels, the reduction stabilized in the later cycles. A subset of patients exhibited increases in PSA levels during cycles 4 and 5, which contributed to an overall rebound in median PSA values. I observed that this trend was reflected in non-significant pairwise comparisons with cycle 4 and cycle 5 ( $p = 0.099$  and  $p = 0.088$ , respectively). My results show that while the therapy initially led to a significant reduction in PSA levels, the effect plateaued in the later cycles, with some patients experiencing a rebound in PSA levels during the final cycles.

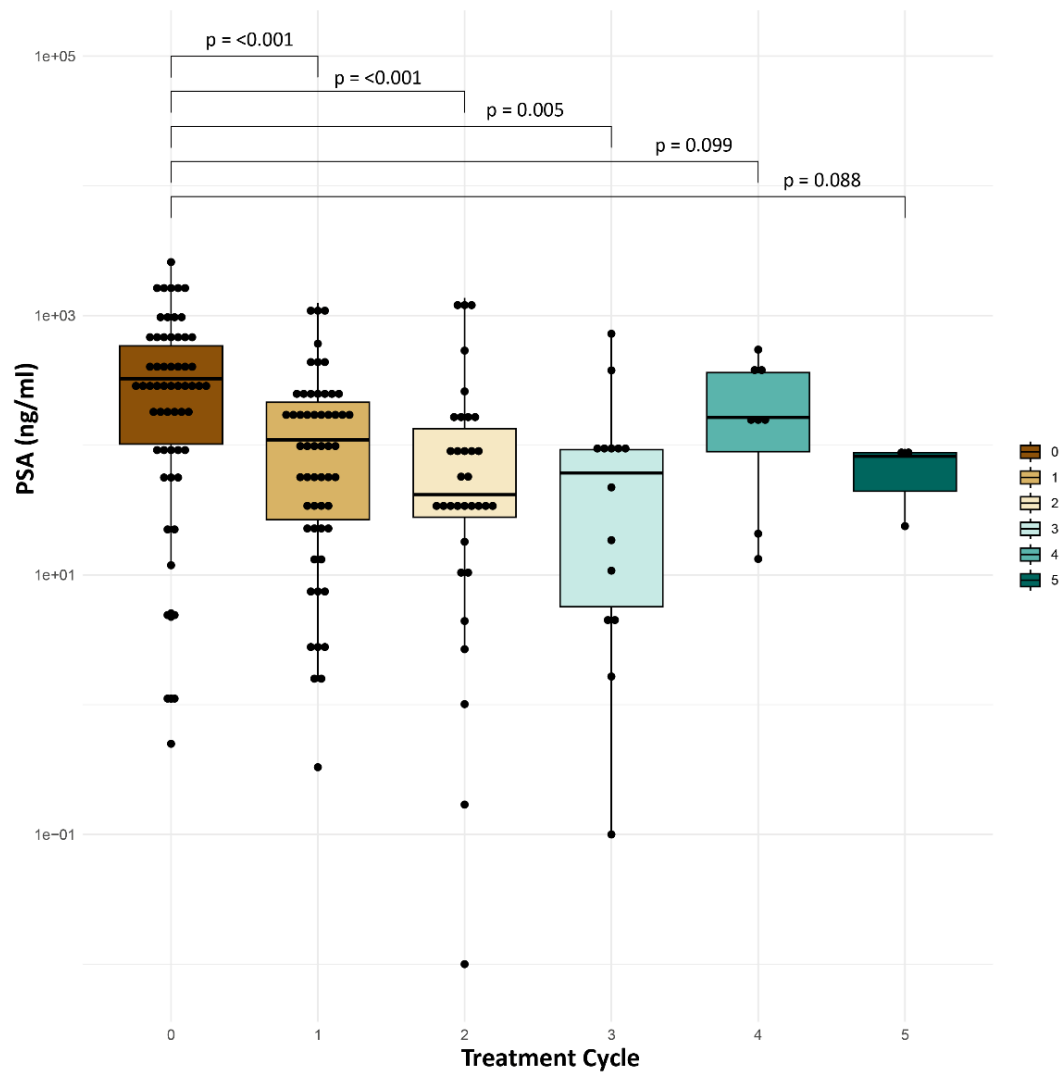


**Figure 20:** PSA dynamics across  $[^{225}\text{Ac}]\text{Ac-}/[^{177}\text{Lu}]\text{Lu-PSMA-617}$  treatment cycles. The x-axis represents treatment cycles from baseline (cycle 0) to cycle 5, while the y-axis shows PSA levels on a  $\log_{10}$  scale to account for inter-patient variability. Box plots display the median, IQR, full range (whiskers), and individual patient values (dots).

## 2.3 ALP across treatment cycles

ALP levels, a marker of bone turnover and metastatic activity, were assessed over five RLT treatment cycles to evaluate treatment response. The distribution of ALP values across cycles is visualized in Figure 21. The box plot illustrates the IQR, with the median ALP level marked by a horizontal line within each box. Whiskers extend to the full range of observed values, while individual data points represent patient-specific ALP measurements. Statistical comparisons were performed using the Wilcoxon signed-rank test, appropriate for paired observations given the repeated ALP measurements within patients. Significant changes across cycles were annotated with corresponding p-values above the plot to highlight key trends. Figure 21 highlights a significant decline in ALP levels during the early treatment cycles, with a statistically significant reduction between baseline and treatment cycle 1 reaching statistical significance ( $p = 0.015$ ). I noted additional decreases in ALP levels in the later cycles, but these did not reach statistical significance: cycle 2 ( $p = 0.081$ ) and cycle 3 ( $p = 0.052$ ). In the later treatment cycles (cycle 4 and cycle 5), I observed that ALP levels stabilized, with pairwise comparisons showing no significant differences ( $p = 0.282$  and  $p = 0.916$ , respectively). My results show that ALP levels significantly decreased during the early cycles, but this reduction plateaued in the later cycles, suggesting that bone turnover and metastatic activity stabilized over time.

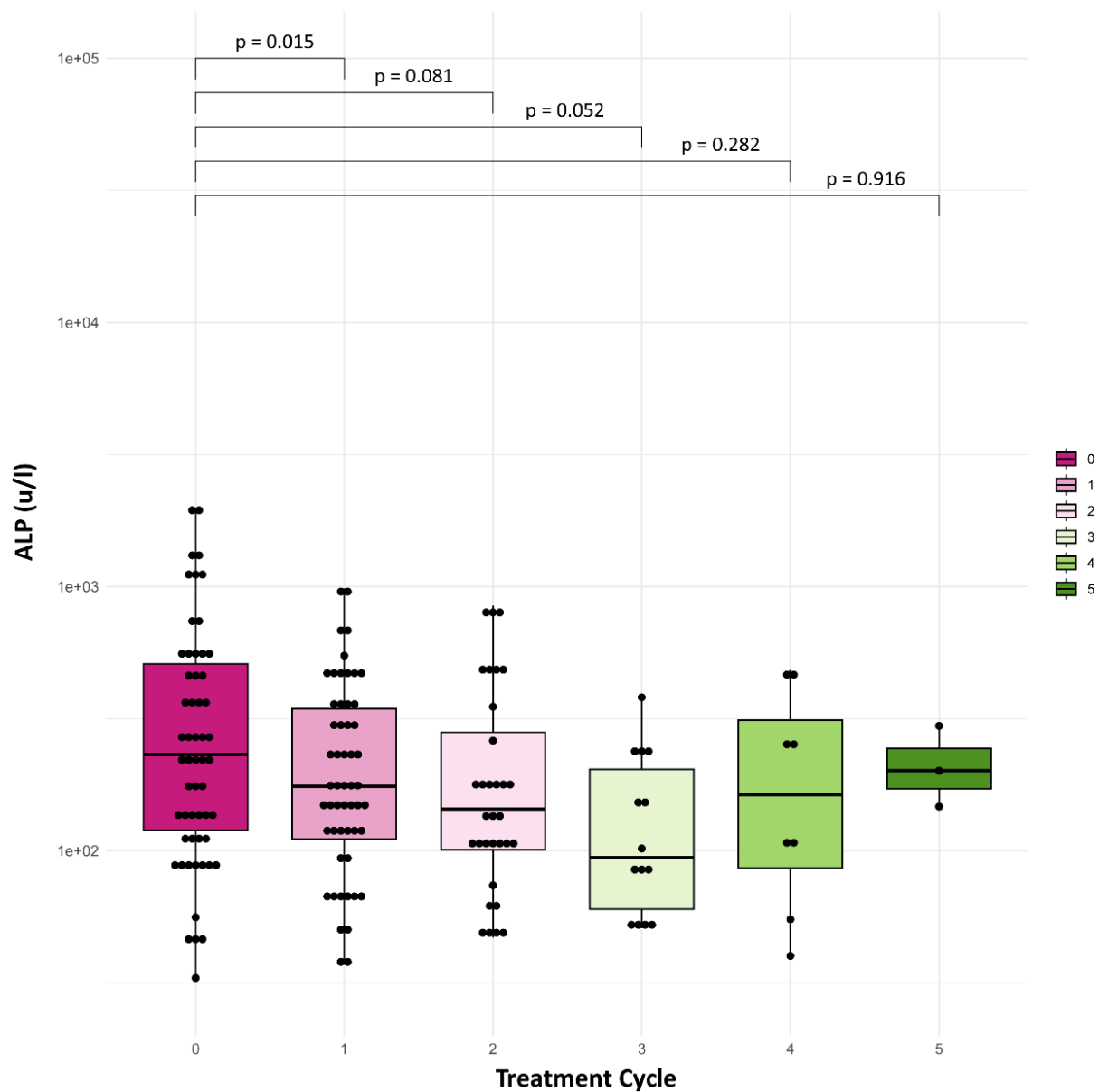


**Figure 21:** ALP dynamics across  $[^{225}\text{Ac}]\text{Ac}/[^{177}\text{Lu}]\text{Lu-PSMA-617}$  treatment cycles. The x-axis represents treatment cycles from baseline (cycle 0) treatment cycle 5, and the y-axis displays ALP levels on a logarithmic scale ( $\log_{10}$ ). Box plots display the median, IQR, full range (whiskers), and individual patient values (dots).

## 2.4 LDH across treatment cycles

LDH levels, a marker of cellular turnover and tumor metabolic activity, were assessed across five treatment cycles to evaluate treatment response. The distribution of LDH values is visualized in Figure 22. The box plot illustrates the IQR, with the median LDH level marked by a horizontal line within each box. Whiskers extend to the full range of observed values, while individual data points represent patient-specific LDH measurements. Statistical comparisons were conducted using the Wilcoxon signed-rank test, appropriate for paired observations due to the repeated LDH measurements within patients. Significant changes across cycles were annotated with corresponding p-values above the plot, highlighting key trends. Figure 22 demonstrates a marked decline in LDH levels during the early treatment cycles, with a statistically significant reduction observed between baseline and treatment cycle 1 ( $p = 0.015$ ). Although I observed reductions in LDH levels between baseline and treatment cycles 2 ( $p = 0.081$ ) and 3 ( $p = 0.052$ ), these changes did not reach statistical significance. In the later treatment cycles (cycles 4 and 5), I noted that LDH levels plateaued, with pairwise comparisons showing no significant differences (cycle 4, cycle 5:  $p = 0.282$ ,  $p = 0.916$ ), indicating a stabilization phase.

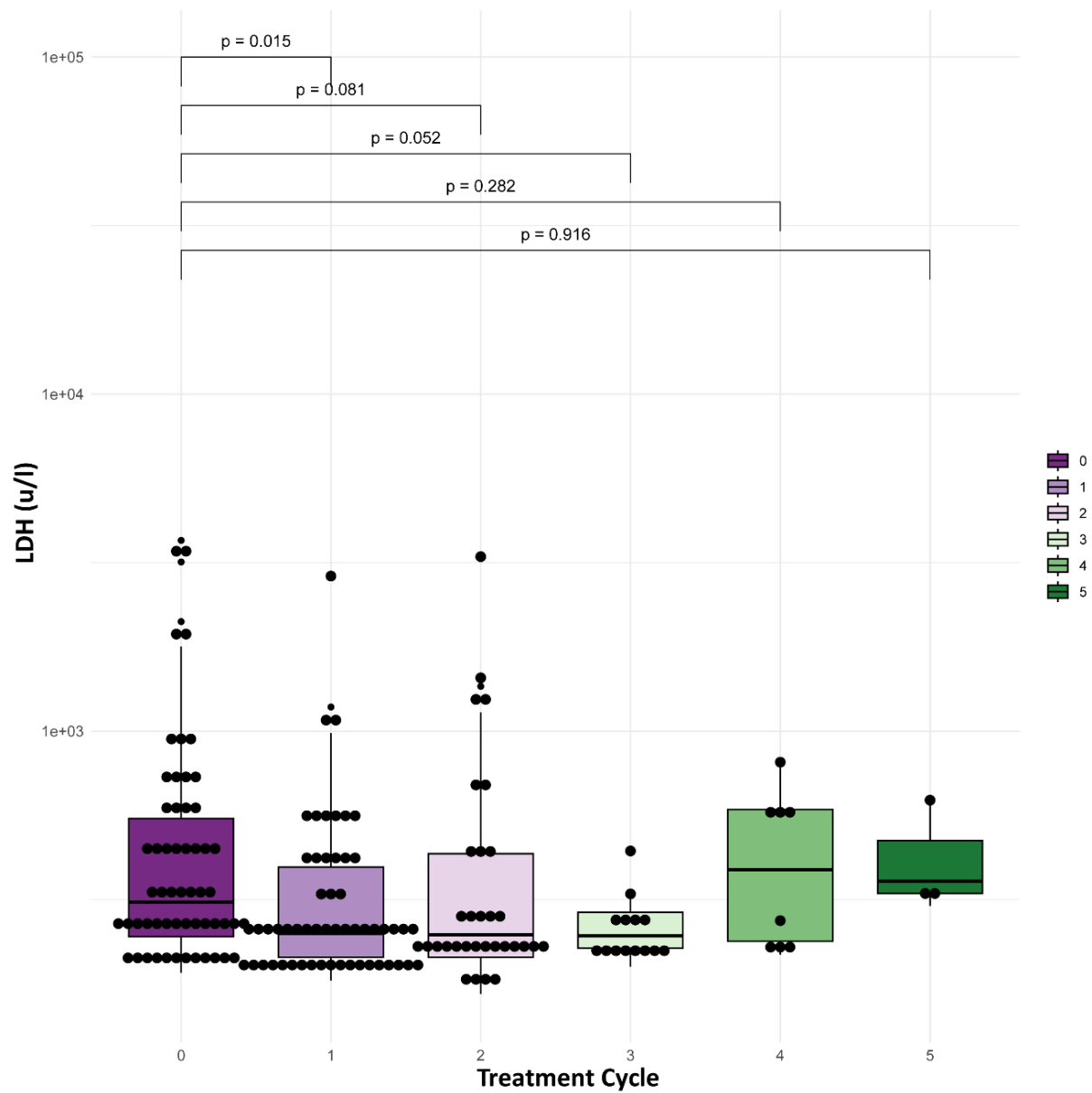


**Figure 22:** LDH dynamics across  $[^{225}\text{Ac}]\text{Ac-}/[^{177}\text{Lu}]\text{Lu-PSMA-617}$  treatment cycles. The x-axis represents treatment cycles from baseline (cycle 0) to cycle 5, and the y-axis displays LDH levels on a logarithmic scale ( $\log_{10}$ ) to account for the wide variability in patient-specific LDH values. Box plots display the median, IQR, full range (whiskers), and individual patient values (dots).



### 3. CORRELATION ANALYSIS

To assess the potential utility of Tfx as a biomarker, I analyzed its correlation with established clinical markers—PSA, ALP, and LDH. The analysis aimed to assess whether Tfx dynamics aligned with or complemented the behavior of established biomarkers, offering additional insights into tumor burden and therapeutic response. I performed a correlation analysis between Tfx and PSA, LDH, or ALP using the entire cohort, incorporating all available timepoints. Additionally, I conducted a separate correlation analysis on a subset of 41 patients who met the inclusion criteria of having both a baseline assessment and at least one follow-up measurement.

#### 3.1 Correlation analysis: Tfx & PSA

The relationship between Tfx and PSA levels is visualized in Figure 23. A statistically significant positive correlation was observed, as indicated by the upward trend of the regression line. The correlation coefficient ( $R = 0.47$ ) and the corresponding p-value ( $p = 7.7e^{-11}$ ) suggest a moderate yet statistically significant association between Tfx and PSA levels. My results indicate that increases in tumor burden, as measured by Tfx, are correlated with elevated PSA levels, supporting the potential role of Tfx as a complementary biomarker for assessing tumor activity and therapeutic response.



**Figure 23:** Scatter plot showing the correlation between Tfx (x-axis) and PSA levels (y-axis). Each red dot represents an individual patient measurement. A black linear regression line indicates the overall trend, with the shaded area representing the confidence interval to reflect data variability.

### 3.2 Correlation analysis: Tfx & LDH

The relationship between Tfx and LDH levels is illustrated in Figure 24. A strong positive correlation was observed between Tfx and LDH levels, as indicated by the upward trend of the regression line. This relationship is supported by a correlation coefficient ( $R = 0.67$ ) and a highly significant p-value ( $p < 2.2e^{-16}$ ), demonstrating a robust and statistically significant association. My results suggest that higher Tfx values are strongly linked to increased LDH levels, reinforcing the role of Tfx as a biomarker for tumor burden and metabolic activity in mCRPC patients.

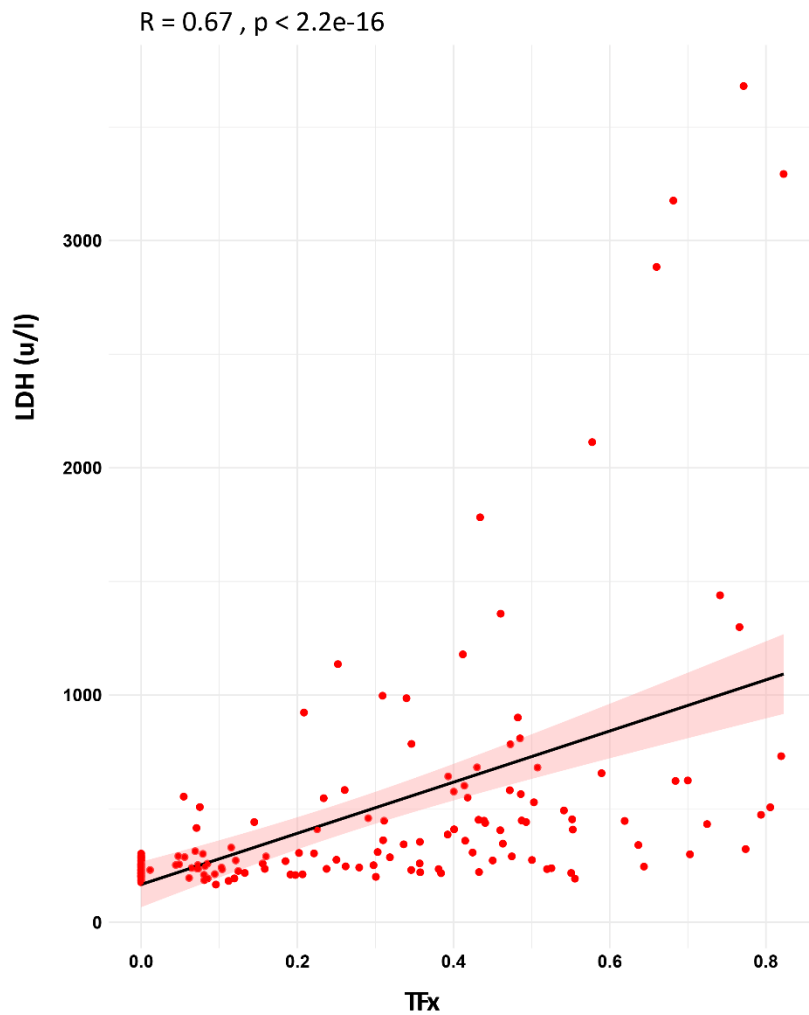


**Figure 24:** Scatter plot showing the correlation between Tfx values (x-axis) and LDH levels (y-axis). Each red dot represents an individual patient measurement, capturing variability within the cohort. A black linear regression line illustrates the overall trend, with the shaded area indicating the confidence interval, reflecting uncertainty around the fit.

### 3.3 Correlation analysis: Tfx & ALP

The relationship between Tfx and ALP levels is illustrated in Figure 25. A moderate positive correlation was observed between Tfx and ALP levels, as indicated by the upward trend of the regression line. The correlation is supported by a correlation coefficient ( $R = 0.47$ ) and a statistically significant p-value ( $p = 7.3e^{-11}$ ). My results suggest that changes in tumor burden, as measured by Tfx, are associated with variations in ALP, a marker of bone turnover and metastatic activity. My findings provide further insight into the potential role of Tfx as a biomarker, particularly in monitoring disease activity related to bone metastases.

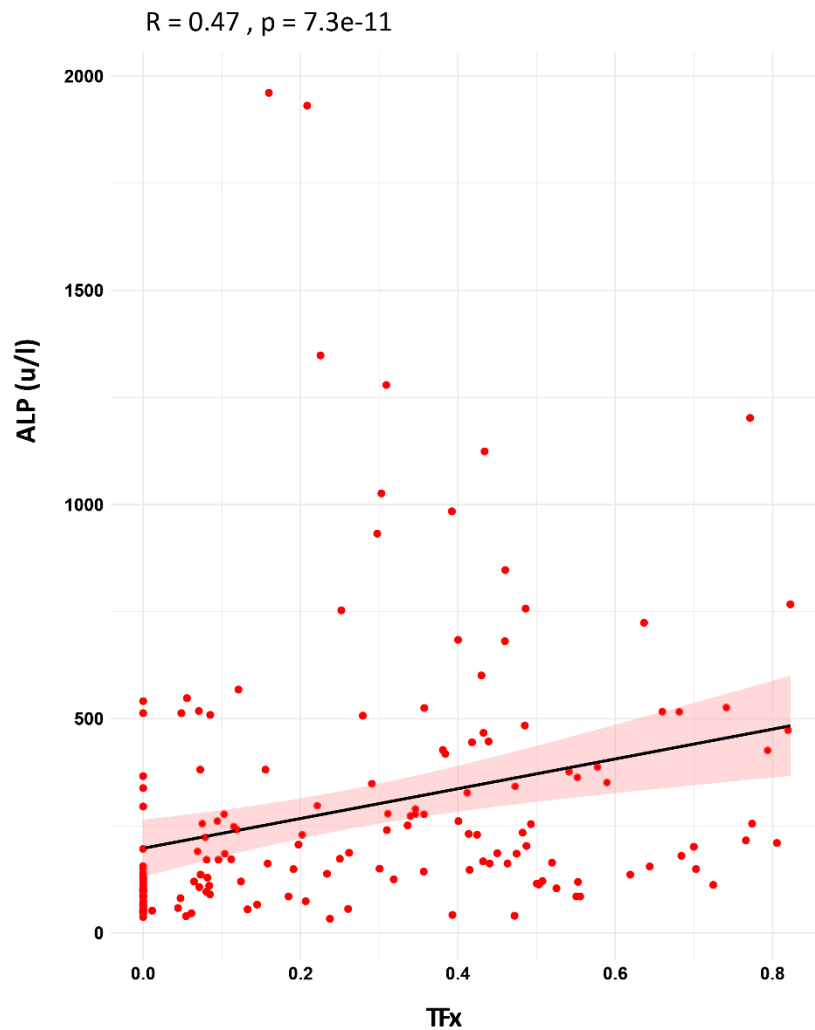


**Figure 25:** Scatter plot showing the correlation between TFX values (y-axis) and ALP levels (x-axis). Each red dot represents an individual patient measurement, capturing variability across the cohort. A linear regression line illustrates the overall trend, with the shaded area indicating the confidence interval and the uncertainty around the fit.

### 3.4 Correlation with clinical outcomes

I conducted patient-specific correlation analyses between TFX, LDH, and PSA levels, selecting these markers based on their statistically significant associations and correlation strengths observed in the initial analysis. The analysis included 41 patients with both baseline and follow-up samples available. I chose these markers for their distinct and complementary roles in assessing tumor burden, as supported by their correlation coefficients and p-values. I found that LDH exhibited the strongest correlation with TFX, with a correlation coefficient (R) of 0.67 and a significant p-value ( $< 2.2e^{-16}$ ). PSA showed a moderate positive correlation with TFX, with a correlation coefficient (R) of 0.47 and a statistically significant p-value ( $7.7e^{-11}$ ). Although ALP also exhibited a moderate correlation with TFX

( $R = 0.47$ ,  $p = 7.3e^{-11}$ ), I excluded it from this analysis. Consequently, I focused on LDH and PSA to investigate their relationships with Tfx, emphasizing their potential as complementary biomarkers for tumor burden and therapeutic response. To further explore the relationship between these markers and clinical outcomes, fold changes in LDH, Tfx, and PSA were calculated across individual patients as described in the material and method section (*6.4 Longitudinal biomarker dynamics and correlation*) and Figure 26. I performed hierarchical clustering to group patients based on similar patterns of biomarker changes and to identify clusters of biomarkers with correlated dynamics. I observed that patients who exhibited significant decreases in LDH, Tfx, and PSA were more frequently associated with favorable clinical outcomes, such as stable disease or partial remission. In contrast, patients with increases in these biomarkers were predominantly linked to disease progression. A clear pattern of concordance between PSA and Tfx changes emerged, not only at single time points but also across treatment cycles. My results suggest that Tfx and PSA may follow similar trends over time, reflecting individual patient responses and potentially reinforcing the role of Tfx as a surrogate marker for treatment monitoring. These findings reveal distinct biomarker patterns that align with clinical responses, offering additional insights into the relationship between fold changes in LDH, Tfx, and PSA, and how I observed these changes relate to patient outcomes during radionuclide ligand therapy.

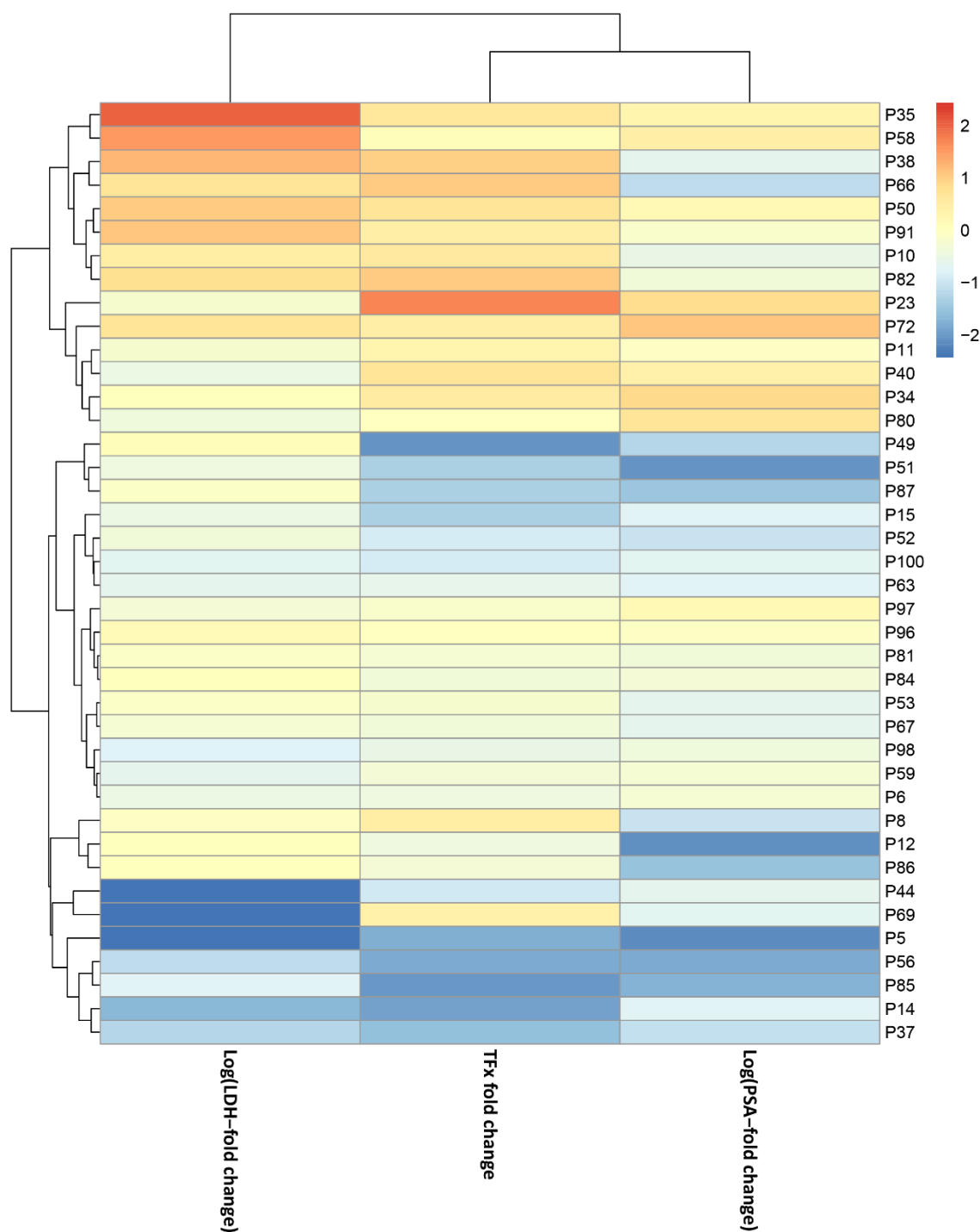


**Figure 26:** Heatmap illustrating fold changes in LDH, TFX, and PSA levels across individual patients. Each row represents a patient, and each column corresponds to a biomarker. The colour scale reflects the direction and magnitude of change: red indicates positive fold changes, blue indicates negative changes, and yellow represents minimal or no change.

## 4. Distribution of Tfx and PSA across metastasis group

To evaluate the association between biomarker levels and metastatic burden at baseline, I analysed the distributions of Tfx and PSA across three distinct metastasis groups: patients with bone-only metastases, those with bone and lymph node involvement, and those with bone, lymph node, and additional organs. This analysis was conducted on a cohort of 57 patients with available baseline samples. Among them, 10 patients (17.5%) had bone-only metastases, 34 patients (59.6%) had bone and lymph node involvement, and 13 patients (22.8%) presented with bone, lymph node, and additional organ metastases. My findings provide insights into how Tfx and PSA levels vary with increasing metastatic spread, offering potential implications for disease characterization and risk stratification.

### 4.1 PSA distribution across metastasis groups

Baseline PSA levels were analysed across three metastasis groups: (1) patients with bone metastases only, (2) those with bone and lymph node metastases, and (3) those with bone, lymph node, and additional organs. Using PSA measurements taken before treatment, I aimed to evaluate whether baseline PSA could help stratify patients based on their metastasis status. The Kruskal-Wallis test, a non-parametric method for comparing medians across multiple groups, was used to evaluate differences in PSA distributions. As shown in Figure 27, the test revealed no statistically significant differences in PSA levels among the three groups ( $p = 0.47$ ). I observed the widest distribution of PSA levels in the bone-only group (Stage 1), while the group with bone, lymph node, and additional organ metastases (Stage 3) showed a narrower distribution. My results suggest that baseline PSA levels do not significantly differ by metastasis status, indicating comparable PSA secretion across the groups at the start of treatment.

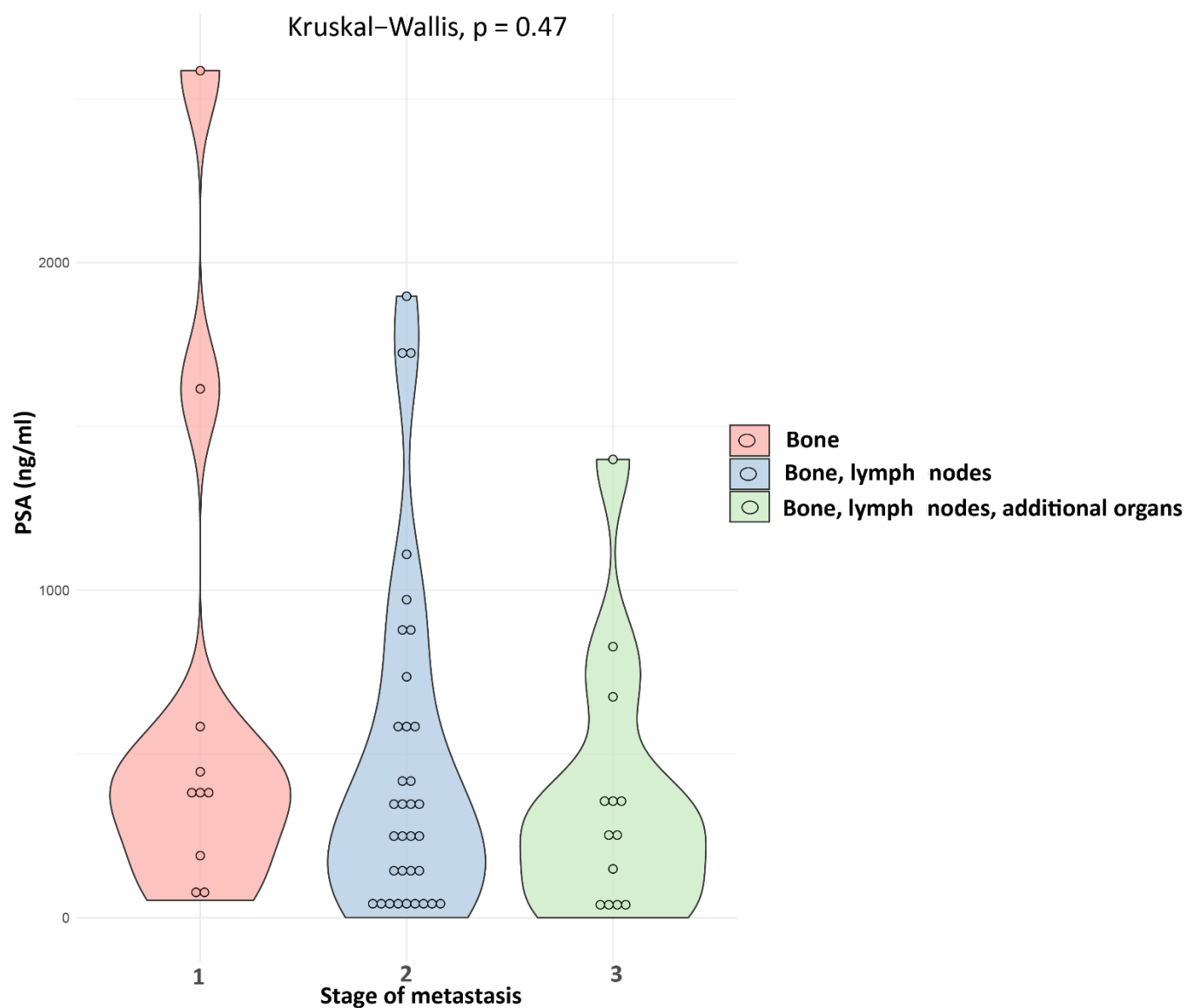


**Figure 27:** Violin plots showing the distribution of baseline PSA levels across three metastasis groups: bone-only, bone and lymph node, and bone, lymph node, and additional organ involvement. The plots depict the density and variability of PSA values within each group, with wider sections indicating greater heterogeneity. Individual patient measurements are overlaid as points.



## 4.2 Tfx distribution across metastasis groups

To further explore Tfx behaviour, baseline Tfx values were analysed across the three metastasis groups. The distribution of these values is visualized in Figure 28. The Kruskal-Wallis test identified statistically significant differences in Tfx distributions across the three metastasis groups ( $p = 0.029$ ). I observed that patients in Stage 1 (bone-only metastases) had the lowest Tfx values, with a relatively narrow distribution. In contrast, Stage 3 patients—those with widespread metastases involving lymph nodes and additional visceral organs—exhibited markedly higher Tfx levels. Stage 2 patients showed intermediate Tfx values but had the widest distribution, ranging from values below the detection limit to approximately 0.8, highlighting substantial variability within this group. My results demonstrate that Tfx is a strong and reliable marker for distinguishing between different metastasis groups in this context.

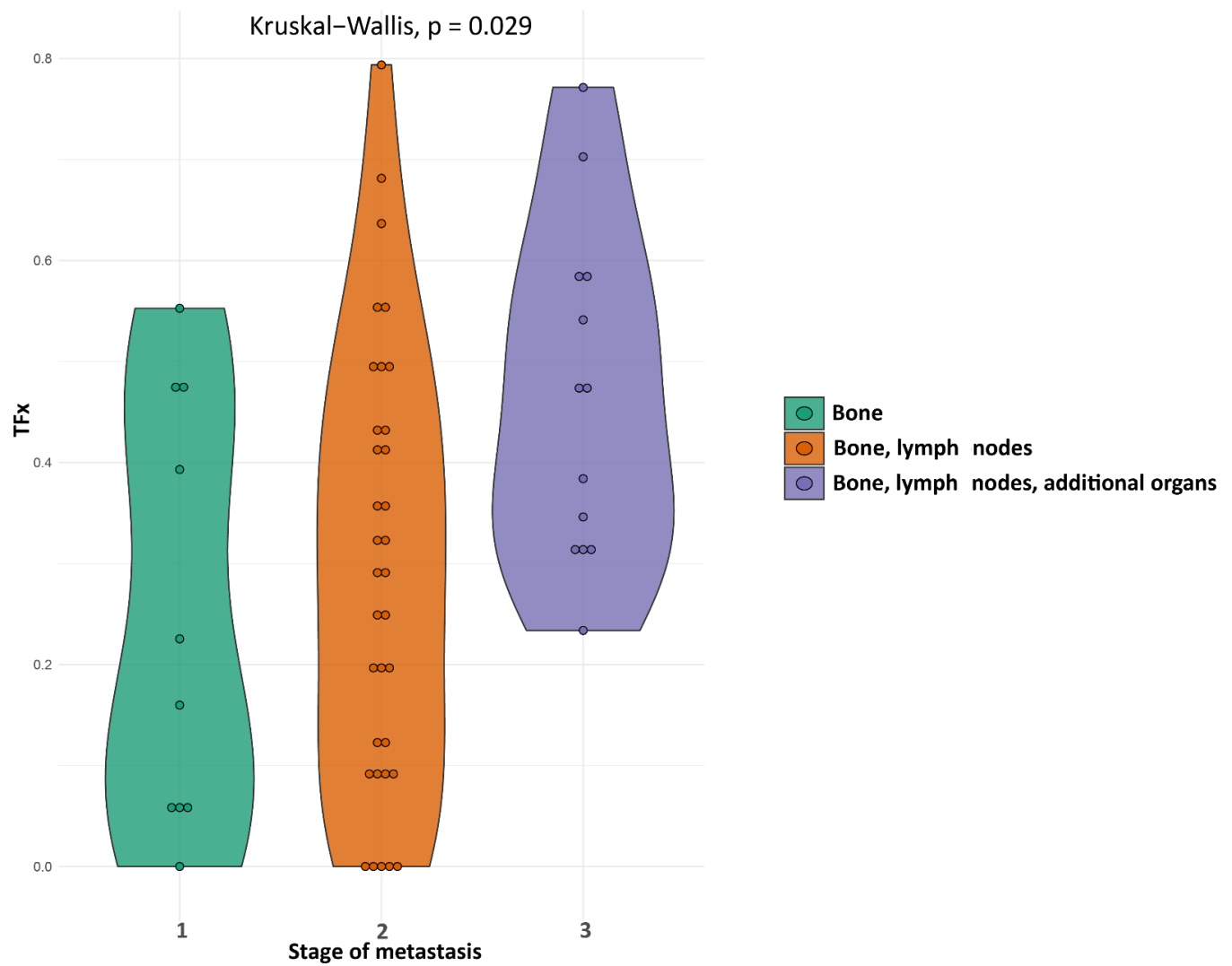


**Figure 28:** Violin plots illustrating the distribution of baseline Tfx levels across three metastasis groups: bone-only, bone and lymph node, and bone, lymph node, and additional organ metastases. The x-axis represents metastasis groups, and the y-axis shows Tfx values on a linear scale. The shape of each violin reflects the density and variability of Tfx values, with wider sections indicating higher data concentration. Individual patient measurements are overlaid as dots to show the spread within each group.

## 5. RISK ANALYSIS: TFx AS A PREDICTIVE BIOMARKER

I evaluated the potential of TFx as a predictive biomarker for treatment response and risk of relapse during [ $^{225}\text{Ac}$ ]Ac-/ [ $^{177}\text{Lu}$ ]Lu-PSMA-617 therapy. To assess its clinical utility, I compared the predictive performance of TFx to that of established biomarkers, including PSA and LDH, in order to determine whether TFx could offer additional insights into patient outcomes. Additionally, I conducted a time-dependent Cox proportional hazards analysis to assess whether increases in TFx serve as a significant risk factor for disease progression. Beyond predictive modeling, the prognostic value of TFx was examined in relation to overall survival (OS) and key clinical and molecular variables, including CNV burden and pretreatment regimens. Kaplan-Meier survival curves were generated to estimate survival probabilities across patient subgroups, with statistical comparisons performed using the log-rank test.

### 5.1 ROC analysis: sensitivity and specificity Test

The predictive performance of pre-cycle PSA levels, TFx, and a combined model incorporating PSA, TFx, and LDH levels for treatment cycle outcomes was evaluated using ROC analysis Figure 29. My analysis assessed the discriminative ability of these biomarkers in distinguishing treatment response and clinical progression, using sensitivity and specificity as performance metrics. Figure 29 presents the ROC curves, where the x-axis represents specificity (1 - false positive rate) and the y-axis represents sensitivity (true positive rate). The ROC curve for pre-cycle PSA levels demonstrated limited predictive capability, with an area under the curve (AUC) of 0.44 (95% CI: 0.29–0.59). In contrast, pre-cycle TFx exhibited improved predictive ability, achieving an AUC of 0.60 (95% CI: 0.50–0.70). I observed the highest predictive accuracy in the combined model that integrated PSA, TFx, and LDH levels, which achieved an AUC of 0.62 (95% CI: 0.51–0.74). My results show that only the TFx ROC curve demonstrated a solid AUC on its own, and although I combined all three markers (TFx, PSA, and LDH), this integration did not lead to an improvement in predictive accuracy.

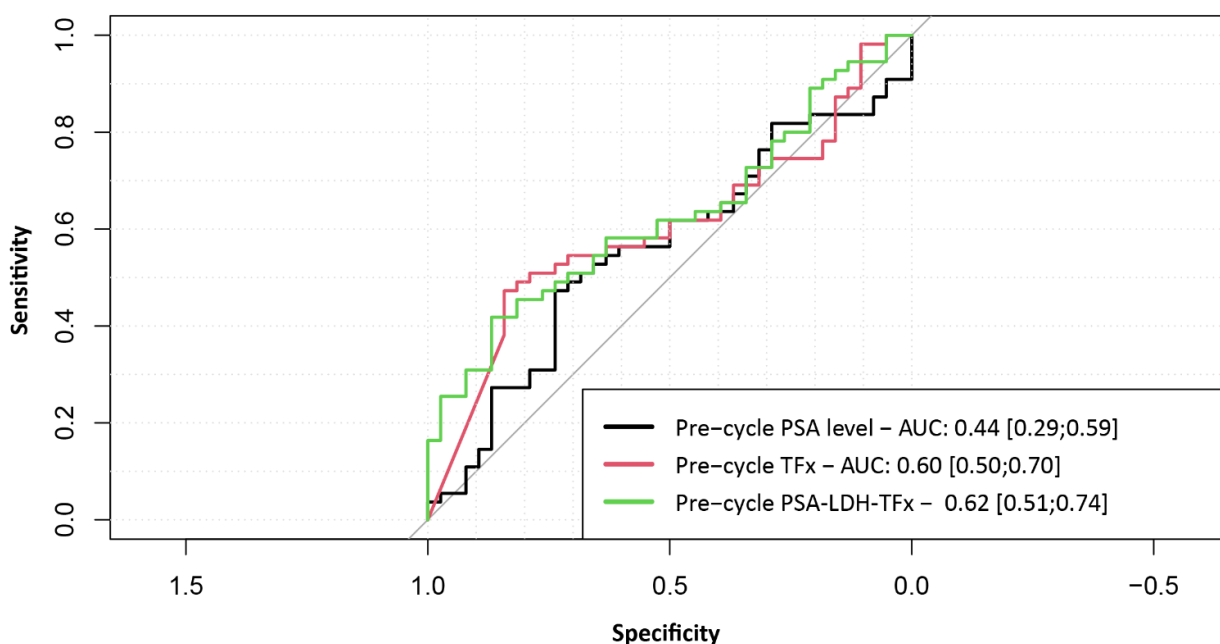


**Figure 29:** The ROC curves depict the predictive performance of pre-cycle PSA levels (black line), pre-cycle Tfx (red line), and a combined model of PSA, Tfx, and LDH (green line). The diagonal grey line denotes a random prediction model with an AUC of 0.50, serving as a baseline for comparison.

## 5.2 Cox hazard ratio analysis: Tfx increases and risk of relapse

I assessed the relationship between Tfx increases and the risk of relapse using a Cox proportional hazards model. My aim was to determine whether changes in Tfx levels—either increases or decreases—could reliably reflect the clinical annotations of response or relapse. I also investigated whether discrepancies at a specific time point were later confirmed by Tfx trends in subsequent treatment cycles. My analysis demonstrated that an increase in Tfx is associated with a statistically significant 5-fold higher probability of relapse in the subsequent treatment cycle, with a p-value = 0.0259. The swimmer plot in Figure 30 provides a visual representation of the 52 patients included in the analysis and the key clinical annotation recorded during the treatment period. A detailed description of the methodology is provided in the Materials and Methods section. Only patients with multiple Tfx assessments were included in the analysis, providing a detailed view of tumor burden dynamics and their association with clinical outcomes.

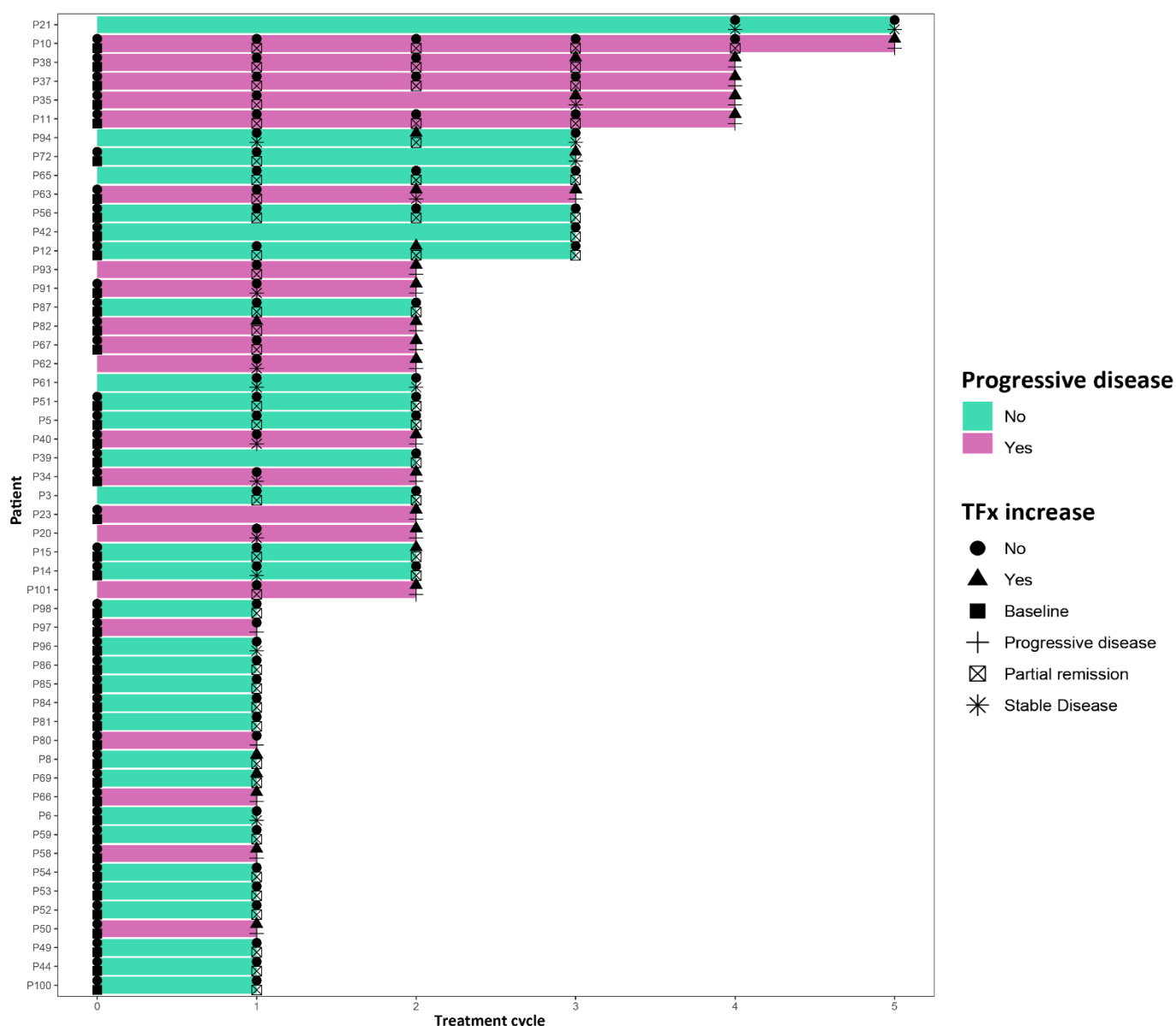


**Figure 30:** Swimmer plot visualizing treatment cycles for individual patients, with green and pink bars indicating non-progressive and progressive disease, respectively, and symbols marking Tfx increases and key clinical milestones. The swimmer plot visualizes individual patient trajectories throughout the treatment course, with the x-axis representing treatment cycles and the y-axis denoting individual patients. Bars indicate the duration of treatment, with green bars representing patients who did not experience clinically annotated progressive disease and pink bars representing those who developed progressive disease during the observation period. Symbols overlaid on the bars denote key clinical milestones, such as baseline assessments, partial remission, or stable disease.

### 5.3 OS based on CNV burden

I assessed the relationship between OS and CNV burden using Kaplan-Meier survival analysis, as shown in Figure 31. The Kaplan-Meier plot depicts survival probability over time (months since therapy initiation) for two patient groups stratified by CNV burden, i.e. low CNV burden (black curve) and high CNV burden (yellow curve). The method I used to define and assess these groups was described in Chapter 7.1. To compare survival distributions between the two groups, I performed a log-rank test, which yielded a p-value of 0.112, indicating no statistically significant difference. However, my data suggest a trend—patients with low CNV burden had a longer median survival (13.8 months) compared to those with high CNV burden (8.3 months). The Kaplan-Meier curves intersected within the first four months and then diverged, revealing two distinct survival patterns: one group experienced prolonged survival, while the other showed a more rapid decline. The curves converged again around the 15-month mark, likely due to a decreased number of patients remaining in both groups.

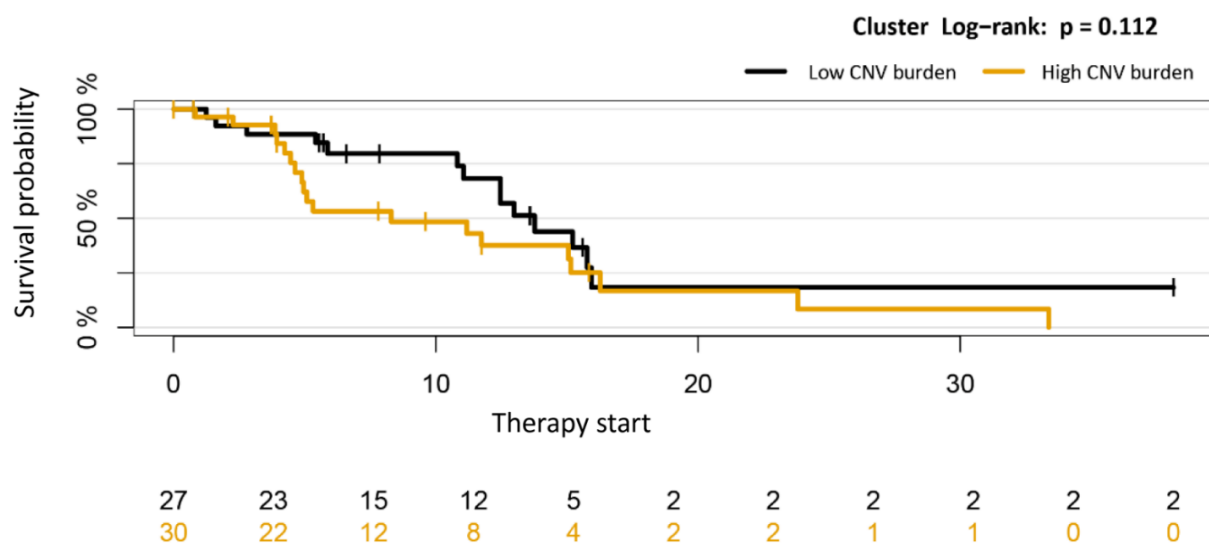


**Figure 31:** Kaplan-Meier survival curves stratified by CNV burden. The plot shows survival probability over time (in months since therapy initiation) for two patient groups: low CNV (black), high CNV (yellow). The y-axis indicates survival probability (0–100%), and the x-axis shows time in months. Patient numbers at risk for each group are listed below the x-axis at defined time points.

## 5.4 OS based on pre-treatment

Figure 32 presents Kaplan-Meier survival curves comparing OS among three patient groups based on their pre-treatment regimens: chemotherapy + ADT (black curve), chemotherapy + ADT + RLT (yellow curve), and chemo-naïve patients (blue curve). Survival probability is plotted over time in months from therapy initiation. Using a log-rank test, I found a statistically significant difference among the groups ( $p = 0.0483$ ). The chemo-naïve group demonstrated the poorest overall survival, with its curve consistently falling below the others and never intersecting them throughout the time points I analysed. I further investigated whether age differences might explain the poorer outcomes in this group, but my analysis showed that reduced survival could not be attributed to age alone. The survival curves for the chemotherapy + ADT and chemotherapy + ADT + RLT groups showed substantial overlap—particularly during the first five months and again in the later months—indicating similar survival patterns overall. These curves diverged slightly between months 11 and 15, and intersected again toward the end of the observation period, likely due to the decreasing number of patients remaining at risk in both groups.

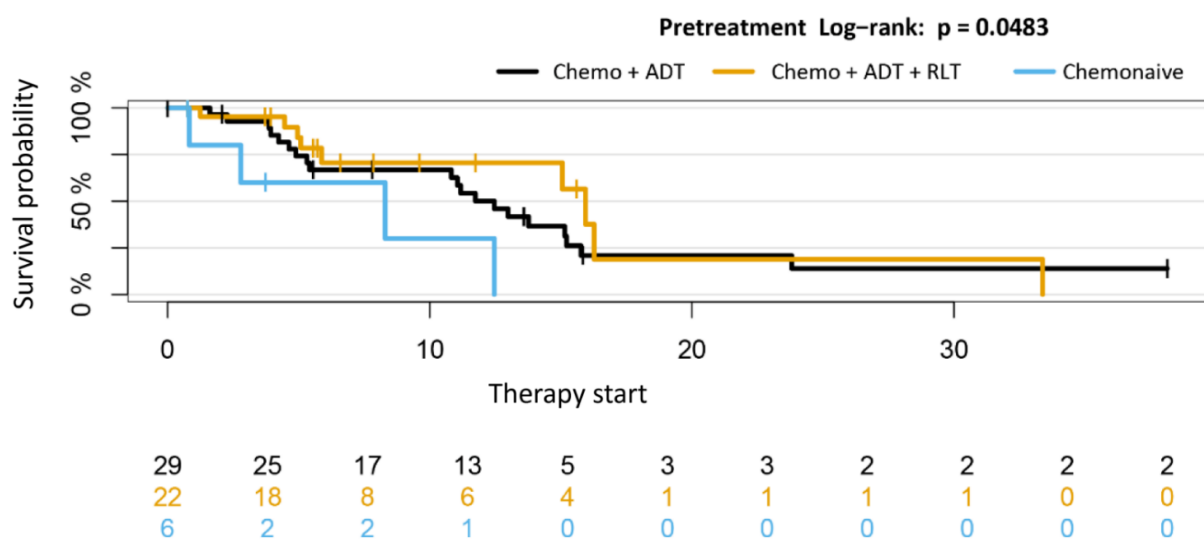


**Figure 32:** Kaplan-Meier survival curves stratified by pre-treatment regimens. The plot shows survival probability over time (in months since therapy initiation) for three patient groups: chemotherapy + androgen deprivation therapy (black), chemotherapy + androgen deprivation therapy + radioligand therapy (yellow), and chemo-naïve (blue). The y-axis indicates survival probability (0–100%), and the x-axis shows time in months. Patient numbers at risk for each group are listed below the x-axis at defined time points.

## 5.5 OS based on Tfx stratification

The relationship between Tfx and OS was evaluated by stratifying patients into three groups based on Tfx ranges: [0.000, 0.225], [0.225, 0.434], and [0.434, 0.794]. The Kaplan-Meier plot in Figure 33, shows survival probabilities over time. Since there are no established thresholds in the literature for stratifying Tfx values, I determined the cut-offs empirically. To compare overall survival across the three groups, I performed a log-rank test, which yielded a p-value of 0.0617—suggesting a trend toward significance, though not statistically significant. Interestingly, I observed that patients with the lowest Tfx values had the longest overall survival. Somewhat unexpectedly, those in the highest Tfx group showed intermediate survival, while patients in the middle Tfx range exhibited the poorest survival among the three. Again, as I observed with the other 2 stratifications, patients began to drop out around the 15-month mark.

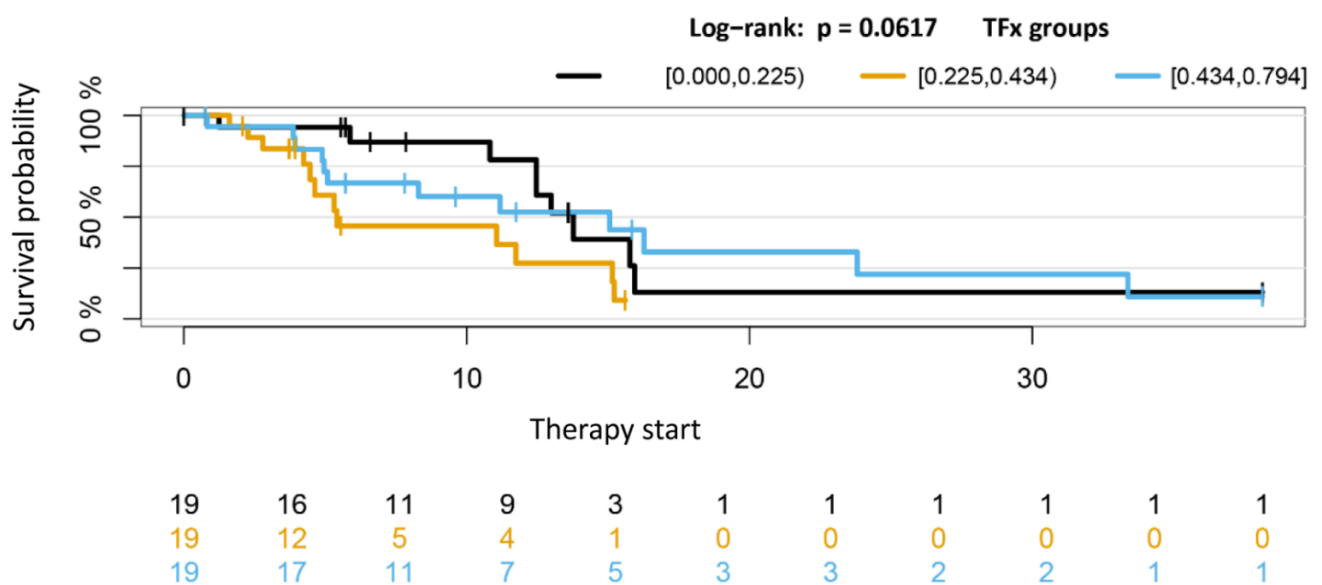


**Figure 33:** Kaplan-Meier survival curves stratified by Tfx groups. Patients were categorized into three Tfx ranges: [0.000–0.225] (black curve), [0.225–0.434] (yellow curve), and [0.434–0.794] (blue curve). The y-axis represents survival probability (0–100%), and the x-axis shows time in months since therapy initiation. The number of patients at risk in each group is displayed below the x-axis at specified time points.



## 6. CNV ANALYSIS

CNVs, which involve the amplification or deletion of chromosomal regions, are common genomic alterations in mCRPC. These variations are indicative of genomic instability and are often linked to tumor progression and treatment resistance. In this section, I performed a genome-wide analysis of CNVs using GISTIC to evaluate their potential association with Tfx and clinical outcomes. The input data consisted of copy number alteration profiles derived from ichorCNA, using baseline samples from a total of 57 patients. These patients were selected based solely on the availability of a baseline sample, obtained prior to the start of treatment. The method I used to extract logR values—essential for identifying deletions and amplifications—was described in section 8.1 *Tumor Fraction Clustering and CNV Burden Correlation Analysis*. Clustering and comparative analyses were performed to evaluate the potential of CNVs as predictive biomarkers for tumor aggressiveness and response to therapy.

### 6.1 CNVs clustering

To investigate genomic alterations associated with mCRPC, I performed a hierarchical clustering on logR values representing CNVs across 1 Mb chromosomal bins spanning chromosomes 1 to 23. The heatmap presented in Figure 34 provides a comprehensive visualization of logR values derived from CNV analysis, organized in a matrix format to explore associations between genomic alterations, Tfx, and clinical outcomes. In this heatmap, logR values of 0 indicate neutral copy number states, negative values represent deletions, and positive values reflect amplifications. The analysis was conducted on baseline samples from 57 patients with available sequencing data. Unsupervised clustering of the CNV profiles revealed two distinct patient groups: cluster 1, characterized by a low CNV burden, and cluster 2, marked by a high CNV burden, indicative of greater genomic instability. To further investigate the link between genomic instability and tumor burden, I overlaid Tfx values onto the CNV heatmap. This integration showed that cluster 2 (high CNV burden) was associated with higher Tfx values, while cluster 1 (low CNV burden) exhibited lower Tfx levels. Additionally, I overlaid treatment response data to assess potential correlations between CNV burden and clinical outcomes. However, I observed no clear relationship, suggesting that while CNV burden correlates with tumor burden, it may not serve as a direct predictor of therapeutic response in this cohort.



**Figure 34:** Heatmap displaying hierarchical clustering of CNVs across 1 Mb chromosomal bins. Amplifications are shown in red, deletions in blue, and neutral CNVs in white. TFx values are overlaid using a color gradient from purple (high TFx = 0.6) to yellow (low TFx = 0). Treatment response is indicated by color-coded bars: blue for responders, orange for mixed responders, and pink for non-responders. Chromosomes are displayed across the top, spanning from chromosome 1 to chromosome Y.

## 6.2 TFx and CNV burden correlation

I further investigated the relationship between TFx and CNV burden by categorizing patients into high and low CNV burden groups. As shown in Figure 35, I observed that patients with high CNV burden exhibited significantly higher TFx values compared to those with low CNV burden. This clear separation between the groups supports a positive association between genomic instability and tumor burden. The difference was statistically significant, as confirmed by the Wilcoxon rank-sum test ( $p = 8.09 \times 10^{-8}$ ).

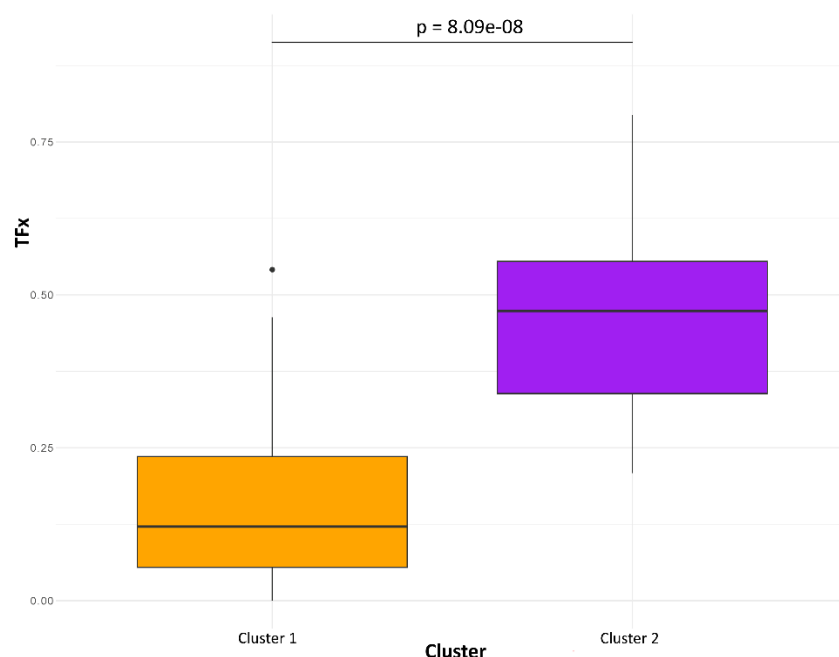


**Figure 35:** Box plot showing the distribution of TFx values across high and low CNV burden groups. The x-axis represents CNV burden categories (low = yellow vs. high = purple) while the y-axis displays TFx values on a linear scale. Boxes indicate the IQR, with the median shown as a horizontal line within each box.

## 7. GENOMIC ANALYSIS

To investigate the genomic landscape of mCRPC, I performed GISTIC analysis on ctDNA samples derived from segmentation data generated using ichorCNA. The analysis aimed to identify recurrent CNAs. The analysis was conducted on baseline samples from a cohort of 57 patients. These patients were selected based solely on the availability of a baseline sample, obtained prior to the start of treatment. To validate my findings, results were compared with a publicly available tumor tissue dataset from the SU2C/PCF Dream Team study on mCRPC, accessible via [https://www.cbiportal.org/study/cnSegments?id=prad\\_su2c\\_2015](https://www.cbiportal.org/study/cnSegments?id=prad_su2c_2015). This dataset includes whole-exome sequencing (WES) and transcriptomic profiling of bone or soft tissue tumor biopsies from a cohort of 150 mCRPC patients, collected through a multi-institutional clinical sequencing effort. The corresponding clinical data for this cohort is available at: [https://www.cbiportal.org/study/clinicalData?id=prad\\_su2c\\_2015](https://www.cbiportal.org/study/clinicalData?id=prad_su2c_2015). In addition to the baseline analysis, I applied GISTIC to subgroup-specific comparisons, focusing on clusters with low and high CNV burden, as identified through prior clustering analysis. This approach allowed me to explore genomic alterations unique to each cluster and their potential implications. To further examine the genomic drivers of relapse, I analyzed paired baseline and progressive disease (PD) samples from 17 patients. My goal was to identify amplifications and deletions that persist or emerge during disease progression, providing insights into key genomic alterations associated with tumor burden, treatment response, and disease progression. Collectively, these analyses contribute to a deeper understanding of the molecular mechanisms underpinning mCRPC and highlight potential therapeutic targets.

## 7.1 GISTIC analysis on baseline ctDNA samples

I conducted a GISTIC analysis on baseline ctDNA samples from 57 patients with mCRPC to identify recurrent CNAs, as shown in Figure 36. My analysis identified key deletions on 1q31.1, 2q22.1, 3q26.31, 5q12.1, 5q21.3, 6q16.1, 8q21.3, 10q23.31, 11q23.2, 13q14.3, 16q23.3, and 18q22.3. I also observed amplifications on 1q32.1, 8q21.3, 9q33.2, 10q22.3, 11q14.1, 12q24.11, and 20q13.33. These recurrent genomic alterations highlight regions that may play critical roles in mCRPC pathogenesis and progression, providing insights into potential mechanisms driving tumor evolution and therapeutic resistance. The plot presented in the figure includes G-scores (top) and q-values (bottom) corresponding to amplifications for all markers across the analyzed genomic regions. The G-scores represent the magnitude of amplification, while q-values reflect the statistical significance of the detected alterations. This dual representation provides a comprehensive view of the genomic landscape in mCRPC.

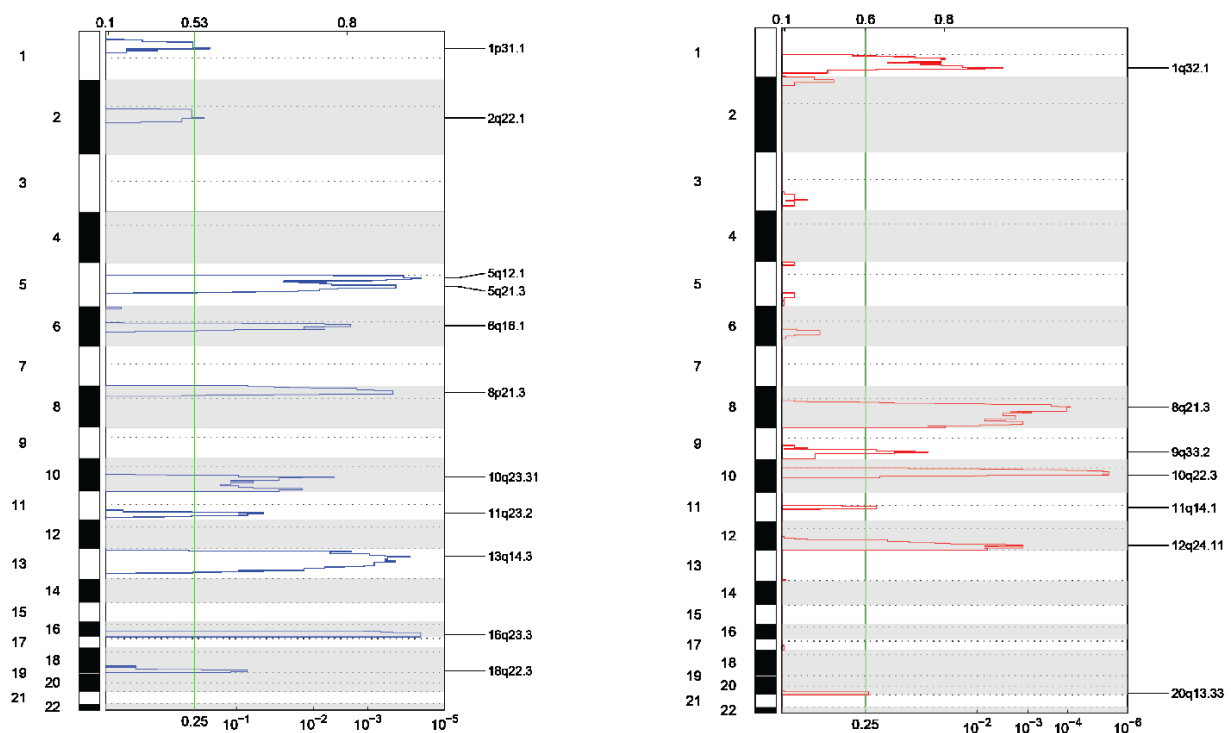


**Figure 36:** GISTIC analysis of cfDNA from 57 mCRPC patients, highlighting significant genomic alterations. The plot displays regions of significant amplifications (red) and deletions (blue), with key loci annotated. The x-axis represents GISTIC q-values, where lower values indicate greater statistical significance. The green vertical line denotes the significance threshold, and the y-axis lists chromosomal regions with notable copy number alterations.

## 7.2 Validation of baseline ctDNA alterations using tumor tissue data

To validate the genomic alterations identified in baseline ctDNA samples, I performed GISTIC analysis on 150 mCRPC tissue samples obtained from the publicly available SU2C/PCF Dream Team dataset (2015) via cBioPortal ([https://www.cbioportal.org/study/cnSegments?id=prad\\_su2c\\_2015](https://www.cbioportal.org/study/cnSegments?id=prad_su2c_2015)) (170). My results, depicted in Figure 37, reveal statistically significant copy number alterations, including deletions (left panel, blue) and amplifications (right panel, red).

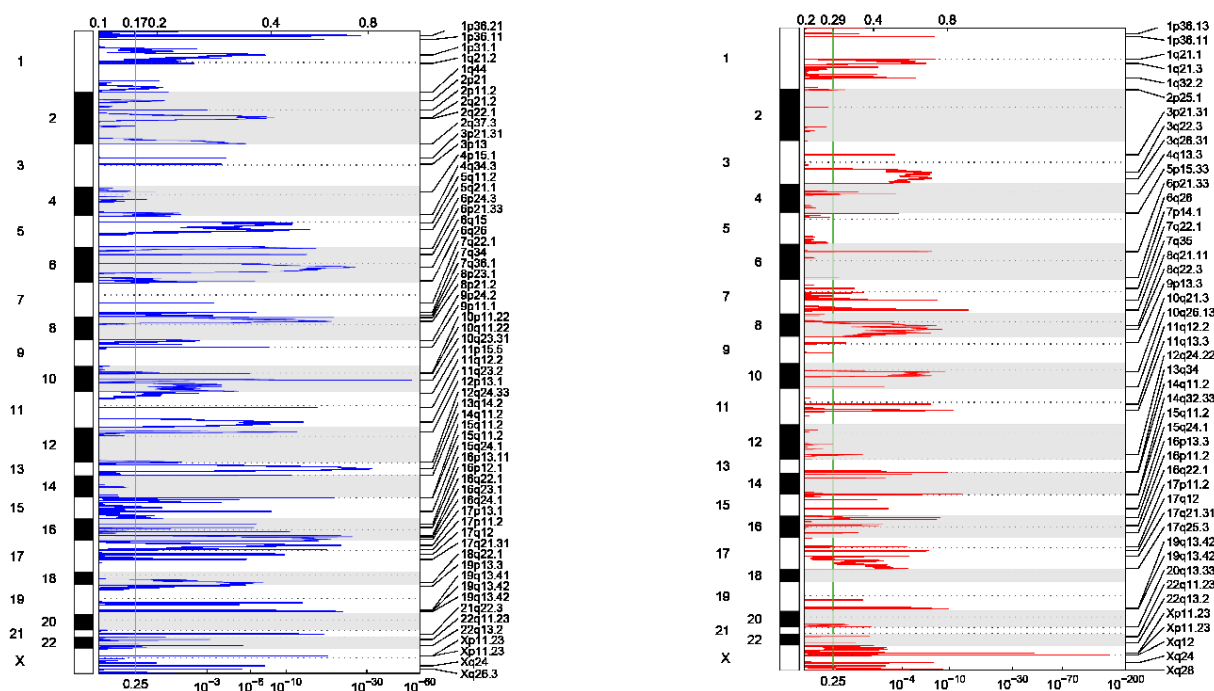


**Figure 37:** GISTIC analysis of tissue samples from the cBioPortal mCRPC dataset, identifying significant genomic deletions (left panel, blue) and amplifications (right panel, red). The top panels display G-scores, indicating the magnitude of alterations, while the bottom panels show q-values, reflecting statistical significance. The green vertical line marks the significance threshold, and key loci are annotated.

### 7.3 GISTIC analysis on Cluster 1

GISTIC analysis was performed on Cluster 1 patients, categorized as the low CNV burden group shown in Figure 38. My analysis identified relatively fewer significant genomic alterations compared to other patient clusters, with deletions observed on 5q21.3 and 6q16.2, and no amplifications detected. Cluster 1 patients exhibited a distinct genomic profile characterized by a lower frequency of copy number alterations, consistent with their classification as a low CNV burden group.

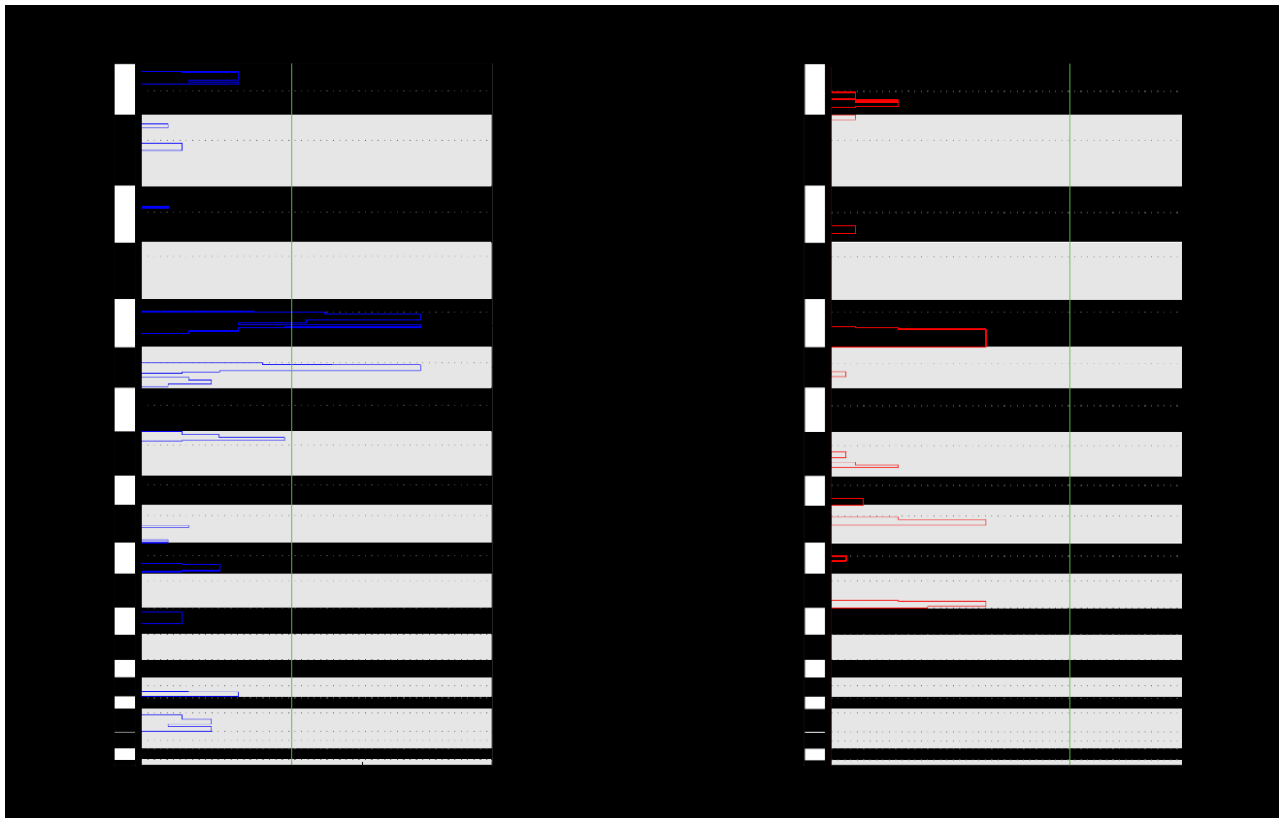


**Figure 38:** GISTIC analysis of Cluster 1 (low CNV burden), showing limited genomic alterations. Deletions are presented in the left panel (blue) and amplifications in the right panel (red). The top panels display G-scores, indicating the magnitude of each alteration, while the bottom panels show q-values representing statistical significance. The green vertical line denotes the significance threshold, and key loci are annotated.

## 7.4 GISTIC analysis on Cluster 2

Cluster 2 patients, classified as the high CNV burden group, were analysed using GISTIC as reported in Figure 39. My results revealed a significantly higher frequency of amplifications (red) and deletions (blue) compared to Cluster 1, indicating increased genomic instability. Notable deletions were identified on 5q11.2, 6q21, 8p21.3, 10q23.31, 11q23.2, 13q14.3, and 16q23.3, while amplifications were detected on 1q32.1, 8q21.3, 9q33.2, 10q22.3, and 12q24.22. My findings validate that Cluster 2 patients possess a distinct genomic profile characterized by a higher frequency of copy number alterations, consistent with their classification as a high CNV burden group.

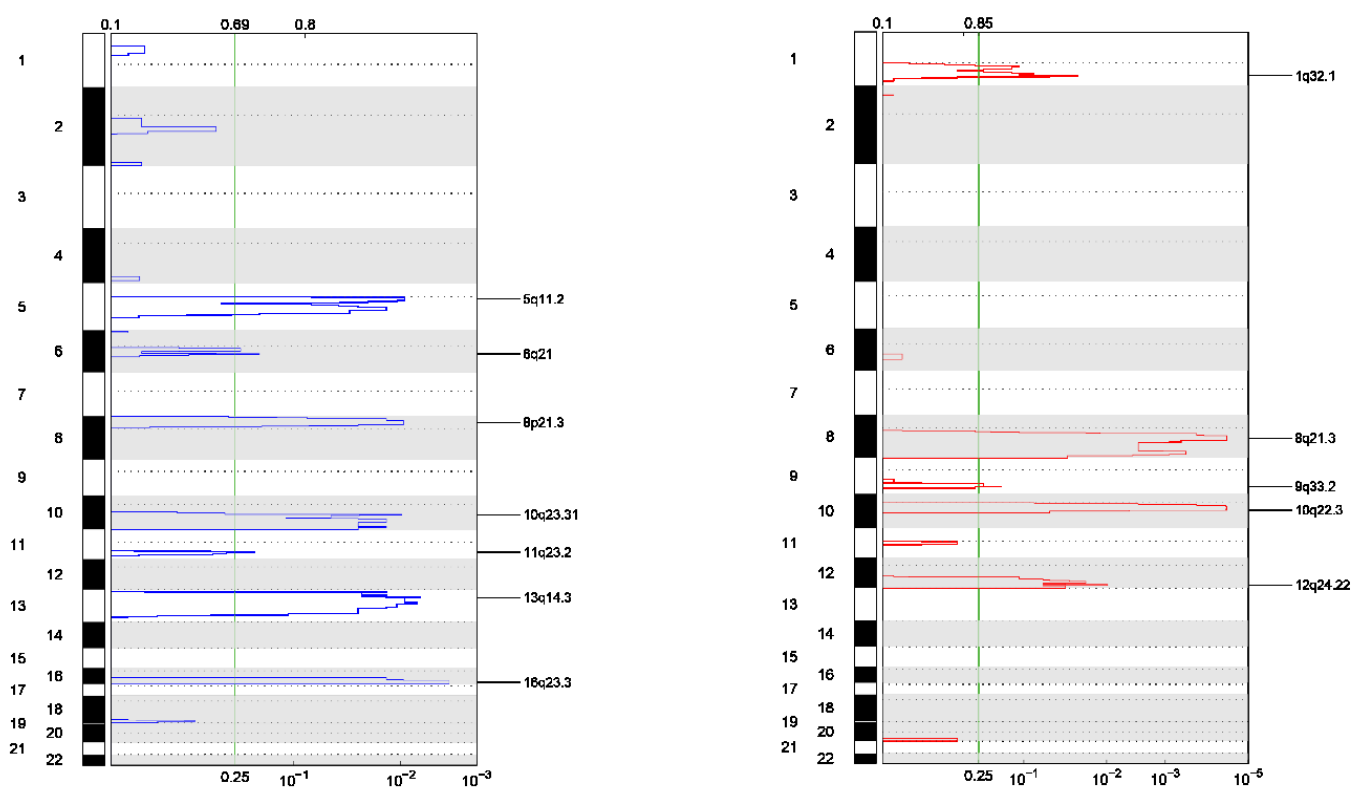


**Figure 39:** GISTIC analysis of Cluster 2 (high CNV burden), highlighting significant genomic alterations. Amplifications (red) and deletions (blue) are shown, with the x-axis representing GISTIC q-values—lower values indicate higher statistical significance—and the y-axis listing chromosomal regions with detected alterations. The green vertical line marks the significance threshold.



## 7.5 GISTIC analysis on baseline and PD samples

To investigate genomic regions potentially associated with treatment resistance or alterations that persist from baseline to disease progression, I performed a GISTIC analysis on ctDNA samples collected at the time of clinically defined PD from 17 metastatic mCRPC patients. To ensure high data quality, I included only samples with a TFX greater than 0.10 in the analysis. Notably, I selected the PD timepoint based on clinical progression, irrespective of the treatment cycle number. In the baseline samples, my analysis identified significant genomic alterations, including a deletion on 5q21.3 and amplifications on 8q21.3, 9q33.2, and 10q21.3 (Figure 40). In contrast, analysis of the PD group revealed amplifications only, specifically on 8q21.3 and 10q21.2 (Figure 41). This comparative analysis reveals that amplification changes are the alterations most likely to persist or evolve between baseline and progressive disease stages, offering important insights into the mechanisms of treatment resistance and tumor evolution in mCRPC.

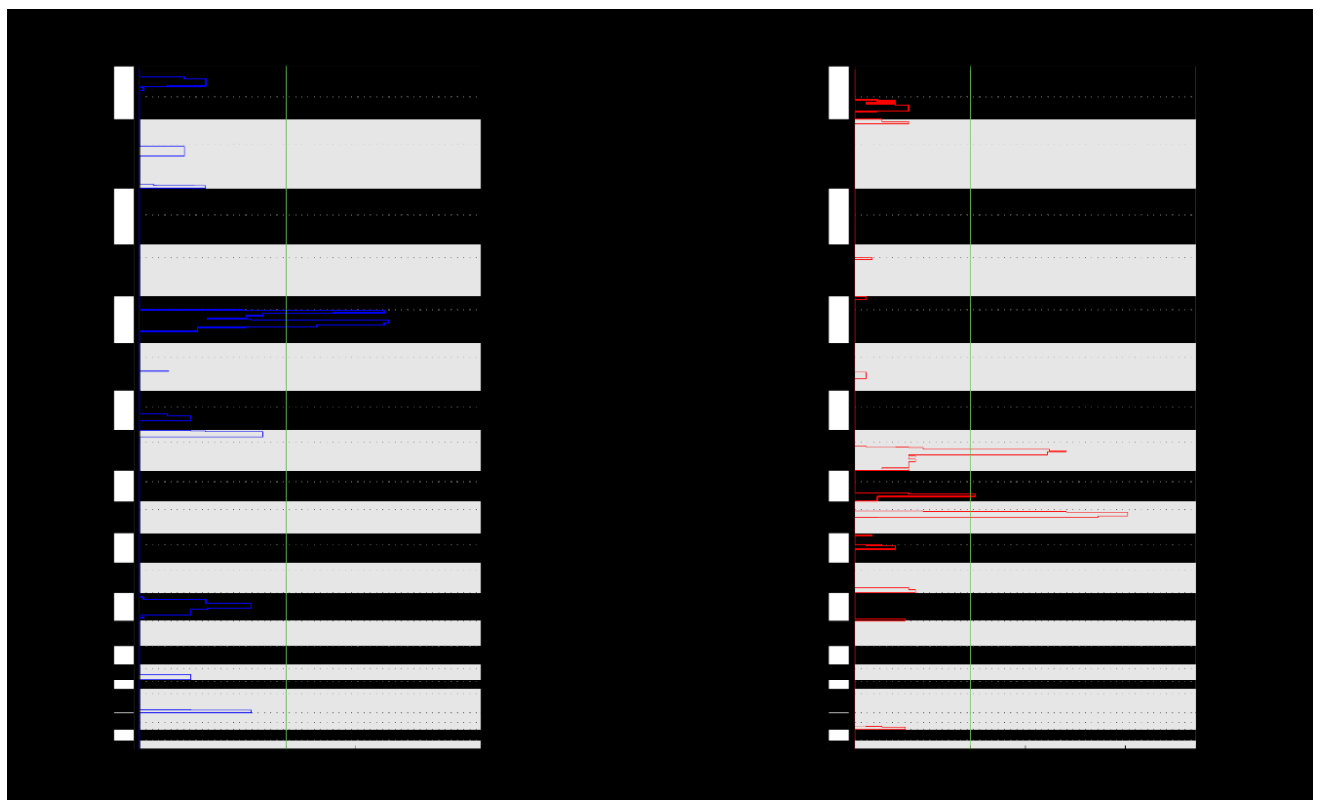


**Figure 40:** GISTIC analysis of baseline ctDNA samples from 17 mCRPC patients with TFX > 0.10, highlighting key genomic alterations. The x-axis represents GISTIC q-values, with lower values indicating greater statistical significance, and the y-axis lists chromosomal regions with notable amplifications and deletions. The green vertical line denotes the threshold for statistical significance.

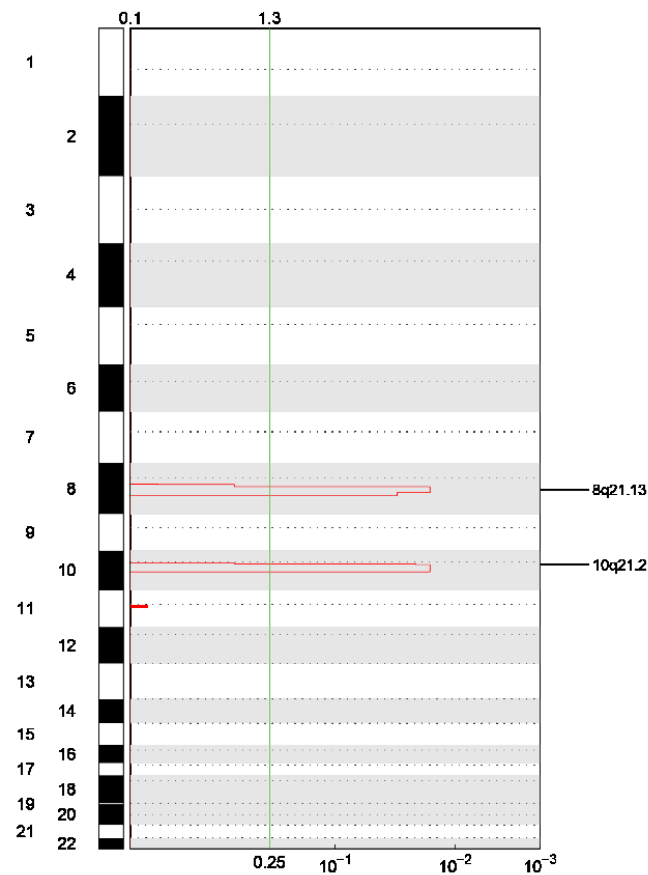


**Figure 41:** GISTIC on 17 patients testing the respective progressive disease group of samples. Filtering for  $TFx > 0.10$ . The x-axis represents GISTIC q-values, with lower values indicating greater statistical significance, and the y-axis lists chromosomal regions with notable amplifications and deletions. The green vertical line denotes the threshold for statistical significance.

## 8. GENE SIGNATURE IDENTIFICATION

Gene signature identification is crucial for unravelling the molecular mechanisms driving mCRPC [<sup>225</sup>Ac]Ac-/ [<sup>177</sup>Lu]Lu-PSMA-617 resistance. In this section, I used GISTIC analysis to examine genomic regions of amplification and deletion, allowing me to isolate key genes associated with these alterations. I then intersected the identified genes with the COSMIC database of oncogenes and tumor suppressor genes to identify critical genomic drivers linked to tumor progression and treatment resistance.

### 8.1 Baseline vs. Cluster 2 gene signatures

As described in Chapter 5.3 Overall Survival Based on CNV Burden, patients within Cluster 2—defined by high CNV burden—demonstrated the poorest overall survival, although the difference was not statistically significant. To further investigate the potential genomic drivers contributing to this trend, we conducted gene-level classification analyses to identify key alterations associated with poor outcomes. Specifically, the analysis outlined in section *8.4 Identification of Oncogenes and Tumor Suppressors* was applied to Cluster 2. In parallel, the same approach was performed using the GISTIC results from baseline samples of the 17 patients who had matched PD samples, as detailed in section *8.5 GISTIC Analysis on Baseline and Progressive Disease Samples*. This dual analysis aimed to uncover consistent gene signatures that may be linked to tumor aggressiveness and treatment resistance. This comparison was conducted primarily as an internal control to assess the consistency of detected gene alterations, given that both datasets represent baseline samples. The goal was to determine whether the same genes would emerge in both analyses, thereby validating the approach. The comparison between the baseline samples and Cluster 2 revealed a largely overlapping set of tumor suppressor deletions, as shown in Figure 42. These included RB1, PTEN, PIK3R1, MGMT, FANCA, BRCA2, ATM, TNC, SUFU, RAD17, PRDM1, LEPROTL1, FAS, SDHD, CCNC, and CPEB3, all commonly altered in both groups. In contrast, a few oncogenes such as PTPN11, MDM4, and TNC showed amplifications exclusively in Cluster 2 and were not altered in the baseline group. Notably, the oncogene CDH17 was consistently amplified in both groups. The overall pattern suggests an increased number of genomic alterations in Cluster 2, with additional deletions and amplifications compared to baseline.

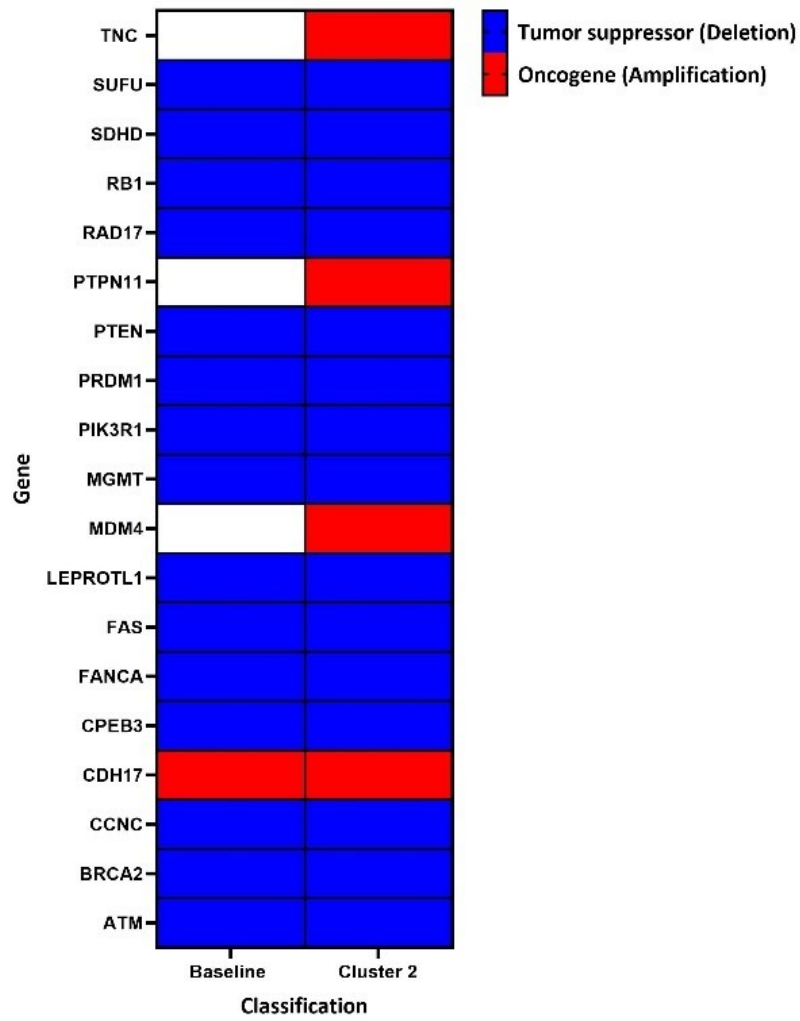


**Figure 42:** Gene signature baseline – progressive disease. The plot provides a visualization of the gene classification across baseline and Cluster 2, depicting the distribution of tumor suppressor deletions (blue) and oncogene amplifications (red).

## 9. EnrichR

To further explore the biological significance of the identified gene signatures, I performed pathway enrichment analysis using EnrichR on the oncogenes and tumor suppressor genes identified in Figure 42. My results revealed key pathways associated with the genomic alterations in these subgroups, highlighting their involvement in critical cellular processes such as DNA damage response, cell cycle regulation, apoptosis, and signalling pathways like PI3K/AKT and TP53 signalling. The enrichment results provide a deeper understanding of the molecular mechanisms driving tumor progression and treatment resistance in patients with high CNV burden and poor clinical outcomes. My findings emphasize the potential of these pathways as therapeutic targets for improving outcomes in mCRPC.

### 9.1 EnrichR pathway analysis of oncogenes in Cluster 2

EnrichR pathway analysis was conducted on oncogenes with gain-of-function alterations in Cluster 2 to identify significantly enriched biological pathways and processes as shown in Figure 43. My analysis revealed key pathways implicated in tumor progression and cellular signalling. Among these, cell-cell communication emerged as the most significantly enriched pathway, followed by MET activation of PTPN11 and STAT5 activation, both critical for signal transduction and cancer development. Additional enriched pathways included Netrin-mediated repulsion signals, MAPK (ERK1/ERK2) activation, and Interleukin-6 signaling, all of which play vital roles in promoting cell proliferation, survival, and metastasis in high CNV burden patients.

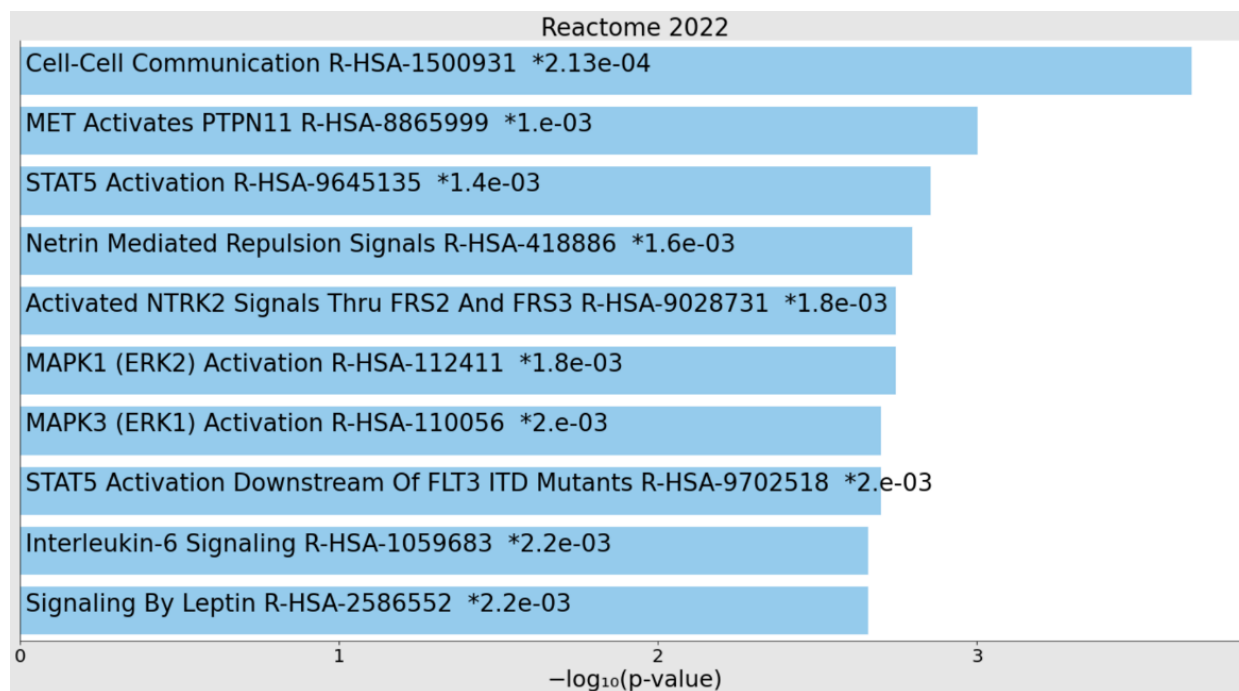


**Figure 43:** EnrichR pathway analysis of oncogenes with gain-of-function alterations in Cluster 2. The x-axis represents pathway enrichment significance as  $-\log_{10}(p\text{-value})$ , highlighting the critical disruptions in DNA damage response and genomic stability.

## 9.2 EnrichR pathway analysis of tumor suppressor genes in Cluster 2

EnrichR pathway analysis was performed on tumor suppressor genes exhibiting loss-of-function alterations in Cluster 2 to identify significantly enriched pathways (Figure 44). My results revealed strong enrichment in pathways associated with DNA damage repair and homologous recombination. Among the most significantly enriched pathways were impaired BRCA2 binding to RAD51, DNA repair, and the presynaptic phase of homologous DNA pairing and strand exchange, underscoring key disruptions in mechanisms maintaining genomic stability. Other pathways, such as defective Homologous Recombination Repair (HRR) due to BRCA2 loss of function, homology directed repair, and transcriptional regulation by TP53, further highlight the compromised DNA repair processes in high CNV burden patients.

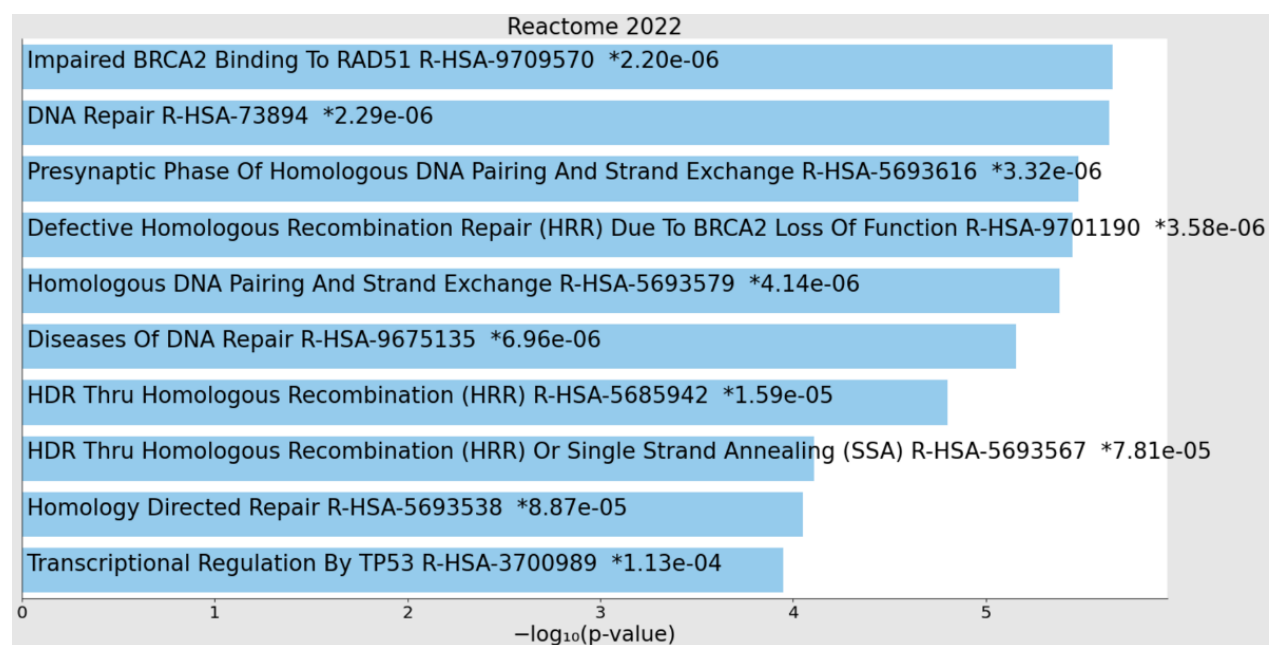


**Figure 44:** EnrichR pathway analysis of tumor suppressor genes with loss-of-function alterations in Cluster 2. The x-axis represents pathway enrichment significance as  $-\log_{10}(p\text{-value})$ , highlighting the critical disruptions in DNA damage response and genomic stability.

## 10. CASE STUDIES: CHEMO-RESISTANT PATIENTS

In this section, I present a comprehensive analysis of patient responses to actinium-lutetium therapy, covering a range of outcomes including complete response, partial response, relapse, and non-response. I describe eight individual case studies, detailing each patient's pre-treatment history, imaging data, and therapy response, which I via tumor marker kinetics over the course of actinium-lutetium therapy. Table 4 and Table 5 summarize the clinical pre-treatment characteristics and initial diagnoses. A detailed description of each treatment course and outcome is provided, offering insights into the common and distinct clinical trajectories observed in PSMA-TRNT. All patients included in this study have undergone complete ctDNA collection cycles, sequencing, and corresponding imaging assessments both before and after treatment, ensuring a thorough evaluation of therapeutic response. A table with reference values for all the markers described in the following section is provided in Table A3 and A4 (Appendix).

**Table 4:** Initial diagnosis status of the case studies patients.

Patient #	Response	iDiagnosis	iGS	iPSA (ng/mL)	iTumor Status
Patient 5	Responder	2012	7b (4 + 3)	19	pT3b, pN0, R0
Patient 10	Responder	2015	9 (4+5)	60	pT3b, pN1
Patient 38	Mixed responder	2015	7a (3+4)	15	pT1a, cN0, cM1
Patient 37	Mixed responder	2009	9 (4+5)	64	pT3b pN1(1/12) M0 R1
Patient 11	Mixed responder	2015	7 (4+3)	170	cN1 cM1b
Patient 34	Non-responder	2018	10 (5+5)	32	pT4, N1, M1
Patient 40	Non-responder	2020	9 (5+4)	100	cM1b
Patient 91	Non-responder	2018	9 (5+4)	NA	pT3 pN1 (2/19) R0

*iDiagnosis: initial diagnosis, iGS: initial Gleason score, a/b in GS: Used to differentiate between Gleason patterns within the same score, iPSA: initial PSA level, iTumor status: initial tumor status. T (Tumor): Size and extent of the primary tumor, N (Nodes): Indicates whether cancer has spread to regional lymph nodes, M (Metastasis): Indicates whether cancer has spread to distant organs, R (Resection Margin): Indicates whether cancer cells are present at the surgical margin after tumor removal.*



**Table 5:** Pre-treatments status of the case studies patients.

Patient #	Hormonal Therapy	Surgery	Chemotherapy	Metastasis	Radiation	Pre PSMA-TRNT
<b>Patient 5</b>	ADT, Enzalutamide Olaparib	Radical prostatectomy	2C Docetaxel/Carboplatin 6C Cisplatin/Etoposid	PUL OSS HEP LYM	External radiation	NA
<b>Patient 34</b>	Enzalutamide, Abiraterone/Prednisone	Radical prostatectomy	12C Docetaxel 6C Cabazitaxel	OSS MAR HEP	Not applied	NA
<b>Patient 38</b>	Leuporeline, Bicalutamide, Enzalutamide	NA	2C Docetaxel	OSS, MAR, HEP	Palliative external radiation	NA
<b>Patient 10</b>	ADT, Enzalutamide, Prednisone, Abiraterone, Olaparib	Radical prostatectomy Lymphadectomy	6C Docetaxel 2C Cabazitaxel	OSS	External radiation	NA
<b>Patient 37</b>	ADT, Enzalutamide, Abiraterone	Radical prostatectomy Lymphadectomy	9C Docetaxel	OSS	External radiation	NA
<b>Patient 40</b>	ADT, Abiraterone	NA	9C Docetaxel	OSS, LYM, ADR	External radiation	NA
<b>Patient 91</b>	ADT, Enzalutamide, Abiraterone	Radical prostatectomy	6C Docetaxel	OSS, LYM, HEP	Not applied	Lutetium
<b>Patient 11</b>	ADT, Enzalutamide, Abiraterone	NA	6C Docetaxel 6C Cabazitaxel	OSS	External radiation	Lutetium

ADT: Androgen Deprivation Therapy, C: Cycles, PUL (Pulmonary): Lungs, OSS (Osseous): Bones, HEP (Hepatic): Liver, LYM (Lymphatic): Lymph nodes, MAR (Marrow): Bone marrow, ADR (Adrenal): Adrenal glands, NA (Not applied)

10.1 Patient 5

Patient 5, with widespread metastatic involvement identified on PSMA-SPECT using [<sup>99m</sup>Tc]Tc-PSMA-GCK01 (Figure 45, Figure 46), underwent actinium-lutetium therapy. Available imaging includes a pre-treatment scan, three post-treatment scans following radioligand administration, and one post-therapy scan for assessing treatment efficacy. An adaptive dosing strategy led to a dramatic reduction in PSA levels, from 0.50 ng/mL to a nadir of 0.01 ng/mL after two cycles (Figure 47A). Simultaneously, Tfx decreased from 0.47 to below detection levels (Figure 47B), as reflected in CNA profiles (Figure 48). These improvements were mirrored in tumor biomarkers AP and LDH, both of which showed a marked decline (Figure 47). Post-treatment imaging demonstrated complete resolution of metastatic lesions on PSMA-SPECT Figure 45 with MRI confirming eradication of liver metastases (Figure 46). Renal function remained generally stable, with intermittent mild impairments (Table 6). However, hematologic side effects, including persistent anaemia and episodic leukopenia, were observed post-treatment.

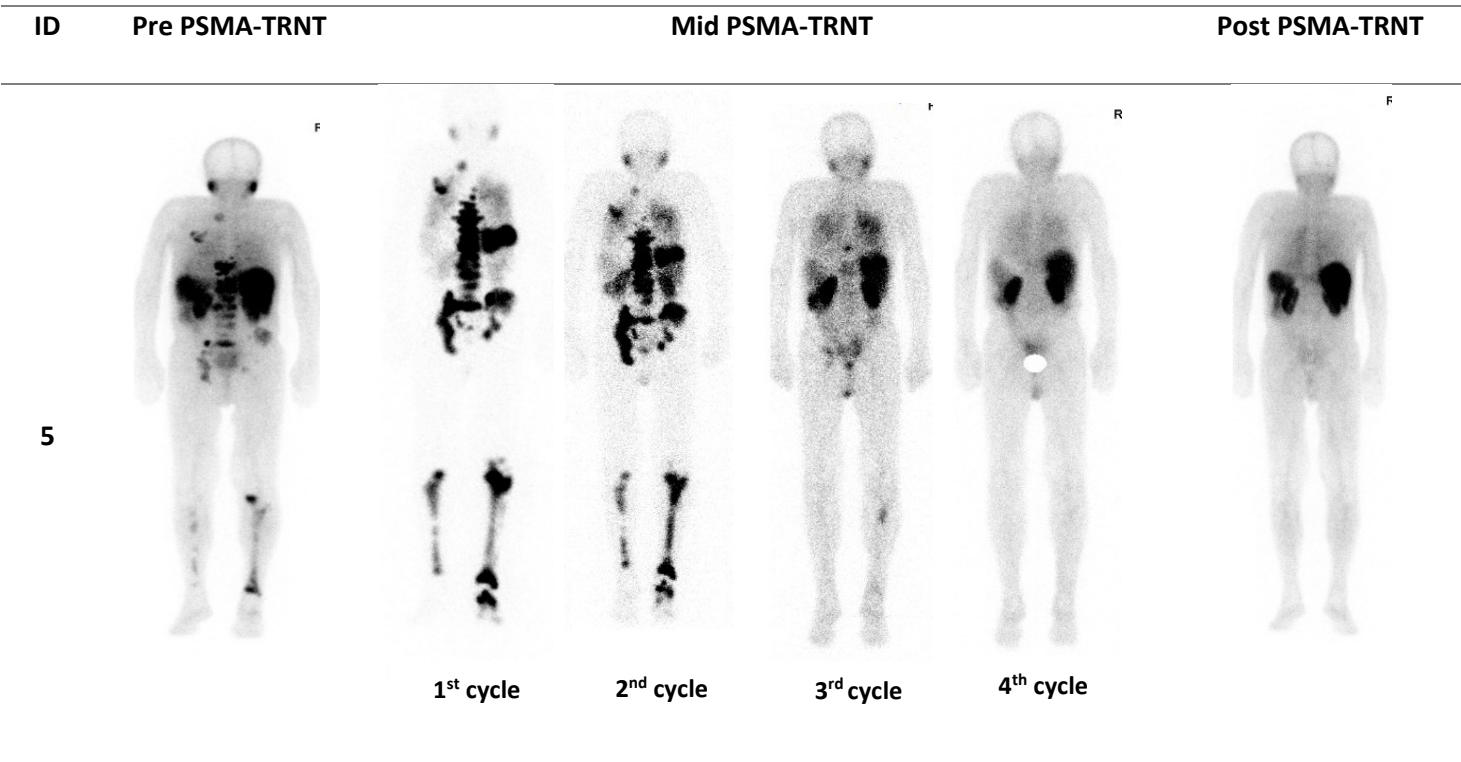


**Figure 45:** Imaging overview of Patient 5 throughout actinium-lutetium PSMA-TRNT. Baseline and post-treatment SPECT imaging were performed using [<sup>99m</sup>Tc]Tc-PSMA-GCK01 to assess initial disease burden and therapeutic response, respectively. Mid-treatment assessment refers to therapy-related scans conducted during the PSMA-TRNT course.

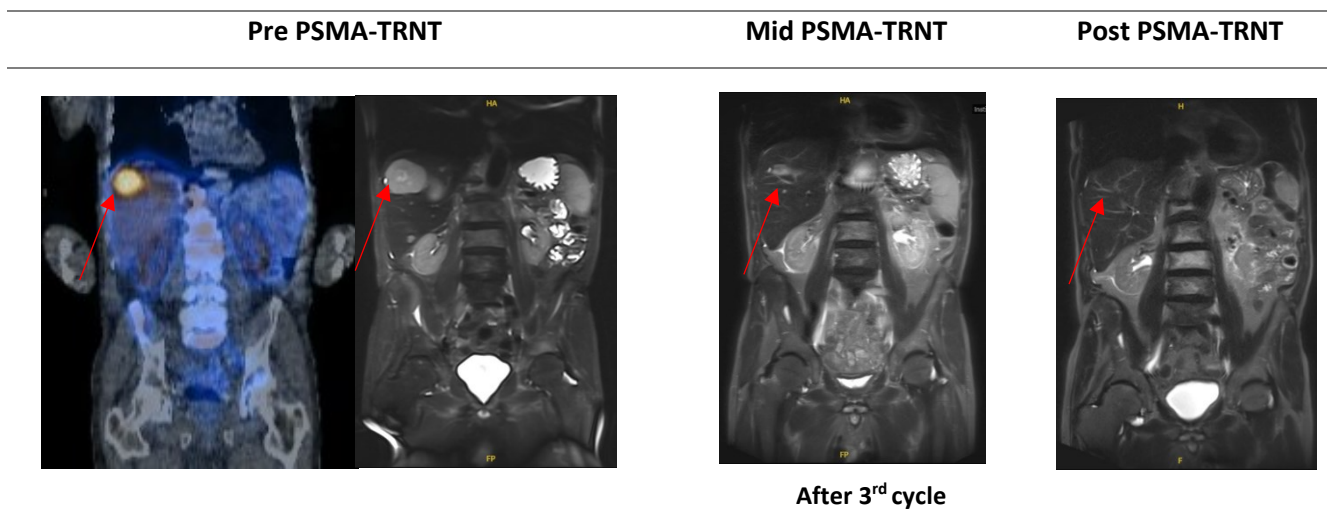


**Figure 46:** Overview image sequence for Patient 5. A liver metastasis (arrow) demonstrates intense uptake of the radiopharmaceutical through initial PSMA-SEPCT and MRI before treatment with  $[^{225}\text{Ac}]\text{Ac}-/[^{177}\text{Lu}]\text{Lu-PSMA-617}$ . Intermediate MRI after the 3<sup>rd</sup> cycle revealing partial remission of this metastasis, and final MRI post-therapy, showcasing successful treatment impact.

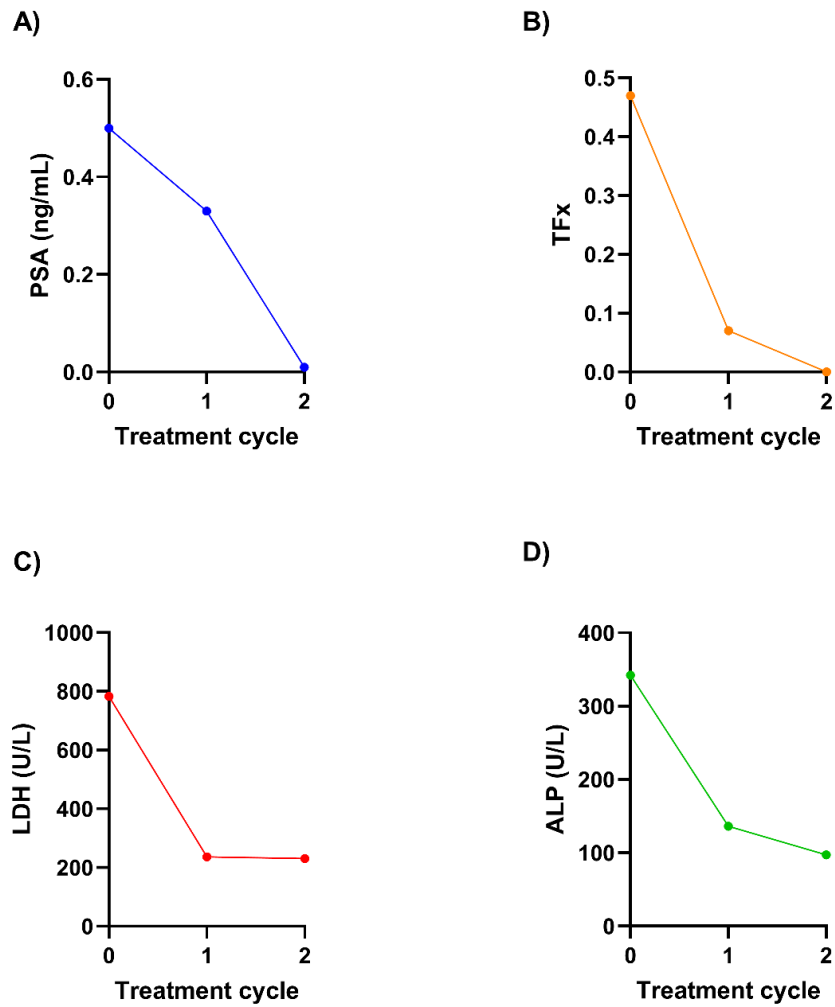


**Figure 47:** Comprehensive overview of the dynamic changes in A) PSA, B) Tfx, C) LDH and D) ALP in Patient 5, following  $[^{225}\text{Ac}]\text{Ac}/[^{177}\text{Lu}]\text{Lu-PSMA-617}$  regimen. Data points are plotted over the treatment period, providing insights into the therapeutic response.

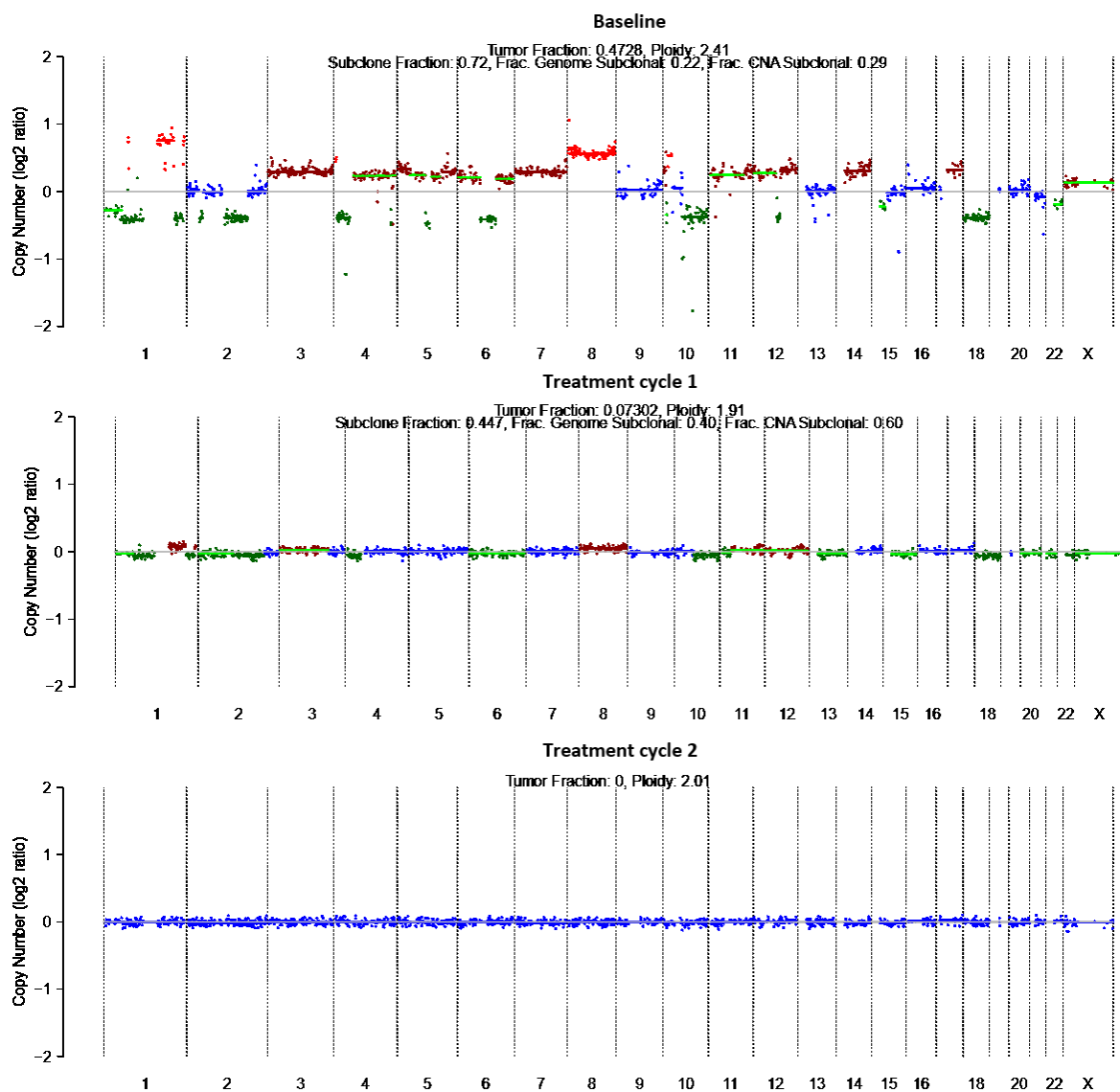


**Figure 48:** CNA profiles for Patient 5 across multiple treatment timepoints. Each panel represents a distinct timepoint, starting with the baseline (pre-treatment) followed by sequential post-treatment cycles. CNV profiles are depicted as log2 copy number ratios plotted against genomic coordinates.




**Table 6:** Longitudinal assessment of GFR-CKD-EPI, creatinine, hemoglobin and leukocyte count during  $[^{225}\text{Ac}]\text{Ac}-/[^{177}\text{Lu}]\text{Lu-PSMA-617}$  application of Patient 5.

Time point	GFR-CKD-EPI (mL/min/1.73qm)	Creatinine (mg/dL)	Hemoglobin (g/dL)	Leukocyte (G/nL)
Baseline	59.1	1.1	9.1	3.9
1 <sup>st</sup> treatment cycle	71.9	0.97	9.6	3.3
2 <sup>nd</sup> treatment cycle	79.8	0.87	8.3	3.5

*GFR-CKD-EPI: Glomerular Filtration Rate estimated using the Chronic Kidney Disease Epidemiology Collaboration (CKD-EPI) equation, expressed in mL/min/1.73 m<sup>2</sup>.*

## 10.2 Patient 10

Patient 10, showing PSMA positive metastasis on PSMA-PET/CT with  $[^{18}\text{F}]\text{PSMA-1007}$  (Figure 49) , exhibited a PSA decline from 190 ng/mL to 21.2 ng/mL over five cycles of actinium-lutetium therapy (Figure 51A), despite the persistence of bone metastases. This reduction in PSA was accompanied by a dramatic decrease in Tfx, dropping from an initial value of 0.46 to below detection levels after the first cycle and remaining undetectable throughout subsequent three cycles (Figure 51B, Figure 53). Renal function remained stable, with normal creatinine levels and high GFR. However, persistent leukopenia and moderate anaemia were observed as side effects (Table 7). After reaching the cumulative renal dose limit, the patient transitioned to a regimen of Abiraterone and Olaparib. Following a two-year hiatus from TRNT, the tumor board reassessed the case (Figure 50). Given the persistence of bone metastases and the patient's ineligibility for conventional therapies, actinium-lutetium therapy was resumed. At the second baseline, the tumor profile had undergone significant changes, presenting a completely different genomic landscape compared to the initial assessment. Tfx increased from 0.41 to 0.61 after the first cycle of the resumed therapy (Figure 52B), with evolving regions of genomic amplification detected (Figure 54). Conversely, PSA levels remained stable, decreasing slightly from 82.1 ng/mL to 73.5 ng/mL (Figure 52). Renal function results indicate impairment, with values of 46.9 and 56 falling below the reference range, along with a persistent anaemia and low leukocyte count (Table 8).

ID	Pre PSMA-TRNT	Mid PSMA-TRNT	Post PSMA-TRNT
10			
	After 3 <sup>rd</sup> cycle		

**Figure 49:** Imaging overview of Patient 10 undergoing actinium-lutetium PSMA-TRNT. [ $^{18}\text{F}$ ]PSMA-1007 PET imaging was performed at three time points: baseline (pre-PSMA-TRNT) for initial staging, mid-therapy following the third treatment cycle to assess interim response, and post-therapy to evaluate overall treatment efficacy.

ID	Pre PSMA-TRNT
10	

**Figure 50:** Imaging conducted after a two-year treatment hiatus and subsequent transition to Olaparib and Abiraterone therapy for Patient 10. PSMA-PET using [ $^{18}\text{F}$ ]PSMA-1007 for evaluating the patient's current clinical status.

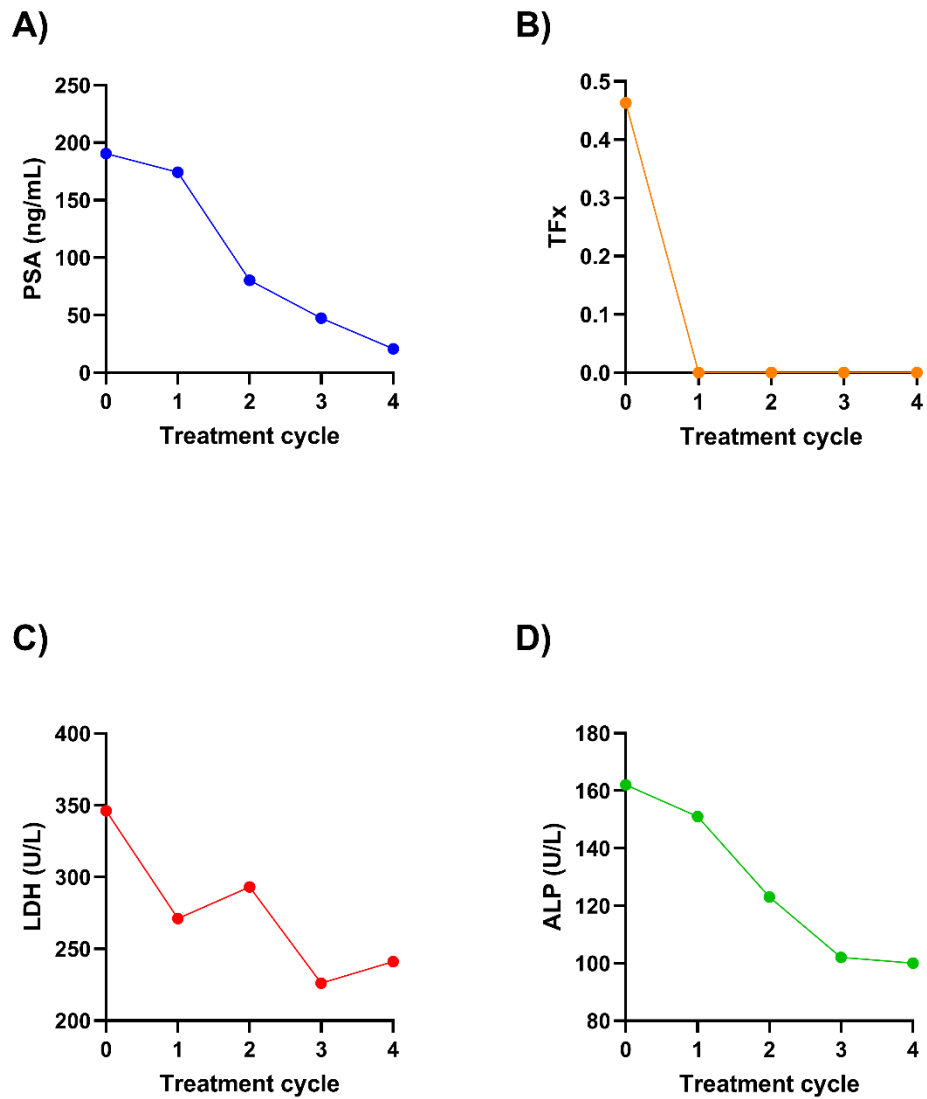


**Figure 51:** Comprehensive overview of the dynamic changes in A) PSA B) TFx, C) ALP, and D) LDH in Patient 10, following  $[^{225}\text{Ac}]\text{Ac-}/[^{177}\text{Lu}]\text{Lu-PSMA-617}$  regimen. Data points are plotted over the treatment period, providing insights into the therapeutic response.



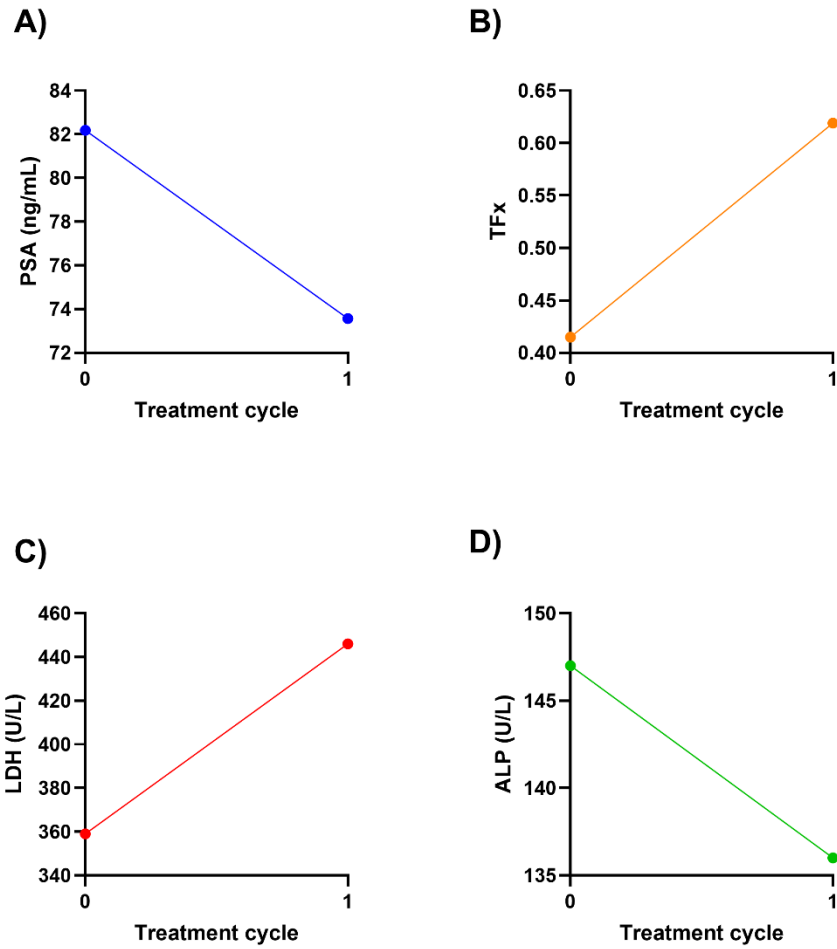


**Figure 52:** Comprehensive overview of the dynamic changes in in A) PSA B) Tfx, C) ALP, and D) LDH in Patient 10, following a two-year treatment break and a therapy switch to Olaparib and Abiraterone.

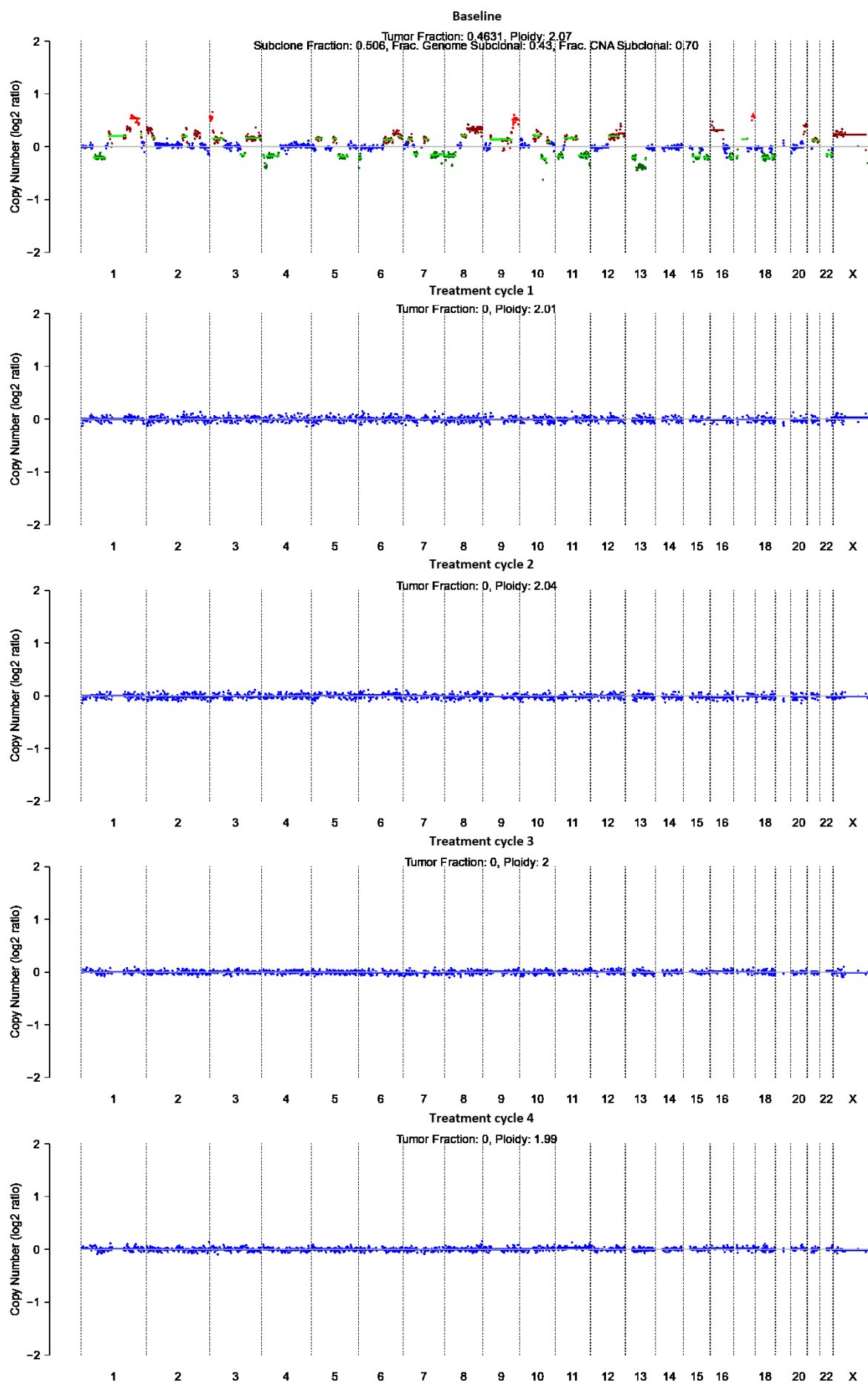


**Figure 53:** CNA profiles for Patient 10 across four treatment timepoints. Each panel represents a distinct timepoint, starting with the baseline (pre-treatment) followed by sequential post-treatment cycles. CNV profiles are depicted as log2 copy number ratios plotted against genomic coordinates.

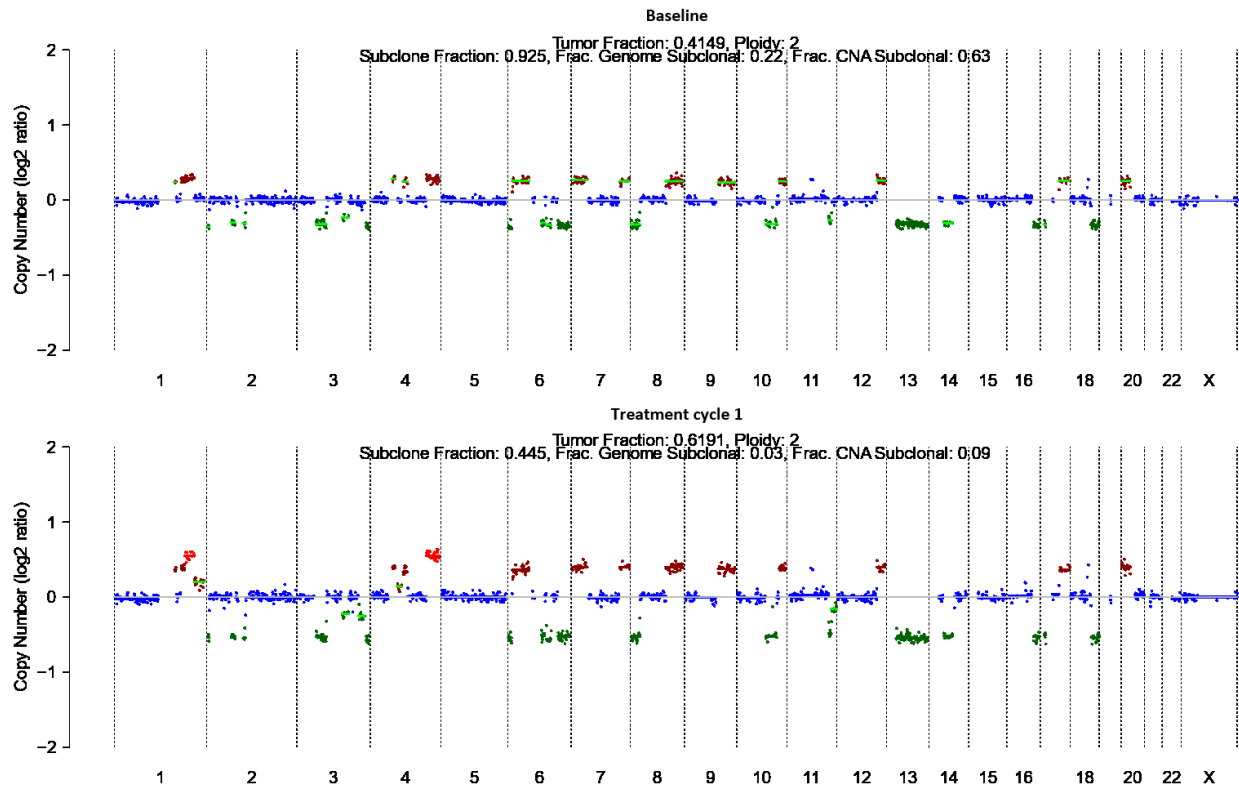


**Figure 54:** CNA profiles for Patient 10 one treatment cycle. Each panel represents a distinct timepoint, starting with the baseline (pre-treatment) following a two-year treatment break and a therapy switch to Olaparib and Abiraterone. Subsequent panels display the CNA profiles after receiving one cycle of [ $^{225}\text{Ac}$ ]Ac-/ [ $^{177}\text{Lu}$ ]Lu-PSMA-617 therapy.

**Table 7:** Longitudinal assessment of GFR-CKD-EPI, creatinine, hemoglobin and leukocyte count during  $[^{225}\text{Ac}]\text{Ac}/[^{177}\text{Lu}]\text{Lu-PSMA-617}$  therapy of Patient 10.

Time point	GFR-CKD-EPI (mL/min/1.73qm)	Creatinine (mg/dL)	Hemoglobin (g/dL)	Leukocyte (G/nL)
Baseline	99.7	0.75	3.6	3.6
1 <sup>st</sup> treatment cycle	99.2	0.76	5.6	2.9
2 <sup>nd</sup> treatment cycle	103	0.70	2.9	2.9
3 <sup>rd</sup> treatment cycle	94.7	0.85	2.3	2.3
4 <sup>th</sup> treatment cycle	91.9	0.90	2.5	2.5

GFR-CKD-EPI: Glomerular Filtration Rate estimated using the Chronic Kidney Disease Epidemiology Collaboration (CKD-EPI) equation, expressed in mL/min/1.73 m<sup>2</sup>.

**Table 8:** Longitudinal assessment of GFR-CKD-EPI, creatinine, hemoglobin and leukocyte count following a two-year treatment break and a therapy switch to Olaparib and Abiraterone.

Time point	GFR-CKD-EPI (mL/min/1.73qm)	Creatinine (mg/dL)	Hemoglobin (g/dL)	Leukocyte (G/nL)
Baseline	46.9	1.5	7.0	4.5
1 <sup>st</sup> treatment cycle	56.0	1.3	5.9	2.9

GFR-CKD-EPI: Glomerular Filtration Rate estimated using the Chronic Kidney Disease Epidemiology Collaboration (CKD-EPI) equation, expressed in mL/min/1.73 m<sup>2</sup>.

10.3 Patient 38

Patient 38 presented with extensive red marrow infiltration observed on PSMA-SPECT using [<sup>99m</sup>Tc]Tc-PSMA-GCK01 before starting TRNT (Figure 55). Actinium-lutetium therapy initially led to a reduction in PSA levels, from over 446 ng/mL to 113 ng/mL (Figure 56A). However, by the fourth cycle, PSA levels increased to 145 ng/mL, indicating relapse. This relapse was preceded by a rise in Tfx to 0.15 during the third cycle (Figure 56B), signalling early disease progression. Tfx further increased to 0.41 in the fourth cycle, confirming the relapse and mirroring baseline genomic patterns (Figure 57). Despite these challenges, renal function remained stable, with creatinine levels and GFR consistently within acceptable ranges. However, hematologic monitoring revealed variability in leukocyte counts and persistent mild to moderate anaemia (Table 9).

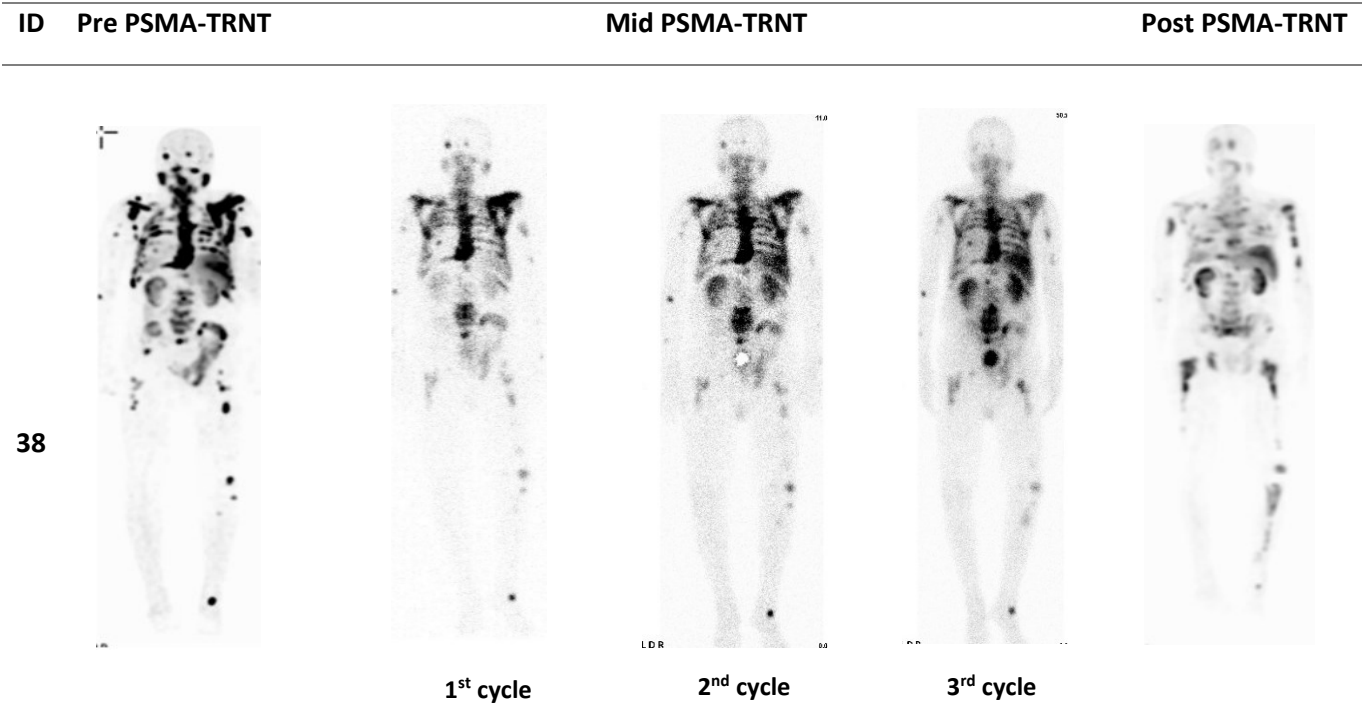


**Figure 55:** Imaging overview of Patient 38 throughout [<sup>225</sup>Ac]Ac-/[<sup>177</sup>Lu]Lu-PSMA-617. Baseline and post-treatment SPECT imaging were performed using [<sup>99m</sup>Tc]Tc-PSMA-GCK01 to assess initial disease burden and therapeutic response, respectively. Mid-treatment assessment refers to therapy-related scans conducted during the PSMA-TRNT course.

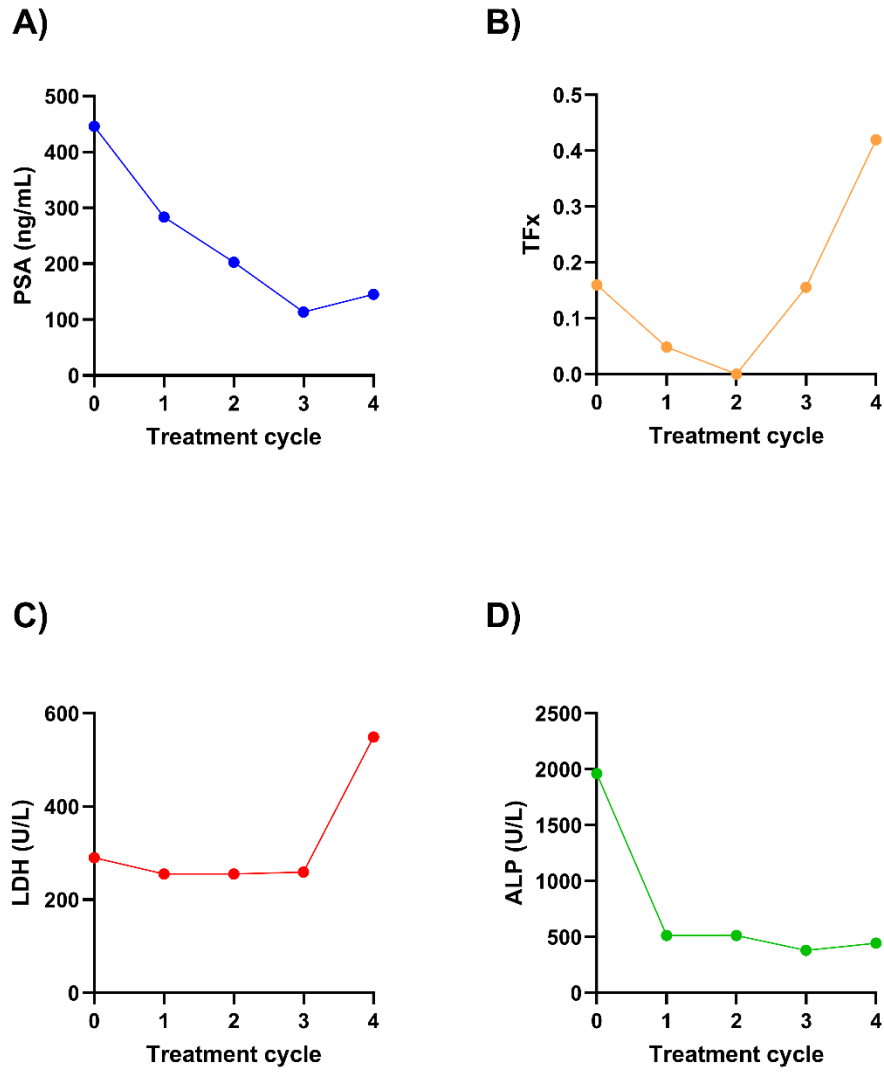


**Figure 56:** Comprehensive overview of the dynamic changes in A) PSA, B) TFx, C) LDH and D) ALP in Patient 38, following with  $[^{225}\text{Ac}]\text{Ac}/[^{177}\text{Lu}]\text{Lu-PSMA-617}$  regimen. Data points are plotted over the treatment period, providing insights into the therapeutic response and disease progression.

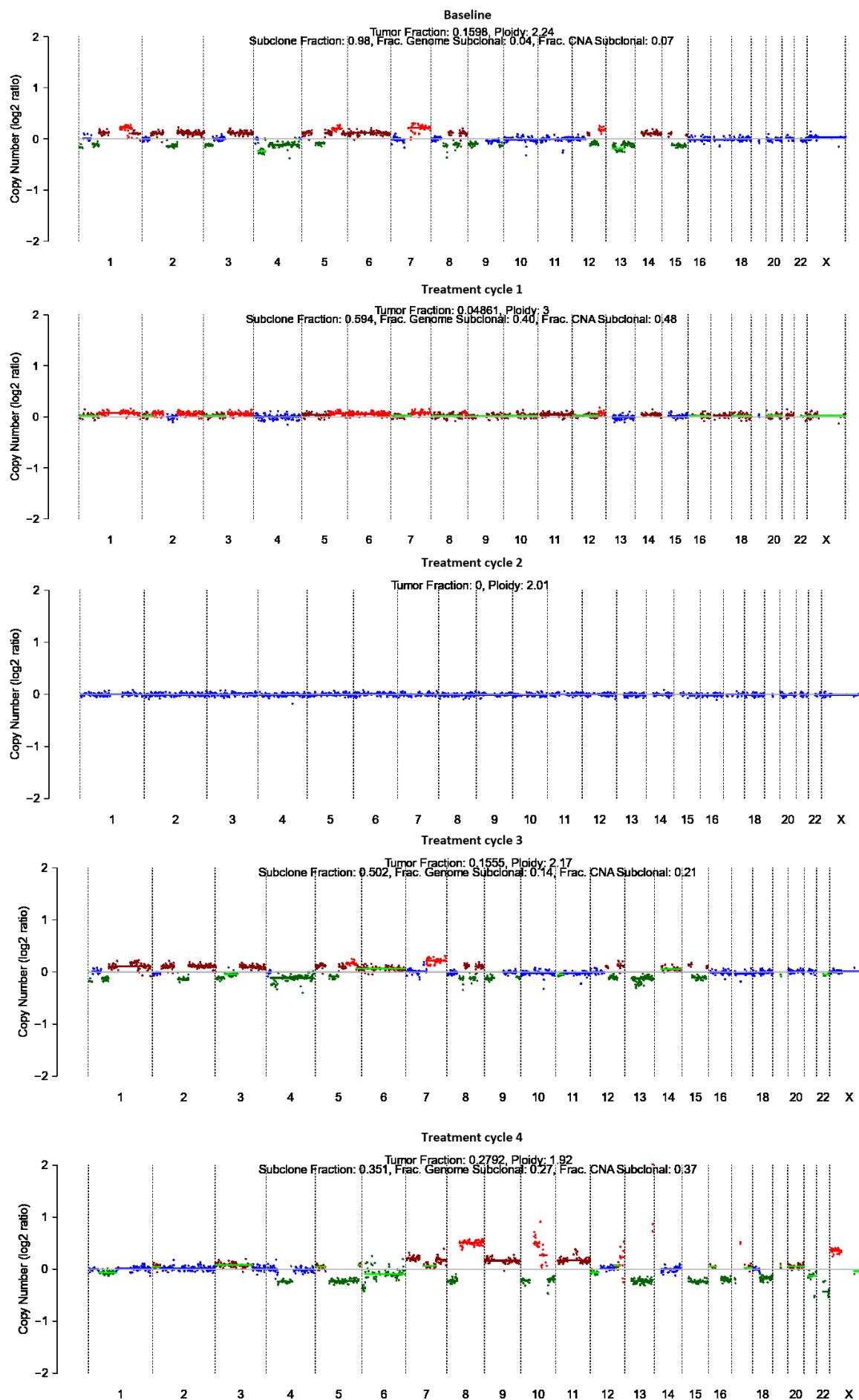


**Figure 57:** CNA profiles for Patient 38 across four treatment timepoints. Each panel represents a distinct timepoint, starting with the baseline (pre-treatment) followed by sequential post-treatment cycles. CNV profiles are depicted as log2 copy number ratios plotted against genomic coordinates.

**Table 9:** Longitudinal assessment of GFR-CKD-EPI, creatinine, hemoglobin and leukocyte count during [<sup>225</sup>Ac]Ac-/[<sup>177</sup>Lu]Lu-PSMA-617 of Patient 38.

Time point	GFR-CKD-EPI (mL/min/1.73qm)	Creatinine (mg/dL)	Hemoglobin (g/dL)	Leukocyte (G/nL)
Baseline	92.0	0.73	9.8	5.5
1 <sup>st</sup> treatment cycle	89.5	0.78	10.1	3.8
2 <sup>nd</sup> treatment cycle	89.4	0.77	10.1	3.9
3 <sup>rd</sup> treatment cycle	84.6	0.88	9.5	3.9
4 <sup>th</sup> treatment cycle	79.5	0.94	8.7	4.3

GFR-CKD-EPI: Glomerular Filtration Rate estimated using the Chronic Kidney Disease Epidemiology Collaboration (CKD-EPI) equation, expressed in mL/min/1.73 m<sup>2</sup>.



10.4 Patient 37

Patient 37 started the therapy with high bone marrow infiltration as shown in Figure 58. Initially, the patient presented with a PSA level of 2586 ng/mL at the baseline. Following the first cycle of PSMA-TRNT, a significant PSA decline to 202 ng/mL was observed, indicating an initial therapeutic response (Figure 59A). The downward trend continued, reaching 84.1 ng/mL after the second cycle and 78.8 ng/mL after the third cycle. However, by the fourth cycle, PSA levels exhibited an increase to 348 ng/mL, suggesting a relapse. Tfx reflects the same kinetics. The initial Tfx value of 0.55 at baseline dropped to below detection levels <0 Tfx after the first cycle and remained undetectable across subsequent cycles. However, during the fourth cycle, Tfx increased to 0.13, further supporting the observation of disease relapse (Figure 59B). The CNV profile of the last cycle as we can observe, reflects the profile of the baseline profile (Figure 60). LDH and ALP levels, which serve as surrogate markers for tumor activity and bone turnover, showed corresponding trends (Figure 59C, Figure 59D). Patient’s white blood cell counts remained stable along with renal function (Table 10).

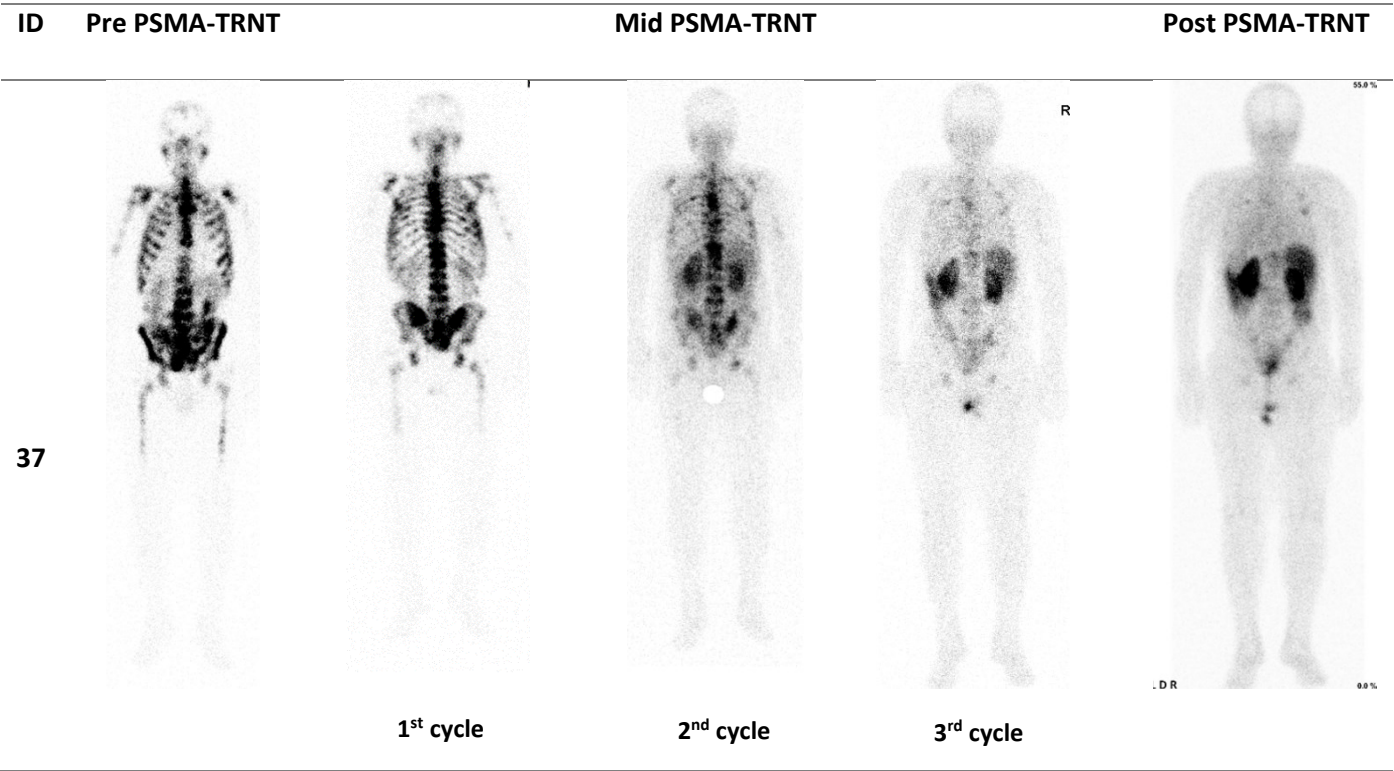


**Figure 58:** Imaging overview of Patient 37 treated with  $[^{225}\text{Ac}]\text{Ac-}/[^{177}\text{Lu}]\text{Lu-PSMA-617}$ . Baseline and post-treatment SPECT imaging were performed using  $[^{99\text{m}}\text{Tc}]\text{Tc-PSMA-GCK01}$  to assess initial disease burden and therapeutic response, respectively. Mid-treatment assessment refers to therapy-related scans conducted during the PSMA-TRNT course.

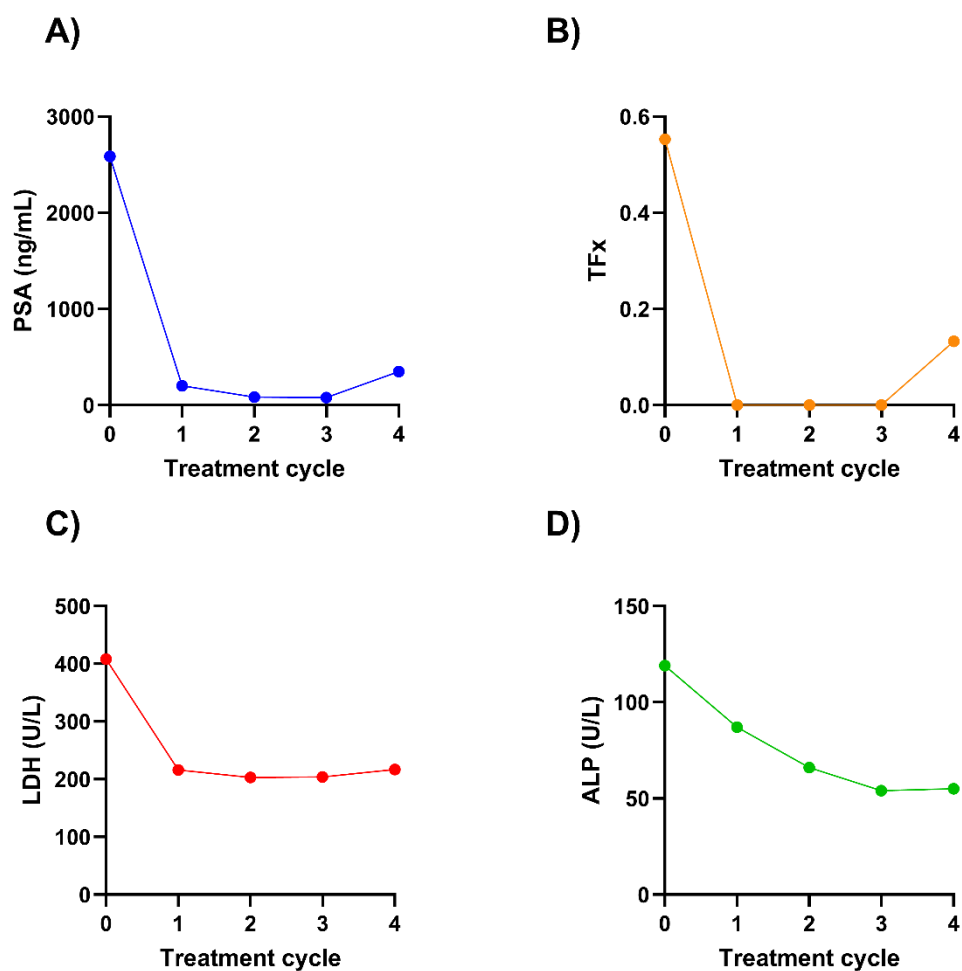


**Figure 59:** Comprehensive overview over the dynamic changes in A) PSA, B) TFx, C) LDH and D) ALP in Patient 37, following  $[^{225}\text{Ac}]\text{Ac-}/[^{177}\text{Lu}]\text{Lu-PSMA-617}$  regimen. Data points are plotted over the treatment period, providing insights into disease progression.

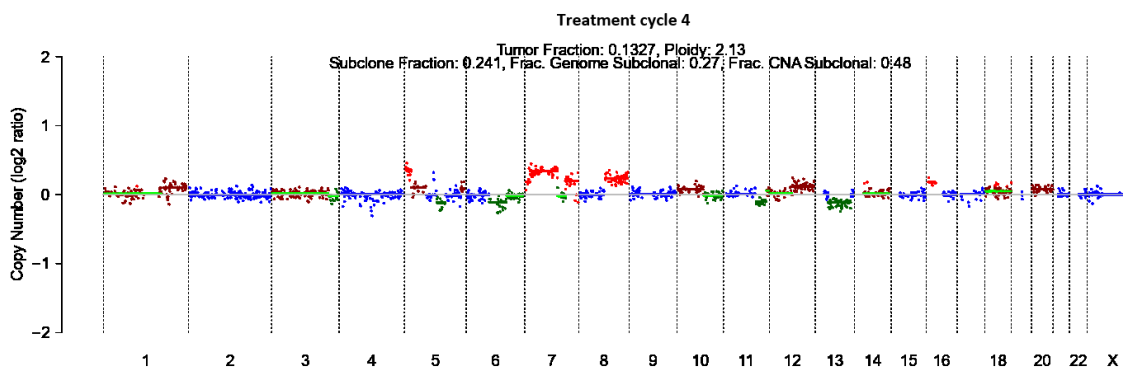
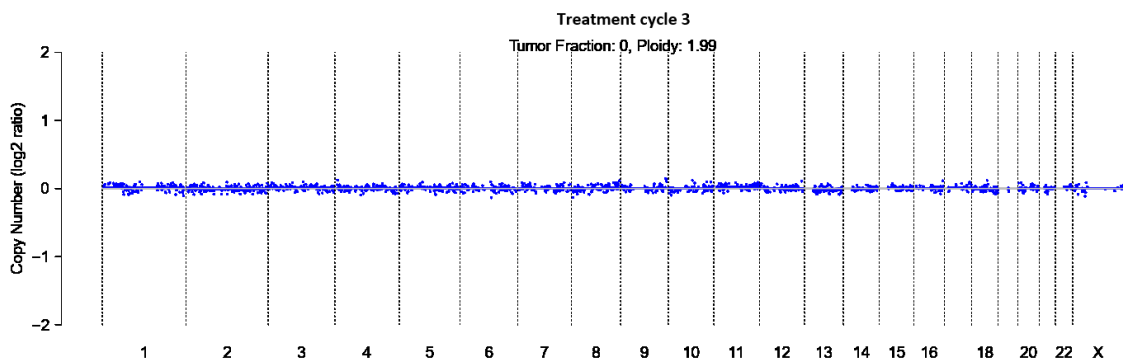
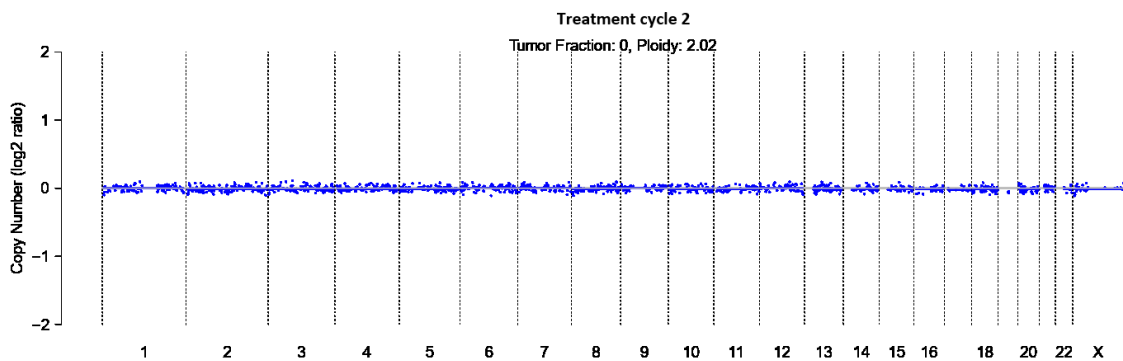
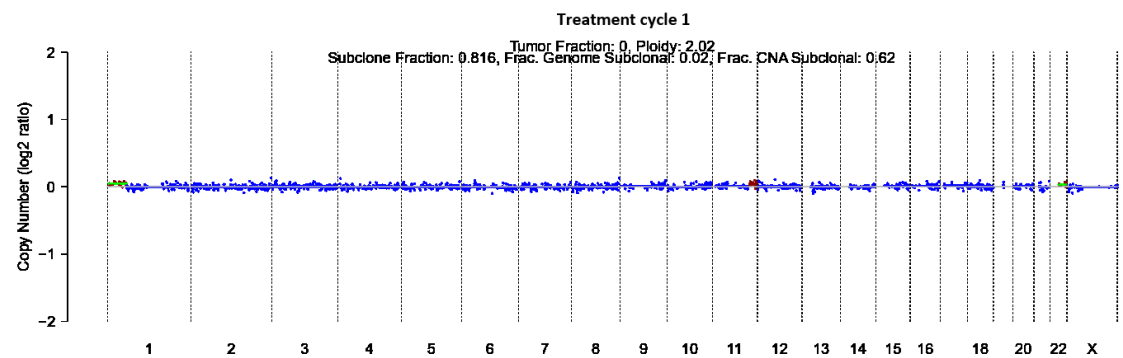
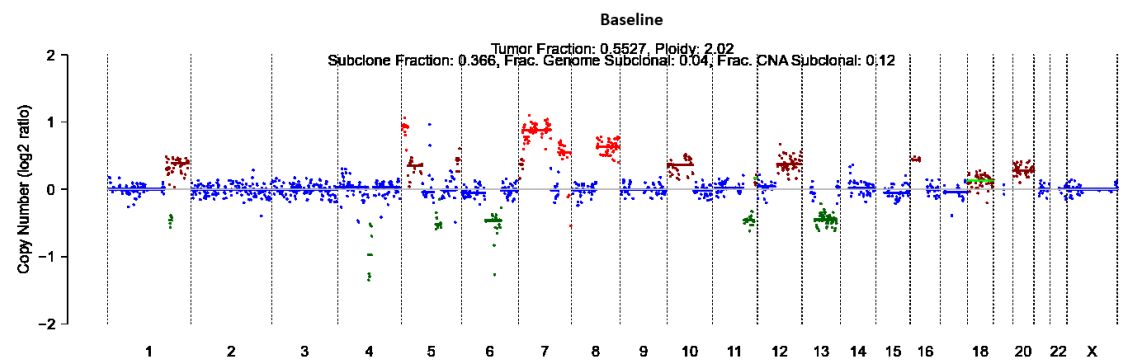


**Figure 60:** CNA profiles for Patient 37 across four treatment timepoints. Each panel represents a distinct timepoint, starting with the baseline (pre-treatment) followed by sequential post-treatment cycles. CNV profiles are depicted as log2 copy number ratios plotted against genomic coordinates.

**Table 10:** Longitudinal assessment of GFR-CKD-EPI, creatinine, hemoglobin and leukocyte count during [<sup>225</sup>Ac]Ac-/[<sup>177</sup>Lu]Lu-PSMA-617 of Patient 37.

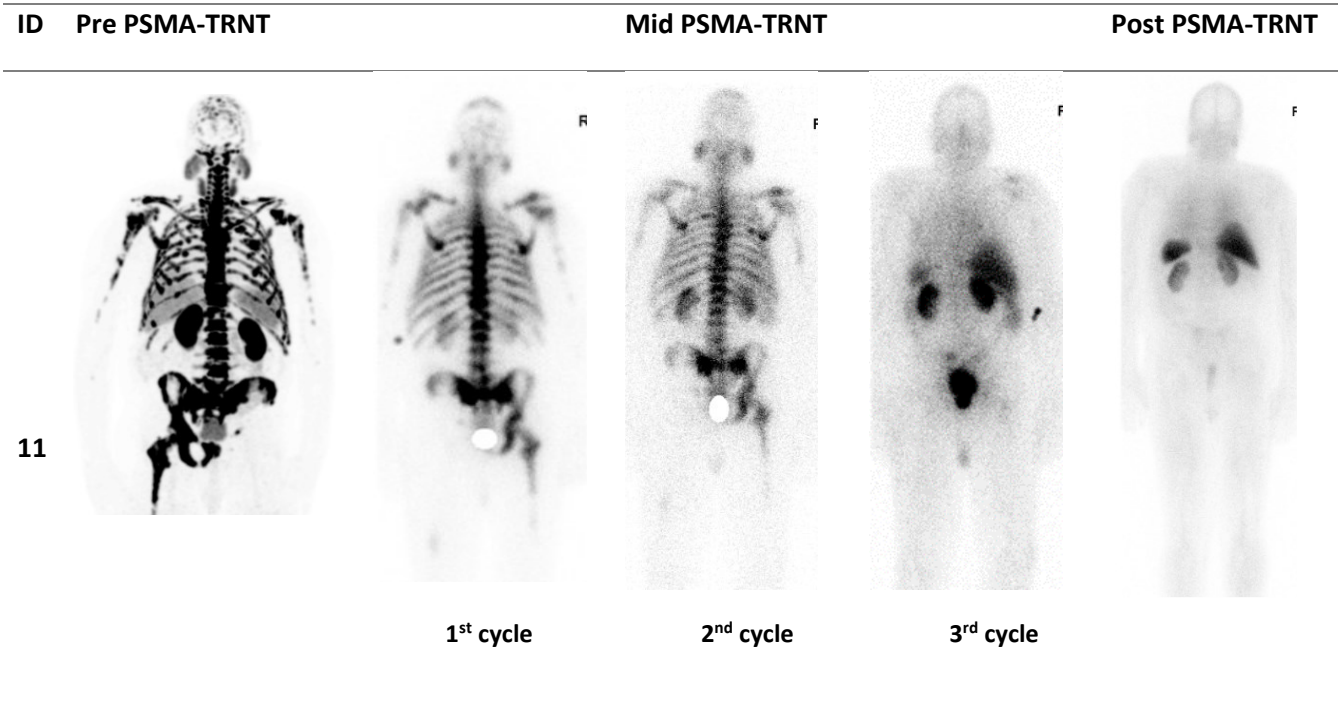
Time point	GFR-CKD-EPI (mL/min/1.73qm)	Creatinine (mg/dL)	Hemoglobin (g/dL)	Leukocyte (G/nL)
Baseline	70.7	1.0	9.6	3.5
1 <sup>st</sup> treatment cycle	64.4	1.1	11.2	5.9
2 <sup>nd</sup> treatment cycle	84.2	0.89	11.1	3.3
3 <sup>rd</sup> treatment cycle	83.6	0.89	9.7	3.0
4 <sup>th</sup> treatment cycle	83.6	0.89	9.6	3.5

GFR-CKD-EPI: Glomerular Filtration Rate estimated using the Chronic Kidney Disease Epidemiology Collaboration (CKD-EPI) equation, expressed in mL/min/1.73 m<sup>2</sup>.

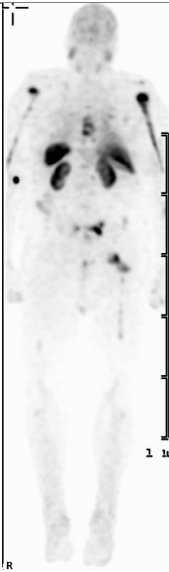
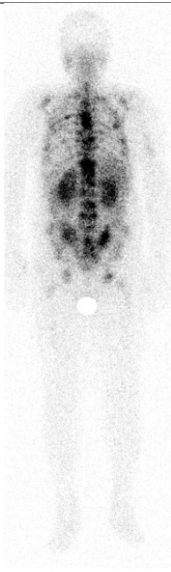
## 10.5 Patient 11

Patient 11 underwent a [<sup>68</sup>Ga]Ga-PSMA-11 PET/CT scan, which revealed extensive skeletal and nodal metastases, indicating a high tumor burden (Figure 61). At baseline, PSA was 584 ng/mL, and Tfx was 0.39. With the initiation of PSMA-RLT, these values demonstrated a marked reduction. Following the first treatment cycle, PSA decreased to 99.4 ng/mL, while Tfx dropped to 0.05. This trend continued through the second cycle, with PSA declining further to 28.2 ng/mL and Tfx becoming undetectable. By the third cycle, PSA reached its nadir at 1.7 ng/mL, and Tfx remained below the detection limit (Figure 63A, Figure 63B). LDH followed a kinetic pattern similar to that of Tfx and PSA, showing a consistent decline during the first three cycles. In contrast, AP exhibited a progressive increase throughout the initial three cycles before decreasing at the onset of clinical relapse (Figure 63C, Figure 63D). Imaging performed after therapy confirmed the therapeutic response. However, a follow-up scan conducted five months post-treatment revealed new metastatic lesions, indicating emerging resistance (Figure 62). By the fourth cycle, PSA had risen sharply to 546 ng/mL, and Tfx increased to

0.47, signifying disease relapse. Consistent CNA profiles were observed throughout the treatment, with the fourth cycle revealing distinct new amplifications and deletions in the genome (Figure 64). Hematological and renal function markers demonstrated impairment throughout the course of treatment (Table 11), with hemoglobin levels falling below the normal range and renal function remaining compromised.



**Figure 61:** Imaging overview of Patient 11 treated with  $[^{225}\text{Ac}]\text{Ac-}/[^{177}\text{Lu}]\text{Lu-PSMA-617}$  therapy. Pre-therapy staging was performed using  $[^{68}\text{Ga}]\text{Ga-PSMA-11}$  PET imaging. Mid-treatment assessment refers to therapy-related scans acquired during the PSMA-TRNT course. Post-therapy response evaluation was conducted using PSMA-SPECT with  $[^{99\text{m}}\text{Tc}]\text{Tc-PSMA-GCK01}$ .

ID	Pre PSMA-TRNT	Mid PSMA-TRNT
11		
		4 <sup>th</sup> cycle

**Figure 62:** Imaging five months staging post-PSMA-RLT in Patient 11 treated with PSMA-TRNT using PSMA-SPECT using [ $^{99m}\text{Tc}$ ]Tc-PSMA-GCK01, followed by treatment scan upon 4<sup>th</sup> treatment administration.

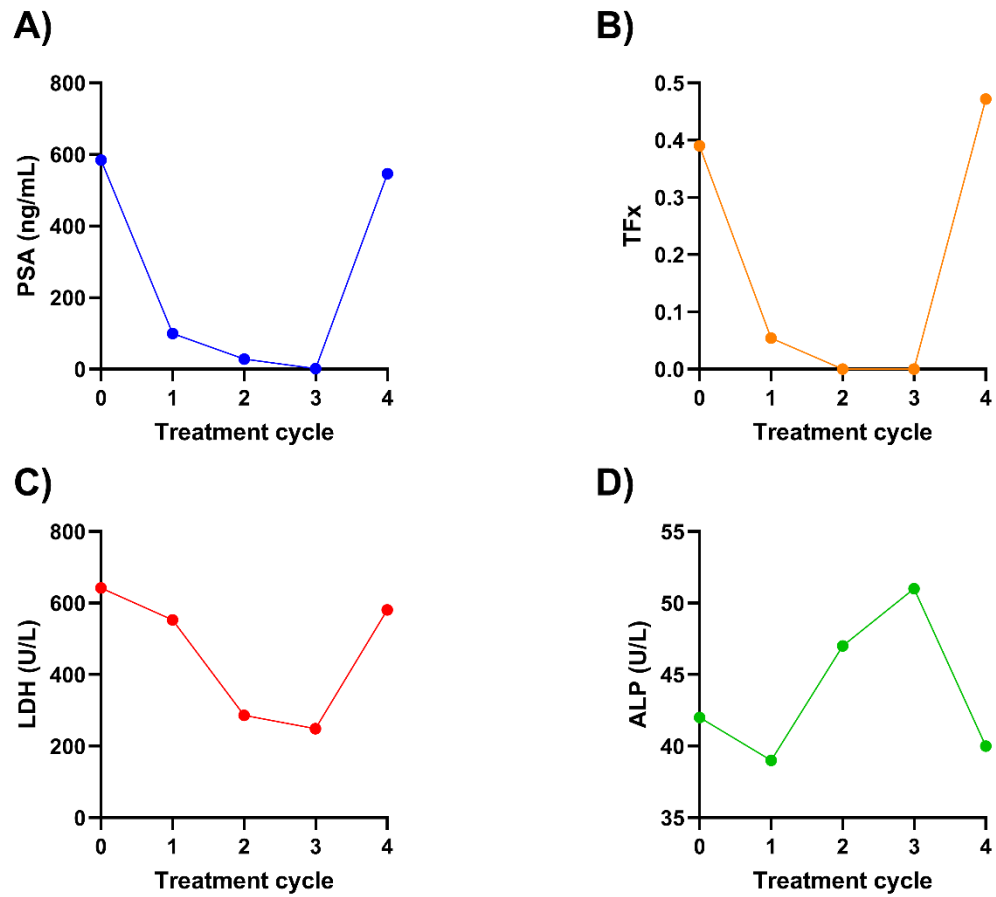


**Figure 63:** Comprehensive overview over the dynamic changes in A) PSA, B) Tfx, C) LDH and D) ALP in Patient 11, following  $[^{225}\text{Ac}]\text{Ac}/[^{177}\text{Lu}]\text{Lu-PSMA-617}$  regimen. Data points are plotted over the treatment period, providing insights into disease progression.

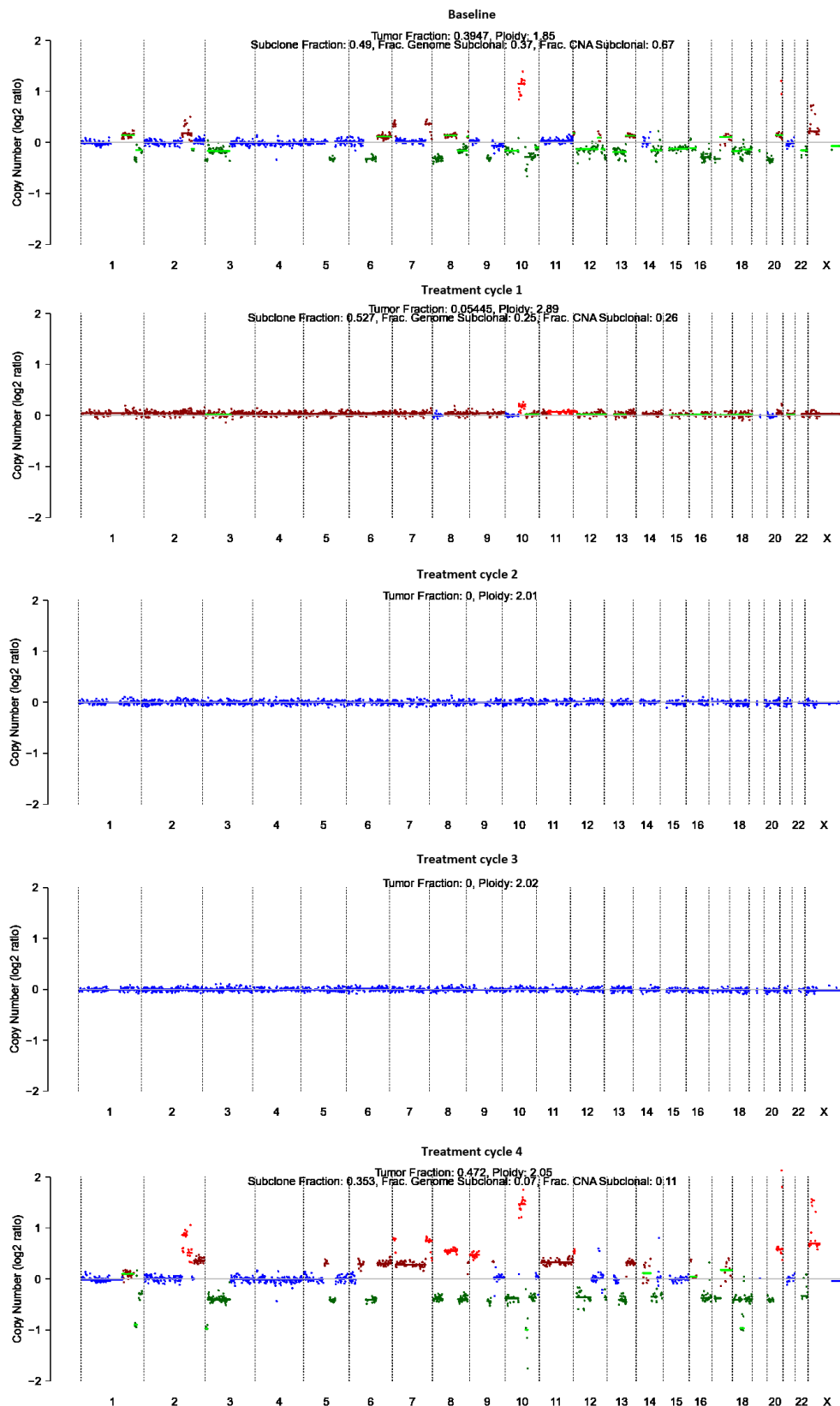


**Figure 64:** CNA profiles for Patient 11 across four treatment timepoints. Each panel represents a distinct timepoint, starting with the baseline (pre-treatment) followed by sequential post-treatment cycles. CNV profiles are depicted as log2 copy number ratios plotted against genomic coordinates.





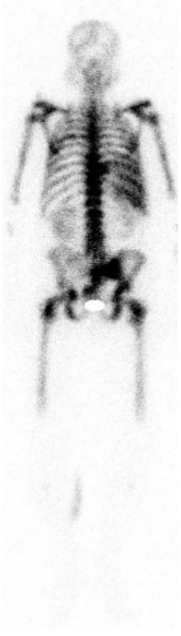
**Table 11:** Longitudinal assessment of GFR -CKD-EPI, creatinine, hemoglobin and leukocyte count during [<sup>225</sup>Ac]Ac-/ [<sup>177</sup>Lu]Lu-PSMA-617 of Patient 11.

Time point	GFR-CKD-EPI (mL/min/1.73qm)	Creatinine (mg/dL)	Hemoglobin (g/dL)	Leukocyte (G/nL)
Baseline	70.6	1.0	10.4	5.9
1 <sup>st</sup> treatment cycle	84.6	0.93	9.2	3.6
2 <sup>nd</sup> treatment cycle	74.8	1.0	9.4	4.9
3 <sup>rd</sup> treatment cycle	79.5	0.98	10.1	6.2
4 <sup>th</sup> treatment cycle	65.0	1.1	11.2	4.4

GFR-CKD-EPI: Glomerular Filtration Rate estimated using the Chronic Kidney Disease Epidemiology Collaboration (CKD-EPI) equation, expressed in mL/min/1.73 m<sup>2</sup>.

10.6 Patient 34

Patient 34, classified as a non-responder, presented with widespread liver and bone marrow lesions identified on a pre-treatment PSMA-SPECT scan using [<sup>99m</sup>Tc]Tc-PSMA-GCK01 (Figure 65). Actinium-lutetium therapy initially reduced PSA levels from 279 ng/mL to 174 ng/mL after the first cycle (Figure 66A). However, by the second cycle, PSA levels rose sharply to 1367 ng/mL, indicating rapid disease progression. Tfx decreased from 0.68 to 0.48 after the first cycle but increased significantly to 0.82 by the second cycle (Figure 66B). The constant tumor burden was also observed due to the consistent CNA detected at each cycle (Figure 67). While the patient’s white blood cell counts remained stable, renal function deteriorated significantly, marked by a sudden rise in creatinine levels and a corresponding drop in GFR, consistent with acute renal impairment (Table 12). Post-therapy imaging is not available.

ID	Pre PSMA-TRNT	Mid PSMA-TRNT	Post PSMA-TRNT
34			NA
			
		1 <sup>st</sup> cycle	2 <sup>nd</sup> cycle

**Figure 65:** Imaging overview of Patient 34 treated with [<sup>225</sup>Ac]Ac-/[<sup>177</sup>Lu]Lu-PSMA-617. Baseline SPECT imaging were performed using [<sup>99m</sup>Tc]Tc-PSMA-GCK01 to assess initial disease burden. Mid-treatment assessment refers to therapy-related scans conducted during the PSMA-TRNT course. Post PSMA-TRNT imaging are not available.

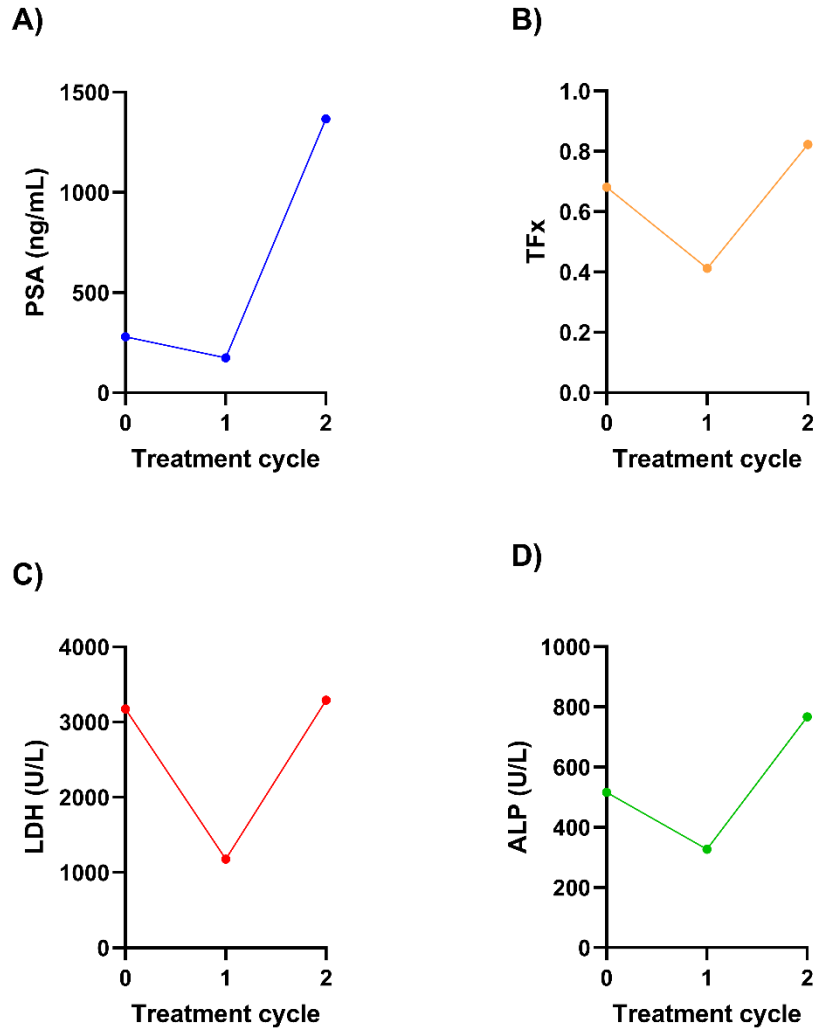


**Figure 66:** Comprehensive overview over the dynamic changes in A) PSA, B) TFx, C) LDH and D) ALP in Patient 34, following  $[^{225}\text{Ac}]\text{Ac-}/[^{177}\text{Lu}]\text{Lu-PSMA-617}$  regimen. Data points are plotted over the treatment period, providing insights into disease progression.

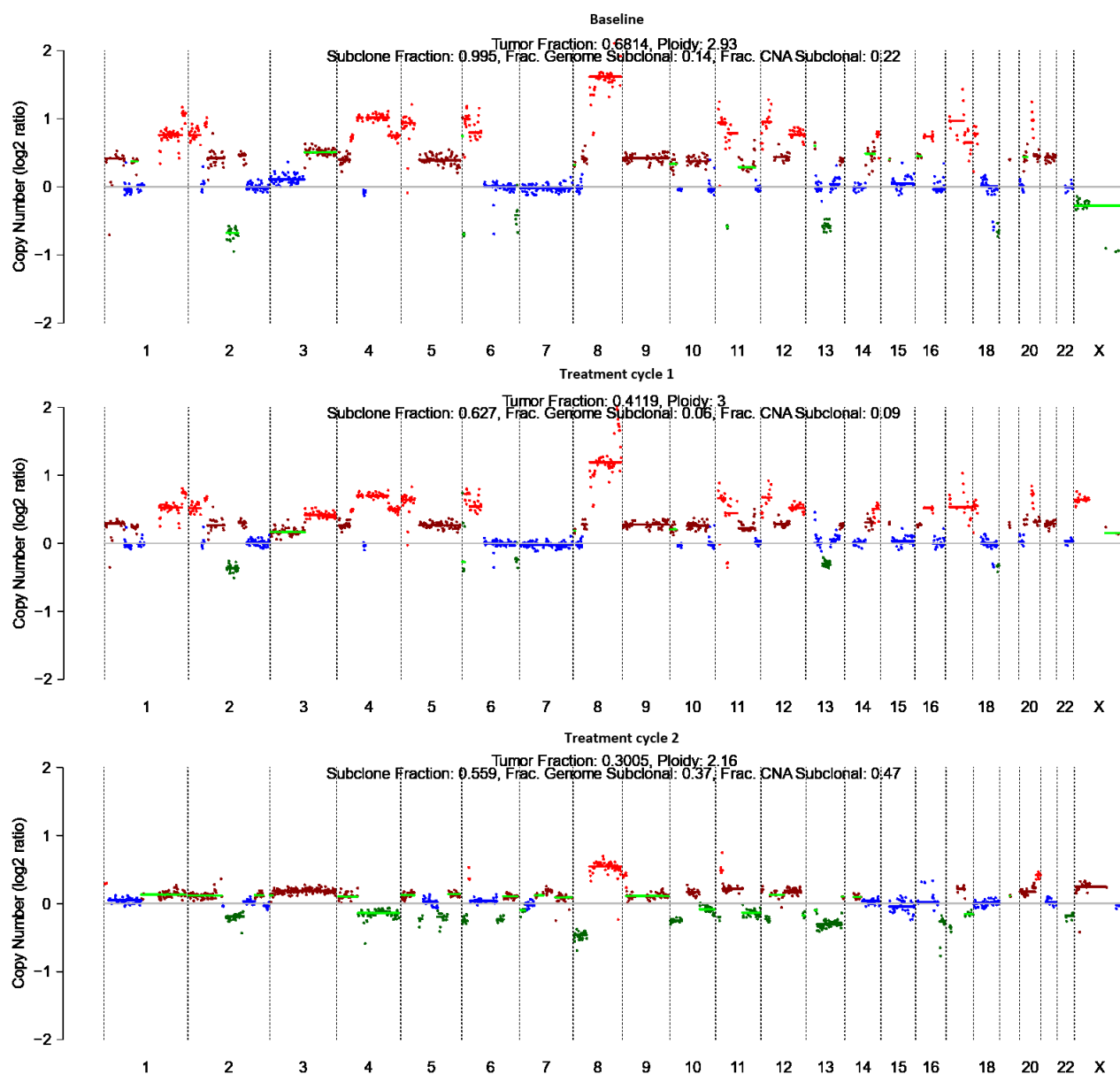


**Figure 67:** CNA profiles for Patient 34 across four treatment timepoints. Each panel represents a distinct timepoint, starting with the baseline (pre-treatment) followed by sequential post-treatment cycles. CNV profiles are depicted as log2 copy number ratios plotted against genomic coordinates.




**Table 12:** Longitudinal assessment of GFR-CKD-EPI, creatinine, hemoglobin and leukocyte count during [<sup>225</sup>Ac]Ac-/[<sup>177</sup>Lu]Lu-PSMA-617 of Patient 34.

Time point	GFR-CKD-EPI (mL/min/1.73qm)	Creatinine (mg/dL)	Hemoglobin (g/dL)	Leukocyte (G/nL)
<b>Baseline</b>	87.6	0.92	7.2	6.4
<b>1<sup>st</sup> treatment cycle</b>	95.9	0.77	7.9	4.3
<b>2<sup>nd</sup> treatment cycle</b>	15.3	3.8	10.1	5.2

*GFR-CKD-EPI: Glomerular Filtration Rate estimated using the Chronic Kidney Disease Epidemiology Collaboration (CKD-EPI) equation, expressed in mL/min/1.73 m<sup>2</sup>.*

## 10.7 Patient 40

Upon therapy initiation, Patient 40 underwent an [<sup>18</sup>F]F-PSMA-1007 PET/CT scan, which revealed extensive metastatic disease involving skeletal, nodal, and visceral sites (Figure 68). Baseline biomarker assessments showed a PSA level of 560 ng/mL, Tfx at 0.26, LDH at 582 U/L, and ALP at 56 U/L. Following the first treatment cycle, Tfx decreased to 0.15, suggesting an initial therapeutic response, despite a slight increase in PSA to 607 ng/mL. Concurrently, LDH declined to 441 U/L, whereas ALP increased to 66 U/L. However, after the second treatment cycle, Tfx sharply increased to 0.44, accompanied by a dramatic PSA surge to 1172 ng/mL (Figure 69A, Figure 69B). LDH levels exhibited a modest increase to 447 U/L, while ALP remained elevated at 65 U/L (Figure 69C, Figure 69D). Imaging findings correlated with these biomarker trends. The initial [<sup>18</sup>F]F-PSMA-1007 PET/CT scan at baseline revealed widespread metastatic lesions with high PSMA tracer uptake. Following the first treatment cycle, PSMA uptake remained stable in skeletal lesions, reflecting the partial metabolic response observed in biomarker kinetics. To further support these findings, CT scans (Figure 70) performed during treatment confirmed the progressive disease status. Regarding CNA profiles, despite a relatively stable tumor fraction, genomic amplification patterns were detected. After the first treatment cycle, while Tfx showed a slight decrease, the genomic profile revealed new amplifications, suggesting the emergence of tumor heterogeneity. By the second cycle, as Tfx and PSA levels increased, genomic amplifications persisted and expanded, providing further evidence of disease progression and emerging resistance (Figure 71). Renal function remained stable, while hemoglobin and leukocyte counts fell below normal range (Table 13).

ID	Pre PSMA-TRNT	Mid PSMA-TRNT		Post PSMA-TRNT
40				NA
		1 <sup>st</sup> cycle	2 <sup>nd</sup> cycle	

**Figure 68:** Imaging overview of Patient 40 treated with  $[^{225}\text{Ac}]\text{Ac}-/[^{177}\text{Lu}]\text{Lu-PSMA-617}$ . Pre-therapy staging was performed using  $[^{18}\text{F}]\text{F-PSMA-1007}$  PET imaging. Mid-treatment assessment refers to therapy-related scans acquired during PSMA-TRNT course. Post-therapy imaging is not available due to disease progression and early discontinuation of treatment.

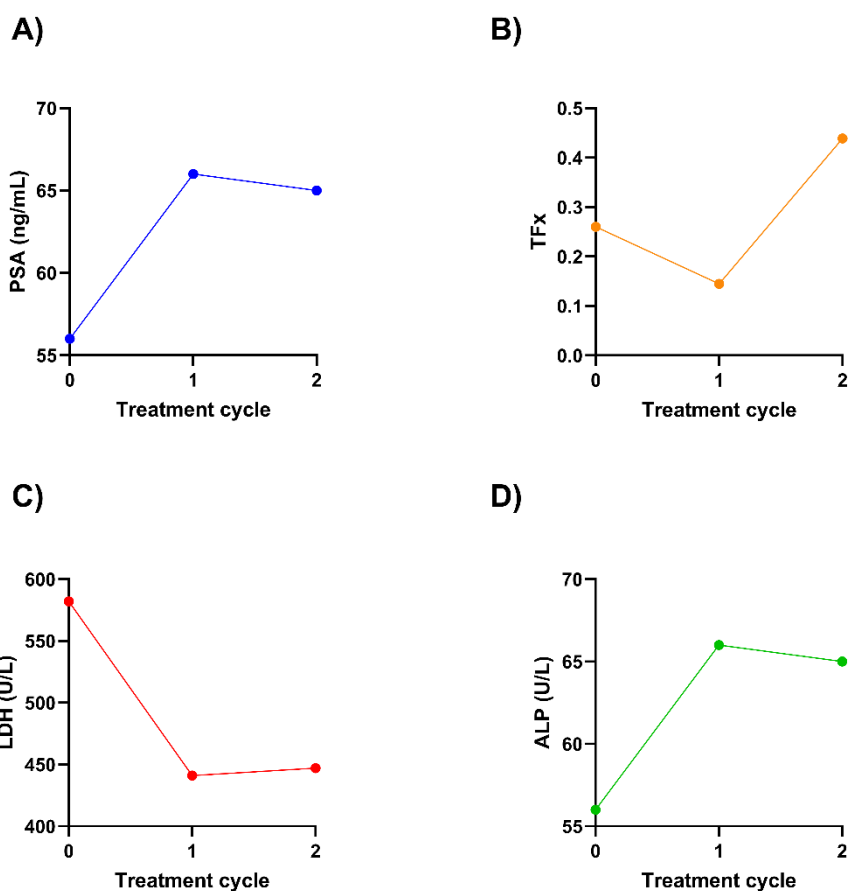


**Figure 69:** Comprehensive overview over the dynamic changes in A) PSA, B) Tfx, C) LDH and D) ALP in Patient 40, following  $[^{225}\text{Ac}]\text{Ac}/[^{177}\text{Lu}]\text{Lu-PSMA-617}$  regimen. Data points are plotted over the treatment period, providing insights into disease progression.

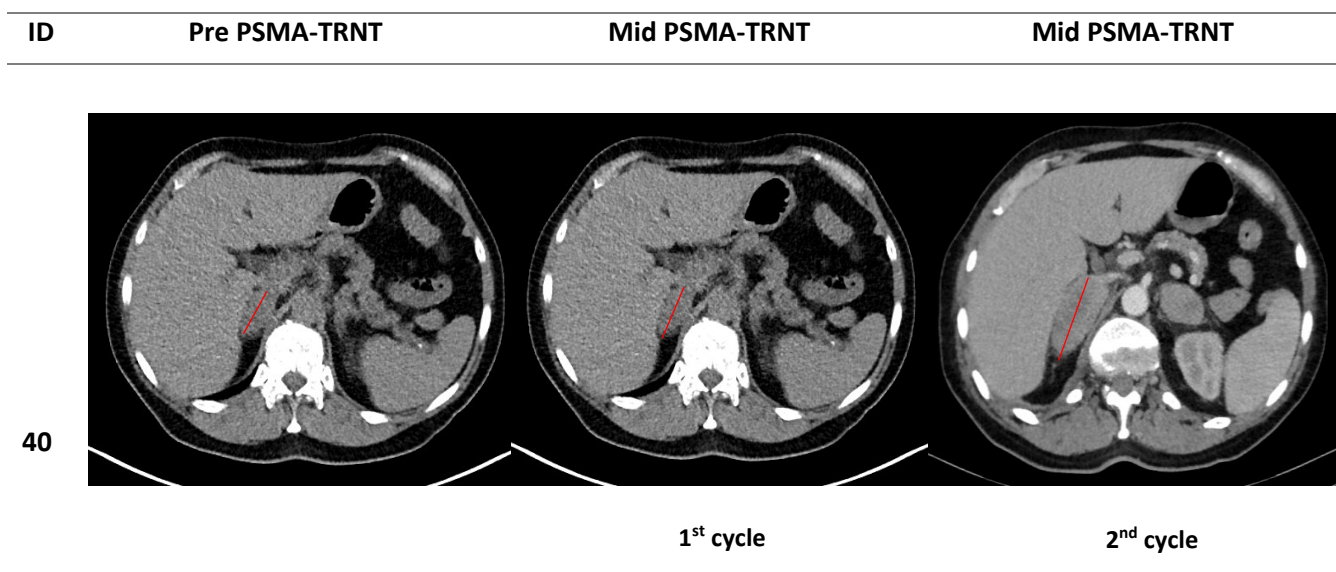


**Figure 70:** CT imaging overviews of Patient 40. Metastasis size throughout the PSMA-TRNT therapy course is indicated in red.

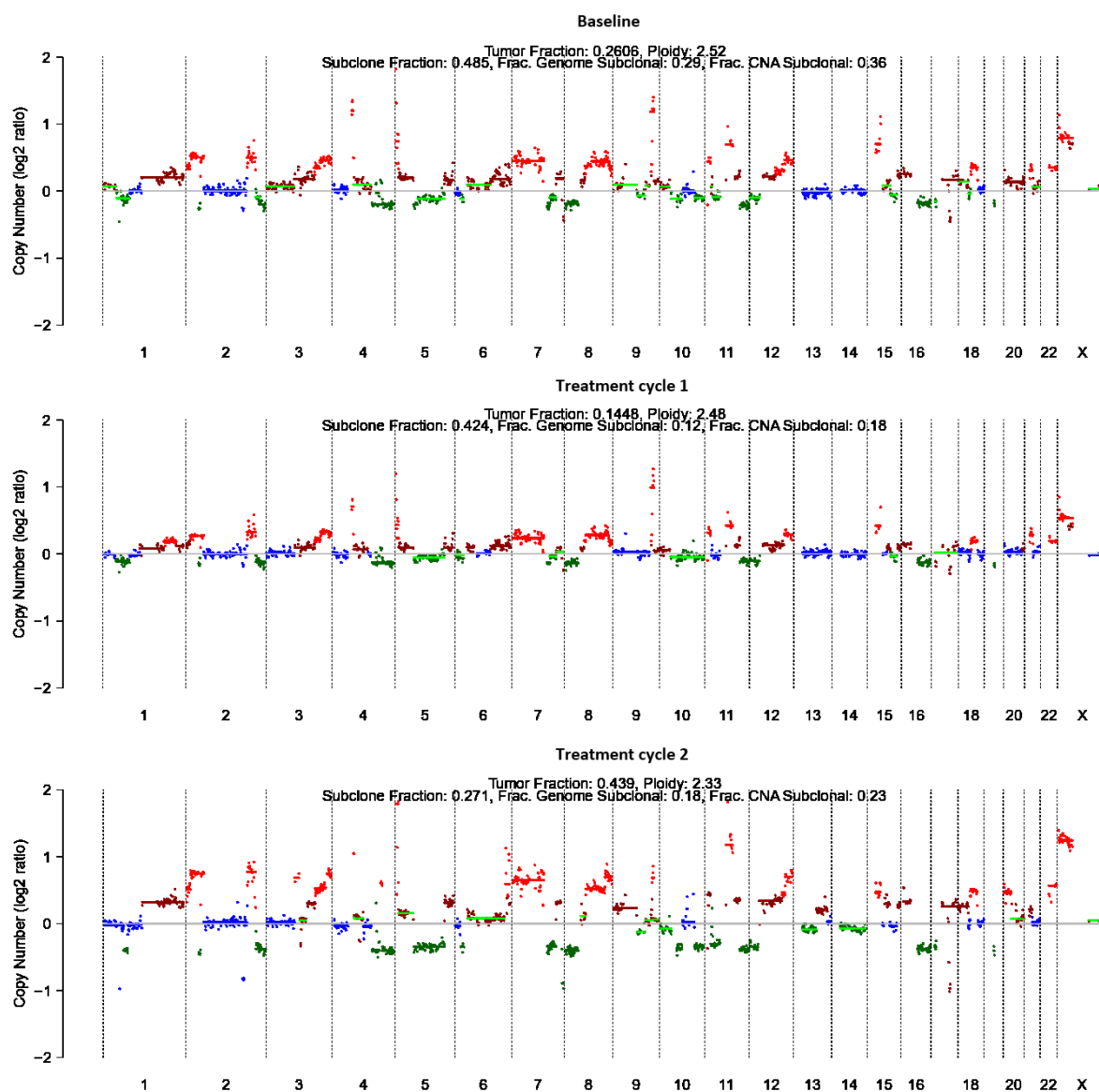


**Figure 71:** CNA profiles for Patient 40 across four treatment timepoints. Each panel represents a distinct timepoint, starting with the baseline (pre-treatment) followed by sequential post-treatment cycles. CNV profiles are depicted as log2 copy number ratios plotted against genomic coordinates.






**Table 13:** Longitudinal assessment of GFR-CKD-EPI, creatinine, hemoglobin and leukocyte count during [<sup>225</sup>Ac]Ac-/[<sup>177</sup>Lu]Lu-PSMA-617 of Patient 40.

Time point	GFR-CKD-EPI (mL/min/1.73qm)	Creatinine (mg/dL)	Haemoglobin (g/dL)	Leukocyte (G/nL)
Baseline	109	0.53	9.1	2.6
1 <sup>st</sup> treatment cycle	111	0.50	8.5	2.6
2 <sup>nd</sup> treatment cycle	104	0.59	8.8	2.7



*GFR-CKD-EPI: Glomerular Filtration Rate estimated using the Chronic Kidney Disease Epidemiology Collaboration (CKD-EPI) equation, expressed in mL/min/1.73 m<sup>2</sup>.*

## 10.8 Patient 91

Patient 91 underwent an [<sup>18</sup>F]-DCFPyL PET imaging, which revealed extensive skeletal disease with widespread metastases throughout the body (Figure 72). Baseline CT scans showed no evidence of liver metastases (Figure 73). At baseline, the patient exhibited a Tfx of 0.35 and PSA of 1399 ng/mL, indicating a high tumor burden. Following TRNT therapy initiation, biomarker levels initially declined during the first treatment cycle, suggesting a partial response. By the end of the first cycle, Tfx decreased to 0.08, and PSA to 949 ng/mL. However, in the subsequent cycle, Tfx sharply increased to 0.46, accompanied by a rise in PSA to 1060 ng/mL (Figure 74A, Figure 74B). A similar kinetic pattern was observed for LDH and ALP, with LDH spiking to 1358 U/L and ALP increasing to 847 U/L (Figure 74C, Figure 74D). Imaging findings further corroborated these biomarker trends. Despite the initial response observed after the first treatment cycle, persistent high bone metastasis involvement was noted in subsequent scans (Figure 72). By the second cycle, new liver metastases were detected, aligning with the marked increases in Tfx, PSA, and LDH, confirming disease progression (Figure 73). CNA profiling mirrored the Tfx kinetics, initially showing a reduction in amplifications and deletions after the first cycle. However, by the second cycle, the CNA profile reverted to the baseline pattern, underscoring the ongoing relapse and tumor progression (Figure 75). Renal function remained stable throughout the treatment cycles, while haematological markers declined, necessitating a transfusion during the final cycle (Table 14).

ID	Pre PSMA-TRNT	Mid PSMA-TRNT		Post PSMA-TRNT
91				NA
		1 <sup>st</sup> cycle	2 <sup>nd</sup> cycle	

**Figure 72:** Imaging of Patient 91 treated with  $[^{225}\text{Ac}]\text{Ac-}/[^{177}\text{Lu}]\text{Lu-PSMA-617}$ . Pre-therapy staging was performed using  $[^{18}\text{F}]\text{-DCFPyL}$  PET. Mid-treatment assessment refers to therapy-related scans acquired during PSMA-TRNT course. Post-therapy imaging is not available due to disease progression and early discontinuation of treatment.

ID	Mid PSMA-TRNT	
91		
	1 <sup>st</sup> cycle	2 <sup>nd</sup> cycle

**Figure 73:** Mid-therapy CT overviews of Patient 91, showing liver metastasis progression. The red arrow indicates newly developed liver metastases following the 2<sup>nd</sup> treatment cycle.

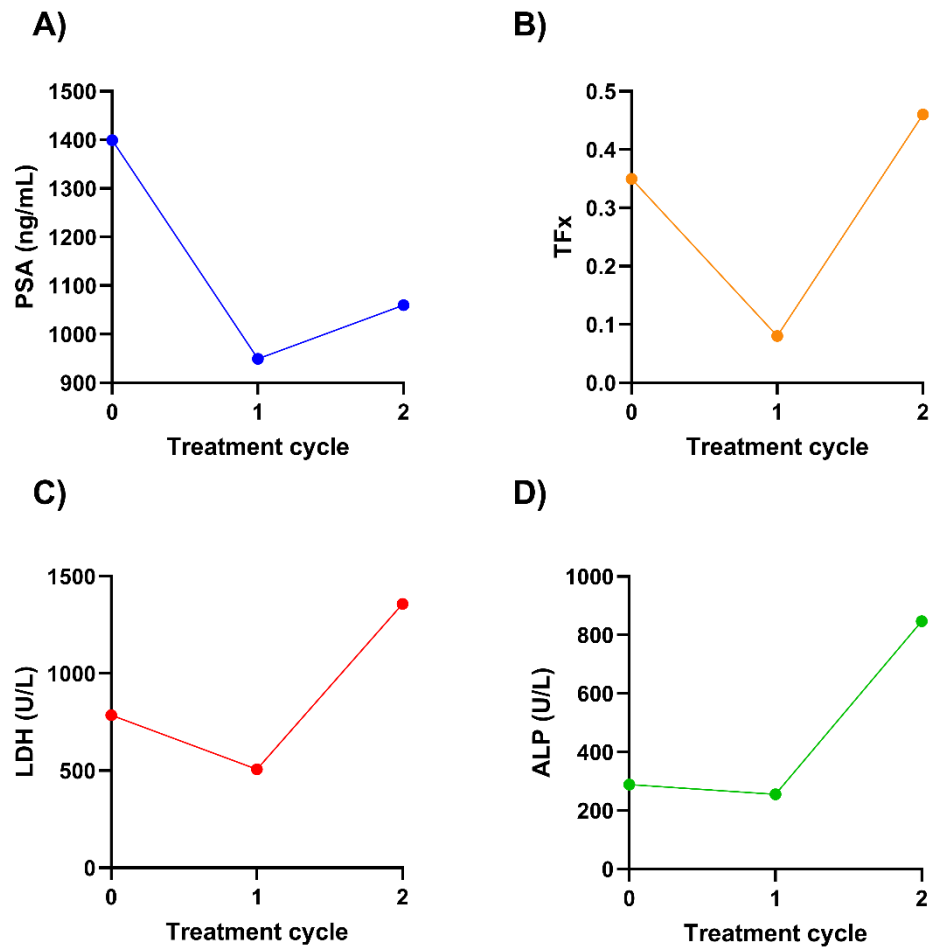


**Figure 74:** Comprehensive overview over the dynamic changes in A) PSA, B) TFx, C) LDH and D) ALP in Patient 91, following  $[^{225}\text{Ac}]\text{Ac-}/[^{177}\text{Lu}]\text{Lu-PSMA-617}$  regimen. Data points are plotted over the treatment period, providing insights into disease progression.

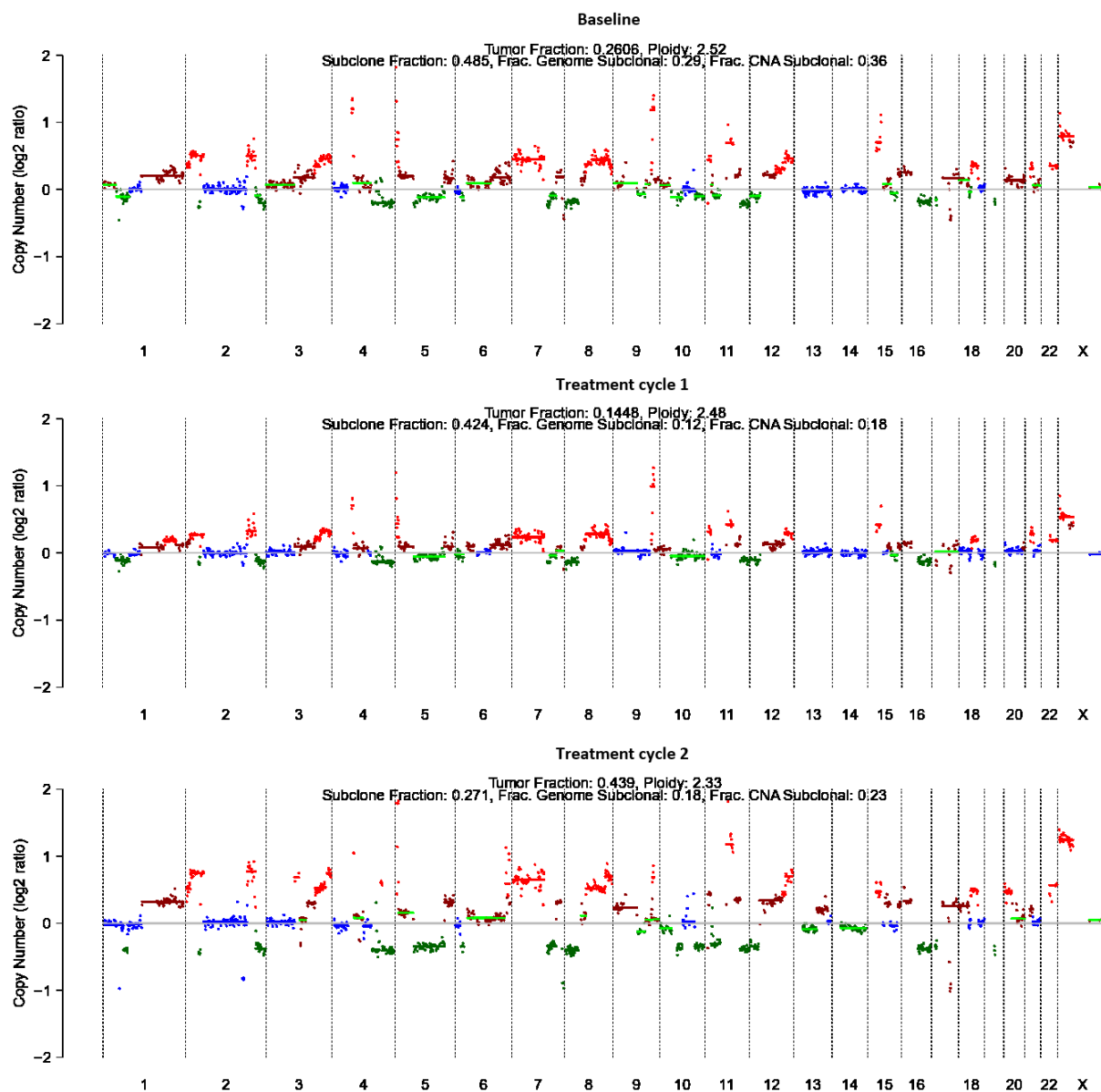


**Figure 75:** CNA profiles for Patient 91 across four treatment timepoints. Each panel represents a distinct timepoint, starting with the baseline (pre-treatment) followed by sequential post-treatment cycles. CNV profiles are depicted as log2 copy number ratios plotted against genomic coordinates.

**Table 14:** Longitudinal assessment of GFR-CKD-EPI, creatinine, hemoglobin and leukocyte count during [<sup>225</sup>Ac]Ac-/[<sup>177</sup>Lu]Lu-PSMA-617 of Patient 91.

Time point	GFR-CKD-EPI (mL/min/1.73qm)	Creatinine (mg/dL)	Hemoglobin (g/dL)	Leukocyte (G/nL)
Baseline	90.9	0.82	9.5	11.3
1 <sup>st</sup> treatment cycle	93.7	0.76	8.9	6.8
2 <sup>nd</sup> treatment cycle	103	0.61	9.5	6.9

GFR-CKD-EPI: Glomerular Filtration Rate estimated using the Chronic Kidney Disease Epidemiology Collaboration (CKD-EPI) equation, expressed in mL/min/1.73 m<sup>2</sup>.

## 11. CASE STUDIES: CHEMO-NAIVE PATIENTS

In this section, I describe the baseline genomic profiles of chemo-naïve patients, including tumor markers, hematological markers, and the whole genome profile of selected individuals. Most of these patients received only a single treatment and did not return for further follow-up. For those who did undergo additional treatment cycles, I included analysis from all available timepoints. Identifying genetic resistance signatures in patients who have undergone extensive chemotherapy is particularly challenging, as prior treatment disrupts cell division and induces DNA damage, leading to a high mutational burden that makes it difficult to isolate mutations specific to actinium-lutetium therapy. By utilizing ctDNA genomic profiles from chemo-naïve mCRPC patients, I aim to identify mutations that are present due to the advanced stage of the disease itself, rather than being induced or influenced by prior chemotherapy. This approach allows me to distinguish genetic alterations that are intrinsic to disease progression and potentially linked to resistance to TRNT, providing a clearer view of the molecular landscape in untreated metastatic prostate cancer and helping to refine therapeutic strategies. Table 15 and Table 16 describes the initial diagnosis status and the clinical history of each patient.

**Table 15:** Initial diagnosis status of the chemo naïve patient.

Patient #	iDiagnosis	iGS	iPSA (ng/mL)	iTumor Status
Patient 25	2011	7(3+4)	NA	cT3b cN0 M0 G3
Patient 60	2008	9	40	pT3a pN1(4/20) cM0 L1 V1
Patient 95	1996	NA	NA	NA
Patient 96	2011	7b	6.4	pT3a pN0 cM0
Patient 23	2016	7b(4+3)	7.4	T1c N0 M0 G3

*iDiagnosis: initial diagnosis, iGS: initial Gleason score, a/b in GS: Used to differentiate between Gleason patterns within the same score, iPSA: initial PSA, iTumor status: initial tumor status. T (Tumor): Size and extent of the primary tumor, N (Nodes): Indicates whether cancer has spread to regional lymph nodes, M (Metastasis): Indicates whether cancer has spread to distant organs, R (Resection Margin): Indicates whether cancer cells are present at the surgical margin after tumor removal, L: Lymphatic invasion, V: Vascular invasion, G: Tumor Grade, NA: Not Available.*


**Table 16:** Pre-treatments status of the chemo naïve patients.

Patient #	Hormonal therapy	Surgery	Metastasis	Radiation	Pre PSMA-TRNT
<b>Patient 25</b>	ADT, Enzalutamide	NA	OSS, LYM	External radiation	NA
<b>Patient 60</b>	ADT	Radical prostatectomy lymphadectomy	OSS, HEP, LYM	NA	NA
<b>Patient 95</b>	ADT, Enzalutamide	NA	OSS	Seeds implantation	Xofigo
<b>Patient 96</b>	ADT, Abiraterone, Apalutamide	Radical prostatectomy lymphadectomy	OSS, HEP, LYM	External radiation	Lutetium-177
<b>Patient 23</b>	ADT, Abiraterone, Bicalutamide	NA	OSS, LYM	External radiation	NA

*ADT: Androgen Deprivation Therapy, NA: Not Applied, OSS (Osseous): Bones, HEP (Hepatic): Liver, LYM (Lymphatic): Lymph nodes.*

## 11.1 Patient 25

At baseline, the patient exhibited significantly elevated tumor markers, such as PSA with a value of 1701 ng/mL, Tfx with 0.79, LDH at 473 U/L and AP with 426 U/L (Table 17). These values reflect a substantial tumor burden, active tissue turnover, and extensive metastatic disease, including osseous involvement as shown in Figure 76. The CNA profile showed total amplifications of chromosomes 7 and 8, along with partial amplification of chromosome 1p (Figure 77). Deletions were also detected in chromosomes 5, 6, 11, 13, 16, 18, and 20; however, these deletions were small and challenging to evaluate due to the low sequencing coverage. Renal function appears normal, and leukocyte count is within the expected range. However, haemoglobin is slightly below the reference value (Table 18).

ID	Pre PSMA-TRNT
25	

**Figure 76:** Imaging overview of Patient 25. Baseline staging was performed using [ $^{18}\text{F}$ ]PSMA-1007 PET imaging.



**Table 17:** Comprehensive overview of PSA, TFX, LDH and ALP in Patient 25, following [<sup>225</sup>Ac]Ac-/[<sup>177</sup>Lu]Lu-PSMA-617 regimen.

Tumor Markers	Baseline	Reference
PSA (ng/mL)	1701	<4
TFx	0.79	>0.10
LDH (U/L)	473	<342
ALP (U/L)	426	40–130

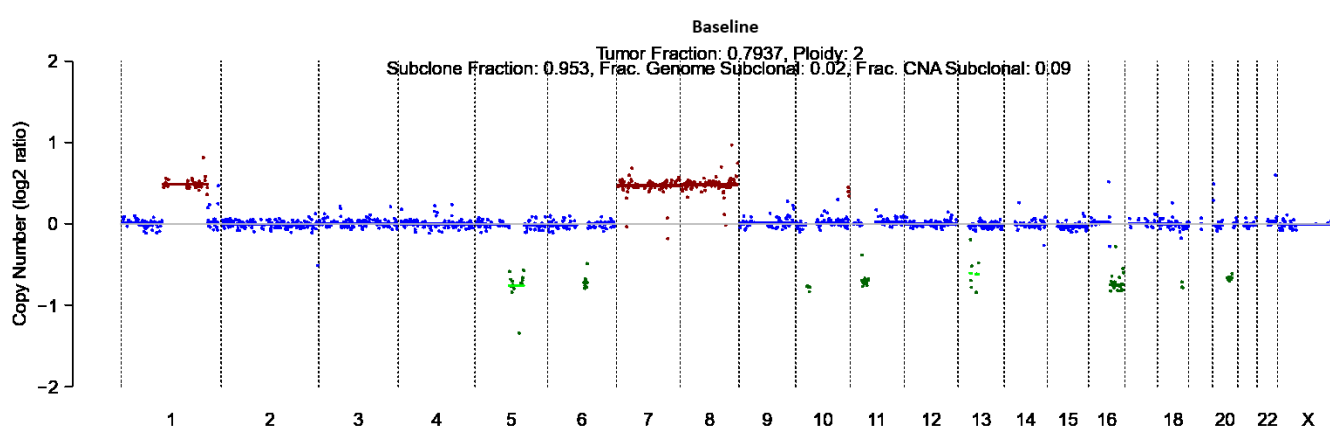


**Figure 77:** CNA profiles for Patient 25 at the baseline (pre-treatment). CNV profiles are depicted as log2 copy number ratios plotted against genomic coordinates.

**Table 18:** Baseline assessment of GFR-CKD-EPI, creatinine, hemoglobin and leukocyte count during [<sup>225</sup>Ac]Ac-/[<sup>177</sup>Lu]Lu-PSMA-617 of Patient 25.

Time point	GFR-CKD-EPI (mL/min/1.73qm)	Creatinine (mg/dL)	Hemoglobin (g/dL)	Leukocyte (G/nL)
Baseline	89.4	0.66	9.7	4.8

GFR-CKD-EPI: Glomerular Filtration Rate estimated using the Chronic Kidney Disease Epidemiology Collaboration (CKD-EPI) equation, expressed in mL/min/1.73 m<sup>2</sup>.

## 11.2 Patient 60

The [<sup>68</sup>Ga]Ga-PSMA-11 PET scan of Patient 60 at baseline revealed widespread metastatic disease involving skeletal, nodal, and visceral sites (Figure 78). At the time of therapy initiation, Patient 60 presented with markedly elevated PSA levels of 268 ng/mL, confirming extensive tumor activity. Tfx was 0.59, indicating widespread metastatic disease. LDH and ALP values were not available in the patient's medical records (Table 19). Renal function and hematologic parameters were assessed prior to therapy administration and revealed severe impairment necessitating dialysis during treatment. Hemoglobin levels were indicative of anaemia. Leukocyte levels were slightly potentially reflecting an inflammatory response associated with tumor progression (Table 20). During the first cycle of RLT, follow-up imaging demonstrated persistent PSMA uptake in multiple lesions, consistent with ongoing disease activity despite initial biomarker reductions. Amplifications, marked in red, showed prominent copy number gains in chromosomes 1, 5, 7, 8, 9, 12, and 16, while notable losses are observed in chromosomes 2, 3, 4, 6, 8, 10, 12, 13, 15, 16, 17 and 18. However, these deletions were small and challenging to evaluate due to the low sequencing coverage. The presence of multiple focal amplifications and deletions suggests a genetically unstable tumor (Figure 79).

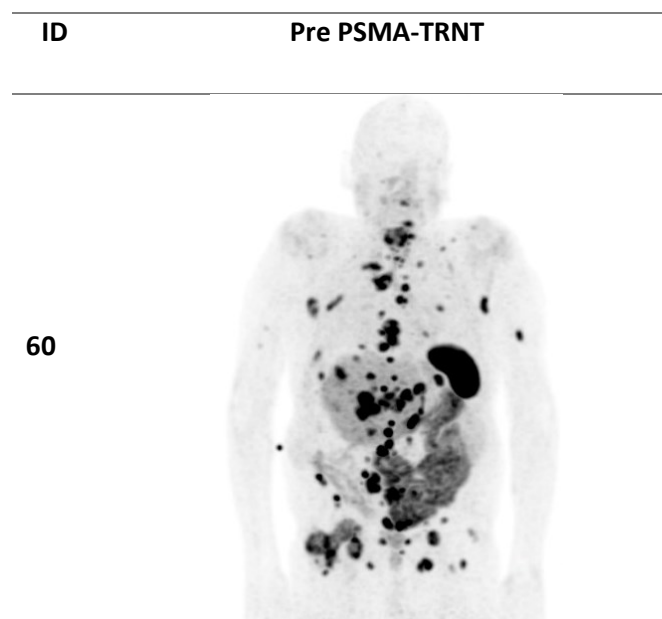


**Figure 78:** Imaging overview of Patient 60. Baseline staging was performed using [ $^{68}\text{Ga}$ ]Ga-PSMA-11 PET imaging.

**Table 19:** Comprehensive overview of PSA, TFX, LDH and ALP in Patient 60, following [ $^{225}\text{Ac}$ ]Ac-/[ $^{177}\text{Lu}$ ]Lu-PSMA-617 regimen.

Tumor Markers	Baseline	Reference
PSA (ng/mL)	268	<4
TFx	0.59	<0.10
LDH (U/L)	NA	<342
ALP (U/L)	NA	40–130

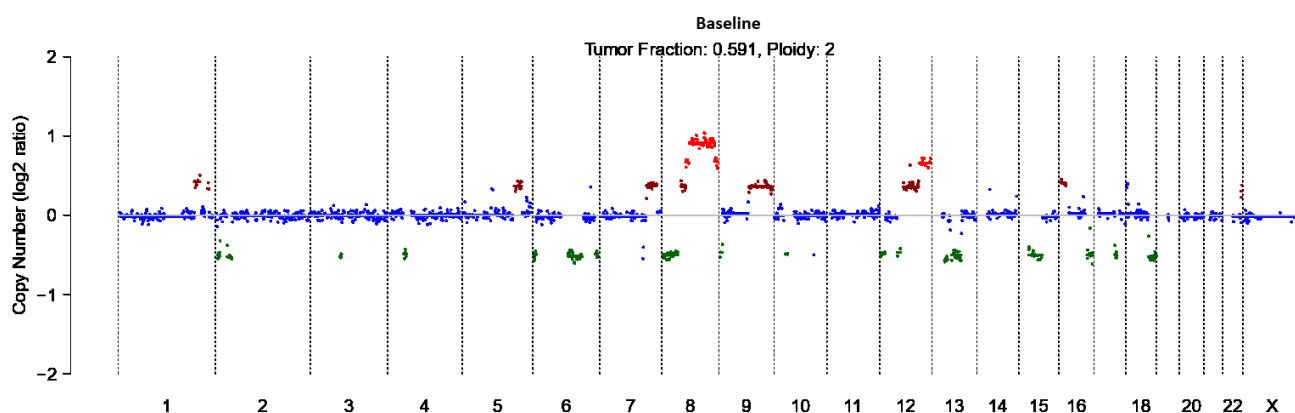


**Figure 79:** CNA profiles for Patient 60 at the baseline (pre-treatment). CNV profiles are depicted as log2 copy number ratios plotted against genomic coordinates.

**Table 20:** Baseline assessment of GFR-CKD-EPI, creatinine, hemoglobin and leukocyte count during  $[^{225}\text{Ac}]\text{Ac-}/[^{177}\text{Lu}]\text{Lu-PSMA-617}$  of Patient 60.

Time point	GFR-CKD-EPI (mL/min/1.73qm)	Creatinine (mg/dL)	Hemoglobin (g/dL)	Leukocyte (G/nL)
Baseline	18.6	2.9	8.7	8.5

*GFR-CKD-EPI: Glomerular Filtration Rate estimated using the Chronic Kidney Disease Epidemiology Collaboration (CKD-EPI) equation, expressed in mL/min/1.73 m<sup>2</sup>.*

### 11.3 Patient 95

Patient 95 underwent  $[^{99\text{m}}\text{Tc}]\text{Tc-PSMA-GCK01}$  SPECT imaging, which revealed tracer accumulation, consistent with extensive bone marrow carcinomatosis and hepatic involvement (Figure 80). At the time of RLT initiation, tumor burden was extensive, as evidenced by markedly elevated PSA levels of 1615 ng/mL and a high mL and a high Tfx of 0.23. LDH was elevated, while AP with a value of 409 U/L was significantly increased, aligning with the presence of extensive bone metastases and osteoblastic activity (Table 21). Renal function was moderately impaired, with a GFR of 39.1 mL/min/1.73m<sup>2</sup> and creatinine levels of 1.54 mg/dL, necessitating careful monitoring for potential nephrotoxicity. Hemoglobin levels were critically low at 6.0 g/dL prior to transfusion, reflecting the impact of bone marrow involvement and chronic disease burden, while leukocyte counts remained within the normal range (Table 22). Genomic analysis revealed extensive copy number gains, particularly in chromosomes 2, 7, 8, 9, 10, 12, and 19, while losses were detected in chromosomes 4, 6, and 16 (Figure 81).

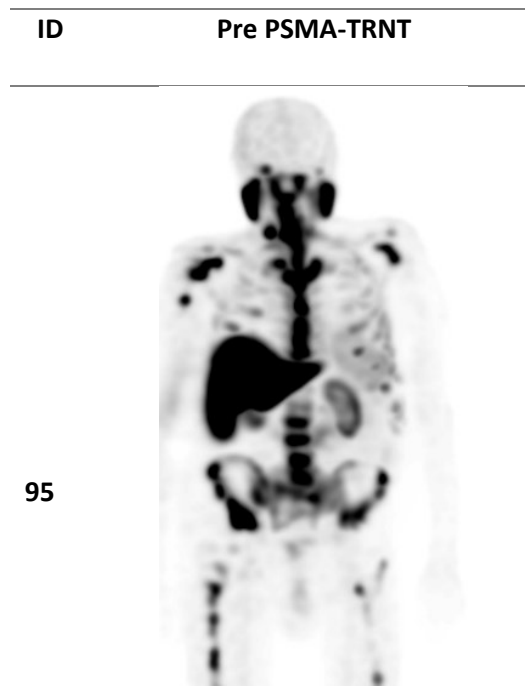


**Figure 80:** Imaging overview of Patient 95. Baseline staging was performed using [ $^{99m}\text{Tc}$ ]Tc-PSMA-GCK01 SPECT.

**Table 21:** Comprehensive overview of PSA, Tfx, LDH and ALP in Patient 95, following [ $^{225}\text{Ac}$ ]Ac-/[ $^{177}\text{Lu}$ ]Lu-PSMA-617 regimen.

Tumor Markers	Baseline	Reference
PSA (ng/mL)	1615	<4
Tfx	0.23	<0.10
LDH (U/L)	409	<342
ALP (U/L)	1348	40–130

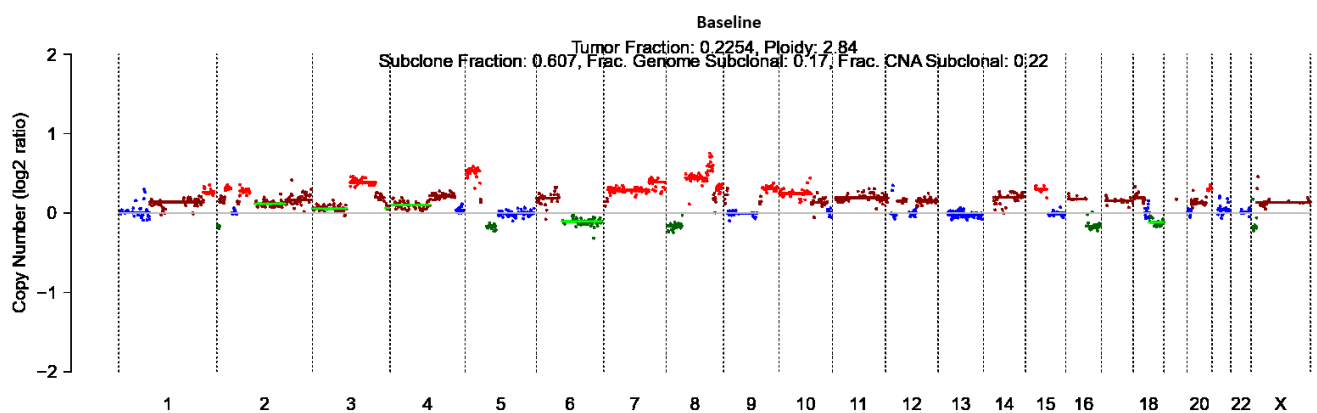


**Figure 81:** CNA profiles for Patient 95 at the baseline (pre-treatment). CNV profiles are depicted as log2 copy number ratios plotted against genomic coordinates.

**Table 22:** Baseline assessment of GFR-CKD-EPI, creatinine, hemoglobin and leukocyte count during  $[^{225}\text{Ac}]\text{Ac-}/[^{177}\text{Lu}]\text{Lu-PSMA-617}$  of Patient 95.

Time point	GFR-CKD-EPI (mL/min/1.73qm)	Creatinine (mg/dL)	Haemoglobin (g/dL)	Leukocyte (G/nL)
Baseline	39.1	1.5	6	6.4

*GFR-CKD-EPI: Glomerular Filtration Rate estimated using the Chronic Kidney Disease Epidemiology Collaboration (CKD-EPI) equation, expressed in mL/min/1.73 m<sup>2</sup>.*

## 11.4 Patient 96

Patient 96 underwent  $[^{68}\text{Ga}]\text{Ga-PSMA-11}$  PET/CT, which revealed extensive skeletal metastases, along with nodal and visceral involvement, consistent with widespread disease progression (Figure 82). Pre-treatment biomarker evaluation confirmed active tumor progression, with PSA at 149 ng/mL, Tfx at 0.38, LDH at 216 U/L, and AP at 418 U/L, reflecting high tumor metabolic activity and extensive bone involvement (Table 23). Baseline renal function and hematologic parameters were within the normal range along with stable hematologic functions (Table 24). Post-treatment evaluations indicated a slight improvement in renal function, while hemoglobin and leukocyte levels declined (Table 24). Genomic profiling assessed at the baseline, revealed a highly unstable genomic landscape, with prominent copy number gains in chromosomes 1, 2, 3 (entirely amplified) 5, 6, 7, 8 (q arm amplified), 10, 11, 12, 15, 21 and 23 (Y chromosome), alongside notable losses in chromosomes 2, 3, 4, 5, 6, 8 (p arm deletion) 9, 10, 13, 16, 18 and 22 (Figure 83).

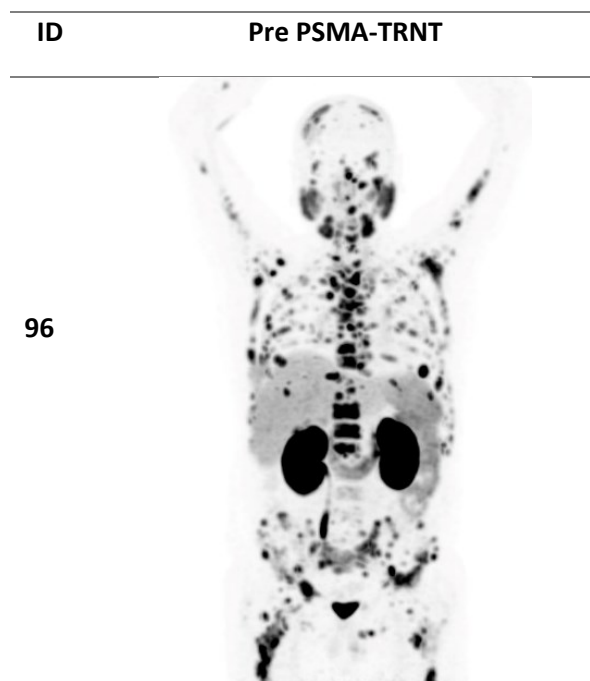


**Figure 82:** Imaging overview of Patient 96. Baseline staging was performed using [ $^{68}\text{Ga}$ ]Ga-PSMA-11.

**Table 23:** Comprehensive overview over the dynamic changes in PSA, Tfx, LDH and ALP in Patient 96, following [ $^{225}\text{Ac}$ ]Ac-/ [ $^{177}\text{Lu}$ ]Lu-PSMA-617 regimen.

Tumor Markers	Baseline	Reference
PSA (ng/mL)	149.4	<4
Tfx	0.38	<0.10
LDH (U/L)	216	<342
ALP (U/L)	418	40–130

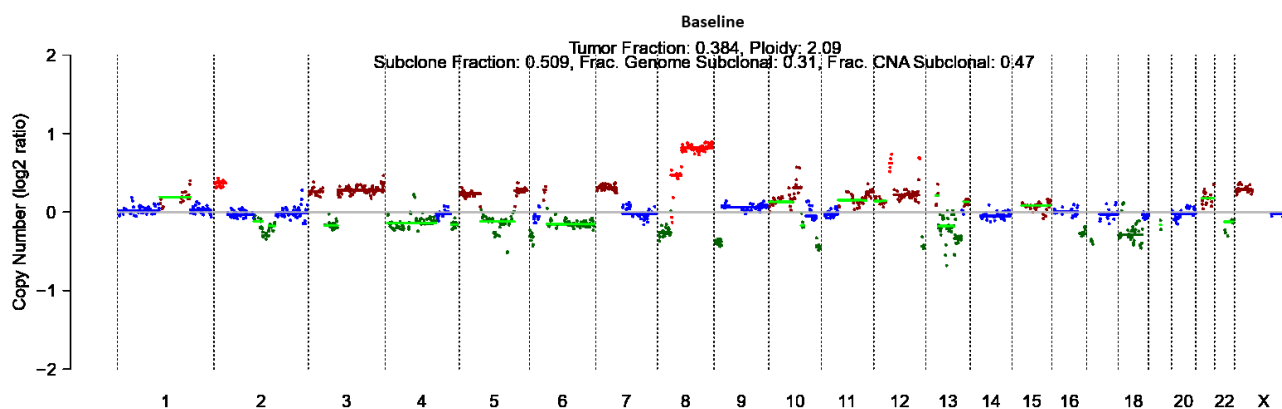


**Figure 83:** CNA profiles for Patient 96 at the baseline (pre-treatment). CNV profiles are depicted as log2 copy number ratios plotted against genomic coordinates.

**Table 24:** Overview of GFR-CKD-EPI, creatinine, hemoglobin and leukocyte count during [<sup>225</sup>Ac]Ac-/[<sup>177</sup>Lu]Lu-PSMA-617 of Patient 96.

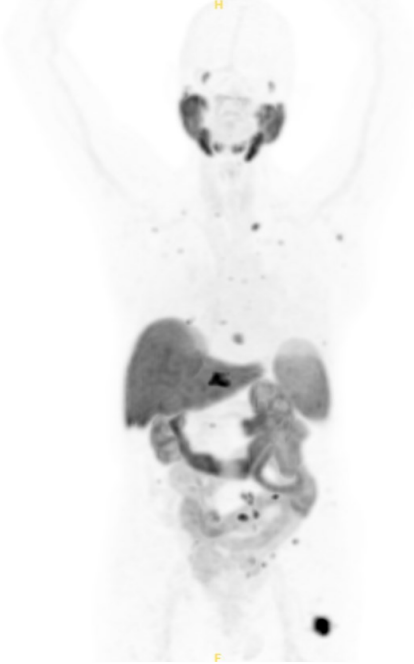

Time point	GFR-CKD-EPI (mL/min/1.73qm)	Creatinine (mg/dL)	Hemoglobin (g/dL)	Leukocyte (G/nL)
Baseline	102	0.73	10.9	7.2
1 <sup>st</sup> treatment cycle	111	0.59	10.5	5.3

*GFR-CKD-EPI: Glomerular Filtration Rate estimated using the Chronic Kidney Disease Epidemiology Collaboration (CKD-EPI) equation, expressed in mL/min/1.73 m<sup>2</sup>.*

## 11.5 Patient 23

Patient 23 underwent pre-therapy [<sup>18</sup>F]PSMA-1007 PET, which revealed small disseminated metastases with minimal bone involvement (Figure 84). At baseline, PSA levels were 82.9 ng/mL, Tfx was 0.18, LDH was 269 U/L, and AP was 85 U/L. Due to poor venous access, biomarker data from the first treatment cycle were unavailable, as sample collection was not feasible. Following the second cycle of actinium-lutetium therapy, PSA levels increased significantly to 187 ng/mL, accompanied by a rise in AP to 104 U/L and Tfx to 0.53, indicating progressive disease activity. By the third cycle, PSA had further increased to 378 ng/mL, with Tfx rising to 0.64, suggesting continued disease progression despite treatment (Table 25). At baseline, renal function was impaired, while hemoglobin and leukocyte levels remained within the normal range. After the second treatment cycle, GFR showed no improvement, whereas hemoglobin and leukocyte levels exhibited a slight decline. By the third cycle, GFR had further decreased to 48.9 mL/min/1.73m<sup>2</sup>, with a concurrent increase in creatinine to 1.35 mg/dL. Meanwhile, hemoglobin and leukocyte counts continued to decline, indicating progressive hematologic suppression (Table 26). Genomic analysis at baseline revealed a CNA profile with limited focal amplifications, primarily on chromosome 8. After the second treatment cycle, these amplifications persisted, accompanied by emerging focal deletions on chromosomes 2, 3, and 4. By the third cycle, amplifications on chromosome 8 had become more pronounced, while deletions extended further across chromosomes 2, 3, 4, and 12 (Figure 85).



ID	Pre PSMA-TRNT	Post PSMA-TRNT
23		

**Figure 84:** Imaging overviews of Patient 23. Pre-therapy and post- PSMA-TRNT PET imaging performed with [ $^{18}\text{F}$ ]PSMA-1007. Mid therapy scans are not available.

**Table 25:** Comprehensive overview over the dynamic changes in PSA, Tfx, LDH and ALP in Patient 23, following [ $^{225}\text{Ac}$ ]Ac-/ [ $^{177}\text{Lu}$ ]Lu-PSMA-617 regimen.

Tumor Markers	Baseline	2 <sup>nd</sup> cycle	3 <sup>rd</sup> cycle	Reference
PSA (ng/mL)	82.9	187	378	<4
Tfx	0.18	0.53	0.64	<0.10
LDH (U/L)	269	238	245	<342
ALP (U/L)	85	104	155	40–130

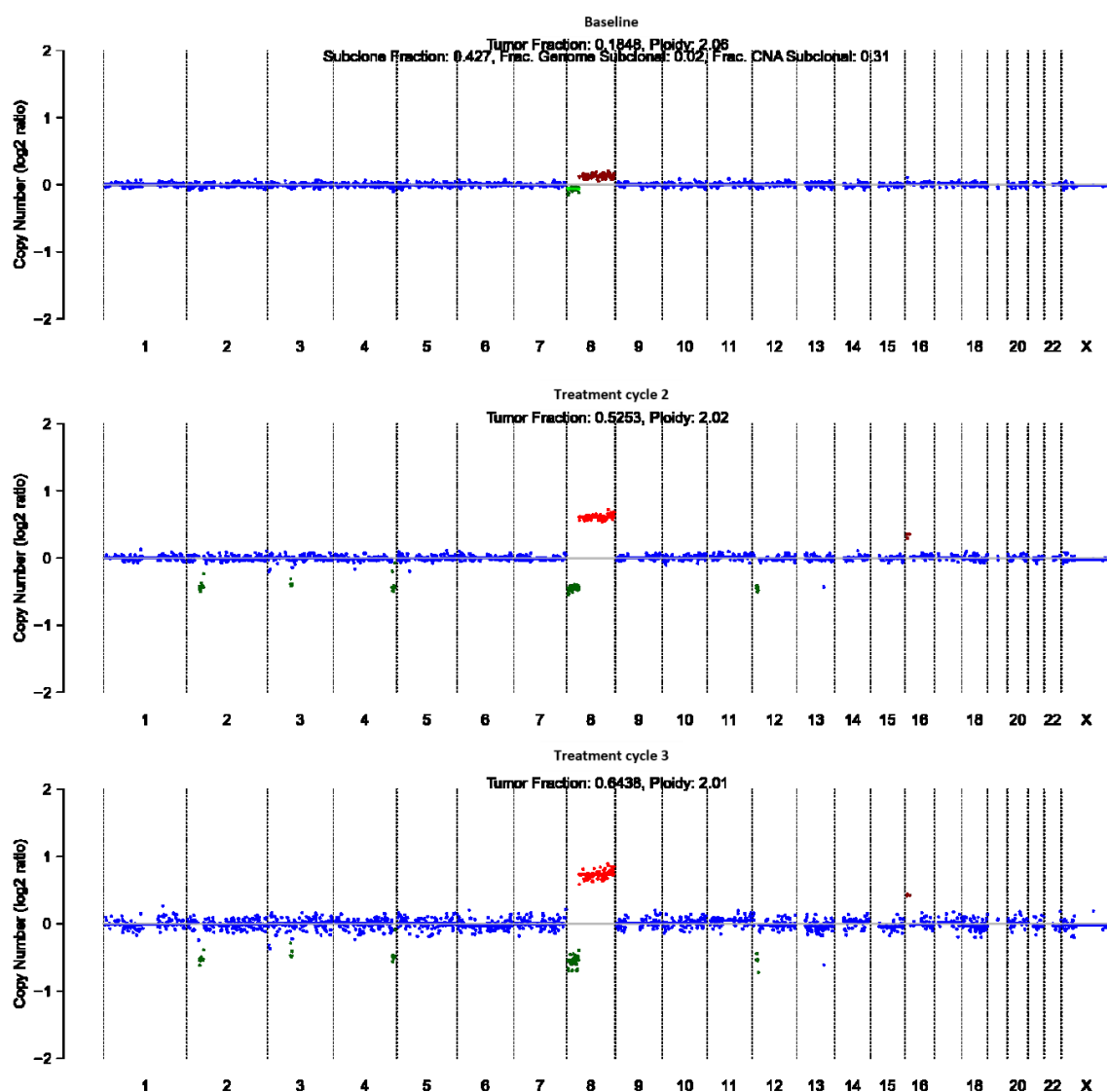


**Figure 85:** CNA profiles for Patient 23 at the baseline (pre-treatment) and at treatment cycle 2 and 3. CNV profiles are depicted as log2 copy number ratios plotted against genomic coordinates.

**Table 26:** Overview of GFR-CKD-EPI, creatinine, hemoglobin and leukocyte count during [ $^{225}\text{Ac}$ ]Ac-/[ $^{177}\text{Lu}$ ]Lu-PSMA-617 of Patient 23.

Time point	GFR-CKD-EPI (mL/min/1.73qm)	Creatinine (mg/dL)	Haemoglobin (g/dL)	Leukocyte (G/nL)
Baseline	42.4	1.5	12.8	9.3
2 <sup>nd</sup> treatment cycle	55.3	1.2	12.0	7.1
3 <sup>rd</sup> treatment cycle	48.9	1.3	11.4	5.0

GFR-CKD-EPI: Glomerular Filtration Rate estimated using the Chronic Kidney Disease Epidemiology Collaboration (CKD-EPI) equation, expressed in mL/min/1.73 m<sup>2</sup>.

## V DISCUSSION

This study systematically investigates the relationship between Tfx, established clinical biomarkers, and genomic alterations in a well-characterized cohort of mCRPC patients receiving [ $^{225}\text{Ac}$ ]Ac-/ $^{177}\text{Lu}$ ]Lu-PSMA-617 therapy as compassionate treatment. It aims to evaluate real-world clinical data, integrating patient stratification and the use of Tfx estimation as a biomarker to monitor treatment response and resistance during tandem actinium-lutetium therapy. This cohort is exceptional due to the limited global access to  $^{225}\text{Ac}$  and TRNT in general. The University Hospital of Heidelberg is worldwide one of the few centers having limited but reliable access to  $^{225}\text{Ac}$  in highest quality provided by the European Joint Research Center (JRC) in Karlsruhe. In fact, several patients in this study travelled from outside Europe to receive this treatment. Through the integration of longitudinal biomarker assessments with molecular and survival analyses, the prognostic and predictive significance of Tfx is evaluated, demonstrating its independent association with validated clinical endpoints and treatment outcomes.

Analysis of 78 prospectively collected and banked plasma samples confirms that ctDNA is a dynamic and clinically relevant biomarker in mCRPC. The longitudinal assessment of Tfx in cfDNA underscores its potential for real-time disease monitoring, risk stratification, and therapeutic response evaluation. These findings reinforce ctDNA as a valuable tool in precision oncology, providing critical insights for optimizing treatment strategies in advanced prostate cancer. ctDNA has been extensively characterized in the management of mCRPC, with a primary focus on AR alterations and their role in predicting resistance to abiraterone, enzalutamide, and [ $^{177}\text{Lu}$ ]Lu-PSMA-617 therapy. These studies highlight that AR alterations detected in ctDNA serve as strong indicators of resistance to AR-targeted treatments and are associated with poorer survival outcomes (171-175). However, to the best of my knowledge, no studies have investigated the application of ctDNA as a predictive biomarker for response to [ $^{225}\text{Ac}$ ]Ac-/ $^{177}\text{Lu}$ ]Lu-PSMA-617 therapy or its potential role in patient stratification based on baseline assessments.

In my initial analysis, I assessed the potential role of Tfx in monitoring response to [ $^{225}\text{Ac}$ ]Ac-/ $^{177}\text{Lu}$ ]Lu-PSMA-617 therapy. The results showed that Tfx declines consistently paralleled reductions in PSA levels—an established biomarker of treatment response—following the initiation of therapy. The observed parallel decline in Tfx and PSA—currently the clinical gold standard for monitoring treatment response—highlights the potential of Tfx as a reliable and dynamic surrogate biomarker in mCRPC. This alignment reinforces the utility of Tfx for real-time assessment of disease progression and therapeutic efficacy. For instance, a similar kinetic pattern in both markers was observed in Patient 5 (Chapter 11.1) and Patient 37 (Chapter 11.5). Despite being the current gold standard biomarker for prostate cancer, PSA levels do not accurately reflect disease burden, posing significant

challenges in clinical decision-making and monitoring, as demonstrated in reported case studies (176, 177). These findings are underlined by my observations for Patient 38 (Chapter 11.3), where PSA failed to accurately predict relapse. The Tfx on the other hand displayed the therapy failure earlier and was only subsequently followed by changes in PSA levels at later time points during the therapy cycles. A similar pattern was observed in Patient 10, where high tumor activity and non-responsiveness to the subsequent treatment cycle were detected via increasing Tfx fractions despite a decline in PSA levels. My findings align with existing reports indicating that, although PSA remains a standard biomarker during early treatment cycles, its utility diminishes in advanced stages of disease—particularly due to neuroendocrine differentiation, which is associated with reduced PSA and PSMA expression and increased SSTR2 overexpression (178, 179).

LDH and ALP, which are often used as supplementary biomarkers for detection of PCa and its therapy response, showed their significance in displaying therapy response only in the first treatment cycle, with subsequent reductions failing to reach statistical relevance (whole cohort analysis). This is in line with literature describing their limited reliability for long-term monitoring (180). In my analysis of both case studies and the entire cohort, LDH and ALP levels—although previously associated with favorable outcomes in mCRPC—did not provide added prognostic value. Their trends closely followed PSA dynamics without enabling earlier relapse detection or improved stratification. These observations are consistent with findings from previous studies, which also reported limited independent utility of LDH and ALP as early response biomarkers (181, 182).

In addition to evaluating biomarker kinetics, correlations between Tfx and individual biomarkers were assessed, revealing that Tfx showed significant positive correlations with PSA, LDH, and ALP levels. A moderate yet statistically significant association was observed between Tfx and PSA ( $R = 0.47$ ,  $p = 7.7e^{-11}$ ) as well as Tfx and ALP ( $R = 0.47$ ,  $p = 7.3e^{-11}$ ), while Tfx and LDH demonstrated a stronger correlation ( $R = 0.67$ ,  $p < 2.2e^{-16}$ ). My findings align with existing literature, where elevated ctDNA levels correlate with higher tumor burden and adverse clinical markers, including increased PSA and LDH levels (171). Tfx reflects overall tumor burden, while LDH is associated with bone metastases, explaining their strong correlation in mCRPC patients (183). I believe the moderate correlation with PSA may be attributed to its reduced expression in late-stage mCRPC, where its prognostic value remains debated. Importantly, the strong correlation between Tfx and LDH observed here is not inconsistent with the previously noted weaker longitudinal kinetics of LDH. The correlation analysis reflects the association between two markers at a single time point, whereas the kinetic analysis captures dynamic changes relative to baseline over time. The correlation between LDH and Tfx reflects shared biological processes, such as tumor metabolism and hypoxia, with elevated LDH levels indicating increased glycolytic activity and cellular turnover, reinforcing its role as a metabolic marker

of tumor burden (69, 184, 185). Although some studies suggest that a decline in PSA may predict treatment response, this association is not always consistent, particularly in advanced disease stages, as also supported by findings in the literature (186, 187). The correlation between Tfx and ALP likely reflects elevated tissue-nonspecific alkaline phosphatase levels associated with skeletal involvement, highlighting ALP's utility in detecting bone metastases while underscoring its limitations as a standalone prognostic marker in mCRPC as reported in the literature (188, 189).

To further analyse the temporal dynamics of patient responses and their correlation with various biomarkers, a multivariable analysis was conducted focusing on Tfx, LDH, and PSA as described in the Results section (Chapter 3.4). I observed that patients who exhibited a negative fold change in LDH, Tfx, and PSA were more frequently associated with favorable clinical outcomes, such as stable disease or partial remission. In contrast, patients with positive fold change in these biomarkers were predominantly linked to disease progression. My results suggest that Tfx and PSA may follow similar trends over time, reflecting individual patient responses and potentially reinforcing the role of Tfx as a surrogate marker for treatment monitoring. While PSA remains a key marker for prostate cancer burden, its strong correlation with Tfx indicates that Tfx reflects additional biological processes beyond PSA dynamics, emphasizing their non-interchangeable nature (176, 190).

Given these findings, I evaluated Tfx for its ability to stratify patients based on their metastatic burden, an area where PSA has demonstrated limitations due to tumor phenotypic shifts and loss of expression in advanced disease stages. Tfx effectively distinguished metastatic groups, with the highest values observed in patients with extensive metastatic involvement, including bone, lymph nodes, and visceral organs, whereas PSA failed to reliably differentiate patients, particularly in late-stage disease where PSA production may decline due to tumor microenvironment changes. As reported in the literature, the limited reliability of PSA as a metastatic burden indicator stems from its susceptibility to confounding factors such as benign prostatic hyperplasia and prostatitis, reducing its specificity in detecting clinically significant prostate cancer (55, 177). These results suggest that absolute PSA levels are not independently reflective of disease burden across patients. This is expected, as aggressive variant prostate cancers with a tendency for visceral metastases, as well as tumors that undergo dedifferentiation in response to therapy, often produce relatively low amounts of PSA (191, 192). In some mCRPC cases, PSA secretion is minimal despite high tumor burden due to neuroendocrine differentiation, which drives androgen independence and poor prognosis, while post-prostatectomy PSA levels further limit its reliability as a sole marker for disease progression (193-195). Studies show that ctDNA and Tfx strongly correlate with disease burden, particularly in patients with liver and bone metastases, making them valuable biomarkers for assessing metastatic spread and treatment response (196, 197).

Given the limitations of PSA in reflecting tumor burden in advanced disease stages, further investigation was conducted to determine how well Tfx predicts clinical outcomes compared to conventional biomarkers. ROC analysis demonstrated that pre-treatment Tfx had moderate predictive ability for clinical outcomes (AUC = 0.60), with only a marginal improvement when PSA and LDH were included (AUC = 0.62), indicating that Tfx independently provides substantial prognostic information with limited additional value from PSA and LDH. These findings align with existing research highlighting ctDNA as a prognostic biomarker, where baseline ctDNA levels and post-treatment changes predict time to progression and survival in mCRPC patients (58, 163, 196). A particularly compelling finding of this study is that an increase in Tfx was significantly associated with a 5-fold higher likelihood of relapse ( $p = 0.0259$ ), underscoring its strong potential as a robust early biomarker for detecting disease progression and emerging therapeutic resistance. On a similar setting, a study on high-grade serous epithelial ovarian cancer (HGS-EOC) demonstrated that the Tfx in baseline plasma ctDNA serves as an independent prognostic marker for disease relapse. Notably, longitudinal ctDNA monitoring outperformed CA-125 (cancer antigen 125) in predicting disease progression, with increases in TF over time anticipating relapse several months in advance—highlighting the superior sensitivity of ctDNA-based approaches for early detection of therapeutic failure and disease recurrence (198). As illustrated in the case of Patient 38 (Chapter 10.3), Tfx served as an early indicator of disease relapse, mirroring the metastatic landscape and signalling tumor resurgence. This capability to detect disease recurrence at a molecular level—preceding conventional biochemical markers or imaging—underscores the value of ctDNA as a prognostic tool. Patient 10 (Chapter 10.2) highlights the profound utility of ctDNA analysis in tracking tumor burden at the genomic level, with values reaching below detection thresholds. Overall, as reported in multiple studies, ctDNA detection facilitates early relapse prediction and disease monitoring. In particular, rising Tfx levels have been shown to strongly correlate with molecular recurrence in breast cancer, gastroesophageal adenocarcinoma, and mCRPC (152, 199, 200).

Notably, for Patient 10 the kinetics of PSA levels mirrored the decline in Tfx similarly. After an initial period of therapeutic success, and discontinuing radioligand treatment for two-years due to reaching the cumulative dose limit resulted in significant changes in the tumor profile. I hypothesis that this interval appears to have facilitated the emergence of a resistant clonal population, reflecting the tumor's adaptive evolution following prior radiation therapy. Upon the patient's return to the clinic, the baseline PSA was 82.2 ng/mL, accompanied by a Tfx of 0.41. Additionally, post-treatment ctDNA changes predict time to progression and overall survival in mCRPC patients, further reinforcing Tfx as a clinically relevant biomarker for guiding timely treatment adjustments (201). This reinforces Tfx as

a dynamic biomarker for early treatment failure detection and risk-adapted therapy modifications (173, 176).

Tissue biopsy remains the diagnostic gold standard due to its accuracy and standardized procedures, but it is invasive, difficult to repeat, and limited by tumor heterogeneity, capturing only a snapshot of a single lesion. In contrast, ctDNA-based liquid biopsy is minimally invasive, cost-effective, and suitable for serial sampling, enabling real-time monitoring of treatment response and tumor evolutions. However, clinical use is still limited due to challenges in assay standardization, sample handling, and sensitivity (202-206).

Alongside biomarker analysis, ctDNA profiling was leveraged to investigate resistance mechanisms and classify patients based on their baseline genomic landscape. In my analysis of baseline samples from 57 patients, I identified two distinct clusters based on CNV profiles: one with low and one with high genomic instability. By overlaying Tfx values, I observed that patients with a high CNV burden also had higher Tfx levels, indicating a potential association between genomic instability and tumor burden. My results demonstrate a strong and statistically significant correlation between baseline CNV burden and Tfx levels, underscoring their potential as complementary prognostic biomarkers in mCRPC and as valuable tools to support clinical decision-making. The prognostic value of CNV burden has been well established in the literature across various cancer types—for instance, in ALK-positive non-small cell lung cancer (NSCLC), where combined copy number and targeted mutation profiling has been shown to improve disease monitoring (207, 208). Although my cohort lacks extensive longitudinal CNV tracking, the observed baseline association nonetheless reinforces the clinical relevance of CNV burden as a marker of tumor aggressiveness and supports its further investigation in the context of liquid biopsy-based monitoring. In mCRPC, while certain CNVs, such as AR amplification, were identified in some treatment courses, they did not consistently correlate with worse prognosis in patients undergoing therapies like abiraterone and enzalutamide (158). On the other hand, findings from De Giorgi et al. indicate that plasma AR gene amplification is associated with resistance to [<sup>177</sup>Lu]Lu-PSMA-617, suggesting that this radioligand therapy may demonstrate greater efficacy when administered in earlier stages of prostate cancer (209). Literature suggests that the influence of CNV burden on clinical outcomes follows a non-linear trend, characterized by a steep initial rise in the risk of disease progression and reduced overall survival, which then plateaus at higher levels of CNV burden (210, 211). My results show that patients with a high CNV burden had a shorter median survival (8.3 months) compared to those with a low CNV burden (13.8 months). Although this comparison did not reach statistical significance ( $p = 0.112$ ), the 5.5-month difference in median survival between the groups may still be clinically relevant. Patient 34 (Chapter 10.6), classified as a non-responder, demonstrated persistent circulating tumor burden and a highly disrupted tumor

genome. Despite a transient reduction in Tfx after the first treatment, the genomic landscape remained characterized by significant amplifications and deletions, highlighting the aggressiveness of the disease. In the context of this cohort and their treatment options, this disparity highlights the potential value of assessing CNV burden at baseline to better inform prognosis and treatment strategies (212). Sobhani et al. identified a correlation between higher CNV burden and increased tumor aggressiveness and disease progression in mCRPC, consistent with findings that pre-treatment Tfx and CNV burden are associated with greater tumor burden and poorer prognosis (151, 213). Furthermore, ctDNA copy number analysis has demonstrated utility in identifying tumor progression patterns in squamous lung cancer, highlighting its potential for real-time disease monitoring and prognostic assessment (154). The Tfx-stratified OS analysis undertaken in this work revealed a paradoxical trend: patients with the lowest Tfx ( $<0.225$ ) had the longest survival, while those with intermediate Tfx levels ( $0.225\text{--}0.434$ ) experienced the shortest survival—despite patients in the highest Tfx group ( $0.434\text{--}0.794$ ) showing better outcomes. Although not statistically significant, I hypothesize that this unexpected pattern may reflect Tfx's limitation in capturing metastatic heterogeneity or distinct clonal populations, despite reflecting total tumor burden. In the context of TRNT, which specifically targets PSMA-expressing tumours, resistance mechanisms such as PSMA loss allow tumor cells to evade treatment, either as a pre-existing condition or an adaptive response (214). Consequently, high Tfx may indicate a substantial tumor burden that is at the same time - depending on the respective molecular characteristics of the tumor cells - susceptible and not susceptible to therapy, potentially explaining the lack of a direct correlation between tumor load and survival outcomes.

Pretreatment significantly impacts survival in mCRPC, as shown by Kaplan-Meier analysis ( $p = 0.0483$ ). The shortest survival was observed in patients who had never received chemotherapy, contradicting existing literature on lutetium-based therapies. Sathekge et al. reported a survival benefit in chemotherapy-naïve patients with advanced metastatic prostate carcinoma, while emphasizing the need for further clinical investigation and trial optimization (215, 216). An important consideration when comparing my cohort to the one described by Sathekge et al. is the age difference—my chemotherapy-naïve patients were relatively older. However, the shorter overall survival observed in this group was not associated with age, effectively ruling out age as a contributing factor to the poorer outcomes. The data suggest that chemotherapy, by inducing DNA damage and disrupting replication pathways, may enhance tumor sensitivity to radiation therapy, potentially improving treatment outcomes. Patients with the longest survival had prior exposure to ADT, chemotherapy, and TRNT, regardless of the radionuclide used. Ahmadzadehfar et al. reported that patients who received [ $^{177}\text{Lu}$ ]Lu-based PSMA-TRNT after Xofigo® ( $^{223}\text{RaCl}_2$ ) experienced prolonged overall survival in the first



10 months compared to those without prior  $^{223}\text{RaCl}_2$  treatment, while maintaining a favourable safety profile (215, 217). Consistent with our findings, Rathke et al. reported a median overall survival (mOS) of 9 months for patients receiving [ $^{225}\text{Ac}$ ]Ac-PSMA-617 monotherapy, compared to 15 months for those treated with the [ $^{225}\text{Ac}$ ]Ac-PSMA-617 and [ $^{177}\text{Lu}$ ]Lu-PSMA-617 combination. This difference in survival is likely due to the higher prevalence of bone marrow infiltration in the monotherapy group, a factor known to be associated with poorer prognosis.

A key limitation of my study is the absence of tissue samples, preventing direct plasma-tumor CNV comparisons. To address this, ctDNA GISTIC analysis was compared with public datasets, confirming deletions and amplifications consistent with prior findings (150, 154, 218, 219). Cluster 1 patients, characterized by a low CNV burden and the longest overall survival, exhibited 5q21.3 and 6q16.2 deletions with no significant amplifications. The 5q21.3 deletion, present in ~23% of prostate cancers, is associated with ERG-negative tumors and occurs late in disease progression, suggesting a role in tumor advancement (220). Meanwhile, 6q16 deletions are associated with poor prognosis, likely due to the loss of tumor suppressor genes contributing to tumor aggressiveness (221). Cluster 2, characterized by a higher CNV burden, was analysed to identify genomic alterations linked to poorer survival outcomes, providing insights into the molecular mechanisms underlying disease progression. Key chromosomal amplifications identified in this study highlight critical drivers of prostate cancer progression and treatment resistance. Chr 1q32.1 amplification, which includes MDM4, suggests a role in disease progression, aligning with prior findings that MDM4 suppression reduces tumor proliferation and induces ferroptosis (222, 223). In Patient 25, alongside various detected amplifications, a distinct signal of chromosome 1 amplification is evident. Similarly, 8q21.3 amplification, a frequently altered region in mCRPC, includes MYC, a key regulator of cell cycle progression and immune evasion, whose overexpression has been linked to increased tumor aggressiveness and therapy resistance (224, 225). In addition, chromosome 9 amplification, which includes TNC, has been associated with tumor progression. TNC promotes tumor migration by interacting with  $\alpha 5\beta 1$  integrins, inhibiting YAP/TAZ signaling, and enhancing tumor-stroma interactions that drive metastasis (226, 227). The amplification of 10q22.3, linked to increased vinculin expression, further supports its role in tumor proliferation and poor clinical outcomes (228). Finally, 12q24.22 amplification, which includes PTPN11, suggests a potential role in prostate cancer progression. While its precise function remains debated, PTPN11 has been implicated in oncogenic signaling through MET and STAT5 activation. Some studies suggest a tumor-suppressive function, while others indicate that gain-of-function mutations contribute to therapy resistance (229-231). Additionally, a chromosome 12 amplification was detected in Patient 60.

The chromosomal deletions identified in this study underscore the critical role of tumor suppressor gene loss in prostate cancer progression and poor prognosis. The deletion of 5q11.2, a recurrent breakpoint, is linked to chromosomal instability and tumorigenesis (232). Similarly, 6q21 deletions, more prevalent in advanced-stage tumours, suggest a late event in disease progression, with CCNC loss (located on chromosome 6) potentially disrupting androgen signalling and driving tumor growth (233, 234). 8p21.3 deletion, often co-occurring with PTEN loss, exacerbates tumor aggressiveness and therapy resistance, partly through lipid metabolism dysregulation via LEPROTL1 (235, 236). Likewise, losses at 8q and 10q, affecting PTEN, RB1, and ENOX1, are strongly associated with poor prognosis and treatment resistance, reinforcing their relevance in patient stratification. Additionally, SUFU deletion (chromosome 10) disrupts Hedgehog pathway regulation, while SDH mutations impair mitochondrial function, collectively driving metabolic and proliferative reprogramming in aggressive prostate cancer (237, 238). Other notable deletions include 11q23.2, previously associated with melanoma and other cancers, though its role in prostate cancer remains unclear (239). The 13q14.3 deletion, encompassing RB1 and ENOX1, is one of the most frequent alterations in prostate cancer and is strongly linked to worse survival outcomes (240). Similarly, the co-deletion of 16q23.3 and PTEN has been implicated in disease progression, further supporting its potential as a biomarker for risk stratification (241).

To identify specific alterations driving poor survival outcomes, further analysis was conducted on 17 patients with clinical recurrence, examining CNVs that persisted from baseline to progressive disease. As Tfx increased in progressive disease samples, CNV analysis became more reliable, allowing for a clearer assessment of genomic alterations. Notably, amplifications at 8q21.3 and 10q21.2 were consistently detected in progressive disease, baseline samples, and Cluster 2, suggesting their key role in tumor progression. Gene signature identification further supports these findings, highlighting key molecular mechanisms underlying resistance in mCRPC treated with [<sup>225</sup>Ac]Ac-/[<sup>177</sup>Lu]Lu-PSMA-617. Chromosome 8 amplification was also extensively observed in chemotherapy-naïve patients, specifically in Patient 60, 25, and 23, highlighting its potential role in disease progression. These regions may serve as potential therapeutic targets, as genes within 8q21.3 and 10q21.2 have been identified as significant amplification events in progressive prostate cancer (224, 242, 243). PTEN inactivation (chr 10) is one of the most frequent genomic alterations in prostate cancer, occurring in ~20% of primary tumor and up to 50% of castration-resistant cases, driving PI3K/AKT pathway dysregulation in over 40% of mCRPC patients (244, 245). Similarly, CDH17 amplification (chr 8) suggests a role in tumor growth and metastasis through NF-κB signaling activation. While its precise function in prostate cancer remains unclear, CDH17 has been associated with Netrin-mediated signaling and MAPK (ERK1/ERK2) activation, both essential for cell proliferation and survival (246).

ctDNA analysis has emerged as a valuable tool for detecting genomic alterations in mCRPC, supporting precision oncology approaches. The PROfound study demonstrated that ctDNA testing effectively identifies BRCA1, BRCA2, and ATM alterations, enabling targeted therapy decisions with PARP inhibitors for patients with defective DNA repair pathways (219, 247). Synthetic lethal interactions, such as those between PARP1 and BRCA1, offer additional therapeutic avenues, particularly in tumors with homologous recombination repair (HRR) deficiencies. Among the genes identified in our gene signature, RAD17 has been shown to be synthetically lethal with CHEK1 inhibition, underscoring its critical role in DNA damage response and checkpoint signaling (248). FANCA, a key tumor suppressor identified in Cluster 2, plays an essential role in DNA damage repair. Alterations in FANCA and other DDR genes have been linked to prostate cancer progression, especially in metastatic disease. Germline FANCA mutations, such as the S1088F variant, disrupt the FANC protein complex, increasing tumor sensitivity to DNA-damaging agents like cisplatin. The role of FANCA in monoubiquitylation of FANCD2 suggests its potential as a biomarker for treatment response (249). Additionally, MGMT variants in exonic regions may impair DNA repair efficiency, potentially influencing biochemical relapse in prostate cancer (250). The tumor suppressor deletions in Cluster 2 further highlight BRCA2's central role in HRR. Its disruption contributes to genomic instability, therapeutic resistance, and increased mutation burden, reinforcing the oncogenic landscape of Cluster 2. The enrichment of DNA repair deficiencies suggests greater reliance on alternative repair mechanisms, emphasizing the role of homology-directed repair (HDR) and TP53-regulated pathways in maintaining genomic stability. These finds are quite in contrast with what has been described in the literature. van der Doelen et al. observed pathogenic BRCA1 mutations in two patients associated with longer survival, suggesting that DDR-deficient tumors may exhibit higher PSMA expression and increased sensitivity to PSMA-TRNT and TAT (164). In contrast, our results indicate a more aggressive disease phenotype linked to DDR alterations. While DDR-deficient tumors are thought to be more vulnerable to TAT due to their impaired ability to repair alpha emitter-induced double-strand DNA breaks, germline or somatic DDR alterations have also been associated with higher PSMA expression, suggesting their potential as biomarkers for PSMA-TRNT (251, 252). One possible explanation for these discrepancies is the nature of the analyzed specimens. Unlike tumor tissue, cfDNA reflects a composite genetic profile from multiple clonal populations, rather than a single tumor site. In patients with multiple metastases, this broader representation complicates drawing conclusions from individual tumor niches, as cfDNA captures the heterogeneity of the entire metastatic burden rather than reflecting a single dominant clone (253). This limitation highlights a critical gap in our ability to fully delineate the metastatic landscape, as complete tumor burden assessment is crucial for informed therapeutic decision-making.

Although broader imaging modalities such as [<sup>18</sup>F]FDG-PET could enhance metastasis detection, their high cost and limited accessibility remain challenges to widespread implementation (254, 255). In this context, ctDNA analysis offers a cost-effective alternative for detecting both PSMA-positive and PSMA-negative lesions, providing a more holistic view of the disease state. Discrepancies with previous studies may also stem from differences in cohort characteristics, selection criteria, and therapeutic approaches. This study focused on a cohort of 78 patients receiving an actinium-lutetium combination, yet was limited by the lack of prospective randomization, systematic adverse event documentation, and standardized radiologic progression-free survival data. These factors highlight the need for further prospective studies to clarify the prognostic and predictive value of DDR alterations in the context of PSMA-TRNT.

## VI CONCLUSION

My PhD work highlights the potential of ctDNA analysis, specifically Tfx estimation, as a valuable biomarker for monitoring treatment response and disease progression in mCRPC patients receiving tandem actinium-lutetium therapy. My results demonstrate that Tfx strongly correlates with conventional clinical biomarkers such as PSA, LDH, and ALP, while also providing additional prognostic value, particularly in advanced disease stages. Given the heterogeneity of our patient cohort, my findings underscore the importance of pre-treatment assessment for patient stratification and overall survival outcomes. Given the global shortage of  $^{225}\text{Ac}$ , the ability to identify non-responders early through biomarkers such as Tfx is not only critical for optimizing patient outcomes, but also for preserving valuable therapeutic resources by enabling timely treatment adaptation. Beyond its role as a biomarker, this study highlights the versatility of ctDNA in offering rich genomic insights. Specifically, CNV burden was extensively characterized, demonstrating a strong correlation with Tfx levels and emerging as a potential molecular stratification tool for patient management. My genomic analysis further identified distinct molecular subgroups, with high CNV burden associated with worse survival outcomes, highlighting its potential role in refining risk assessment and guiding therapeutic decisions in mCRPC. In PSMA-TRNT, not only does CNV burden play a crucial role, but pre-treatment factors also significantly influence treatment response. Understanding these factors is essential for optimizing therapy outcomes and improving patient stratification strategies. My study also underscores the potential of DDR gene alterations, highlighting discrepancies with prior findings that associate these mutations with increased PSMA expression and therapeutic sensitivity. A key next step would be the validation of these gene signatures in independent cohorts to confirm their predictive value and clinical relevance.

While these insights provide a deeper understanding of the molecular landscape of mCRPC, the study is inherently limited by the absence of matched tissue samples, lack of prospective randomization, and cohort heterogeneity. These factors, along with the challenges in distinguishing between clonal populations in cfDNA analysis, underscore the need for further validation through larger, prospective studies.



## VII OUTLOOK

Future research should aim to validate these findings in a larger, prospectively stratified cohort with integrated tissue and plasma analyses. Expanding genomic profiling efforts, particularly through single-cell sequencing approaches, could provide a deeper understanding of tumor heterogeneity and clonal evolution under therapy.

From a clinical perspective, optimizing TFX-based stratification for treatment decision-making may enhance patient selection for PSMA-TNRT, especially in cases with heterogeneous metastatic burdens. Additionally, prospective clinical trials investigating actinium-lutetium therapy are crucial to assess safety, define the optimal therapeutic regimen (e.g., ideal dosing strategy), and evaluate the efficacy of the actinium-lutetium combination therapy.

A notable limitation of this study is the small patient cohort and the lack of full longitudinal sample collection. Given that these treatments were provided under compassionate use, patient follow-up was inconsistent, leading to missing data and limited long-term tracking. Therefore, a broader, systematic clinical evaluation of [ $^{225}\text{Ac}$ ]Ac-/[ $^{177}\text{Lu}$ ]Lu-PSMA-617 therapy is necessary to establish clear treatment guidelines and identify key clinical factors influencing therapy resistance.

Another critical area for further investigation is the role of DDR mutations in modulating treatment response, which remains a topic of ongoing debate. Functional studies are essential to determine their impact on alpha-particle therapy efficacy and their potential contribution to therapy resistance mechanisms.

For validation, it would be ideal to obtain primary tumor material from patients and perform longitudinal assessments. Following clinical validation, these findings could be further explored through functional studies using gene knockouts in cell lines and subsequently evaluated in preclinical models, such as mouse models, to establish mechanistic insights and therapeutic relevance.

Given the remarkable success of Pluvicto<sup>®</sup>, there is great anticipation that tandem [ $^{225}\text{Ac}$ ]Ac-/[ $^{177}\text{Lu}$ ]Lu-PSMA-617 therapy could achieve a similar breakthrough, capitalizing on the complementary strengths of both radionuclides. Looking ahead, this combination therapy may not remain solely an option for terminal patients, but could also be introduced earlier in the treatment paradigm, allowing a broader patient population to benefit from its therapeutic potential, ultimately improving long-term clinical outcomes.





## VIII REFERENCES

1. Hanahan D, Weinberg Robert A. Hallmarks of Cancer: The Next Generation. *Cell*. 2011;144(5):646-74.
2. Bacolla A, Tainer JA. DNA damage response mechanisms and structures fundamental to cancer research progress. *Prog Biophys Mol Biol*. 2019;147:1-3.
3. Adi PKJ, Konidala KK, Yellapu NK, Balasubramanyam L, Matcha B. CGMD: An integrated database of Cancer Genes and Markers. *bioRxiv*. 2014-11-10.
4. Nasheuer HP, Onwubiko NO. Lagging Strand Initiation Processes in DNA Replication of Eukaryotes-Strings of Highly Coordinated Reactions Governed by Multiprotein Complexes. *Genes (Basel)*. 2023;14(5).
5. Mehlen P, Puisieux A, Mehlen P, Puisieux A. Metastasis: a question of life or death. *Nature Reviews Cancer* 2006 6:6. 2006/06;6(6).
6. Fares J, Fares MY, Khachfe HH, Salhab HA, Fares Y, Fares J, et al. Molecular principles of metastasis: a hallmark of cancer revisited. *Signal Transduction and Targeted Therapy* 2020 5:1. 2020-03-12;5(1).
7. Yayan J, Franke K-J, Berger M, Windisch W, Rasche K. Adhesion, metastasis, and inhibition of cancer cells: a comprehensive review. *Molecular Biology Reports*. 2024;51(1):165.
8. Ilin O, Friedl P. Mechanisms of collective cell migration at a glance. *J Cell Sci*. 2009;122(Pt 18):3203-8.
9. Dai X, Xiang L, Li T, Bai Z. Cancer Hallmarks, Biomarkers and Breast Cancer Molecular Subtypes. *J Cancer*. 2016;7(10):1281-94.
10. Brown JS, Amend SR, Austin RH, Gatenby RA, Hammarlund EU, Pienta KJ. Updating the Definition of Cancer. *Molecular Cancer Research*. 2023/11/01;21(11).
11. Watson DM, Barrett A, Spence RA, Twelves C. Pathogenesis of cancer. *Oncology*. 2006/6/01.
12. Jemal A, Bray F, Center MM, Ferlay J, Ward E, Forman D. Global cancer statistics. *CA Cancer J Clin*. 2011;61(2):69-90.
13. Kalender E, Ekin E, Elboğa U, Şahin E. Evaluation of Adrenal Metastases in Prostate Cancer Patients with [68GA]GA-PSMA PET/CT Imaging. *Current Oncology*. 2025;32(3):127.
14. Guo Z, He J, Pan J, Huang L, Cao J, Bai Z, et al. Prevalence and risk factors for incidental prostate cancer in patients after transurethral resection of the prostate with negative results on prostate biopsy: A retrospective study. *Investig Clin Urol*. 2022;63(2):201-6.
15. Lenz J, Michal M, Michal M, Hes O, Konečná P, Lenz D, et al. First Molecular Genetic Characterization of Skene's Gland Adenocarcinoma. *International Journal of Surgical Pathology*. 2021-6;29(4).
16. Narita S, Nara T, Sato H, Koizumi A, Huang M, Inoue T, et al. Research Evidence on High-Fat Diet-Induced Prostate Cancer Development and Progression. *Journal of Clinical Medicine*. 2019 Apr 30;8(5).
17. Bell KJ, Mar CD, Wright G, Dickinson J, Glasziou P. Prevalence of incidental prostate cancer: A systematic review of autopsy studies. *International Journal of Cancer Journal International du Cancer*. 2015 Apr 21;137(7).
18. Osama S, Serboiu C, Taciuc IA, Angelescu E, Petcu C, Priporeanu TA, et al. Current Approach to Complications and Difficulties during Transrectal Ultrasound-Guided Prostate Biopsies. *J Clin Med*. 2024;13(2).
19. Bubendorf L, Schöpfer A, Wagner U, Sauter G, Moch H, Willi N, et al. Metastatic patterns of prostate cancer: an autopsy study of 1,589 patients. *Hum Pathol*. 2000;31(5):578-83.
20. Kim DK, Kim SJ, Moon HS, Park SY, Kim YT, Choi HY, et al. The Role of TURP in the Detection of Prostate Cancer in BPH Patients with Previously Negative Prostate Biopsy. *Korean J Urol*. 2010;51(5):313-7.
21. Mapelli P, Picchio M, Mapelli P, Picchio M. Initial prostate cancer diagnosis and disease staging—the role of choline-PET—CT. *Nature Reviews Urology* 2015 12:9. 2015-08-11;12(9).

22. Gordetsky J, Epstein J. Grading of prostatic adenocarcinoma: current state and prognostic implications. *Diagnostic Pathology*. 2016 Mar 9;11(1).
23. Paner GP, Stadler WM, Hansel DE, Montironi R, Lin DW, Amin MB. Updates in the Eighth Edition of the Tumor-Node-Metastasis Staging Classification for Urologic Cancers. *Eur Urol*. 2018;73(4):560-9.
24. D'Amico AV, Whittington R, Malkowicz SB, Schultz D, Blank K, Broderick GA, et al. Biochemical Outcome After Radical Prostatectomy, External Beam Radiation Therapy, or Interstitial Radiation Therapy for Clinically Localized Prostate Cancer. *JAMA*. 1998/09/16;280(11).
25. Mottet N, Bellmunt J, Bolla M, Briers E, Cumberbatch MG, De Santis M, et al. EAU-ESTRO-SIOG Guidelines on Prostate Cancer. Part 1: Screening, Diagnosis, and Local Treatment with Curative Intent. *Eur Urol*. 2017;71(4):618-29.
26. Haney CM, Kowalewski KF, Westhoff N, Holze S, Checcuci E, Neuberger M, et al. Robot-assisted Versus Conventional Laparoscopic Radical Prostatectomy: A Systematic Review and Meta-analysis of Randomised Controlled Trials. *Eur Urol Focus*. 2023;9(6):930-7.
27. Stephenson AJ, Eastham JA. Role of salvage radical prostatectomy for recurrent prostate cancer after radiation therapy. *J Clin Oncol*. 2005;23(32):8198-203.
28. Chin YF, Lynn N. Systematic Review of Focal and Salvage Cryotherapy for Prostate Cancer. *Cureus*. 2022 Jun 28;14(6).
29. Baskar R, Lee KA, Yeo R, Yeoh K-W. Cancer and Radiation Therapy: Current Advances and Future Directions. *International Journal of Medical Sciences*. 2012/2/27;9(3).
30. Bolla M, Collette L, Blank L, Warde P, Dubois JB, Mirimanoff RO, et al. Long-term results with immediate androgen suppression and external irradiation in patients with locally advanced prostate cancer (an EORTC study): a phase III randomised trial. *Lancet*. 2002;360(9327):103-6.
31. Parker C, Nilsson S, Heinrich D, Helle SI, O'Sullivan JM, Fosså SD, et al. Alpha Emitter Radium-223 and Survival in Metastatic Prostate Cancer. 2013-07-18.
32. Huggins C, Hodges CV. Studies on prostatic cancer. I. The effect of castration, of estrogen and androgen injection on serum phosphatases in metastatic carcinoma of the prostate. *CA Cancer J Clin*. 1972;22(4):232-40.
33. Fernandes R, Costa C, Fernandes R, Barros AN. Inflammation in Prostate Cancer: Exploring the Promising Role of Phenolic Compounds as an Innovative Therapeutic Approach. *Biomedicines*. 2023;11(12):3140.
34. Harris WP, Mostaghel EA, Nelson PS, Montgomery B, Harris WP, Mostaghel EA, et al. Androgen deprivation therapy: progress in understanding mechanisms of resistance and optimizing androgen depletion. *Nature Clinical Practice Urology* 2009 6:2. 2009/02;6(2).
35. Ryan CJ, Smith MR, Fong L, Rosenberg JE, Kantoff P, Raynaud F, et al. Phase I clinical trial of the CYP17 inhibitor abiraterone acetate demonstrating clinical activity in patients with castration-resistant prostate cancer who received prior ketoconazole therapy. *J Clin Oncol*. 2010;28(9):1481-8.
36. de Bono JS, Logothetis CJ, Molina A, Fizazi K, North S, Chu L, et al. Abiraterone and Increased Survival in Metastatic Prostate Cancer. 2011-05-26.
37. Quinn DI, Sandler HM, Horvath LG, Goldkorn A, Eastham JA. The evolution of chemotherapy for the treatment of prostate cancer. *Annals of Oncology*. 2017/11/01;28(11).
38. Sekhoacha M, Riet K, Motloung P, Gumunku L, Adegoke A, Mashele S, et al. Prostate Cancer Review: Genetics, Diagnosis, Treatment Options, and Alternative Approaches. *Molecules* 2022, Vol 27, Page 5730. 2022-09-05;27(17).
39. Waterschoot RABv, Lagas JS, Wagenaar E, Rosing H, Beijnen JH, Schinkel AH. Individual and combined roles of CYP3A, P-glycoprotein (MDR1/ABCB1) and MRP2 (ABCC2) in the pharmacokinetics of docetaxel. *International Journal of Cancer*. 2010/12/15;127(12).
40. AL-Mansouri L, Arasaratnam M, Gurney H. Continuing cabazitaxel beyond 10 cycles for metastatic castrate-resistant prostate cancer: is there a benefit? *European Journal of Hospital Pharmacy*. 2021-03-01;28(2).

41. Rouyer M, Oudard S, Joly F, Fizazi K, Tubach F, Jove J, et al. Overall and progression-free survival with cabazitaxel in metastatic castration-resistant prostate cancer in routine clinical practice: the FUJI cohort. *British Journal of Cancer* 2019 121:12. 2019-11-13;121(12).
42. Watson AS, Gagnon R, Batuyong E, Alimohamed N, Lee-Ying R. Real-World Cabazitaxel Use and Outcomes in Metastatic Castrate-Resistant Prostate Cancer: The Impact of Response to First ARPI. *Clinical Genitourinary Cancer*. 2022/10/01;20(5).
43. Corfield J, Crozier J, Joshua AM, Bolton DM, Lawrentschuk N. Understanding the role of new systemic agents in the treatment of prostate cancer. *BJU International*. 2016;118(S3).
44. Schrader AJ, Boegemann M, Ohlmann C-H, Schnoeller TJ, Krabbe L-M, Hajili T, et al. Enzalutamide in Castration-resistant Prostate Cancer Patients Progressing After Docetaxel and Abiraterone. *European Urology*. 2014/01/01;65(1).
45. Culig Z, Culig Z. Molecular Mechanisms of Enzalutamide Resistance in Prostate Cancer. *Current Molecular Biology Reports* 2017 3:4. 2017-10-23;3(4).
46. Zhang T, Zhu J, George DJ, Armstrong AJ. Enzalutamide versus abiraterone acetate for the treatment of men with metastatic castration-resistant prostate cancer. *Expert Opin Pharmacother*. 2015;16(4):473-85.
47. Chandrasekar T, Yang JC, Gao AC, Evans CP, Chandrasekar T, Yang JC, et al. Targeting molecular resistance in castration-resistant prostate cancer. *BMC Medicine* 2015 13:1. 2015-09-01;13(1).
48. Crowley F, Sterpi M, Buckley C, Margetich L, Handa S, Dovey Z. A Review of the Pathophysiological Mechanisms Underlying Castration-resistant Prostate Cancer. *Research and Reports in Urology*. 2021-06-30;Volume 13.
49. Zustovich F, Fabiani F. Therapeutic opportunities for castration-resistant prostate cancer patients with bone metastases. *Critical Reviews in Oncology/Hematology*. 2014/08/01;91(2).
50. Arbuznikova D, Eder M, Grosu A-L, Meyer PT, Gratzke C, Zamboglou C, et al. Towards Improving the Efficacy of PSMA-Targeting Radionuclide Therapy for Late-Stage Prostate Cancer—Combination Strategies. *Current Oncology Reports*. 2023;25(11):1363-74.
51. Rahbar K, Ahmadzadehfard H, Kratochwil C, Haberkorn U, Schäfers M, Essler M, et al. German Multicenter Study Investigating <sup>177</sup>Lu-PSMA-617 Radioligand Therapy in Advanced Prostate Cancer Patients. *Journal of Nuclear Medicine*. 2017-01-01;58(1).
52. Khreish F, Ebert N, Ries M, Maus S, Rosar F, Bohnenberger H, et al. (225)Ac-PSMA-617/(177)Lu-PSMA-617 tandem therapy of metastatic castration-resistant prostate cancer: pilot experience. *Eur J Nucl Med Mol Imaging*. 2020;47(3):721-8.
53. Kratochwil C, Bruchertseifer F, Giesel FL, Weis M, Verburg FA, Mottaghy F, et al. 225Ac-PSMA-617 for PSMA-Targeted alpha-Radiation Therapy of Metastatic Castration-Resistant Prostate Cancer. *J Nucl Med*. 2016;57(12):1941-4.
54. Chrenková E, Študentová H, Holá K, Kahounová Z, Hendrychová R, Souček K, et al. Castration-resistant prostate cancer monitoring by cell-free circulating biomarkers. *Front Oncol*. 2024;14:1394292.
55. Bryce AH, Alumkal JJ, Armstrong A, Higano CS, Iversen P, Sternberg CN, et al. Radiographic progression with nonrising PSA in metastatic castration-resistant prostate cancer: post hoc analysis of PREVAIL. *Prostate Cancer and Prostatic Diseases* 2017 20:2. 2017-01-24;20(2).
56. Li D, Lv H, Hao X, Hu B, Song Y. Prognostic value of serum alkaline phosphatase in the survival of prostate cancer: evidence from a meta-analysis. *Cancer Manag Res*. 2018;10:3125-39.
57. Forkasiewicz A, Dorociak M, Stach K, Szelachowski P, Tabola R, Augoff K, et al. The usefulness of lactate dehydrogenase measurements in current oncological practice. *Cellular & Molecular Biology Letters* 2020 25:1. 2020-06-09;25(1).
58. Reichert ZR, Morgan TM, Li G, Castellanos E, Snow T, Dall'Olio FG, et al. Prognostic value of plasma circulating tumor DNA fraction across four common cancer types: a real-world outcomes study☆. *Annals of Oncology*. 2023/01/01;34(1).

59. Torquato S, Pallavajjala A, Goldstein A, Toro PV, Silberstein JL, Lee J, et al. Genetic Alterations Detected in Cell-Free DNA Are Associated With Enzalutamide and Abiraterone Resistance in Castration-Resistant Prostate Cancer. *JCO Precision Oncology*. 2019-4(3).
60. Stamey TA, Yang N, Hay AR, McNeal JE, Freiha FS, Redwine E. Prostate-Specific Antigen as a Serum Marker for Adenocarcinoma of the Prostate. *New England Journal of Medicine*. 1987-10-08;317(15).
61. Lilja H, Ulmert D, Vickers AJ, Lilja H, Ulmert D, Vickers AJ. Prostate-specific antigen and prostate cancer: prediction, detection and monitoring. *Nature Reviews Cancer* 2008 8:4. 2008/04;8(4).
62. Thompson IM, Pauler DK, Goodman PJ, Tangen CM, Lucia MS, Parnes HL, et al. Prevalence of Prostate Cancer among Men with a Prostate-Specific Antigen Level  $\leq 4.0$  ng per Milliliter. *New England Journal of Medicine*. 2004-05-27;350(22).
63. Catalona WJ, Southwick PC, Slawin KM, Partin AW, Brawer MK, Flanigan RC, et al. Comparison of percent free PSA, PSA density, and age-specific PSA cutoffs for prostate cancer detection and staging. *Urology*. 2000/08/01;56(2).
64. Yousef GM, Diamandis EP. The new human tissue kallikrein gene family: structure, function, and association to disease. *Endocr Rev*. 2001;22(2):184-204.
65. Darson MF, Pacelli A, Roche P, Rittenhouse HG, Wolfert RL, Young CY, et al. Human glandular kallikrein 2 (hK2) expression in prostatic intraepithelial neoplasia and adenocarcinoma: a novel prostate cancer marker. *Urology*. 1997;49(6):857-62.
66. Koukourakis MI, Giatromanolaki A, Sivridis E, Bougioukas G, Didilis V, Gatter KC, et al. Lactate dehydrogenase-5 (LDH-5) overexpression in non-small-cell lung cancer tissues is linked to tumour hypoxia, angiogenic factor production and poor prognosis. *British Journal of Cancer*. 2003 Aug 26;89(5).
67. Pérez-Tomás R, Pérez-Guillén I. Lactate in the Tumor Microenvironment: An Essential Molecule in Cancer Progression and Treatment. *Cancers*. 2020 Nov 3;12(11).
68. Chen Y, Zhang H, Xu A, Li N, Liu J, Liu C, et al. Elevation of serum l-lactate dehydrogenase B correlated with the clinical stage of lung cancer. *Lung Cancer*. 2006;54(1):95-102.
69. Koukourakis MI, Giatromanolaki A, Panteliadou M, Pouliliou SE, Chondrou PS, Mavropoulou S, et al. Lactate dehydrogenase 5 isoenzyme overexpression defines resistance of prostate cancer to radiotherapy. *British Journal of Cancer* 2014 110:9. 2014-04-08;110(9).
70. Malhotra G, Gattani RG, Shinde RK, Gianchandani SG, Nayak K, Salwan A. Significance of Serum Lactate Dehydrogenase as a Prognostic Marker and Outcome Predictor in Patients With Breast Cancer. *Cureus*. 2024;16(3):e55932.
71. Li G, Gao J, Tao YL, Xu BQ, Tu ZW, Liu ZG, et al. Increased pretreatment levels of serum LDH and ALP as poor prognostic factors for nasopharyngeal carcinoma. *Chin J Cancer*. 2012;31(4):197-206.
72. Mohseny AB, Hogendoorn PC, Cleton-Jansen AM. Osteosarcoma models: from cell lines to zebrafish. *Sarcoma*. 2012;2012:417271.
73. Roodman GD, Guise T. Mechanisms of Osteolytic and Osteoblastic Skeletal Lesions. *Primer on the Metabolic Bone Diseases and Disorders of Mineral Metabolism* 2018. p. 737-42.
74. Makris K, Mousa C, Cavalier E. Alkaline Phosphatases: Biochemistry, Functions, and Measurement. *Calcif Tissue Int*. 2023;112(2):233-42.
75. Jiang Y, Li X, Walt DR. Single-Molecule Analysis Determines Isozymes of Human Alkaline Phosphatase in Serum. *Angewandte Chemie International Edition*. 2020/10/05;59(41).
76. Shen J, Sun Y, Liu X, Zhu Y, Bao B, Gao T, et al. EGFL6 regulates angiogenesis and osteogenesis in distraction osteogenesis via Wnt/ $\beta$ -catenin signaling. *Stem Cell Research & Therapy* 2021 12:1. 2021-07-22;12(1).
77. Ishida M, Kawao N, Mizukami Y, Takafuji Y, Kaji H. Serpinb1a suppresses osteoclast formation. *Biochemistry and Biophysics Reports*. 2021/07/01;26.

78. Mhawech-Fauceglia P, Zhang S, Terracciano L, Sauter G, Chadhuri A, Herrmann FR, et al. Prostate-specific membrane antigen (PSMA) protein expression in normal and neoplastic tissues and its sensitivity and specificity in prostate adenocarcinoma: an immunohistochemical study using multiple tumour tissue microarray technique. *Histopathology*. 2007;50(4):472-83.
79. Tao R, Ni Z, Liu C, Zhu M, Ji X, Chen X, et al. Expression, purification and identification of an immunogenic fragment in the ectodomain of prostate-specific membrane antigen. *Exp Ther Med*. 2016;11(3):747-52.
80. Rinker-Schaeffer CW, Hawkins AL, Griffin CA, Isaacs JT. Localization and physical mapping of the prostate-specific membrane antigen (PSM) gene to human chromosome 11. *Genomics*. 1995;11/01;30(1).
81. Hao G, Kumar A, Dobin T, Öz OK, Hsieh J-T, Sun X. A Multivalent Approach of Imaging Probe Design To Overcome an Endogenous Anion Binding Competition for Noninvasive Assessment of Prostate Specific Membrane Antigen. *Molecular Pharmaceutics*. June 28, 2013;10(8).
82. Szponar P, Petrasz P, Brzeźniakiewicz-Janus K, Drewa T, Zorga P, Adamowicz J. *Frontiers | Precision strikes: PSMA-targeted radionuclide therapy in prostate cancer – a narrative review. Frontiers in Oncology*. 2023/11/16;13.
83. O'Keefe DS, Bacich DJ, Huang SS, Heston WDW. A Perspective on the Evolving Story of PSMA Biology, PSMA-Based Imaging, and Endoradiotherapeutic Strategies. *J Nucl Med*. 2018;59(7):1007-13.
84. Ristau BT, O'Keefe DS, Bacich DJ. The prostate-specific membrane antigen: Lessons and current clinical implications from 20 years of research. *Urologic oncology*. 2013 Dec 8;32(3).
85. Schmittgen TD, Teske S, Vessella RL, True LD, Zakrajsek BA. Expression of prostate specific membrane antigen and three alternatively spliced variants of PSMA in prostate cancer patients. *Int J Cancer*. 2003;107(2):323-9.
86. Yao V, Parwani A, Maier C, Heston WD, Bacich DJ. Moderate expression of prostate-specific membrane antigen, a tissue differentiation antigen and folate hydrolase, facilitates prostate carcinogenesis. *Cancer Res*. 2008;68(21):9070-7.
87. Mackay S, Oduor IO, Burch TC, Main BP, Troyer DA, Semmes OJ, et al. Increased  $\alpha 2,3$ -sialyl N-glycosylated prostate-specific membrane antigen (PSMA) in post-DRE urine is associated with high grade group prostate cancer. *Prostate*. 2024;84(11):1067-75.
88. Farag M, Bolton D, Lawrentschuk N. Prostate-specific membrane antigen for the surgical oncologist: interpreting expression beyond the prostate. *ANZ J Surg*. 2020;90(5):715-8.
89. Zhang S, Wang X, Gao X, Chen X, Li L, Li G, et al. Radiopharmaceuticals and their applications in medicine. *Signal Transduction and Targeted Therapy* 2024 10:1. 2025-01-03;10(1).
90. Kramer-Marek G, Capala J. The role of nuclear medicine in modern therapy of cancer. *Tumour Biol*. 2012;33(3):629-40.
91. Vaz SC, Oliveira F, Herrmann K, Veit-Haibach P. Nuclear medicine and molecular imaging advances in the 21st century. *The British Journal of Radiology*. 2020 May 9;93(1110).
92. Caglic I, Kovac V, Barrett T. Multiparametric MRI - local staging of prostate cancer and beyond. *Radiol Oncol*. 2019;53(2):159-70.
93. Yang DJ, Kim EE, Inoue T. Targeted molecular imaging in oncology. *Ann Nucl Med*. 2006;20(1):1-11.
94. Beheshti M, Langsteger W, Fogelman I. Prostate cancer: role of SPECT and PET in imaging bone metastases. *Semin Nucl Med*. 2009;39(6):396-407.
95. Zamani-Siahkali N, Mirshahvalad SA, Farbod A, Divband G, Pirich C, Veit-Haibach P, et al. SPECT/CT, PET/CT, and PET/MRI for Response Assessment of Bone Metastases. *Seminars in Nuclear Medicine*. 2024/05/01;54(3).
96. Vargas-Ahumada JE, González-Rueda SD, Sinisterra-Solís FA, Casanova-Triviño P, Pitalúa-Cortés Q, Soldevilla-Gallardo I, et al. Diagnostic Performance of (99m)Tc-iPSMA SPECT/CT in the Initial Staging of Patients with Unfavorable Intermediate-, High-, and Very High-Risk Prostate Cancer: A Comparative Analysis with (18)F-PSMA-1007 PET/CT. *Cancers (Basel)*. 2023;15(24).

97. Farolfi A, Calderoni L, Mattana F, Mei R, Telo S, Fanti S, et al. Current and emerging clinical applications of PSMA-PET diagnostic imaging for prostate cancer. *Journal of Nuclear Medicine*. 2021-03-12;62(5).
98. Wallitt KL, Khan SR, Dubash S, Tam HH, Khan S, Barwick TD. Clinical PET Imaging in Prostate Cancer. *Radiographics*. 2017;37(5):1512-36.
99. Mouliere F, Chandrananda D, Piskorz AM, Moore EK, Morris J, Ahlborn LB, et al. Enhanced detection of circulating tumor DNA by fragment size analysis. *Science Translational Medicine*. 2018;10(466):eaat4921.
100. Sartor O, Bono Jd, Chi KN, Fizazi K, Herrmann K, Rahbar K, et al. Lutetium-177–PSMA-617 for Metastatic Castration-Resistant Prostate Cancer. *New England Journal of Medicine*. 2021-09-16;385(12).
101. Nuhn P, De Bono JS, Fizazi K, Freedland SJ, Grilli M, Kantoff PW, et al. Update on Systemic Prostate Cancer Therapies: Management of Metastatic Castration-resistant Prostate Cancer in the Era of Precision Oncology. *Eur Urol*. 2019;75(1):88-99.
102. Benešová M, Schäfer M, Bauder-Wüst U, Afshar-Oromieh A, Kratochwil C, Mier W, et al. Preclinical Evaluation of a Tailor-Made DOTA-Conjugated PSMA Inhibitor with Optimized Linker Moiety for Imaging and Endoradiotherapy of Prostate Cancer. *Journal of Nuclear Medicine*. 2015;56(6):914-20.
103. Broyelle A, Delanoy N, Bimbai AM, Le Deley MC, Penel N, Villers A, et al. Taxanes Versus Androgen Receptor Therapy as Second-Line Treatment for Castrate-Resistant Metastatic Prostate Cancer After First-Line Androgen Receptor Therapy. *Clin Genitourin Cancer*. 2023;21(3):349-56.e2.
104. Shore N, Heidenreich A, Saad F. Predicting Response and Recognizing Resistance: Improving Outcomes in Patients With Castration-resistant Prostate Cancer. *Urology*. 2017;109:6-18.
105. Shore ND, Laliberté F, Ionescu-Iltu R, Yang L, Mahendran M, Lejeune D, et al. Real-World Treatment Patterns and Overall Survival of Patients with Metastatic Castration-Resistant Prostate Cancer in the US Prior to PARP Inhibitors. *Adv Ther*. 2021;38(8):4520-40.
106. Benesova M, Schafer M, Bauder-Wust U, Afshar-Oromieh A, Kratochwil C, Mier W, et al. Preclinical Evaluation of a Tailor-Made DOTA-Conjugated PSMA Inhibitor with Optimized Linker Moiety for Imaging and Endoradiotherapy of Prostate Cancer. *J Nucl Med*. 2015;56(6):914-20.
107. Sheehan B, Neeb A, Buroni L, Paschalis A, Riisnaes R, Gurel B, et al. Prostate-Specific Membrane Antigen Expression and Response to DNA Damaging Agents in Prostate Cancer. *Clin Cancer Res*. 2022;28(14):3104-15.
108. O'Neill E, Kersemans V, Allen PD, Terry SY, Torres JB, Mosley M, et al. Imaging DNA Damage Repair In Vivo After 177Lu-DOTATATE Therapy. *Journal of Nuclear Medicine*. 2020 May;61(5).
109. Matsuya Y, Kai T, Parisi A, Yoshii Y, Sato T, Matsuya Y, et al. Application of a simple DNA damage model developed for electrons to proton irradiation. *Physics in Medicine & Biology*. 2022-10-31;67(21).
110. Nikjoo H, O'Neill P, Wilson WE, Goodhead DT, Nikjoo H, O'Neill P, et al. Computational Approach for Determining the Spectrum of DNA Damage Induced by Ionizing Radiation. *Radiation Research*. 2001/11;156(5).
111. Kratochwil C, Haberkorn U, Giesel FL. (225)Ac-PSMA-617 for Therapy of Prostate Cancer. *Semin Nucl Med*. 2020;50(2):133-40.
112. Sathekge MM, Lawal IO, Bal C, Bruchertseifer F, Ballal S, Cardaci G, et al. Actinium-225-PSMA radioligand therapy of metastatic castration-resistant prostate cancer (WARMTH Act): a multicentre, retrospective study. *The Lancet Oncology*. 2024/02/01;25(2).
113. Feurecker B, Tauber R, Knorr K, Heck M, Beheshti A, Seidl C, et al. Activity and Adverse Events of Actinium-225-PSMA-617 in Advanced Metastatic Castration-resistant Prostate Cancer After Failure of Lutetium-177-PSMA. *European Urology*. 2021/03/01;79(3).
114. van der Doelen MJ, Mehra N, van Oort IM, Looijen-Salamon MG, Janssen MJR, Custers JAE, et al. Clinical outcomes and molecular profiling of advanced metastatic castration-resistant prostate

cancer patients treated with (225)Ac-PSMA-617 targeted alpha-radiation therapy. *Urol Oncol*. 2021;39(10):729.e7-.e16.

115. Kratochwil C, Bruchertseifer F, Giesel FL, Weis M, Verburg FA, Mottaghy F, et al. 225Ac-PSMA-617 for PSMA-Targeted  $\alpha$ -Radiation Therapy of Metastatic Castration-Resistant Prostate Cancer. *Journal of Nuclear Medicine*. 2016-12-01;57(12).

116. Lawal IO, Morgenstern A, Vorster M, Knoesen O, Mahapane J, Hlongwa KN, et al. Hematologic toxicity profile and efficacy of [225Ac]Ac-PSMA-617  $\alpha$ -radioligand therapy of patients with extensive skeletal metastases of castration-resistant prostate cancer. *European Journal of Nuclear Medicine and Molecular Imaging* 2022 49:10. 2022-04-06;49(10).

117. Kratochwil C, Bruchertseifer F, Rathke H, Bronzel M, Apostolidis C, Weichert W, et al. Targeted  $\alpha$ -Therapy of Metastatic Castration-Resistant Prostate Cancer with 225Ac-PSMA-617: Dosimetry Estimate and Empiric Dose Finding. *Journal of Nuclear Medicine*. 2017-10-01;58(10).

118. Feurecker B, Tauber R, Knorr K, Heck M, Beheshti A, Seidl C, et al. Activity and Adverse Events of Actinium-225-PSMA-617 in Advanced Metastatic Castration-resistant Prostate Cancer After Failure of Lutetium-177-PSMA. *Eur Urol*. 2021;79(3):343-50.

119. Langbein T, Kulkarni HR, Schuchardt C, Mueller D, Volk GF, Baum RP. Salivary Gland Toxicity of PSMA-Targeted Radioligand Therapy with (177)Lu-PSMA and Combined (225)Ac- and (177)Lu-Labeled PSMA Ligands (TANDEM-PRLT) in Advanced Prostate Cancer: A Single-Center Systematic Investigation. *Diagnostics (Basel)*. 2022;12(8).

120. Rosar F, Hau F, Bartholoma M, Maus S, Stemler T, Linxweiler J, et al. Molecular imaging and biochemical response assessment after a single cycle of [(225)Ac]Ac-PSMA-617/[(177)Lu]Lu-PSMA-617 tandem therapy in mCRPC patients who have progressed on [(177)Lu]Lu-PSMA-617 monotherapy. *Theranostics*. 2021;11(9):4050-60.

121. Mandel P, Metais P. [Nuclear Acids In Human Blood Plasma]. *C R Seances Soc Biol Fil*. 1948;142(3-4):241-3.

122. Tatischeff I. Cancer-Devoted Liquid Biopsies and Applications to Prostate Cancer. *Journal of Neoplasms*. 2018/05/30;3(2).

123. Cisneros-Villanueva M, Hidalgo-Perez L, Rios-Romero M, Cedro-Tanda A, Ruiz-Villavicencio CA, Page K, et al. Cell-free DNA analysis in current cancer clinical trials: a review. *Br J Cancer*. 2022;126(3):391-400.

124. Heitzer E, Perakis S, Geigl JB, Speicher MR. The potential of liquid biopsies for the early detection of cancer. *NPJ Precis Oncol*. 2017;1(1):36.

125. Wu K, Xing F, Wu S-Y, Watabe K. Extracellular vesicles as emerging targets in cancer: Recent development from bench to bedside. *Biochimica et Biophysica Acta (BBA) - Reviews on Cancer*. 2017/12/01;1868(2).

126. Alix-Panabières C, Pantel K. Liquid Biopsy: From Discovery to Clinical Application. *Cancer Discovery*. 2021;11(4):858-73.

127. Narayan P, Ghosh S, Philip R, Barrett JC, McCormack RT, Odegaard JI, et al. State of the Science and Future Directions for Liquid Biopsies in Drug Development. *The Oncologist*. 2020/09/01;25(9).

128. Alix-Panabières C, Pantel K. Liquid Biopsy: From Discovery to Clinical Application. *Cancer Discovery*. 2021/04/01;11(4).

129. Zulato E, Attili I, Pavan A, Nardo G, Del Bianco P, Boscolo Bragadin A, et al. Early assessment of KRAS mutation in cfDNA correlates with risk of progression and death in advanced non-small-cell lung cancer. *Br J Cancer*. 2020;123(1):81-91.

130. Zulato E, Del Bianco P, Nardo G, Attili I, Pavan A, Boscolo Bragadin A, et al. Longitudinal liquid biopsy anticipates hyperprogression and early death in advanced non-small cell lung cancer patients treated with immune checkpoint inhibitors. *Br J Cancer*. 2022;127(11):2034-42.

131. Zulato E, Tosello V, Nardo G, Bonanno L, Del Bianco P, Indraccolo S. Implementation of Next Generation Sequencing-Based Liquid Biopsy for Clinical Molecular Diagnostics in Non-Small Cell Lung Cancer (NSCLC) Patients. *Diagnostics (Basel)*. 2021;11(8).

132. Bidard FC, Fehm T, Ignatiadis M, Smerage JB, Alix-Panabières C, Janni W, et al. Clinical application of circulating tumor cells in breast cancer: overview of the current interventional trials. *Cancer Metastasis Rev.* 2013;32(1-2):179-88.
133. Pantel K, Alix-Panabières C. Real-time liquid biopsy in cancer patients: fact or fiction? *Cancer Res.* 2013;73(21):6384-8.
134. Barbany G, Arthur C, Liedén A, Nordenskjöld M, Rosenquist R, Tesi B, et al. Cell-free tumour DNA testing for early detection of cancer – a potential future tool. *Journal of Internal Medicine.* 2019;286(2):118-36.
135. Thierry AR, El Messaoudi S, Gahan PB, Anker P, Stroun M. Origins, structures, and functions of circulating DNA in oncology. *Cancer Metastasis Rev.* 2016;35(3):347-76.
136. Barbany G, Arthur C, Liedén A, Nordenskjöld M, Rosenquist R, Tesi B, et al. *Journal of Internal Medicine* | Wiley Online Library. *Journal of Internal Medicine.* 2019/08/01;286(2).
137. Jahr S, Hentze H, Englisch S, Hardt D, Fackelmayer FO, Hesch RD, et al. DNA fragments in the blood plasma of cancer patients: quantitations and evidence for their origin from apoptotic and necrotic cells. *Cancer Res.* 2001;61(4):1659-65.
138. Kujala J, Hartikainen JM, Tengström M, Sironen R, Auvinen P, Kosma VM, et al. Circulating Cell-Free DNA Reflects the Clonal Evolution of Breast Cancer Tumors. *Cancers (Basel).* 2022;14(5).
139. Tug S, Helmig S, Deichmann ER, Schmeier-Jürchott A, Wagner E, Zimmermann T, et al. Exercise-induced increases in cell free DNA in human plasma originate predominantly from cells of the haematopoietic lineage. *Exerc Immunol Rev.* 2015;21:164-73.
140. Snyder MW, Kircher M, Hill AJ, Daza RM, Shendure J. Cell-free DNA Comprises an In Vivo Nucleosome Footprint that Informs Its Tissues-Of-Origin. *Cell.* 2016;164(1-2):57-68.
141. Tamkovich SN, Cherepanova AV, Kolesnikova EV, Rykova EY, Pyshnyi DV, Vlassov VV, et al. Circulating DNA and DNase activity in human blood. *Ann N Y Acad Sci.* 2006;1075:191-6.
142. Lo YM, Zhang J, Leung TN, Lau TK, Chang AM, Hjelm NM. Rapid clearance of fetal DNA from maternal plasma. *Am J Hum Genet.* 1999;64(1):218-24.
143. Cervena K, Vodicka P, Vymetalkova V. Diagnostic and prognostic impact of cell-free DNA in human cancers: Systematic review. *Mutation Research/Reviews in Mutation Research.* 2019/07/01;781.
144. Mattox AK, Douville C, Wang Y, Popoli M, Ptak J, Silliman N, et al. The origin of highly elevated cell-free DNA in healthy individuals and patients with pancreatic, colorectal, lung, or ovarian cancer. *Cancer discovery.* 2023 Oct 5;13(10).
145. Yan Y-y, Guo Q-r, Wang F-h, Adhikari R, Zhu Z-y, Zhang H-y, et al. Cell-Free DNA: Hope and Potential Application in Cancer. *Frontiers in Cell and Developmental Biology.* 2021 Feb 22;9.
146. Aquino IMC, Pascut D. Liquid biopsy: New opportunities for precision medicine in hepatocellular carcinoma care. *Annals of Hepatology.* 2024/03/01;29(2).
147. Mouliere F, Chandrananda D, Piskorz AM, Moore EK, Morris J, Ahlborn LB, et al. Enhanced detection of circulating tumor DNA by fragment size analysis. *Science Translational Medicine.* 2018-11-07.
148. Lapin M, Olteidal S, Tjensvoll K, Buhl T, Smaaland R, Garresori H, et al. Fragment size and level of cell-free DNA provide prognostic information in patients with advanced pancreatic cancer. *Journal of Translational Medicine* 2018 16:1. 2018-11-06;16(1).
149. Bronkhorst AJ, Holdenrieder S, Bronkhorst AJ, Holdenrieder S. The changing face of circulating tumor DNA (ctDNA) profiling: Factors that shape the landscape of methodologies, technologies, and commercialization. *Medizinische Genetik.* 2023-12-01;35(4).
150. Silva S, Danson S, Teare D, Taylor F, Bradford J, McDonagh AJG, et al. Genome-Wide Analysis of Circulating Cell-Free DNA Copy Number Detects Active Melanoma and Predicts Survival. *Clinical Chemistry.* 2018/09/01;64(9).
151. Tsui DWY, Murtaza M, Wong ASC, Rueda OM, Smith CG, Chandrananda D, et al. Dynamics of multiple resistance mechanisms in plasma DNA during EGFR-targeted therapies in non-small cell lung cancer. *EMBO Molecular Medicine.* 2018 May 30;10(6).



152. Openshaw MR, Suwaidan AA, Ottolini B, Fernandez-Garcia D, Richards CJ, Page K, et al. Longitudinal monitoring of circulating tumour DNA improves prognostication and relapse detection in gastroesophageal adenocarcinoma. *Br J Cancer*. 2020;123(8):1271-9.
153. Paracchini L, Beltrame L, Grassi T, Inglesi A, Fruscio R, Landoni F, et al. Genome-wide Copy-number Alterations in Circulating Tumor DNA as a Novel Biomarker for Patients with High-grade Serous Ovarian Cancer. *Clinical Cancer Research*. 2021/05/01;27(9).
154. Chen X, Chang C-W, Spoerke JM, Yoh KE, Kapoor V, Baudo C, et al. Low-pass Whole-genome Sequencing of Circulating Cell-free DNA Demonstrates Dynamic Changes in Genomic Copy Number in a Squamous Lung Cancer Clinical Cohort. *Clinical Cancer Research*. 2019/04/01;25(7).
155. Kwan EM, Fettke H, Bukczynska P, Ng N, Hauser C, Graham L-JK, et al. Plasma cell-free DNA (cfDNA) profiling of copy number variation (CNV) to identify poor prognostic biomarkers in metastatic castration-resistant prostate cancer (mCRPC). *Journal of Clinical Oncology*. 2020-02-20;38(6\_suppl).
156. Dietz S, Christopoulos P, Yuan Z, Angeles AK, Gu L, Volckmar A-L, et al. Longitudinal therapy monitoring of ALK-positive lung cancer by combined copy number and targeted mutation profiling of cell-free DNA. *EBioMedicine*. 2020 Nov 9;62.
157. Gambaro K, Marques M, McNamara S, Tertre MCd, Diaz Z, Hoffert C, et al. Copy number and transcriptome alterations associated with metastatic lesion response to treatment in colorectal cancer. *Clinical and Translational Medicine*. 2021 May 1;11(4).
158. Belic J, Graf R, Bauernhofer T, Cherkas Y, Ulz P, Waldispuehl-Geigl J, et al. Genomic alterations in plasma DNA from patients with metastasized prostate cancer receiving abiraterone or enzalutamide. *International Journal of Cancer*. 2018/09/01;143(5).
159. Romano C, Martorana F, Pennisi MS, Stella S, Massimino M, Tirrò E, et al. Opportunities and Challenges of Liquid Biopsy in Thyroid Cancer. *Int J Mol Sci*. 2021;22(14).
160. Gorges K, Wiltfang L, Gorges TM, Sartori A, Hildebrandt L, Keller L, et al. Intra-Patient Heterogeneity of Circulating Tumor Cells and Circulating Tumor DNA in Blood of Melanoma Patients. *Cancers (Basel)*. 2019;11(11).
161. Noguchi T, Sakai K, Iwahashi N, Matsuda K, Matsukawa H, Yahata T, et al. Changes in the gene mutation profiles of circulating tumor DNA detected using CAPP-Seq in neoadjuvant chemotherapy-treated advanced ovarian cancer. *Oncology Letters*. 2020 Jan 28;19(4).
162. Kang S, Li Q, Chen Q, Zhou Y, Park S, Lee G, et al. CancerLocator: non-invasive cancer diagnosis and tissue-of-origin prediction using methylation profiles of cell-free DNA. *Genome Biol*. 2017;18(1):53.
163. Liu H. The prognostic significance of circulating tumor DNA in prostate cancer: A systematic review and meta-analysis. *Journal of Clinical Oncology*. 2025;43(5\_suppl):214-.
164. van der Doelen MJ, Mehra N, van Oort IM, Looijen-Salamon MG, Janssen MJR, Custers JAE, et al. Clinical outcomes and molecular profiling of advanced metastatic castration-resistant prostate cancer patients treated with (225)Ac-PSMA-617 targeted alpha-radiation therapy. *Urol Oncol*. 2021;39(10):729 e7- e16.
165. Kratochwil C, Bruchertseifer F, Rathke H, Hohenfellner M, Giesel FL, Haberkorn U, et al. Targeted  $\alpha$ -Therapy of Metastatic Castration-Resistant Prostate Cancer with (225)Ac-PSMA-617: Swimmer-Plot Analysis Suggests Efficacy Regarding Duration of Tumor Control. *J Nucl Med*. 2018;59(5):795-802.
166. Adalsteinsson VA, Ha G, Freeman SS, Choudhury AD, Stover DG, Parsons HA, et al. Scalable whole-exome sequencing of cell-free DNA reveals high concordance with metastatic tumors. *Nature Communications* 2017 8:1. 2017-11-06;8(1).
167. Choudhury AD, Werner L, Francini E, Wei XX, Ha G, Freeman SS, et al. Tumor fraction in cell-free DNA as a biomarker in prostate cancer. *JCI Insight*. 2018;3(21).
168. Obuchowski NA. Nonparametric analysis of clustered ROC curve data. *Biometrics*. 1997;53(2):567-78.

169. Mermel CH, Schumacher SE, Hill B, Meyerson ML, Beroukhi R, Getz G, et al. GISTIC2.0 facilitates sensitive and confident localization of the targets of focal somatic copy-number alteration in human cancers. *Genome Biology* 2011 12:4. 2011-04-28;12(4).
170. Robinson D, Van Allen EM, Wu YM, Schultz N, Lonigro RJ, Mosquera JM, et al. Integrative clinical genomics of advanced prostate cancer. *Cell*. 2015;161(5):1215-28.
171. Annala M, Vandekerckhove G, Khalaf D, Taavitsainen S, Beja K, Warner EW, et al. Circulating Tumor DNA Genomics Correlate with Resistance to Abiraterone and Enzalutamide in Prostate Cancer. *Cancer Discovery*. 2018/04/01;8(4).
172. Seitz AK, Thoene S, Bietenbeck A, Nawroth R, Tauber R, Thalgott M, et al. AR-V7 in Peripheral Whole Blood of Patients with Castration-resistant Prostate Cancer: Association with Treatment-specific Outcome Under Abiraterone and Enzalutamide. *Eur Urol*. 2017;72(5):828-34.
173. Knutson TP, Luo B, Kobilka A, Lyman J, Guo S, Munro SA, et al. AR alterations inform circulating tumor DNA detection in metastatic castration resistant prostate cancer patients. *Nature Communications* 2024 15:1. 2024-12-11;15(1).
174. Ledet EM, Cotogno P, Hatton W, Jaeger E, Moses MW, Manogue C, et al. Androgen receptor cfDNA longitudinal mutational analysis in metastatic castrate-resistant prostate cancer. *Journal of Clinical Oncology*. 2020-02-20;38(6\_suppl).
175. De Giorgi U, Sansovini M, Severi S, Nicolini S, Monti M, Gurioli G, et al. Circulating androgen receptor gene amplification and resistance to (177)Lu-PSMA-617 in metastatic castration-resistant prostate cancer: results of a Phase 2 trial. *Br J Cancer*. 2021;125(9):1226-32.
176. Choudhury AD, Werner L, Francini E, Wei XX, Ha G, Freeman SS, et al. Tumor fraction in cell-free DNA as a biomarker in prostate cancer. *JCI Insight*. 2018/11/02;3(21).
177. Prensner JR, Rubin MA, Wei JT, Chinnaiyan AM. Beyond PSA: The next generation of prostate cancer biomarkers. *Science translational medicine*. 2012 Mar 28;4(127).
178. Gafita A, Heck MM, Rauscher I, Tauber R, Cala L, Franz C, et al. Early Prostate-Specific Antigen Changes and Clinical Outcome After 177Lu-PSMA Radionuclide Treatment in Patients with Metastatic Castration-Resistant Prostate Cancer. *Journal of Nuclear Medicine*. 2020-10-01;61(10).
179. Bakht MK, Derecichei I, Li Y, Ferraiuolo R-M, Dunning M, Oh SW, et al. Neuroendocrine differentiation of prostate cancer leads to PSMA suppression. *Endocrine-Related Cancer*. 2019-02-01;26(2).
180. Tourinho-Barbosa R, Srougi V, Nunes-Silva I, Baghdadi M, Rembeye G, Eifel SS, et al. Biochemical recurrence after radical prostatectomy: what does it mean? *International Brazilian Journal of Urology : official journal of the Brazilian Society of Urology*. Jan-Feb 2018;44(1).
181. Bräuer A, Grubert LS, Roll W, Schrader AJ, Schäfers M, Bögemann M, et al. (177)Lu-PSMA-617 radioligand therapy and outcome in patients with metastasized castration-resistant prostate cancer. *Eur J Nucl Med Mol Imaging*. 2017;44(10):1663-70.
182. Schlack K, Krabbe L-M, Rahbar K, Isenberg K, Semjonow A, Schrader AJ, et al. ALP bouncing and LDH normalization in bone metastatic castration-resistant prostate cancer patients under therapy with Enzalutamide: an exploratory analysis. *Translational Andrology and Urology*. 2021 Oct;10(10).
183. Li F, Xiang H, Pang Z, Chen Z, Dai J, Chen S, et al. Association between lactate dehydrogenase levels and oncologic outcomes in metastatic prostate cancer: A meta-analysis. *Cancer Medicine*. 2020 May 26;9(19).
184. Mishra D, Banerjee D. Lactate Dehydrogenases as Metabolic Links between Tumor and Stroma in the Tumor Microenvironment. *Cancers*. 2019 May 29;11(6).
185. Lukacova S, Sørensen BS, Alsner J, Overgaard J, Horsman MR. The impact of hypoxia on the activity of lactate dehydrogenase in two different pre-clinical tumour models. *Acta Oncol*. 2008;47(5):941-7.
186. Karzai FH, Madan RA, Figg WD. Beyond PSA: Managing Modern Therapeutic Options in Metastatic Castration-Resistant Prostate Cancer. *Southern medical journal*. 2015 Apr;108(4).

187. Hartrampf PE, Bundschuh RA, Weinzierl F-X, Serfling SE, Kosmala A, Seitz AK, et al. mCRPC patients with PSA fluctuations under radioligand therapy have comparable survival benefits relative to patients with sustained PSA decrease. *European Journal of Nuclear Medicine and Molecular Imaging*. 2022 Jul 19;49(13).
188. Heinrich D, Bruland Ø, Guise TA, Suzuki H, Sartor O. Alkaline phosphatase in metastatic castration-resistant prostate cancer: reassessment of an older biomarker. *Future Oncol*. 2018;14(24):2543-56.
189. Jiang T, Zeng Q, He J. Do alkaline phosphatases have great potential in the diagnosis, prognosis, and treatment of tumors? *Translational Cancer Research*. 2023 Oct 20;12(10).
190. Annala M, Vandekerckhove G, Khalaf D, Taavitsainen S, Beja K, Warner EW, et al. Circulating Tumor DNA Genomics Correlate with Resistance to Abiraterone and Enzalutamide in Prostate Cancer. *Cancer Discovery*. 2018;8(4):444-57.
191. Bluemn EG, Coleman IM, Lucas JM, Coleman RT, Hernandez-Lopez S, Tharakan R, et al. Androgen Receptor Pathway-Independent Prostate Cancer Is Sustained through FGF Signaling. *Cancer Cell*. 2017;32(4):474-89.e6.
192. Beltran H, Tomlins S, Aparicio A, Arora V, Rickman D, Ayala G, et al. Aggressive Variants of Castration-Resistant Prostate Cancer. *Clinical Cancer Research*. 2014;20(11):2846-50.
193. Aggarwal R, Romero GR, Friedl V, Weinstein A, Foye A, Huang J, et al. Clinical and genomic characterization of Low PSA Secretors: a unique subset of metastatic castration resistant prostate cancer. *Prostate Cancer and Prostatic Diseases* 2020 24:1. 2020-04-14;24(1).
194. Yuan T-C, Veeramani S, Lin M-F, Yuan T-C, Veeramani S, Lin M-F. Neuroendocrine-like prostate cancer cells: neuroendocrine transdifferentiation of prostate adenocarcinoma cells. *Endocrine-Related Cancer*. 2007-09-01;14(3).
195. Reichard CA, Gregg JR, Achim MF, Aparicio AM, Pettaway CA, Pisters LL, et al. Radical Prostatectomy in Metastatic Castration-resistant Prostate Cancer: Feasibility, Safety, and Quality of Life Outcomes. *European Urology*. 2018/08/01;74(2).
196. Fonseca NM, Maurice-Dror C, Herberts C, Tu W, Fan W, Murtha AJ, et al. Prediction of plasma ctDNA fraction and prognostic implications of liquid biopsy in advanced prostate cancer. *Nature Communications* 2024 15:1. 2024-02-28;15(1).
197. Carbonell C, Frigola J, Pardo N, Callejo A, Iranzo P, Valdivia A, et al. Dynamic changes in circulating tumor DNA assessed by shallow whole-genome sequencing associate with clinical efficacy of checkpoint inhibitors in NSCLC. *Mol Oncol*. 2023;17(5):779-91.
198. Paracchini L, Beltrame L, Grassi T, Inglesi A, Fruscio R, Landoni F, et al. Genome-wide Copy-number Alterations in Circulating Tumor DNA as a Novel Biomarker for Patients with High-grade Serous Ovarian Cancer. *Clinical Cancer Research*. 2021;27(9):2549-59.
199. Nader-Marta G, Monteforte M, Agostinetto E, Cinquini M, Martins-Branco D, Langouo M, et al. Circulating tumor DNA for predicting recurrence in patients with operable breast cancer: a systematic review and meta-analysis☆. *ESMO Open*. 2024/03/01;9(3).
200. Sweeney CJ, Petry R, Xu C, Childress M, He J, Fabrizio D, et al. Circulating Tumor DNA Assessment for Treatment Monitoring Adds Value to PSA in Metastatic Castration-Resistant Prostate Cancer. *Clinical Cancer Research*. 2024/09/15;30(18).
201. Garcia-Murillas I, Cutts RJ, Walsh-Crestani G, Phillips E, Hrebien S, Dunne K, et al. Longitudinal monitoring of circulating tumor DNA to detect relapse early and predict outcome in early breast cancer. *Breast Cancer Research and Treatment* 2024 209:3. 2024-10-18;209(3).
202. Wang K, Wang X, Pan Q, Zhao B. Liquid biopsy techniques and pancreatic cancer: diagnosis, monitoring, and evaluation. *Mol Cancer*. 2023;22(1):167.
203. Abbosh C, Birkbak NJ, Swanton C. Early stage NSCLC - challenges to implementing ctDNA-based screening and MRD detection. *Nat Rev Clin Oncol*. 2018;15(9):577-86.
204. Siravegna G, Marsoni S, Siena S, Bardelli A. Integrating liquid biopsies into the management of cancer. *Nat Rev Clin Oncol*. 2017;14(9):531-48.

205. Aravanis AM, Lee M, Klausner RD. Next-Generation Sequencing of Circulating Tumor DNA for Early Cancer Detection. *Cell*. 2017;168(4):571-4.
206. Wan JCM, Massie C, Garcia-Corbacho J, Mouliere F, Brenton JD, Caldas C, et al. Liquid biopsies come of age: towards implementation of circulating tumour DNA. *Nat Rev Cancer*. 2017;17(4):223-38.
207. Dietz S, Christopoulos P, Yuan Z, Angeles AK, Gu L, Volckmar AL, et al. Longitudinal therapy monitoring of ALK-positive lung cancer by combined copy number and targeted mutation profiling of cell-free DNA. *EBioMedicine*. 2020;62:103103.
208. Dietz S, Christopoulos P, Gu L, Volckmar AL, Endris V, Yuan Z, et al. Serial liquid biopsies for detection of treatment failure and profiling of resistance mechanisms in KLC1-ALK-rearranged lung cancer. *Cold Spring Harb Mol Case Stud*. 2019;5(6).
209. De Giorgi U, Sansovini M, Severi S, Nicolini S, Monti M, Gurioli G, et al. Circulating androgen receptor gene amplification and resistance to 177Lu-PSMA-617 in metastatic castration-resistant prostate cancer: results of a Phase 2 trial. *British Journal of Cancer*. 2021;125(9):1226-32.
210. Grist E, Friedrich S, Brawley C, Mendes L, Parry M, Ali A, et al. Accumulation of copy number alterations and clinical progression across advanced prostate cancer. *Genome Medicine*. 2022;14(1):102.
211. Fadlullah MZH, Nix D, Herberts C, Maurice-Dror C, Wyatt AW, Schmidt B, et al. Multi-gene risk score for prediction of clinical outcomes in treatment-naïve metastatic castrate-resistant prostate cancer. *JNCI Cancer Spectr*. 2025;9(2).
212. Rathke H, Winter E, Bruchertseifer F, Röhrich M, Giesel FL, Haberkorn U, et al. Deescalated 225Ac-PSMA-617 Versus 177Lu/225Ac-PSMA-617 Cocktail Therapy: A Single-Center Retrospective Analysis of 233 Patients. *Journal of Nuclear Medicine*. 2024-07-01;65(7).
213. Sobhani N, Sirico M, Generali D, Zanconati F, Scaggiante B. Circulating cell-free nucleic acids as prognostic and therapy predictive tools for metastatic castrate-resistant prostate cancer. *World J Clin Oncol*. 2020;11(7):450-63.
214. Afshar-Oromieh A, Debus N, Uhrig M, Hope TA, Evans MJ, Holland-Letz T, et al. Impact of long-term androgen deprivation therapy on PSMA ligand PET/CT in patients with castration-sensitive prostate cancer. *Eur J Nucl Med Mol Imaging*. 2018;45(12):2045-54.
215. Ahmadzadehfard H, Rahbar K, Baum RP, Seifert R, Kessel K, Bögemann M, et al. Prior therapies as prognostic factors of overall survival in metastatic castration-resistant prostate cancer patients treated with [177Lu]Lu-PSMA-617. A WARMTH multicenter study (the 617 trial). *European Journal of Nuclear Medicine and Molecular Imaging* 2020 48:1. 2020-05-08;48(1).
216. Sathekge M, Bruchertseifer F, Knoesen O, Reyneke F, Lawal I, Lengana T, et al. (225)Ac-PSMA-617 in chemotherapy-naïve patients with advanced prostate cancer: a pilot study. *Eur J Nucl Med Mol Imaging*. 2019;46(1):129-38.
217. Ahmadzadehfard H, Zimbelmann S, Yordanova A, Fimmers R, Kürpig S, Eppard E, et al. Radioligand therapy of metastatic prostate cancer using 177 Lu-PSMA-617 after radiation exposure to 223 Ra-dichloride. *Oncotarget*. 2017-02-25;8(33).
218. Wyatt A, Annala M, Aggarwal R, Beja K, Feng F, Youngren J, et al. Concordance of Circulating Tumor DNA and Matched Metastatic Tissue Biopsy in Prostate Cancer. *Journal of the National Cancer Institute*. 2017.
219. Chi KN, Barnicle A, Sibilla C, Lai Z, Corcoran C, Barrett JC, et al. Detection of BRCA1, BRCA2, and ATM Alterations in Matched Tumor Tissue and Circulating Tumor DNA in Patients with Prostate Cancer Screened in PROfound. *Clin Cancer Res*. 2023;29(1):81-91.
220. Kluth M, Al Kilani Z, Özden C, Hussein K, Frogh S, Möller-Koop C, et al. 5q21 deletion is often heterogeneous in prostate cancer. *Genes Chromosomes Cancer*. 2019;58(8):509-15.
221. Kluth M, Jung S, Habib O, Eshagzaei M, Heini A, Amschler N, et al. Deletion lengthening at chromosomes 6q and 16q targets multiple tumor suppressor genes and is associated with an increasingly poor prognosis in prostate cancer. *Oncotarget*. 2017 Nov 11;8(65).

222. Enfield KSS, Anderson C, Marshall E, Ng KW, Minatel BdC, Rowbotham DA, et al. ELF3 amplification at 1q32.1 promotes SMAD4-independent tumorigenesis. *Journal of Thoracic Oncology*. 2016/02/01;11(2).
223. Mejía-Hernández JO, Raghu D, Caramia F, Clemons N, Fujihara K, Riseborough T, et al. Targeting MDM4 as a Novel Therapeutic Approach in Prostate Cancer Independent of p53 Status. *Cancers*. 2022 Aug 16;14(16).
224. Alshalafa M, Nguyen T, Stopsack K, Khan A, Franco I, Seldon C, et al. Chromosome 8q Arm Overexpression is Associated with Worse Prostate Cancer Prognosis. *Urologic oncology*. 2022 Nov 15;41(2).
225. Chen Y, Sadasivan SM, She R, Datta I, Taneja K, Chitale D, et al. Breast and prostate cancers harbor common somatic copy number alterations that consistently differ by race and are associated with survival. *BMC Medical Genomics* 2020 13:1. 2020-08-20;13(1).
226. Choudhury AD, Schinzel AC, Cotter MB, Lis RT, Labella K, Lock YJ, et al. Castration resistance in prostate cancer is mediated by the kinase NEK6. *Cancer research*. 2016 Nov 29;77(3).
227. Lee YC, Lin SC, Yu G, Zhu M, Song JH, Rivera K, et al. Prostate tumor-induced stromal reprogramming generates Tenascin C that promotes prostate cancer metastasis through YAP/TAZ inhibition. *Oncogene*. 2022;41(6):757-69.
228. Ruiz C, Holz DR, Oeggerli M, Schneider S, Gonzales IM, Kiefer JM, et al. Amplification and overexpression of vinculin are associated with increased tumour cell proliferation and progression in advanced prostate cancer. *J Pathol*. 2011;223(4):543-52.
229. Chan RJ, Feng G-S. PTPN11 is the first identified proto-oncogene that encodes a tyrosine phosphatase. *Blood*. 2006 Oct 19;109(3).
230. Sattler H-P, Rohde V, Bonkhoff H, Zwergel T, Wullich B. Comparative genomic hybridization reveals DNA copy number gains to frequently occur in human prostate cancer. *The Prostate*. 1999/05/01;39(2).
231. Nunes-Xavier CE, Mingo J, López JI, Pulido R. The role of protein tyrosine phosphatases in prostate cancer biology. *Biochimica et Biophysica Acta (BBA) - Molecular Cell Research*. 2019/01/01;1866(1).
232. Pan Y, Lui W-O, Nupponen N, Larsson C, Isola J, Visakorpi T, et al. 5q11, 8p11, and 10q22 are recurrent chromosomal breakpoints in prostate cancer cell lines. *Genes, Chromosomes and Cancer*. 2001/02/01;30(2).
233. Jividen K, Kedzierska KZ, Yang C-S, Szlachta K, Ratan A, Paschal BM, et al. Genomic analysis of DNA repair genes and androgen signaling in prostate cancer. *BMC Cancer* 2018 18:1. 2018-10-10;18(1).
234. Konishi N, Nakamura M, Kishi M, Ishida E, Shimada K, Matsuyoshi S, et al. Genetic mapping of allelic loss on chromosome 6q within heterogeneous prostate carcinoma. *Cancer Sci*. 2003;94(9):764-8.
235. Kluth M, Amschler NN, Galal R, Möller-Koop C, Barrow P, Tsourlakis MC, et al. Deletion of 8p is an independent prognostic parameter in prostate cancer. *Oncotarget*. 2016 Nov 17;8(1).
236. Cai Y, Crowther J, Pastor T, Abbasi Asbagh L, Baietti MF, De Troyer M, et al. Loss of Chromosome 8p Governs Tumor Progression and Drug Response by Altering Lipid Metabolism. *Cancer Cell*. 2016;29(5):751-66.
237. Jakoubek P, Cutano V, González-Morena JM, Keckesova Z. Mitochondrial Tumor Suppressors—The Energetic Enemies of Tumor Progression. *Cancer Research*. 2021 Jun 28;81(18).
238. Cheng SY, Yue S. Role and regulation of human tumor suppressor SUFU in Hedgehog signaling. *Adv Cancer Res*. 2008;101:29-43.
239. Herbst RA, Gutzmer R, Matiaske F, Mommert S, Casper U, Kapp A, et al. Identification of two distinct deletion targets at 11q23 in cutaneous malignant melanoma. *International Journal of Cancer*. 1999/01/18;80(2).

240. Kluth M, Scherzai S, Büschek F, Fraune C, Möller K, Höflmayer D, et al. 13q deletion is linked to an adverse phenotype and poor prognosis in prostate cancer. *Genes, Chromosomes and Cancer*. 2018/10/01;57(10).
241. Kluth M, Runte F, Barow P, Omari J, Abdelaziz ZM, Paustian L, et al. Concurrent deletion of 16q23 and PTEN is an independent prognostic feature in prostate cancer. *International Journal of Cancer*. 2015/11/15;137(10).
242. Ulz P, Belic J, Graf R, Auer M, Lafer I, Fischereder K, et al. Whole-genome plasma sequencing reveals focal amplifications as a driving force in metastatic prostate cancer. *Nature Communications* 2016 7:1. 2016-06-22;7(1).
243. Konig JJ, Teubel W, Romijn JC, Schroder FH, Hagemeljer A. Gain and loss of chromosomes 1, 7, 8, 10, 18, and Y in 46 prostate cancers. *Human Pathology*. 1996/07/01;27(7).
244. Jamaspishvili T, Berman DM, Ross AE, Scher HI, Marzo AMD, Squire JA, et al. Clinical implications of PTEN loss in prostate cancer. *Nature reviews Urology*. 2018 Feb 20;15(4).
245. Chakraborty G, Nandakumar S, Hirani R, Nguyen B, Stopsack KH, Kreitzer C, et al. The Impact of PIK3R1 Mutations and Insulin-PI3K-Glycolytic Pathway Regulation in Prostate Cancer. *Clin Cancer Res*. 2022;28(16):3603-17.
246. Wang J, Kang W-M, Yu J-C, Liu Y-Q, Meng Q-B, Cao Z-J. Cadherin-17 induces tumorigenesis and lymphatic metastasis in gastric cancer through activation of NFκB signaling pathway. *Cancer Biology & Therapy*. 2013-3-1;14(3).
247. Warner E, Herberts C, Fu S, Yip S, Wong A, Wang G, et al. BRCA2, ATM, and CDK12 Defects Differentially Shape Prostate Tumor Driver Genomics and Clinical Aggression. *Clinical Cancer Research*. 2021/03/15;27(6).
248. Shen JP, Srivas R, Gross A, Li J, Jaehnig EJ, Sun SM, et al. Chemogenetic profiling identifies RAD17 as synthetically lethal with checkpoint kinase inhibition. *Oncotarget*. 2015 Sep 30;6(34).
249. Wilkes DC, Sailer V, Xue H, Cheng H, Collins CC, Gleave M, et al. A germline FANCA alteration that is associated with increased sensitivity to DNA damaging agents. *Molecular Case Studies*. 2017-09-01;3(5).
250. Furini HH, Fukushima K, M DEN, MF DES, Rodrigues MRS, BB DEM, et al. An MGMT Allelic Variant Can Affect Biochemical Relapse in Prostate Cancer Patients. *Anticancer Res*. 2023;43(1):369-79.
251. Velho PI, Qazi F, Hassan S, Carducci MA, Denmeade SR, Markowski MC, et al. Efficacy of Radium-223 in Bone-metastatic Castration-resistant Prostate Cancer with and Without Homologous Repair Gene Defects. *European Urology*. 2019/08/01;76(2).
252. Paschalis A, Sheehan B, Riisnaes R, Rodrigues DN, Gurel B, Bertan C, et al. Prostate-specific Membrane Antigen Heterogeneity and DNA Repair Defects in Prostate Cancer. *European Urology*. 2019/10/01;76(4).
253. Kinnaman MD, Zaccaria S, Makohon-Moore A, Arnold B, Levine MF, Gundem G, et al. Subclonal Somatic Copy-Number Alterations Emerge and Dominate in Recurrent Osteosarcoma. *Cancer Res*. 2023;83(22):3796-812.
254. McGeorge S, Kwok M, Jiang A, Emmett L, Pattison DA, Thomas PA, et al. Dual-Tracer Positron-Emission Tomography Using Prostate-Specific Membrane Antigen and Fluorodeoxyglucose for Staging of Prostate Cancer: A Systematic Review. *Advances in Urology*. 2021 Aug 18;2021.
255. Alberts I, Schepers R, Zeimpekis K, Sari H, Rominger A, Afshar-Oromieh A. Combined [68 Ga]Ga-PSMA-11 and low-dose 2-[18F]FDG PET/CT using a long-axial field of view scanner for patients referred for [177Lu]-PSMA-radioligand therapy. *European Journal of Nuclear Medicine and Molecular Imaging*. 2023;50(3):951-6.

## ACKNOWLEDGEMENTS

First and foremost, I would like to express my deepest gratitude to my supervisor, Dr. Martina Benešová-Schäfer, for her invaluable guidance, continuous support, and unwavering trust throughout my PhD journey. Her scientific insight and encouragement have been instrumental in shaping both this thesis and my development as a researcher.

A heartfelt thank you goes to Dr. Mareike Roscher, whose mentorship, patience, and practical advice were essential at every step of this work. Her dedication and attention to detail helped me navigate many of the challenges I faced along the way.

I am incredibly grateful to my research group, Translational Radiotheranostics at DKFZ E270, for fostering such a collaborative and motivating environment. I also deeply appreciate our partners at the University Hospital Heidelberg for providing the clinical samples that formed the backbone of this project. A special thank you goes to Dr. Clemens Kratochwil for his invaluable support in patient recruitment, sample collection, and assistance with the clinical evaluation. I would also like to extend my sincere thanks to Dr. Alfred Morgenstern and Dr. Frank Bruchertseifer for their guidance, support, and contributions throughout this project.

Special thanks to Dr. Vladimir Benes, Dr. Tobias Rausch and M.Sc. Hilal Ozgur and the team at the EMBL Genomics Core Facility for their outstanding support in generating and guiding the sequencing work. I truly appreciate their expertise and responsiveness throughout this process.

Finally, I would like to acknowledge the Biostatistics Core Facility and specifically Dr. Thomas Hielsher at DKFZ for their support in the statistical analysis and for always being available to help interpret complex data with clarity and precision.

A very special thanks go to my first Ph.D. thesis advisor, Prof. Gert Fricker from the Heidelberg University, for joining my Thesis Defence Committee and for his helpful feedback, support and evaluation of my doctoral thesis. I wish to thank also to other members of my Thesis Advisory Committee, Prof. Nina Papavasiliou from the DKFZ, for his valuable advice, contributions during my Ph.D. studies and for being part of my Thesis Defence Committee. My thanks also go to Prof. Holger Sültmann for joining my Thesis Advisory Committee and Thesis Defence Committee for the experiences that he shared with me and help provided along my PhD journey.

This thesis would not have been possible without the contribution of each of these individuals and institutions. I am deeply thankful for their support.

I would like to express my heartfelt gratitude to my family for their unwavering support. To my beloved parents and dear brothers—thank you for your constant encouragement, love, and strength throughout this journey.

GRAZIE MILLE A TUTTI  
HERZLICHEN DANK AN ALLE  
THANKS TO  
EVERYBODY

شكراً لكم



## LIST OF PUBLICATIONS

Amghar M., et al: *Future treatment strategies for cancer patients combining targeted alpha therapy with pillars of cancer treatment: External beam radiation therapy, checkpoint inhibition immunotherapy, cytostatic chemotherapy, and brachytherapy*. Pharmaceuticals, 17(8), 1031. <https://doi.org/10.3390/ph17081031> (2024).

Amghar M., et al: *Circulating Tumor DNA as Predictor of Response to [<sup>225</sup>Ac]Ac-/[<sup>177</sup>Lu]Lu-PSMA-617 in Metastatic Castration-Resistant Prostate Cancer*. (In preparation).

Amghar M., et al: *[<sup>225</sup>Ac]Ac-/[<sup>177</sup>Lu]Lu-PSMA-617 mutational landscape in circulating tumor DNA (ctDNA): early clinical outcome prediction in metastatic castration-resistant prostate cancer*. (In preparation).

Amghar M. et al: *Case Study: [<sup>225</sup>Ac]Ac-/[<sup>177</sup>Lu]Lu-PSMA-617 Therapy in a Chemotherapy-Naïve metastatic castration-resistant prostate cancer patients*. (In preparation).



## ABSTRACTS FROM CONFERENCES

Amghar M., et al: DαRT and PSMA-TαT combination therapy for prostate cancer as a precision medicine approach. 45<sup>th</sup> Joint Scientific Program DKFZ-MOST, Virtual conference, **2022**.

Amghar M., et al: *Molecular Radiation Resistance Signature Induced by Alpha Emitters in Metastatic Castration-resistant Prostate Cancer: Early Clinical Outcome Prediction*. 25<sup>th</sup> ISRS Conference, Honolulu (Hawaii, USA), **2023**.

Amghar M., et al: *DαRT and PSMA-TαT combination therapy for prostate cancer as a precision medicine approach*. 46<sup>th</sup> Joint Scientific Program DKFZ-MOST, Tel Aviv (Israel), **2023**.

Amghar M., et al: *[<sup>225</sup>Ac]Ac-PSMA-617 mutational landscape in circulating tumor DNA (ctDNA): early clinical outcome prediction in metastatic castration- and chemo-resistant prostate cancer*. 36<sup>th</sup> EANM Conference, Vienna (Austria), **2023**.

Amghar M. et al: *Ca201 - <sup>225</sup>Ac-PSMA-617 mutational landscape in circulating tumor DNA (ctDNA): early clinical outcome prediction in metastatic castration-resistant prostate cancer*. 48<sup>th</sup> Joint Scientific Program DKFZ-MOST, Heidelberg, (Germany), **2024**.

Amghar M., et al: *Alpha-particle therapy in mCRPC: Case studies utilizing ctDNA as a therapeutic biomarker for early clinical outcome prediction*. 37<sup>th</sup> EANM Conference, Hamburg (Germany), **2024**.

Amghar M., et al: *Molecular Radiation Resistance Signatures Induced by Alpha Emitters in mCRPC: Predicting Early Clinical Outcomes*. AGRR/grpw Conference, Mannheim (Germany), **2024**.

Amghar M., et al: *Genetic Variations in Chemo-naïve mCRPC: Insights into Alpha Therapy Resistance*. 26<sup>th</sup> ISRS Conference, Gold Coast (Australia), **2025**.

Amghar M., et al: *Predictive Role of Tumor Fraction and Copy Number Alteration Burden in mCRPC Patients Receiving Tandem Actinium-Lutetium Radionuclide Therapy*. 67<sup>th</sup> ASTRO annual meeting, San Francisco (California, USA), **in submission**.

## SELECTION OF INVITED LECTURES

Amghar M., et al: *[<sup>225</sup>Ac]Ac-PSMA-617 mutational landscape in circulating tumor DNA (ctDNA): early clinical outcome prediction in metastatic castration-resistant prostate cancer*. Harvard Medical School, Virtual lecture, **2024**.

Amghar M., et al: *[<sup>225</sup>Ac]Ac-PSMA-617 mutational landscape in circulating tumor DNA (ctDNA): early clinical outcome prediction in metastatic castration-resistant prostate cancer*. University of Technology di Sydney (UTS), Sydney (Australia), **2024**.

## LIST OF ABBREVIATIONS & ACRONYMS

<b>PSMA</b>	Prostate-Specific Membrane Antigen
<b>PCa</b>	Prostate Cancer
<b>DRE</b>	Digital rectal examination
<b>ERBT</b>	External beam radiation therapy
<b>CRPC</b>	Castration resistant prostate cancer
<b>mCRPC</b>	Metastatic castration resistant prostate cancer
<b>ARPIs</b>	Androgen receptor pathway inhibitors
<b>LET</b>	Linear energy transfer
<b><sup>177</sup>Lu</b>	Lutetium
<b><sup>255</sup>Ac</b>	Actinium
<b>SSB</b>	Single strand break
<b>DSB</b>	Double strand break
<b>PSA</b>	Prostate-Specific Antigen
<b>DNA</b>	Deoxyribonucleic Acid
<b>LDH</b>	Lactate Dehydrogenase
<b>CNV</b>	Copy Number Variation
<b>ALP</b>	Alkaline Phosphatase
<b>CKD</b>	Chronic Kidney Disease
<b>EPI</b>	Epidemiology (likely part of GFR-CKD-EPI formula)
<b>TRNT</b>	Targeted Radioligand Therapy
<b>Cox PH</b>	Cox Proportional Hazard
<b>PET</b>	Positron Emission Tomography
<b>GFR</b>	Glomerular Filtration Rate
<b>cfDNA</b>	Circulating free DNA
<b>ctDNA</b>	Circulating tumor DNA
<b>CTCs</b>	Circulating tumor cells
<b>NGS</b>	Next generation sequencing
<b>MRD</b>	Minimal residual disease

<b>GCR</b>	Good clinical practice
<b>GDPR</b>	General data protection regulations
<b>PE</b>	Pair end
<b>Mb</b>	Mega bases
<b>HMM</b>	Hidden Markov model
<b>HETD</b>	Hemizygous deletion
<b>NEUT</b>	Copy neutral
<b>GAIN</b>	Gain
<b>AMP</b>	Amplification
<b>HLAM</b>	Higher level copy
<b>CNA</b>	Copy number alteration
<b>TFx</b>	Tumor Fraction
<b>GISTIC</b>	Genomic Identification of Significant Targets in Cancer
<b>CT</b>	Computed Tomography
<b>CNA</b>	Copy Number Alteration
<b>SPECT</b>	Single-Photon Emission Computed Tomography
<b>ROC</b>	Receiver Operating Characteristic
<b>OS</b>	Overall Survival
<b>ADT</b>	Androgen Deprivation Therapy
<b>CNVs</b>	Copy Number Variations
<b>IQR</b>	Interquartile range
<b>AR</b>	Androgen Receptor
<b>RLT</b>	Radioligand Therapy
<b>TM</b>	Tumor Marker
<b>ULP</b>	Ultra-Low Pass
<b>WGS</b>	Whole Genome Sequencing
<b>MRI</b>	Magnetic Resonance Imaging
<b>AUC</b>	Area Under the Curve
<b>NSCLC</b>	Non-small cell lung cancer
<b>DDR</b>	DNA repair damage

<b>HDR</b>	Homology directed repair
<b>HRR</b>	Homology repair recombination
<b>PD</b>	Progressive disease
<b>SD</b>	Stable disease
<b>PR</b>	Partial remission





# APPENDIX

**Table A1:** *Number of samples per patient sequenced.*

Patient	Number of samples per patient
P10	7
P100	2
P101	2
P11	5
P12	4
P14	3
P15	3
P16	2
P20	2
P21	2
P23	3
P25	1
P27	1
P28	1
P3	2
P30	1
P33	1
P34	3
P35	4
P36	1
P37	5
P38	5
P39	2
P4	2
P40	3
P41	1
P42	2
P43	3
P44	2
P45	1
P46	1
P47	1
P48	1
P49	2
P5	3
P50	2
P51	3
P52	2
P53	2
P54	2
P55	1

---

P56	4
P58	2
P59	2
P6	2
P60	1
P61	2
P62	2
P63	4
P65	3
P66	2
P67	3
P69	2
P7	1
P70	1
P72	3
P75	1
P8	2
P80	2
P81	2
P82	3
P83	1
P84	2
P85	2
P86	2
P87	3
P88	1
P89	1
P9	1
P90	2
P91	3
P93	2
P94	3
P95	1
P96	2
P97	2
P98	2
P99	2

---

**Table A2:** List of R Packages Utilized for Data Analysis. This table provides an overview of the various R packages employed to conduct the analysis. Each package is identified with its specific function or role in processing, analysing, or visualizing the data, ensuring a comprehensive approach to the research methodology.

R Packages
readxl
robustrank
ggpubr
broom
plyr
survival
swimplot
pROC
Publish
table1
Hmisc
limma
prodlim
openxlsx
pheatmap
dplyr
tidyr
VennDiagram
ggplot2
MetBrewer
stringr
UpSet
ComplexHeatmap
Grid
gridGraphics
scales
wesanderson
svglite
ggsignif
cluster
GenomicFeatures
GenVisR
knitr
kableExtra
viridis

**Table A3:** Reference values for PSA, Tfx and LDH.

Tumor Marker	Reference
PSA ng/mL	<4
Tfx	<0.10
LDH (U/L)	<342
ALP (U/L)	40-130

**Table A4:** Reference values for GFR-CKD-EPI, Creatinine, Hemoglobin, Leukocyte.

Parameter	Reference
GFR-CKD-EPI (mL/min/1.73qm)	≥ 90
Creatinine (mg/dL)	0.6 – 1.4
Hemoglobin (g/dL)	13-17
Leukocyte (G/nL)	4-10